TECHNISCHE UNIVERSITÄT MÜNCHEN

Fakultät für Chemie, Lehrstuhl Technische Elektrochemie

Novel Electrolyte Solvents and Additives for Lithium-Ion Batteries and Different Materials Degradation Phenomena

Rebecca Juliane Bernhard

Vollständiger Abdruck der von der Fakultät für Chemie der Technischen Universität München zur Erlangung des akademischen Grades eines

Doktors der Naturwissenschaften

(Dr. rer. nat.)

genehmigten Dissertation.

Vorsitzender: Univ.-Prof. Dr. Ville R. I. Kaila

Prüfer der Dissertation:

1. Univ.-Prof. Dr. Hubert A. Gasteiger

2. Univ.-Prof. Dr. Bernhard Rieger

Diese Dissertation wurde am 05.08.2014 bei der Technischen UniversitätMünchen eingereicht und durch die Fakultät für Chemie am 01.09.2014 angenommen.

Ein Gelehrter in seinem Laboratorium ist nicht nur ein Techniker; er steht auch vor den Naturgesetzen wie ein Kind vor der Märchenwelt.

– Marie Curie (1867 - 1934) –

Für meine Familie

Contents

1. Statement of authorship / Selbständigkeitserklärung

Technische Universität München
Fakultät für Chemie
Lehrstuhl Technische Elektrochemie
Lichtenbergstrasse 4
D-85748 Garching bei München

Name: Rebecca Juliane Bernhard

Hiermit erkläre ich ausdrücklich, dass es sich bei der von mir eingereichten schriftlichen Dissertation, zur Erlangung des akademischen Grades eines Doktors der Naturwissenschaften, mit dem Titel

Novel Electrolyte Solvents and Additives for Lithium-Ion Batteries and Different Materials Degradation Phenomena

um eine von mir selbstständig und ohne fremde Hilfeleistung verfasste schriftliche Arbeit handelt. Ich erkläre zudem, dass ich sämtliche verwendeten Angaben aus der Literatur (Internet, Bücher, wissenschaftliche Zeitungen und wörtlich übernommene Tabellen und Graphiken etc.) als solche kenntlich gemacht habe. Abbildungen und Tabellen, die aus eigenen Veröffentlichungen stammen, sind ebenfalls als solche kenntlich gemacht.

Garching bei München, den ....

....
(Rebecca Bernhard)

2. Acknowledgment

Then, I want to thank Dr. Frédéric Hasché for his advices during the editing process and the great time at TEC during the last years.

Thanks to the whole TEC group – It was a great time and a pleasure to work with you!

Also, a big "Thank you" to my friends Carina Rein and Michael Stekly for spending their free-time on proofreading my thesis.

Zu guter Letzt möchte ich mich noch herzlich bei meiner Familie und meinen Freunden bedanken (leider kann ich euch hier nicht alle namentlich aufführen, aber ihr wisst ja, dass ihr gemeint seid :-)). Dabei gilt natürlich ein besonderer Dank meinen Eltern Klaus-Peter & Petra Simone Zeh, sowie meinen Großeltern Heinz & Helga Kramer und Lothar & Renate Zeh und meinem "kleinen" Bruder Adrian Zeh für die langjährige und großzügige finanzielle, sowie liebevolle Unterstützung während meines Studiums und der Doktorarbeit. Ich danke euch dafür, dass ihr mir den Alltag erleichtert und immer ein offenes Ohr für meine größeren und kleineren Anliegen habt. Ihr seid die Besten! Danke, dass ihr alle immer für mich da seid. Ein besonders großes Dankeschön geht natürlich auch an meinen lieben Mann Andreas Bernhard, der neben Korrekturlesen und "Händchen-halten" mit seiner besonnenen Art immer dafür sorgt, dass ich den "Blick für das Wesentliche im Leben" nicht verliere. Du weißt ja: "bis zur Unendlichkeit und noch viel weiter".

3. Abstract

Due to the demand on energy storage systems for renewable energies, lithium-ion batteries seem to be a promising solution. Unfortunately there are several unknown aging aspects for almost all lithium-ion battery systems. Several aspects like overcharging, high temperature, impurities, loss of electric or ionic contact or increase of the overall resistance of the battery system are already known [1–3]. However, these aspects are insufficiently evaluated and discussed. For this reason the main focus of this work lies on the investigation of electrolyte additives and degradation ("aging") behaviors influencing lithium-ion battery systems and its components. Measurements were performed in half cell and full cell test set-up using lithium titanate ($Li_4Ti_5O_{12}$, LTO), lithium iron phosphate ($LiFePO_4$, LFP) and also graphite as active material.

Several measurements were performed in home designed and manufactured laboratory test cell systems. The development of the three-electrode Swagelok ® test cell was developed in cooperation with F. Kindermann during his master thesis, his supervisors R. Karl and Prof. Dr. A Jossen (Chair of Electrical Energy Storage Systems (EES), TU München) and with consultation of Dr. Milos Vracar (Karlsruhe Institute of Technology (KIT)).

A novel electrolyte solvent and an ionic liquid as an additives were under investigation to improve the safety of the electrolytes and to find proper solvent mixtures to increase the thermal and electrochemical stability. On the one hand additives should assure an adequate ionic conductivity and cycling performance, but on the other hand a high safety with a low vapor pressure and non-flammable behavior. In addition, we have focused on different aging aspects like the corrosion behavior of current collector materials with the use of lithium bis-(trifluoromethanesulfonyl)-imide (LiTFSI) as conductive salt. Some experiments were performed by Susanne Herden during her Bachelor thesis. In cooperation with researchers from FRM II (Forschungs-Neutronenquelle Heinz Maier-Leibnitz, Garching bei München) the iron dissolution of the LFP olivine structure in contact with $LiPF_6$ was investigated with prompt gamma ray activation analysis (PGAA). In the last chapters the gassing behavior of LTO and graphite anode containing cells were discussed and analyzed using on-line electrochemical mass spectrometry (OEMS) for gas fraction detection during the charge and discharge of the cells.

Heutzutage ist eine der bedeutendsten wissenschaftlichen Herausforderungen die Entwicklung von Energiespeichersystemen zur nachhaltigen Speicherung von erneuerbaren Energien wie Wind-, Sonnen- und Wasserkraft. Einige wissenschaftliche Recherchen im Bereich der Batterieforschung zeigen, dass Lithium-Ionen Batterien grundsätzlich geeignet wären, um in diesem Gebiet Anwendung zu finden. Allerdings ist eine kommerzielle Anwendung vorhandener Batteriesysteme derzeit noch nicht möglich, da es sehr viele bisher unbekannte Alterungsaspekte für nahezu alle bekannten Lithium-Ionen Batteriesysteme gibt. Zu den Aspekten gehören neben einem optimalen Zellmanagement

auch Überladungseffekte, erhöhte Temperaturen, die im Sommer oder bei Überhitzung eine tragende Rolle spielen könnten, Verunreinigung durch die Elektrodenmaterialien selbst oder Nebenprodukte, die bei einer Elektrolytzersetzung entstehen können. Zu dem können der elektrische oder ionische Kontaktverlust, sowie ein Anstieg des Zellwiderstands die Batteriesysteme schnell und unkontrolliert altern lassen und sind derzeit noch nicht ausreichend erforscht und verstanden.

Aus diesem Grund liegt der Fokus dieser Arbeit zum einen auf grundsätzlichen Konzepten, wie zum Beispiel einer Verbesserung des Zellsystems durch neuartige Elektrolytlösungsmittel und Zusätze, um die Flammbarkeit des Elektrolyten herabzusetzen, die thermische und elektrochemische Stabilität zu erhöhen und trotzdem eine gute ionische Leitfähigkeit und Zyklenstabilität zu erreichen. Bestimmte Alterungsaspekte wie zum Beispiel die Stromabnehmerkorrosion von Aluminium durch Verwendung verschiedener Leitsalze wurden untersucht. Hierzu wurden einige Messungen von Susanne Herden im Rahmen ihrer Bachelorarbeit durchgeführt. Ein weiteres Thema ist Eisenauflösung aus LFP Elektroden, die in Kontakt mit $LiPF_6$-haltigem Elektrolyt standen. Hier wurden in Zusammenarbeit mit Dr. S. Seidlmayer, Dr. V. Zinth und Dr. P. Kudejova der Forschungs-Neutronenquelle Heinz Maier-Leibnitz (FRMII) (Garching bei München) gealterte Elektroden mit prompter Gamma-Aktivierungs-Analyse (PGAA) analysiert. In den letzten beiden Kapiteln wird Gasentwicklung bei Wasserverunreinigung an den beiden Anodenmaterialien $Li_4Ti_5O_{12}$ (LTO) und Graphit (Untersuchung mit on-line elektrochemischer Massenspektrometrie (OEMS) wurden untersucht und quantifiziert.

Sämtliche Zellmessungen wurden in selbst designten Stahltestzellen durchgeführt - sowohl für Zwei- und Drei-Elektrodenanordnung. Das Drei-Elektroden Zelldesign wurde im Rahmen einer Masterarbeit von F. Kindermann (Lehrstuhl für Elektrische Energiespeicher Technik (EES), TU München, Betreuer R. Karl und Prof. Dr. A. Jossen) und mit freundlicher Unterstützung von Dr. Milos Vracar (Karlsruher Institut für Technologie (KIT)) entwickelt.

This doctoral thesis integrates experiments and results performed and gained in the laboratories of Prof. Dr. H. A. Gasteiger and Prof. Dr. B. Scrosati (visiting doctoral-candidate from May to August 2012 at the University La Sapienzá in Rome (Italy)) during my time as doctoral candidate at the Chair of Technical Electrochemistry (TEC) at the Technische Universität München from October 2010 until July 2014. The thesis contains a general introduction about lithium-ion battery technology, as well as an overview about the experimental background and several results of basic and aging aspects of advanced lithium-ion batteries.

4. Introduction - A brief Review of the Working Principle of Li-Ion Batteries

Not only since the nuclear incident in Fukushima (Japan) in March, 2011 a world-wide demand for alternative electrical power supply is discussed in politics. After the last alarming incident in Japan, the German government forced the shut-down of seven old nuclear power plants and the simultaneous energy turnaround [4]. Therefore, the use of renewable energy sources like wind- and solar is subsidized and promoted. Politicians, researchers and engineers are confronted with a big challenge to find a suitable storage solution for these power sources. Nowadays storage technologies like pumped storage hydro power stations cover about 99 % of the world wide demand for free storage capacity and correspond to $\approx$ 127 GW, whereby only 10 % of the average daily maximum demand is covered by pumped storage hydro power stations [5]. Geographic suitable regions for pumped storage hydro power stations are limited and not infinitely available. For this purpose, electrochemical battery storage systems are promising candidates for this application in the future time.

For example, lithium-ion (li-ion) batteries are used in a wide range of applications, depending on energy and power density, cell voltage, cell chemistry and size. Application areas are for example electro-mobility for cars in plug-in hybrid electric vehicles (PHEVs), hybrid electric vehicles (HEVs) and full battery electric vehicles (BEVs), scooters and bicycles, aeronautics, portable devices like computers and cell phones. They are also suitable for stationary energy storage devices, which can work as reservoir conservation connected to wind and solar power plants, for both windless and rainy days as well as at night time. According to the different requirements of applications, the battery needs to be reliable in a wide temperature range, which exhibits a big challenge for research and engineering. Li-ion technology possesses a high charge and discharge efficiency and different adaptable characteristics of energy- and power content. In general, this technology has a high cycle life and persistence, low maintenance costs and the possibility for a modular application. A main disadvantage of the use of lithium-ion technology are the high manufacturing price, not fully understood reactions occurring during charging and discharging, thermal stability of conductive salts in the electrolyte and safety issues. For this reason, there is a world wide effort in many research groups to investigate lithium-ion technology and to solve present problems.

Li-ion batteries were introduced to the market by Sony in 1991 [6, 7] for portable applications. However, in the meantime modern batteries gain a higher energy density, which is a factor of 2.5 higher than in former times [8], compared to the first commercial versions sold in 1991 and are in addition about ten times cheaper. According to the state-of-art, the limits for price reduction and energy density are almost reached [9]. For this reason, several issues like high voltage materials (high voltage spinel oxides or lithium cobalt phosphate (Lcp, $LiCoPO_4$)) to increase the energy density [10, 11], improvement of cycle and shelf life to reduce the cost per year, and safety issues like
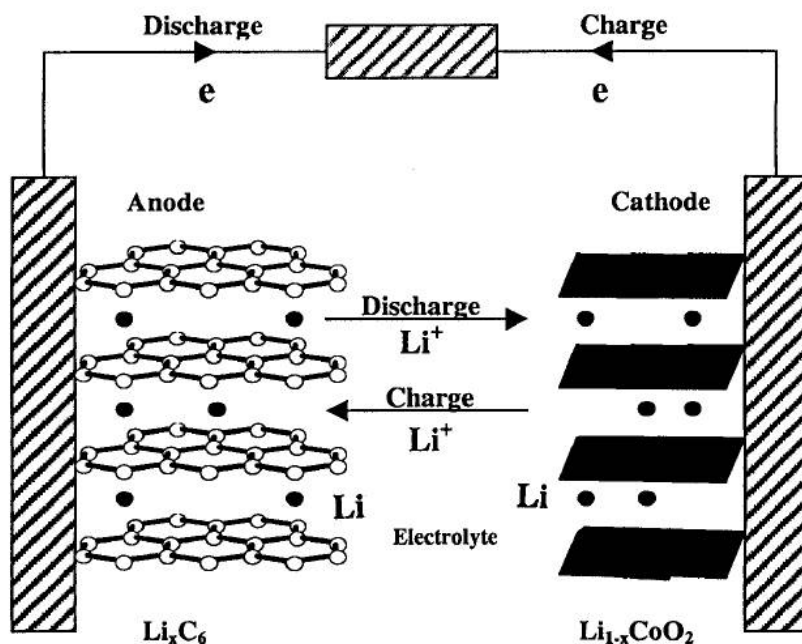
Figure 1: Simplified charge and discharge scheme of a lithium-ion battery with a graphite anode and a lithium cobalt oxide cathode [19].

replacing common flammable liquid organic carbonates used in the electrolyte [12, 13]. Those issue as well as the replacement of the anode material to reduce dendrite growing after a longer time of cycling [14], are discussed and investigated from several research groups. Some approaches make use of batteries based on a renewing electrode chemistry - chemical reactive electrode materials like it is the case for lithium-sulfur, for example, which was discovered by Herbert and Ulam in 1962 [15], or lithium-air (lithium-oxygen) introduced in the late 1990s from K.M. Abraham and coworkers [16] - instead of the common lithium-ion intercalation materials like graphite, lithium titanate (first reported in Prof. Dahn's group by Colbow et al. and E. Rossen et al. in 1989 and early 1990s [17,18]) on the anode or lithium metal oxides, lithium metal phosphates or high voltage spinels on the cathode side.

At the beginning one should concentrate on lithium-ion intercalation materials like it is known for common lithium-ion batteries. The scheme in **Figure 1** briefly explains the charge and discharge reaction of a typical lithium-ion intercalation system consisting of a graphite anode and a lithium cobalt oxide cathode. For the charging reaction of the battery system, lithium-ions are de-intercalated from the cathode species due to an oxidation reaction (**Figure 1**). Lithium-ions are solvated from the solvent molecules in the electrolyte and migrate through the separator, wetted with electrolyte, to the anode side, where lithium-ions are re-intercalated into the graphite layers under a reduction reaction. Both electrodes are connected with an external electric circuit which transports electrons (e$^-$) from the redox reactions between electrodes. The discharge reaction oc-
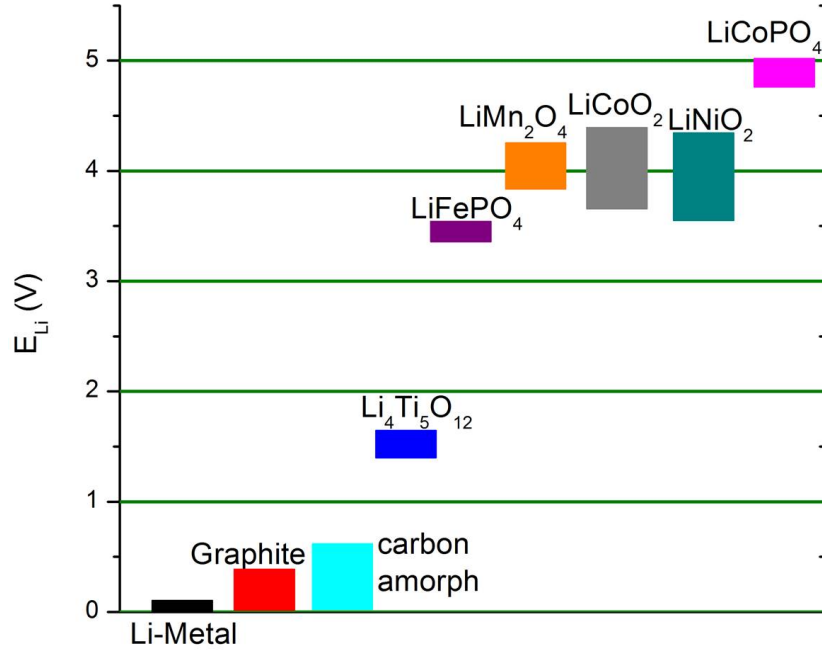
Figure 2: Characteristic redox potentials of different known electrode materials used in lithium-ion batteries (In dependence of figure in reference [22] and information [23]).

curs vice-versa. Layered graphite exhibits a specific capacity of 336 mAh/$g_{Graphite}$ [20]. However, this fact is also depending on the type of graphite, higher capacities are reported [19, 21] with a working potential of lower 0.5 V_{Li} [22]. This capacity is about 10 times smaller compared to metallic lithium. However, the use of graphite offers significant advantages for cycling, storage and safety [19]. The mentioned cathode material lithium cobalt oxide (Lco, $LiCoO_2$) offers a capacity of $\approx$ 140 mAh/g_{LiCoO2} with a redox potential of 3.5 to 4.3 V_{Li}. With these specifications and **Equation (1)** one can calculate the specific energy of the different electrode combinations in a battery system;

$$specific\ energy\ [Wh/kg] = C_{cell}\ [Ah/kg] \cdot E_{cell}\ [V] \tag{1}$$

Whereby C is the specific capacity of the cell, given in [mAh/g] or [Ah/kg] and E is the cell potential in [V]. Increasing either the specific capacity or cell voltage, one can also increase the energy content of the battery cell. An overview of the different redox potentials of common used electrode materials is shown in the following **Figure 2**. With the use of high voltage spinels like Lcp or phosphates with nickel, manganese or also doped versions, one can provide an increased energy of $\approx$ 20% compared to common systems [23].

The focus of this work is on electrode materials like graphite, lithium titanate (Lto, $Li_4Ti_5O_{12}$) and lithium iron phosphate (Lfp, $LiFePO_4$). Battery systems consisting of Lto and Lfp show, according to **Equation (1)**, a very low specific energy, which makes this system not interesting for the use as a power supply in battery vehicles. However,
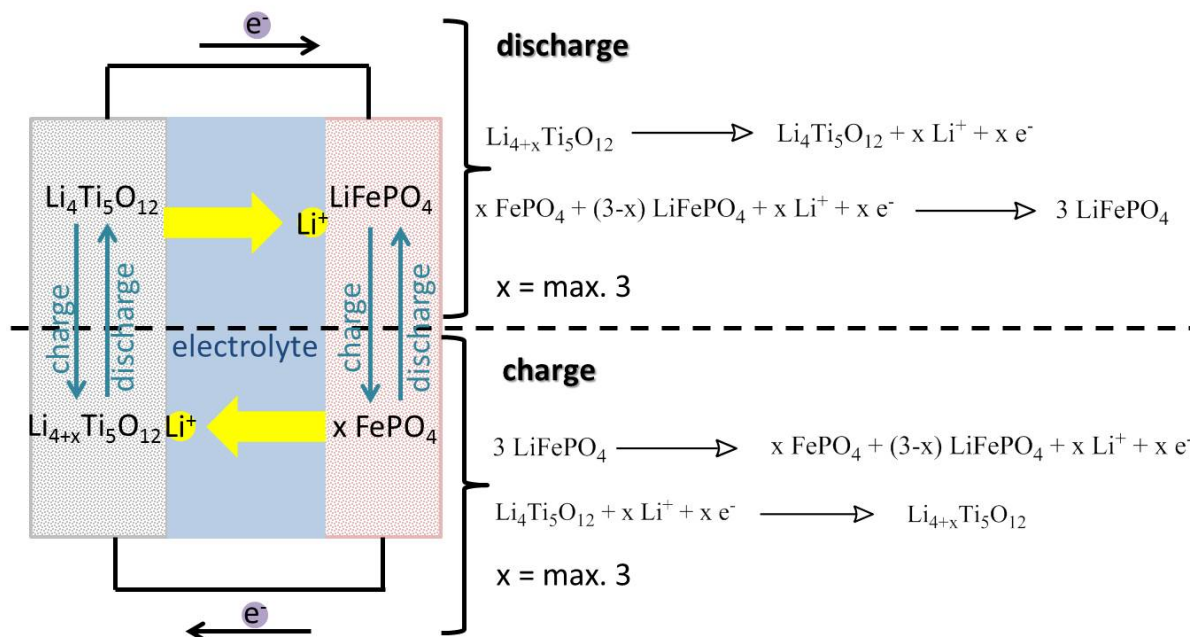
Figure 3: Working principle during discharge (upper part) and charge (bottom part) of a LTO/LFP full cell and its redox reactions occurring on both electrode sides.

both materials show interesting characteristics and are worth to investigate more effort into research.

LTO is used as a high potential anode material with a redox potential at 1.55 V_{Li} [24–26]. It is known to be a very safe material in terms of dendrite formation and less electrolyte reduction reactions. In contrast to layered graphite, spinel LTO is known as a zero-strain material, which shows practically no volumetric change during charge and discharge [27, 28]. These characteristics lead to the fact, that LTO shows a very good long term performance with almost no capacity fade. LFP as cathode material is also very interesting, because it is a cheap, non-toxic and environmentally benign component [29, 30]. Due to its relative low working potential at $\approx$ 3.4 V_{Li} [31], the electrochemical stability of the electrolyte is warranted. Potentials between 4 and 4.5 V_{Li} lead to a reduction of solvent molecules like propylene carbonate, resulting to the formation of gaseous CO_2 [32–34], which reduces the cycling stability and capacity retention of the cell.

The schematic working principle of a LTO/LFP battery cell is shown in **Figure 3**. During the charge of the electrode, the Fe^{2+} species of LFP gets oxidized to Fe^{3+} forming iron phosphate (FP). Li^+-ions are released into the electrolyte, are solvated and transported through the separator to the LTO anode side. At the same time electrons (e^-) are conducted via an external circuit to the anode side. Here, lithium-ions and electrons react under intercalation into the spinel structure of LTO forming with $Li_4Ti_5O_{12}$ the charged $Li_{4+x}Ti_5O_{12}$-species, under reduction of the Ti^{5+}-species, forming a mixed

14
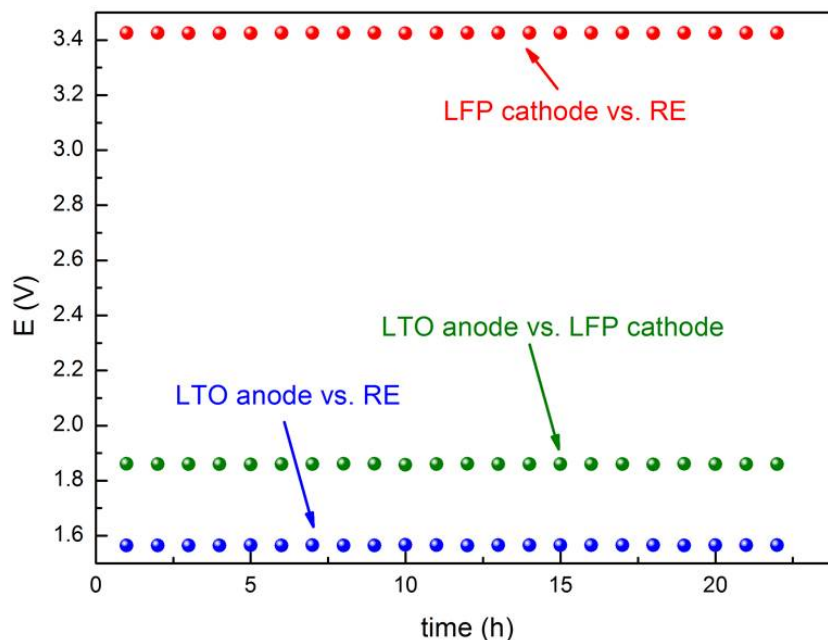
Figure 4: Recorded potentials of a LTO/LFP full cell measured with a 3-electrode set-up over 24 hours at room temperature.

oxidation state of Ti^{4+} and Ti^{5+}. The maximum possible amount of lithium ions intercalating into the LTO is x = 3. The discharge process is vice versa and shown in the upper part of **Figure 3**. Combining these electrode materials to a full cell, one can record the resulting cell potential in a 3-electrode test cell (further details about cell set-up is given in the experimental part in **Chapter 5.1.4**). The use of a metallic lithium reference electrode in the 3-electrode set-up allows to follow the potential of anode and cathode separately from the full cell potential. These potentials are plotted in **Figure 4**. According to the redox potential of each active material on the anode and cathode side, one can calculate the redox potential of the full cell combination to be 1.85 V. The typical cell profile of a LTO/LFP cell is shown in **Figure 5** with a redox potential plateau located at $\approx$ 1.9 V in the charging step and $\approx$ 1.8 V in the discharging step. The theoretical value for the redox potential is shown by the dotted line located at 1.85 V graph. The plateaus for charge and discharge are slightly lower or higher, respectively, namely $\approx$ 0.05 V, than expected. This fact is related to the overpotential resulting due to IR-drops caused by ohmic losses for example of the separators, electronic contact between electrode coatings and current collectors, and compression of the electrode itself. An important issue for the performance of full cells is the so called N/P ratio (capacity ratio calculated by dividing the areal loading of the negative electrode (anode) by the positive electrode (cathode)) [35]. However, this is not well explored [36, 37]. N/P-ratios, which are used very often have a range from 1.1 to 1.3 to avoid lithium deposition on the anode surface [38].

The introduced LTO/LFP system is a promising candidate for a system in the field
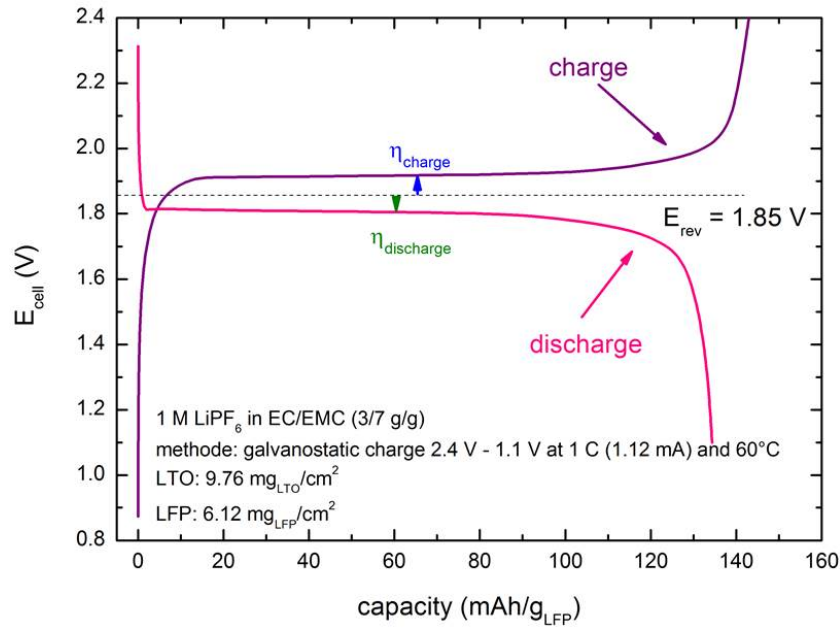
Figure 5: Typical cell profile of a LTO/LFP full cell comprising a LTO anode, LFP cathode and three-layer polymer separator soaked with organic carbonate based electrolyte solution. The cell was charged in a potential window of 2.4 V to 1.1 V at a rate of 1C, whereby the capacity is limited to the cathode (N/P ratio 1.6).

of long-term stationary storage application. Therefore, a low energy density plays an ancillary role, whereby, the cost, life-time for cycling and storage are the most important arguments. In 2010, researchers from Hydro Quebec in Canada have shown that LTO/LFP is able to be charged and discharged about 20.000 times with a stable capacity at high C-rates with an organic electrolyte [39, 40]. This high cycle-life show almost no degradation of the battery components.

5. General Experimental Concepts

5.1. General Background on Electrochemistry

5.1.1. Electrochemical Reactions

An electrochemical process is defined by a connection of a *chemical* reaction with *electric* current. Reactions take place in aqueous or organic solutions at the interface of a porous electrode, metal or semi-conductor (electron conductor) and the electrolyte (ionic conductor). That means, an electron transfer to or from an electrochemical material or species (electrode material) leads to an reduction or oxidation of the active species (change of the oxidation state). A general electrochemical process is defined by **Equation (2)**; in general, both species are separated from each other and connected by an external electric circuit.

$$Oxidized\ species + n\ e^- \rightleftarrows reduced\ species \tag{2}$$

Ions are transported via the internal ion-conductive circuit and the electrons (e^-) via an external electric circuit. An electrochemical reaction can be forced due to an external applied voltage, as it is the case for reactions like *e.g.* water electrolysis or if the chemical reaction creates a voltage like *e.g.* in batteries during discharge or in the galvantic cell and is (in general) fully reversible, without considering losses due to parasitic side-reactions.

The different redox-potentials are depended on the activities of the reduced (a_{Red}) and oxidized (a_{Ox}) species, temperature (T in [K]), pressure of gaseous reactants and the potential at standard conditions (E_0 in [V]), also known as standard half cell potential, whereby the electrochemical potential is the driving force for redox reactions. The Nernst equation gives the reversible equilibrium potential (E_{equ} in [V]) for an electrochemical reaction, shown in **Equation (3)** [41, 42].

$$E_{equ} = E_0 + \frac{R \cdot T}{n \cdot F} \cdot ln\left(\frac{a_{Ox}}{a_{Red}}\right) \tag{3}$$

With this equation the equilibrium potential can be calculated in dependency on the activity a_{Ox} and a_{Red} (considering an activation factor f=1, the activity is equal to the concentration), whereby R is the gas constant 8.3145 J/mol K, F the Faraday constant 96485.34 C/mol, standard temperature 25°C or 298 K and n the number of transfered electrons during the redox process. Standard potentials E_0 of several half cell reactions can be found in the electrochemical series.

5.1.2. Electrochemical Double Layer

As mentioned before, electrochemical processes take part at the interface between the surface of an electron conductor (electrode/metal) and ionic conductor (electrolyte),

17
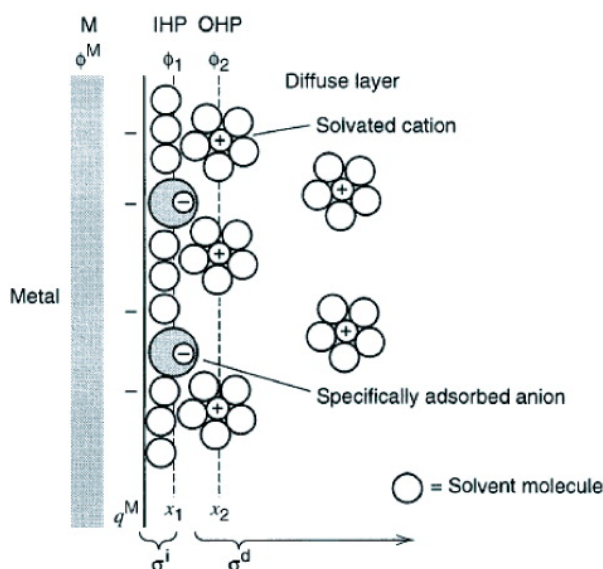
Figure 6: Schematic model of the electrochemical double-layer in direct environment to the electrode surface [41].

which form a so called electrochemical double layer. A schematic model of this double layer is shown in **Figure 6**. The double layer itself consists of several "layers" - inner Helmholz-plane (IHP), where ions or molecules from the electrolyte are specifically adsorbed without solvation shell on the electrode/metal surface and a three dimensional diffuse outer Helmholz-plane (OHP), where solvated ions of the electro active species (anions or cations) are non specifically adsorbed on the surface. The OHP is extended to the bulk solution. If an electrochemical-active species is located in the OHP and not specific adsorbed on the electrode surface, then causes a potential drop across the diffuse layer. The electrochemical double layer can be characterized by the behavior of a capacitor, whereby the electrode and the OHP takes the role of each capacitor plate. The gap between both plates is the IHP, filled with ions and solvent molecules with a certain dipole moment. Both "plates" have a defined distance, which is in the range of tens of Ångstroms ($\mathring{A}$) and give a capacitance within the range of 10 to 40 $\mu F/cm^2$ [43]. This double layer capacitor can be charged and discharged, like it is known from a "real" capacitor, by changing the potential difference between the electrode and electrolyte.

5.1.3. Ohmic Voltage Losses and Electrode Kinetics

Potential losses are *e.g.* caused by concentration gradients in the electrolyte (see **Chapter 5.1.2**) or ohmic resistors caused by bad electric contacts (R_{ext}), ionic conductivity of the electrolyte (R_{ionic}) and electric conductivity of the electrode material ($R_{electrode}$). These losses can be characterized by a deviation of the measured cell potential E_{cell} from the calculated Nernst potential E_{equ}. Overpotentials arise from current densities between charge and discharge of the cell. The simplified schematic electrochemical cell
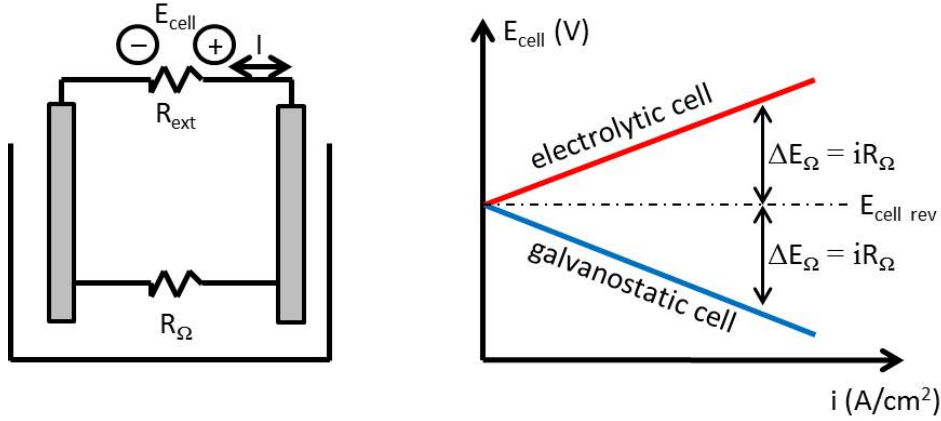
Figure 7: A schematic model of an equivalent circuit of an electrochemical cell with two electrodes and the ohmic internal resistance consisting of the ionic and electrode resistance (R_{ionic} + $R_{electrode}$) and the external electric resistance (R_{ext}). The right plot shows a potential versus current density scheme with the idealized potential drop of electrolytic and galvanic cell in dependence of the current density (according to [43]).

in **Figure 7** represents only resistances coming from ionic conductivity of the electrolyte and conductivity of the electrode itself (R_{ionic} + $R_{electrode}$ = $R_{internal}$) and the external electric resistance (R_{ext}) between two electrodes; both resistances are summarized to R_{ohmic}. To drive an electrochemical reaction, an external voltage needs to be applied. The total ohmic resistance R_{ohmic} is multiplied by the current density, resulting in the potential loss or ohmic overpotential ΔE_{ohmic}. The electrolytic resistance is calculated by the sum of the Nernst potential E_{equ} and ΔE_{ohmic}. In an galvanic process, the obtained cell voltage is calculated by subtracting ΔE_{ohmic} from E_{equ}. This process is shown in the right plot of **Figure 7**. This model is very simple and does not consider kinetic and diffusion resistances.

Due to the fact that reactions on the electrode surface cannot be infinite fast, other types of overpotentials must be taken into account. The kinetic overpotential (η_{kin}) is related to charge-transfer reaction kinetics on the electrode surface and is given by the Butler-Volmer **Equation (4)** [41, 42];

$$i = i_0 \cdot exp \left(\frac{\alpha_a nF}{RT} \cdot \eta_{kin} \right) - exp \left(\frac{-\alpha_c nF}{RT} \cdot \eta_{kin} \right) \tag{4}$$

whereby i is the current density in [mAcm^2], i_0 exchange current density, T is the temperature in [K], n is the number of transfered electrons, F the Faraday constant in [C/mol] and R the gas constant in [J/molK], α is a symmetric factor and η the kinetic overpotential.

Furthermore, overpotentials caused by mass transport are represented by $\eta_{transport}$, which are caused by transport inhibition of the reactants to the electro-active surface on the electrodes.
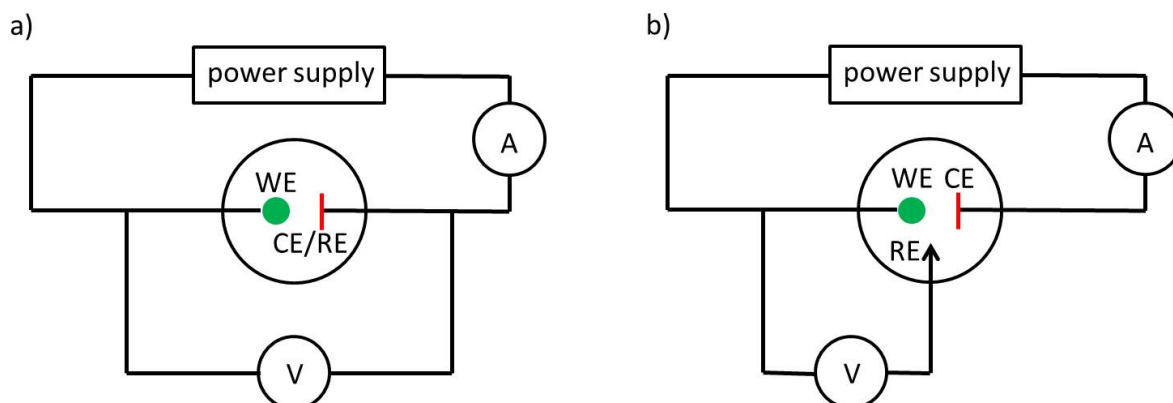
Figure 8: A scheme of a two-eletrode cell in a) and a three-electrode cell in b) with a separated counter
and reference electrode (scheme in depenence on [41]).

5.1.4. Two- and Three-electrode Cell Set-up and Potential Scale for Lithium Batteries

To examine electrochemical reactions, a suitable test cell set-up is necessary. Mostly, the interest is set in reactions taking part only on the working electrode (WE). The WE is always coupled with a second electrode of a known, idealized non-polarized and stable potential (counter and reference electrode CE/RE), because absolute electrode potentials cannot be measured. The potential between these two electrodes is monitored and varied or the current caused by electrochemical reaction is detected in dependence on the measured working electrode potential. A negative current is applied on the WE, which corresponds to a cathodic process, whereby the electro-active species of the WE is reduced. For a positive current, the process on the WE is inverted to an anodic reaction with a subsequent oxidation. In general, one need to distinguish between the use of a two- and a three-electrode design. In the first configuration, a two-electrode set-up, shown in **Figure 8a)**, the RE is combined with the CE. The potential RE of this cell set-up deviates from its equilibrium by a certain overpotential, because the measurement during volt-amperometric techniques is not constant. In this case, the combination of CE/RE is called pseudo-reference electrode. To avoid these problems and to guarantee a stable potential at the RE with a currentless measurement, one need to separate CE and RE. The schematic set-up is shown in **Figure 8b)**. Electrochemical reactions take place between the WE and CE. The RE is only used to monitor and control the potential of the WE. For measurements in the field of lithium-ion batteries, the potential of electrode materials are usually reported in dependence of the potential of metallic lithium, which is also used as material on the reference electrode. The standard potential of metallic lithium is located at around -3.05 V_{SHE} [19]. Potentials of the WE are displayed in $V_{Li/Li+}$ or V_{Li}. For measurements performed in a two-electrode set-up, the material on the CE is used as RE as well. In half cell measurements the material on the CE/RE side is usually metallic lithium. If one analyzes a full cell without a separated RE, one

can only monitor and measure the potential between anode and cathode. This fact can cause problems for data interpretation, because the material of the anode is also electrochemical active and therefore without a RE not controllable.

5.2. Electrode Coating Optimization

To achieve a good and stable cell performance, the optimization process for the different electrode coatings is very essential to allow a good wettability of the electrode coating with the electrolyte mixture and a good adhesive behavior of the coating on the current collector material.

For lithium-ion batteries, the cathodic electrode coating is supported on metallic aluminum and the anodic coating on copper. Commonly, an electrode coating mainly consists of active material (AM) with additions of conductive amorphous carbon powders (C) and polymeric binders. To achieve a good coating, the AM to binder and carbon ratio needs to be high, the coating itself should have a high electronic conductivity, an optimized packing density to achieve a very good mass transport of the lithium ions through the whole coating, and an optimized surface area of the electrode, because degradation reactions of the electrolyte mixture occur faster and earlier on materials with a high surface area, which affects the efficiency and life-cycle of the battery cell [44].

In general, liquid electrode inks consisting of AM, conductive carbon, polymer binder and a solvent which is able to fully dissolve the binder (in our case: N-methyl-pyrrolidone (Nmp)) are mixed and spread on the current collector foils. After the evaporation of the solvent and drying the coating, electrodes in a defined diameter can be punched out.

However, the described procedure is not as easy as it seems. The mixing, coating and drying process was optimized over a long time period.

The development of the ink preparation procedure is schematically shown in **Figure 9**. At the beginning of this work, the inks were prepared, like it is shown in **Route a)**, by simply mixing the solid components and the solvent under stirring in a vessel on a hot plate at 60°C and 1200 rpm with a magnetic stirring bar for at least 3 h. This procedure resulted in partial coagulative inks, which were inhomogeneous after 3 h of stirring. In most cases, the stirring time was prolonged for several hours ensuring to get a homogeneous ink. In the first modification step, shown in **Figure 9 Route b)**, the Nmp solvent was added stepwise. This method enables a better control for the homogeneity and a better regulation of the quality. Nonetheless, with a pre solved binder in **Route c)** the ink had a better quality and homogeneity compared to the procedures **Route a)** and **b)**. In the last optimization step, a planetary Thinky mixer (2000 rpm, 5 min, 50 mbar) was used (see **Figure 9 Route d)**). Like in **Route a)**, solids and Nmp were pre mixed with a spatula in a ratio of 2.2 mL$_{NMP}$ per gram of solids. With this really simple and fast procedure, one reached a great improvement in terms of homogeneity and quality of the inks and even a better economy of time. In the following, different ink coating and drying procedures were investigated, as shown in **Figure 10**. The simplest
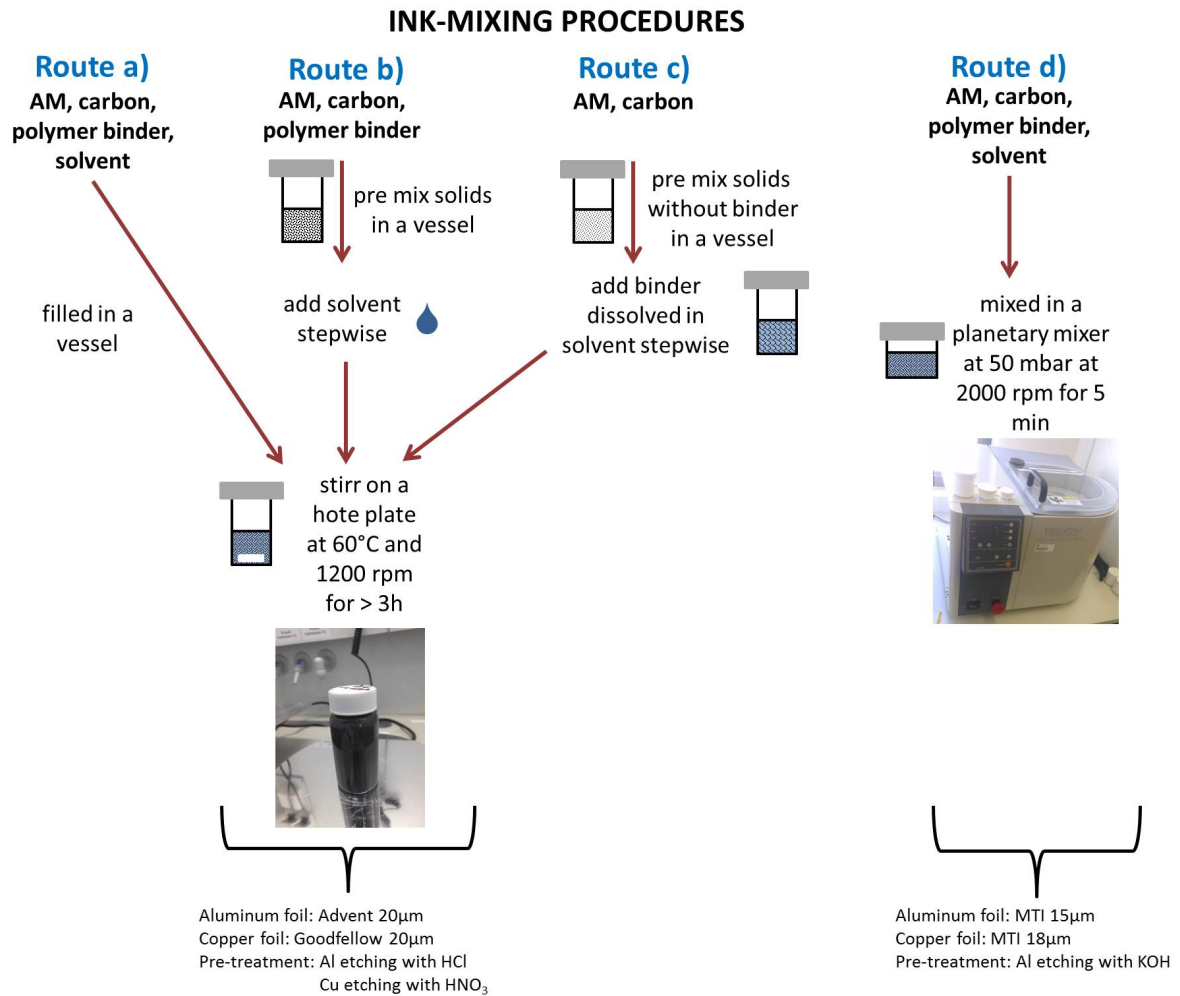
Figure 9: Development of the ink preparation procedure for lithium-ion electrode coatings.

way was in the beginning in **Route a)**. The coating of the ink on a aluminum foil with a gap bar or mayer rod with a variety of different wet-film thicknesses from 80 μm to 500 μm by hand. Afterwards, the coating was dried over night on a hot plate at 60°C. Combined with the ink mixing method in **Route a)**, the coatings broke several times. In addition the reproducibility was not good in terms of the loading of the coating and the performance of the later assembled cells. One important step in the coating procedure was the use of an automotive coating machine (RK Print, Germany) in **Figure 10 in Route b)**. One could reach reproducible electrode loadings, but still, the amount of broken or detached coatings was high, especially at higher loadings. At the same time Lfp inks were coated on aluminum foil supplied from Advent with a thickness of 20 μm, whereby Lto was coated on a 20 μm thick copper foil from Goodfellow. Both foil types were pretreated by cleaning steps with MilliQ water and ethanol. After cleaning aluminum foils were etched with diluted HCl (ca. 0.1 M), copper foils with diluted HNO_3 (ca. 0.1 M), respectively, to get a better adhesive behavior of the coating after drying. Then, the acid was removed with MilliQ water and the foil was dried with a paper. In route **Route c)** and **Route d)** the use of a drying oven, which works with a constant temperature (120°C) and low pressure [44], was introduced to assure a constant drying of the coating and avoiding cracks or scratches. In addition, new types of foils were used. Aluminum was pre etched with KOH instead of HCl, from now on. It was not certain, if chloride anions form intermediates with aluminum and affects the cell performance. An additional important part of a battery is the use of a proper separator. There is a high variety of separator materials like glass fiber pads, polymer foils with different components and layers and solid electrolytes, which are used as separators as well. The following studies in **Chapter 6** mostly VWR ® glass fiber separator pads or three-layer polymer Celgard ® separators were used. A glass fiber separator is a fluffy and very easy manageable separator pad (see **Figure 11a)**) with a thickness of $\approx 250\mu$m and a very high porosity of $\approx 90\%$. This separator material is wettable with every organic solvent and therefore also suitable for solvents, which do not wet polymeric foils. However, a drawback of this material is that the dendrite growth through the separator structure is easily taking place and that cells assembled with this separator show a slightly increased ohmic resistance in comparison to Celgard ® foils. The used Celgard ® separator foils 2325 and C480 show a three-layered structure (see **Figure 11b)**). The thickness for 2325 is $\approx 25\mu$m (10 times thinner than VWR glass fiber separator) with a porosity of $\approx 39\%$. For C480 the thickness is $\approx 21.5\mu$m and $\approx 50\%$ in porosity. Both separators show beside a high chemical and thermal stability and even a zero TD shrinkage at 90°C [46, 47]. The three-layered structure is made of poly-propylene (Pp) and poly-ethylene (Pe), whereby Pp is used as an outer layer and Pe is sandwiched between. Pp shows a good oxidation resistance and were therefore suitable for cycling performances. Pe is used as an inner layer, which provides a shutdown capability because of its low melting point and it is used as a protective layer. With an internal short circuit caused *e.g.* by dendrite growth, the generated heat will lead to a melting of the Pe layer, whereby pores are blocked and lithium-ion transport is stopped.

INK-COATING and DRYING PROCEDURES
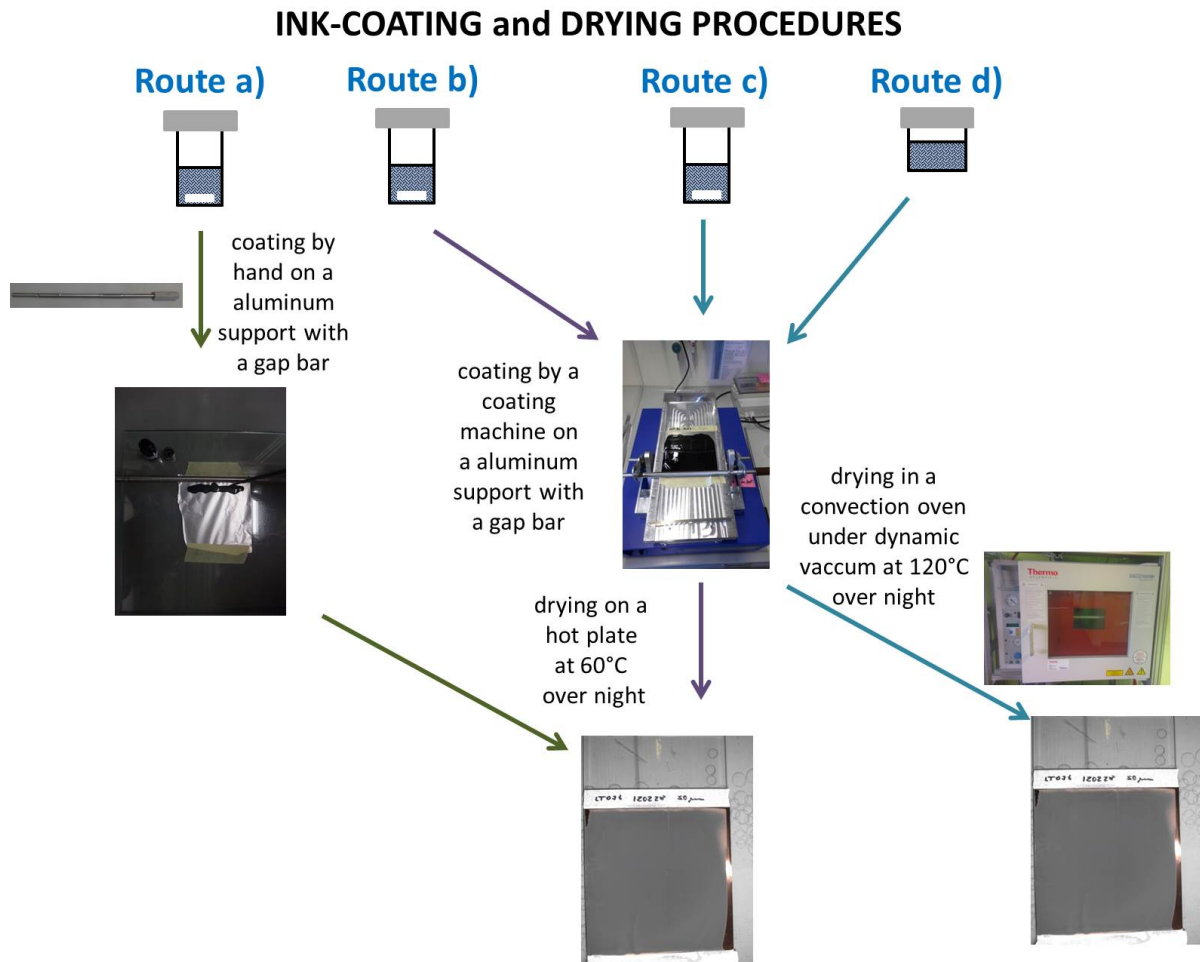
Figure 10: Development for a general coating and drying procedure for lithium-ion electrode coatings.
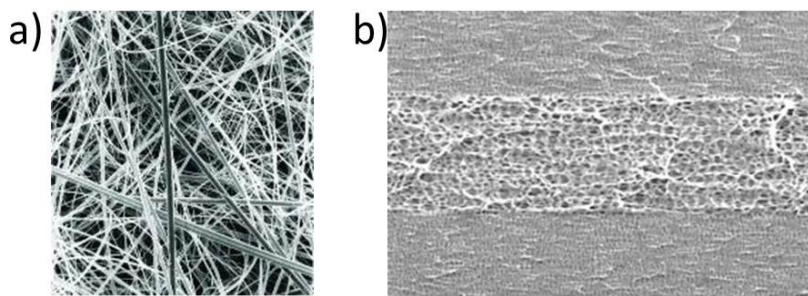
Figure 11: a) Structure of a VWR ® glass fiber separator [45] and b) Pp/Pe/Pp (Poly-propylene/Poly-ethylene/Poly-propylene) three-layer Celgard ® polymer separator foil [46].

Figure 12: Poor wettability of three-layer Celgard ® 2325 with solvent mixtures of Ec/Dmc.

However, Celgard ® separators are not suitable for every organic solvents. Due to the polymeric structure, the polarity of the solvent and polymer surface plays an important role. Solvents like di-methyl-sulfoxide (Dmso) or di-methyl-carbonate (Dmc) do not fully, or even very slowly, wet the separator foils. A poor wetted separator leads to an increased inner resistance, not reproducible cycling data or lowered capacity at higher cycling rates. The wettablity of Celgard ® 2325 with Dmc is shown in **Figure 12**. As one can see, the initial color of the separator foil is white (left separator); after wetting a proper wetted separator turns colorless and clear. In case of Dmc, the separator remains white at the outer part and the solvent rolls off. But only after a prolonged time, the separator turns clear. Unfortunately, this fact has received no consideration for a longer time in several experiments. Nonetheless, results and discussion given in **Chapter 6**, Dmc was only used in combination with VWR ® glass fiber separators. Ethyl-methyl-carbonate (Emc) was used instead of Dmc in combination with Celgard ® foils, which provides a good wettablity. The rate capability of half cells with Lfp electrodes prepared with different procedures and cycled under different conditions in a stainless steel T-fitting are shown in the comparative **Figure 13a)** and **b)**. In graph **a)** the inks were prepared with different thicknesses. The different routes are shown in **Figures 9b)** and **10b)**. Celgard ® 2325 was used as separator in combination with 80 μL of 1 M LiPF$_6$ in Ec/Dmc 1/1 g/g. As mentioned and shown before in **Figure 12** the use of Dmc with Celgard ® results in an unsatisfactory capacity of 130 mAh/g$_{LFP}$ at slow rates (C/10) for a high loading of active material and a fast decreasing capacity at higher rates. A rate higher than 1C reaches no capacity of the Lfp electrode. This poor behavior is also related to the first chosen non utilizing potential window from 3.8 to 3.1 V$_{Li}$, which leads to a partial charge of the active material, resulting in low charge and discharge capacities. Note that the rate capability for thin coatings (green balls) of 0.91 mg/cm^2 is better because of a better and faster mass transport through the electrode coating. However, the reached capacity at C/10 is slightly higher than theoretically possible, which indicates a weighing error of the electrodes by using a balance with a wrong accuracy. If one compares this data with the graph shown in **Figure 13b)**, one can clearly see that the performance is much better. The capacity at C/10 reaches 155 mAh/g$_{LFP}$. This value is also below the theoretical capacity, but electrodes are assembled with-

out further treatment like compression, which would increase the performance as well. However, cycling with a rate of 1C shows almost no loss in capacity and reaches values of more than 140 mAh/g_{LFP} and at a rate of 10C 80 mAh/g_{LFP}. These cells show reproducible capacity data. Note that for this measurement, the inks were prepared as described in **Figures 9c)** and **10c)**, whereby cells were assembled using VWR $^{®}$ glass fiber separators and a better adapted potential window of 4.0 to 2.0 V_{Li} to reach a fully charged LFP cell.

5.3. Handling and Preparation of Electrolyte Solutions

In this work, cyclic and linear carbonates as well as poly-ethylene oxide glycol di-methyl ethers like short and long chained glymes (all from Sigma Aldrich) were used as solvent or additives, depicted in **Figure 14**. All solvents, salts and prepared electrolyte mixtures were stored in an Argon filled glove box (MBraun < 0.1 ppm O_2 and H_2O). Pure solvents were stored and dried over molecular sieves (Sylobead MS 564C zeolytes, 3 $\mathring{A}$, Grace Division) until the water content was below 20 ppm. The water content was controlled with Karl-Fischer Titration before mixing electrolytes. The cyclic carbonate ethylene carbonate (EC) was used as received without further purification, because of its solid state at room temperature. The long-chained glyme PEG500DME was dried at 80°C for several hours under dynamic vacuum and later over molecular sieves. Lithium conductive salt lithium bis-(trifluoromethanesulfonyl)-imide (LiTFSI) was dried under dynamic vacuum at 120°C. Due to its low thermal stability, LiPF$_6$ was purchased in battery grade and used as received.

Electrolyte mixtures containing LiPF$_6$ as conductive salt were mixed in aluminum vessels, to protect electrolyte from UV radiation. All other mixtures were stored in normal glass vessels. Some standard electrolyte mixtures were purchased in pre mixed solutions like 1 M LiPF$_6$ in EC/DMC 1/1 g/g (LP30; Selectilyte BASF SE) 1 M LiPF$_6$ in EC/EMC 3/7 g/g (LP57; provided by BASF SE) and 1 M LiPF$_6$ in EC/EMC 3/7 g/g plus 2% VC (LP572; provided by BASF SE).

5.4. Development of a Three-Electrode Test Cell Set-up and Assembly

Besides an optimized ink preparation, coating and drying procedure, as well as a suitable separator and electrolyte mixture, one need a working cell design for test cells in the laboratory. The idea of a three-electrode test cell is very important, especially for lithium-ion cells, because, due to the use of a third reference electrode, anode and cathode, could be studied separately. This design can be realized using T-fittings with three openings. The two opposite openings are for current collector rods of the working and counter electrode (cathode and anode). The third, vertical opening is used for a reference electrode. Therefore, several Swagelok $^{®}$ T-fittings made from different materials were used to proof their suitability. The different fittings are shown in **Figure 15**. The
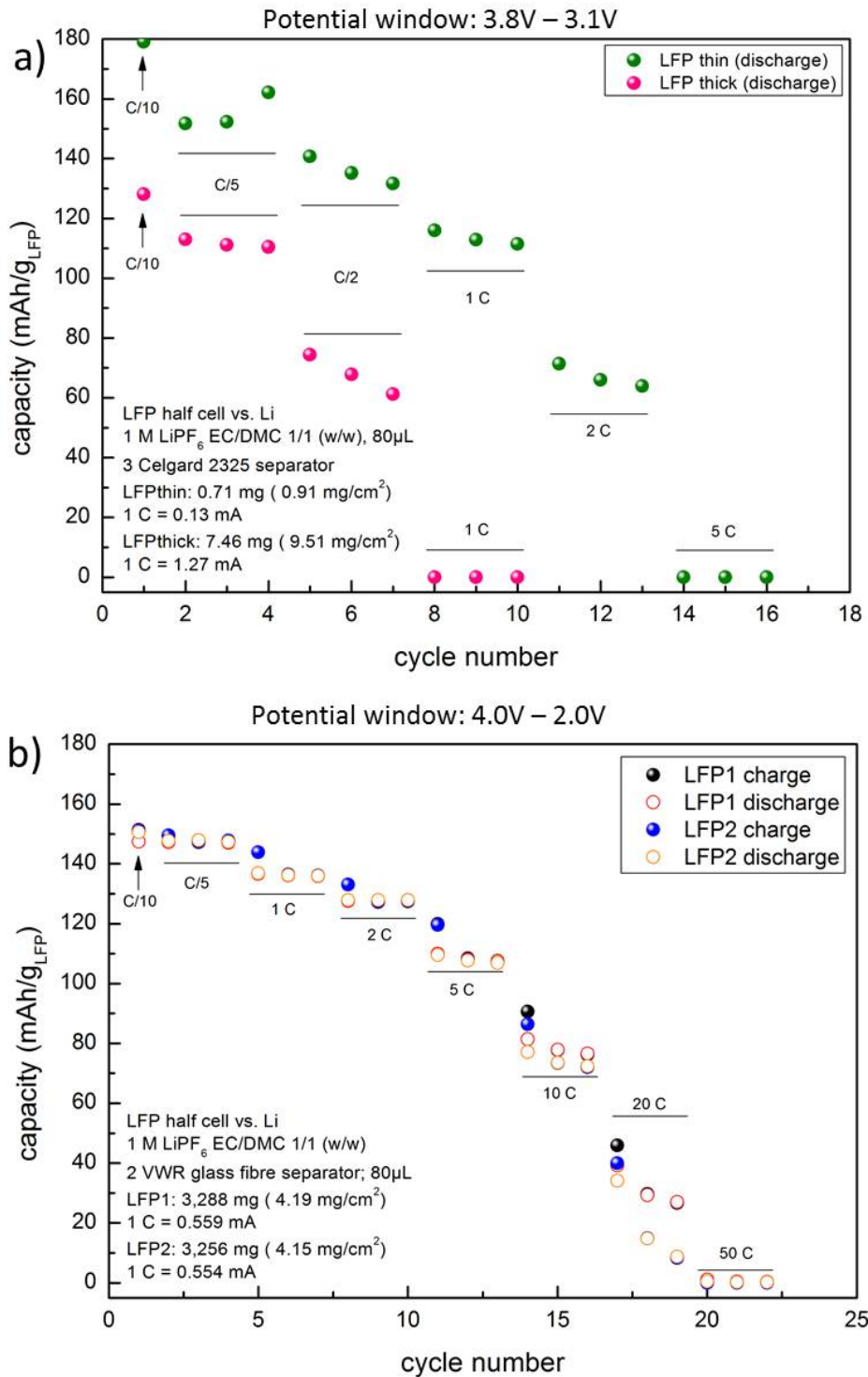
Figure 13: Different cell performance for LFP half cells using in a) ink preparation of **Figure 9b)** and coating/drying procedure of **Figure 10b)** in combination with 3 Celgard ® 2325 separators, 80 μL of 1 M LiPF$_6$ in EC/DMC 1/1 g/g and a potential window of 3.8 to 3.1 V$_{Li}$. In b) the ink preparation method of **Figure 9c)** and coating/drying procedure of **Figure 10c)** in combination with 2 VWR glass fiber separators, 80 μL of 1 M LiPF$_6$ in EC/DMC 1/1 g/g and a potential window of 4.0 to 2.0 V$_{Li}$ was used.
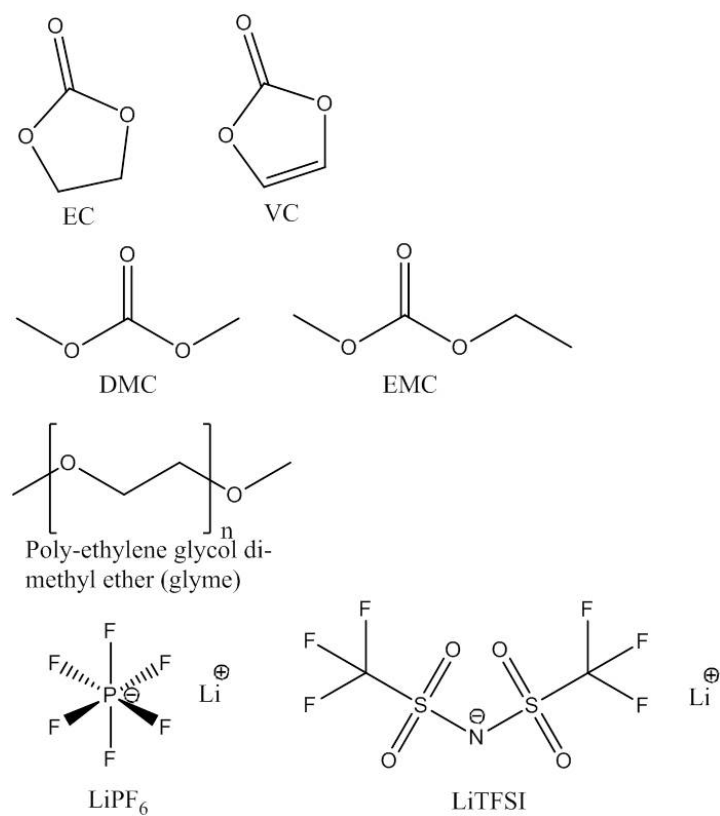
Figure 14: Chemical structures of different electrolyte components like solvents and salts.
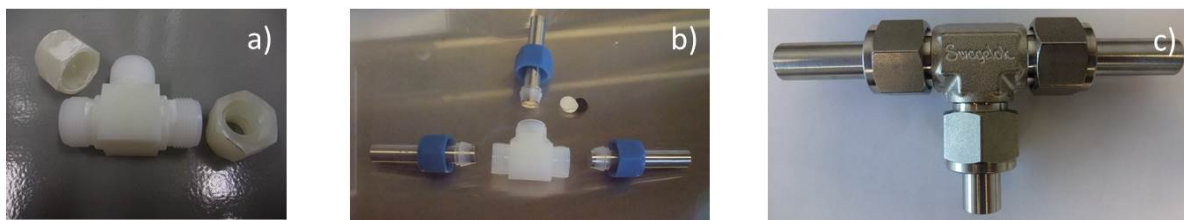
Figure 15: Different Swagelok T-fittings for a laboratory test cell with three electrodes for lithium-ion batteries: a) Nylon, b) Teflon and c) stainless steel.

fitting shown in **a)** was made of nylon-polymer. As one can clearly see in the picture, this material was not compatible with the organic electrolyte. The nuts and cell body turned white and porous after some time. That is why, the cell bodies were replaced by using teflon (PTFE) fittings. Unfortunately, after several tests, it was clear that it is not easy to close the cells properly and to generate reproducible data. Another significant fact for this material is that the permeation coefficients for water and oxygen are very high for this material, therefore long-term cycling or storage tests would not be possible [48]. Subsequently, a third T-fitting was introduced. This fitting was made from 316L stainless steel, which is inert in contact with organic solvents, fluorinated salts, elevated temperature and has no permeability for water or oxygen. However, a main drawback is the problem of internal short circuits caused by contact of the metallic current collector rods/foils with the metallic cell body. For this reason, influenced from the cell design used by Dr. Milos Vracar at the Karlsruher Institut für Technologie (KIT), the interior of the cell was modified with an insulated HDPE-cap (high density poly-ethylene) on the anode side and a HDPE-ring on the reference electrode to avoid short circuits inside the cell. A detailed overview of the cell components is shown in the left picture of **Figure 16a)**. A schematic assembled cell of the described type is shown in **Figure 16b)** on the right. The central part is the cell body of the T-fitting, which is used to attach and align the current collector rods for anode (CE), cathode (WE) and RE. Each current collector can be connected with 2 mm pins to a multipotentiostat or battery cycler. To adjust the pressure between the anode and cathode, a stainless steel compression spring with a spring constant of 3.71 N/mm is used on the cathode side, which is always compressed to 4 mm in the assembled state resulting to a contact pressure between both electrodes of 1.89 bar. The contact pressure p can be calculated by the following **Equations (5)** and **(6)**;

$$F = D \cdot \Delta L \tag{5}$$

$$p = F/A \tag{6}$$

Whereby F is the force, resulting from the spring constant [N/mm] D and ΔL the compression length of the spring [4 mm], A is the bearing area [78.54 mm²].

The assembling procedure of such a test cell will be explained in the following. First of all, the current collector rod for the anode side toped with the insulating cylindric
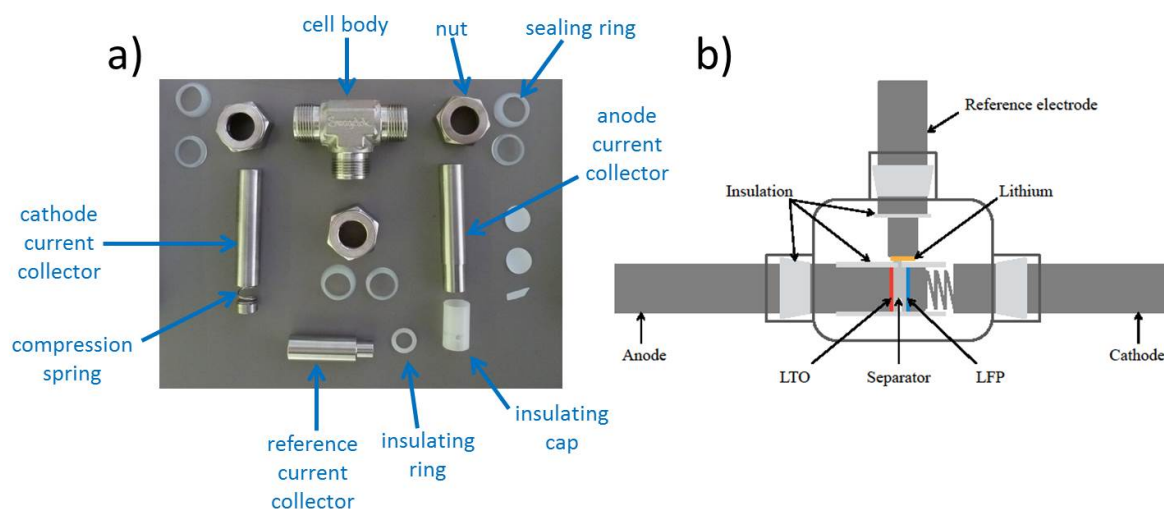
Figure 16: Modified Swagelok stainless steel T-fitting with the different components on the left a) and b) a schematic detailed scheme of an assembled cell on the right [49].
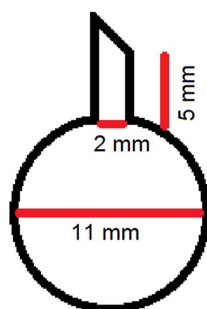
Figure 17: Shape of a flagged separator [49].

cap is aligned and fixed with the nut and the sealing rings in the cell body. During the alignment it is necessary to mind to place the hole of the cylindric cap facing the third opening. The hole will be used as a lead through for the flagged separator to allow an ionic contact of metallic lithium of the RE and the inner part of the cell. Then the anode/counter electrode (diameter of 11 mm) is placed inside the cap on top of the current collector rod. If the cell is assembled with a total amount of 80 μL of electrolyte, 20 μL are added on top of the anode coating or a lithium foil in case of a half cell. Afterwards, one need to place a separator (glass fiber or Celgard ® with diameter of 11 mm) on the anode. Note to be sure that it is fully wetted by the electrolyte. A second separator with a little flag on one side is placed. Thereby, the flag (see **Figure 17**) is leaded through the top facing hole. Additional 20 μL of electrolyte are added on top plus a third separator foil. Then the cathode (diameter of 10 or 11 mm) is placed, whereby the coated area faces the separator, with 20 μL of electrolyte. Following, the cathodic current collector rod is aligned and fixed opposite to the anodic one, whereby, previously the small cylinder is placed on the cathode and the spring is placed on top of it. Thirdly,

30
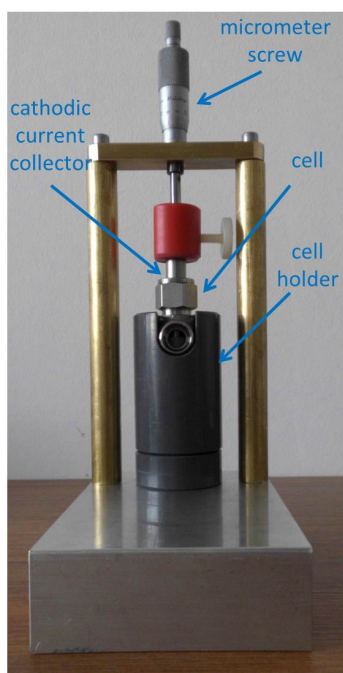
Figure 18: Cell holder with micrometer screw to set the contact pressure between anode and cathode [49].

the long rod is fixed with sealing rings and the nut. Afterwards the half assembled cell is placed in a special cell holder, which is equipped with a micrometer screw to adjust the contact pressure of the electrodes. The cell is clamped between the holder and the micrometer screw. While turning the micrometer screw, the compression of 4 mm is set. As long as the cell is fixed in the holder, the nut is tightened with a wrench. The last part is adjusting the reference electrode. A metallic lithium foil (diameter 6 mm) is placed in the middle of the rod. Then a small separator pad is topped. The remaining 20 μL of electrolyte is used to carefully wet the reference separator pad and flag. The rest is added to the interior of the cell. Finally, the reference is placed in the third hole of the fitting and fixed with a nut. After the assembling, all nuts are tightened with a torque of 30 Nm and the OCV of the cell is checked with a multimeter. To avoid short circuits, the cells are always placed on a paper or glove while working in the glovebox/chambers or electric conductive surroundings.

5.5. Additional used Test Cell Set-ups and Assembling Procedures

5.5.1. Cell Designs

For measurements of the gassing study shown in **Chapters 6.5** and **6.6** a two electrode cell design was used, which was originally designed for usage in the field of lithium-oxygen batteries [50]. This cell design consists of two stainless steel plates, a bottom and upper part, which are separated from each other by a cylindric plastic spacer of 28 mm inner
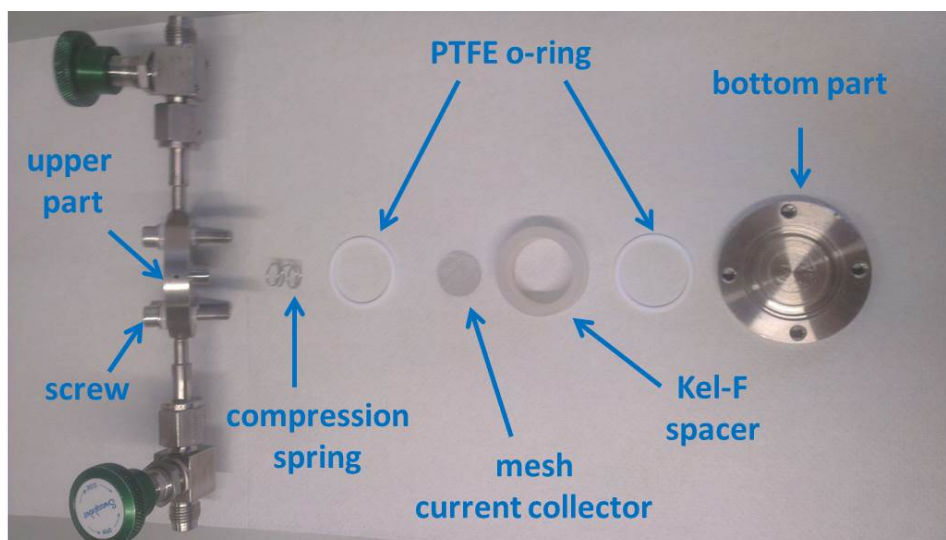
Figure 19: Components of the two-electrode cell design, which was designed for Li-O_2 batteries [50].

diameter made of poly-chlorotrifluoro-ethylene (Kel-F) to avoid a short circuit. On each steel plate is a grove for a teflon sealing ring. The electrodes and separators are placed and aligned on the bottom plate. For an electrical connection between electrodes and upper steel plate, a compression spring is used. In the discussed measurements LTO and graphite electrodes were coated on the porous separator material and aligned to be the upper electrode, to allow a gas flow of evolved gases to the capillary leak in the mass spectrometer cell-design. In all cases a stainless steel mesh was used as a current collector for the upper electrode to get electric contact but not clog the gas transport. Due to the used spacer, the cell has a defined cell volume of 9 cm^3, which allows a precise evaluation of gas evolution rates on the mass spec. As mentioned, for the cell design of the mass spec cell, a capillary with a leak of 1 μL/min is attached on top of the upper steel plate, which can be connected to the mass spectrometer by a Swagelok $^{\circledR}$ nut.

5.5.2. Cell Assembly

Compared to the previous described assembling procedure for the T-cells, the assembly of introduced two electrode cells is very easy and reproducible. Note, that given diameters or some details in this procedure are especially for assembling lithium-ion cell-configurations, which were concerted for gassing experiments shown in **Chapters 6.5** and **6.6**. A detailed exploded view of the cell components are given in **Figure 19**. For the assembling lithium-ion test cells, a lithium foil with 17 mm diameter or a LFP electrode coated on aluminum with 18 mm diameter, respectively, was placed on the bottom plate. 20 μL of electrolyte were added on top, followed by the addition of alternating two separators and again two times 20 μL of electrolyte. Afterwards a LTO or graphite electrode with 15 mm diameter is placed on top with facing up the coated side. After aligning the current collector mesh on the upper electrode, additional 20 μL of
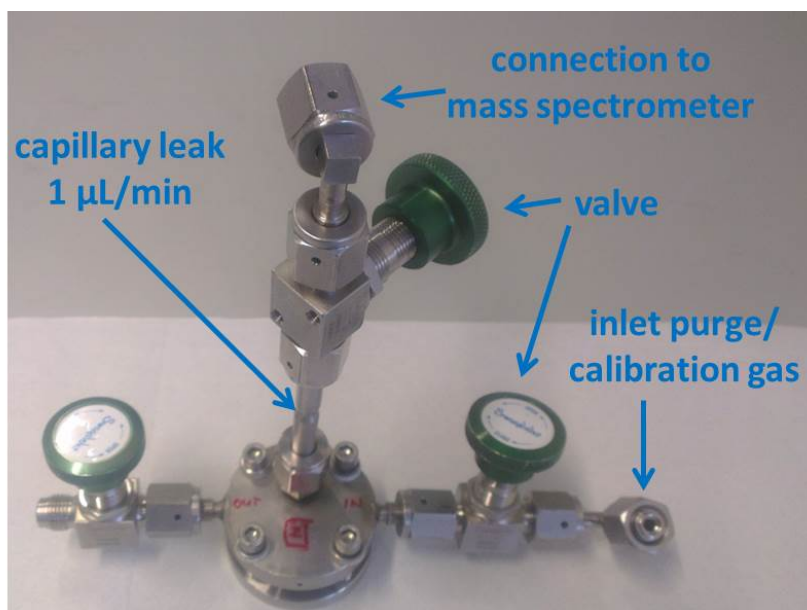
Figure 20: Assembled OEMS cell with its special connections to the mass spectroscopy system.

electrolyte were added . Finally, teflon o-rings were placed into the groves of the bottom and upper part and the upper cell part is carefully placed on the spacer and afterwards sealed with a torque of 6 Nm on all 4 screws. The detailed electrode set-up for each experiment is shown in the particular chapters.

An assembled cell for measurements in connection to the On-Line Electrochemical Mass Spectrometer (OEMS) is shown in **Figure 20**. The interior of this cell is equal to the two-electrode cell described before in **Figure 19**. The main difference is the set-up of the upper stainless steel part. As one can see, the upper plate possesses a capillary leak in combination with a valve and a connection nut to the mass spectrum system. With this apparatus the cell can be connected air tight to mass spectrum. Due to the defined leak, the gas flow from the inside is constant. A second valve below can be used as a gas inlet for purging and calibration gas at the end of the measurement. More details about the background and complete experimental set-up is given in **Chapter 5.7**.

5.6. Electrochemical Methods

5.6.1. Battery Cycling

In contrast to primary cells like alkaline primary batteries (zinc and manganese dioxide; Zn/MnO_2), a secondary battery or accumulator should be chargeable and dis-chargeable for several times with a good efficiency. A central experimental method in battery research is to test the cyclability of the test cells depending on scan rate (current per time), temperature, potential window or other variables. This behavior can be analyzed with different charge and discharge procedures in connection to a battery cycler or potentio-
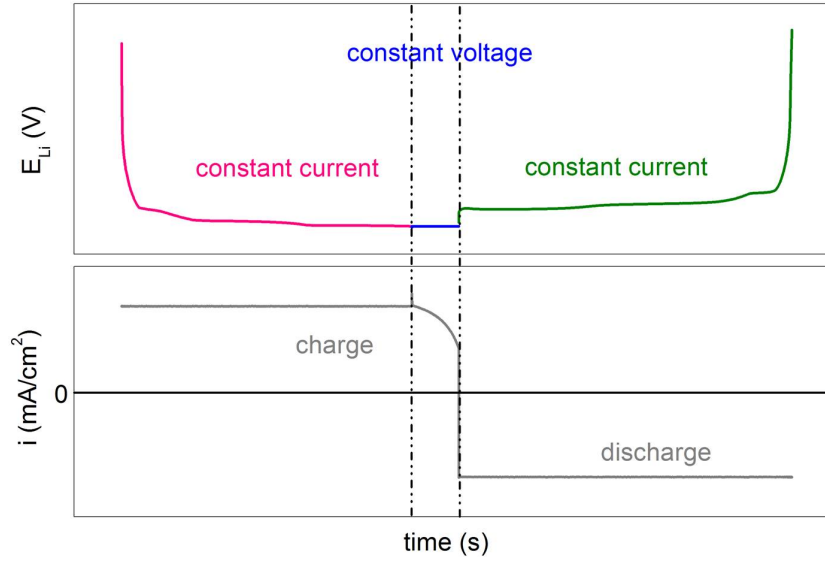
Figure 21: Voltage profile of one cycle of a test cell (top) with a CC (magenta) and CV (blue) charging
step and a CC (green) discharge in comparison with the corresponding current density
(bottom) in grey.

stat. A cell can be charged or discharged, either in the galvanostatic or potentiostatic
mode or combined. Galvanostatic means that a constant current is applied (CC) and
potentiostatic is used for a certain voltage, which is hold (CV). For most electrode ma-
terials a galvanstatic procedure is preferred. However, electrode materials like graphite
should be charged in a CCCV mode, where constant current and constant voltage is
used in combination. The reason for this, is its fast dropping potential plateau, which is
located near the redox potential of lithium. To avoid lithium plating, graphite cells are
normally first charged in a CC mode to 0.01 V_{Li}. After the potential set point is reached,
the cell potential is hold until the current drops to a defined value. For the discharge
(lithium de-intercalation) a simple CC mode is preferred, whereby the current is applied
with a change of sign. The described CCCV charge and CC discharge for one cycle
(bottom) is shown with its corresponding voltage profile (top) in **Figure 21**. Electrode
materials like LTO, LFP or nickel/manganese/cobalt oxide (NMC) are normally charged
in CC mode. The capacity [mAh/g or mAh/cm²] of the cell can be calculated by mul-
tiplying the applied current [I in mA] with the duration of the charge or discharge [t in
h] and divided by the mass of the cell system, electrode or more common the amount of
active material [g]. For the areal capacity, the mAh are divided by the electrode area A
[cm²] (see **Equation (7)**).

$$C[mAh/cm^2] = \frac{I\ [mA] \cdot t\ [h]}{A\ [cm^2]} \tag{7}$$
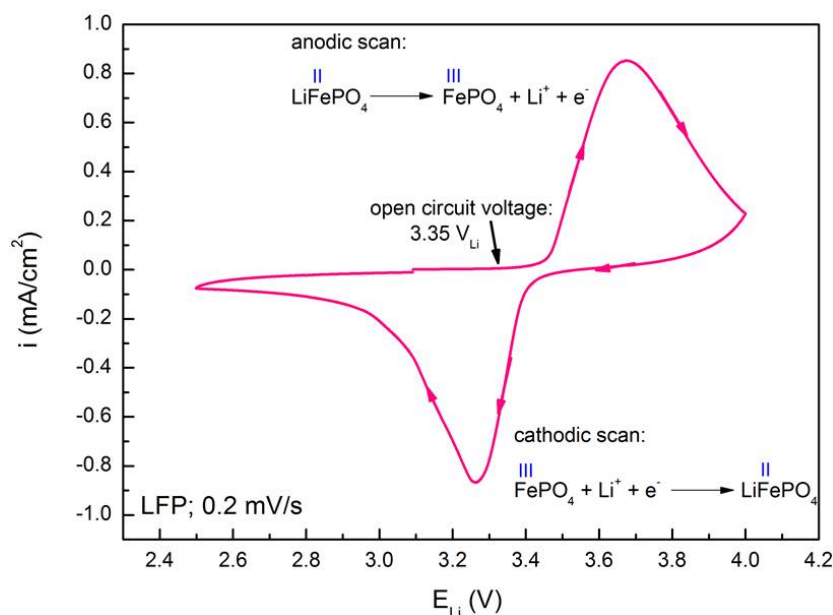
Figure 22: CV of LFP, a reversible redox system, with a scan rate of 0.2 mV/s.

Each electrode material possesses one or more specific potential plateaus during the charge and discharge procedure. The location and occurrence of each plateau is depending on the redox potential of the electrochemcial active species and if it is a one or more electron process. The electrochemical processes of the material can also overlap with other electrochemical reactions occurring in the cell at the same time. Therefore, cycling data can give information about electrode stability, quality of used electrode material, presence of side reactions (shifted specific potential plateaus) and life time of the cell.

5.6.2. Cyclic Voltammetry

Cyclic voltammetry (CV) is a well known technique in the field of electrochemistry. With this technique one applies a triangular alternating voltage between WE and CE. The voltage changes with a defined scan rate. A RE is used to adjust the potential on the WE. To study the different redox processes of the sample, time and current in dependence of the potential are recorded during each scan [42]. With changing the potential step by step in a CV, one can record the increase or decrease of the current for different redox reactions. If a redox system is reversible, the forward and backward scan would lead to current peak with an equal integral area. An example for a reversible redox system is the cathode material LFP, assembled in a half cell with lithium as CE and RE, respectively. A CV with a scan rate of 0.2 mV/s is shown in **Figure 22**. The cell starts at its equilibrium potential (open circuit voltage - OCV) of 3.35 V_{Li}. The potential is first increased in the anodic scan to 4.0 V_{Li}. At ≈ 3.5 V_{Li} a raise in current density is recorded, which corresponds to the oxidation reaction of the Fe^{2+}-species during lithium ion de-intercalation from the olivine structure forming iron phosphate. At the anodic

35

reversal point, the potential is lowered stepwise. The peak of the current density at 3.25 V_{Li} is assigned to the reversible cathodic reaction of iron phosphate and reduction of Fe^{3+}-species during re-intercalation of lithium-ions forming the original compound LFP.

The CV technique was used, for example, to study the corrosion behavior of different current collector materials like aluminum and stainless steel. Due to the raise in current density as a function of the potential, electrochemical processes during oxidative corrosion could be detected. One could analyze that the use of different conductive salts forces an electrochemical corrosion of current collector materials starting at very low potentials (≈ 3.5 V_{Li}) (see **Chapter 6.3**)
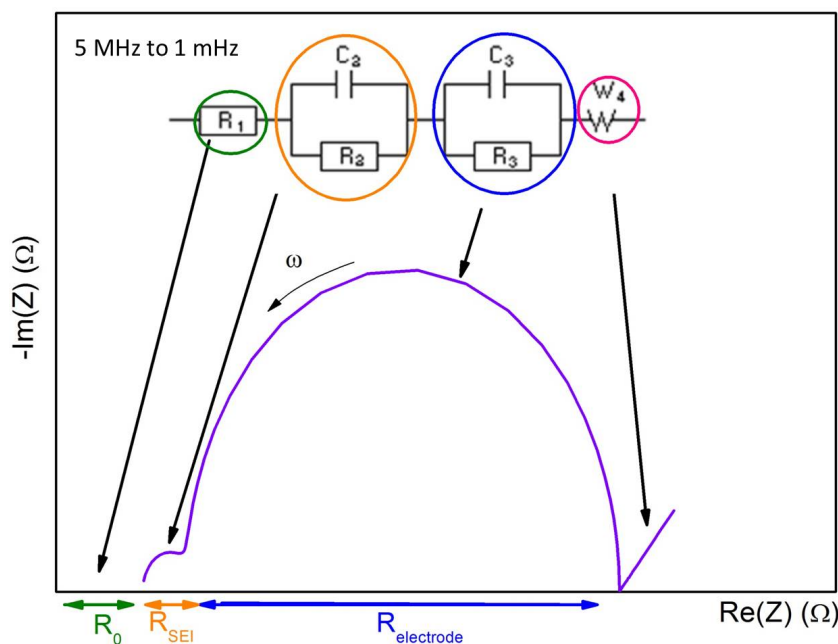
5.6.3. Electrochemical Impedance Spectroscopy (EIS)

This method is based on a frequency ω dependent resistance of electric equivalent circuits. The system is excited from the equilibrium, due to a voltage (U) or current (I) perturbance. As a result one gets a phase-shifted (angle θ) alternating current signal. According to Ohm's Law (R = U/I), one can calculate the impedance. Using Euler's formula (see **Equation (8)**) one get the definition of impedance, shown in **Equation (9)**. The impedance consists of a real part, which is given be ohmic resistances and an imaginary part, if the resistance is frequency dependent like capacitors or inductors. For ohmic resistances, the value is independent from the frequency ω and the phase-shift θ is zero. In an EIS measurement real and imaginary values are recorded for each frequency. These values are plotted in a so-called Nyquist plot with a real (Re(Z); x-axis) and an imaginary axis (-Im(Z); y-axis).

$$exp(-i \cdot \theta) = \cos \theta - i \cdot \sin \theta \tag{8}$$

$$Z[\omega] = \frac{\widehat{U}}{\widehat{I}} \cdot \cos \theta + i \cdot \left(\frac{\widehat{U}}{\widehat{I}} \cdot \sin \theta \right) \tag{9}$$

A Nyquist plot for a fictive simulated electrochemical cell is given in **Figure 23** (purple). The corresponding equivalent circuit is given at the top. Due to the independence of ohmic resistances (green), the whole curve is shifted on the real x-axis for a certain value, also called high frequency resistance (HFR; R_0). The first interception point of the purple curve with the x-axis is therefore related to the resistance of the electrolyte, separators and electric contacts. With lowering the frequency, a small semi cycle appears, which corresponds to the R_2/C_2-circuit (orange). A second semi cycle is related to the blue marked R_3/C_3-circuit. Each semi cycles have also an interception with the x-axis, which means a second and third real resistance related to the charge transfer resistance of an SEI layer and the electrode itself. Each charge transfer resistance is related to an electrochemical reaction. The last component of the equivalent circuit is the so-called Warburg impedance (magenta), which is related to the diffusion limitation in each

Figure 23: Schematic Nyquist plot of an electrochemical cell measured in a potentiostatic electrochemical impedance spectroscopy (PEIS) with the equivalent circuit (top).

system at low frequencies. One can use the EIS technique to characterize electrodes in electrochemical cells and study the change of electrochemical actives surfaces after or within different electrochemical treatments or one can identify problems of cell assembly, such as a abnormal HFR due to a short circuit (HFR would be zero). In the latter, for example, this technique was used to study the growth of an solid electrolyte interface (SEI) for graphite electrodes as a function of time and cycle number depending on the use of different electrolyte mixtures (see **Chapter 6.6**).

5.7. On-Line Electrochemical Mass Spectrometry (OEMS)

5.7.1. Background

With electrochemical mass spectrometry (EMS) it is possible to analyze very complex systems, like lithium-batteries or fuel cells, *in-operando* for a certain time period and under different conditions. This powerful method allows the detection and mass analysis of gas fractions, which were created inside the cell during treatment. With On-Line Electrochemical Mass Spectrometry (OEMS) a exact calibration and determination of the gas amount or evolution rate is accomplished.

Especially the Differential Electrochemical Mass Spectrometry (DEMS) system was extensively studied in the fuel cell area. With this technique one can analyze volatile formed fragments and get information about the stability of the ionomer membranes, electrodes and other components. However, the DEMS set-up is not suitable for an

application in the field of lithium-ion batteries, because it requires a high gas flow of several mL/min, which is possible for fuel cells due to the continous gas flow, anyway. In batteries one would fail, because of small evolution rates of the gases (in the range of several ppm/s).

In order to avoid a full evacuation of the headspace, a DEMS system is permanently flushed with a constant flow of inert gas [51]. This makes the data treatment relatively complicated, because absolute gas amounts are not determinable. In contrast, the OEMS is designed to our specification and it is not designated to purge with a gas flow to determine in the data treatment absolute gas amounts and evolution rates. However, due to the abdication of purging gas, the time period for experiments is restricted to ≈ 50 hours or a cell pressure below $\approx 7 \cdot 10^{-8}$ mbar.

5.7.2. Experimental Set-up

The used OEMS device for cell measurement was designed in a three staged set-up of pressure reduction from ambient pressure of the cell to the integrated analytical detectors at high vacuum of ca. 10^{-7} mbar. The picture of the laboratory system, combined with a schematic illustration is given in **Figure 24** to explain the used set-up from the left to the right in detail.

The assembled test cell with ambient pressure, shown in **Figure 20**, is stored in a climatic chamber at constant temperature and is connected to the mass spectrum system via the marked connection nut. By opening the valve between cell and mass spectrum one achieves a gas flow rate via the integrated calibrated capillary leak for ≈ 1 μL/min. This low flow rate allows a very fast response time. The mass spectrum system itself is heated to 100°C and evacuated by a vacuum pump (Pfeiffer Vacuum QMA 410) to $\approx 10^{-5}$ mbar for the pumped cross-beam ionization source to ionize the sampled gas. The third area with a quadrupol mass analyzer for detection and secondary electron multiplier (SEM) is at high vacuum around 10^{-7} mbar, to reach a quantification level of ppm for evolved gases. The detection limit for the shown system is $\approx 10^{-14}$ mbar. In parallel to the OEMS measurement, the test cell is connected to a potentiostat for the cell treatment and *e.g.* cycling data is recorded. After each measurement, the system is calibrated with different calibration gas mixtures containing gases of interest, for example hydrogen, ethylene, carbon dioxide and so on, to quantify the different mass fractions. The shown OEMS set-up was developed by Dr. Tsiouvaras in our laboratories [52].

5.7.3. Data Treatment

Is a battery connected to the OEMS apparatus, the gas evolution during cycling can be detected *in-operando* and due to the defined headspace and a subsequent calibration with calibration gas. To obtain the evolved gas amount or gas evolution rates, one needs to follow a complex data treatment, which is schematically shown in **Figure 25**. First
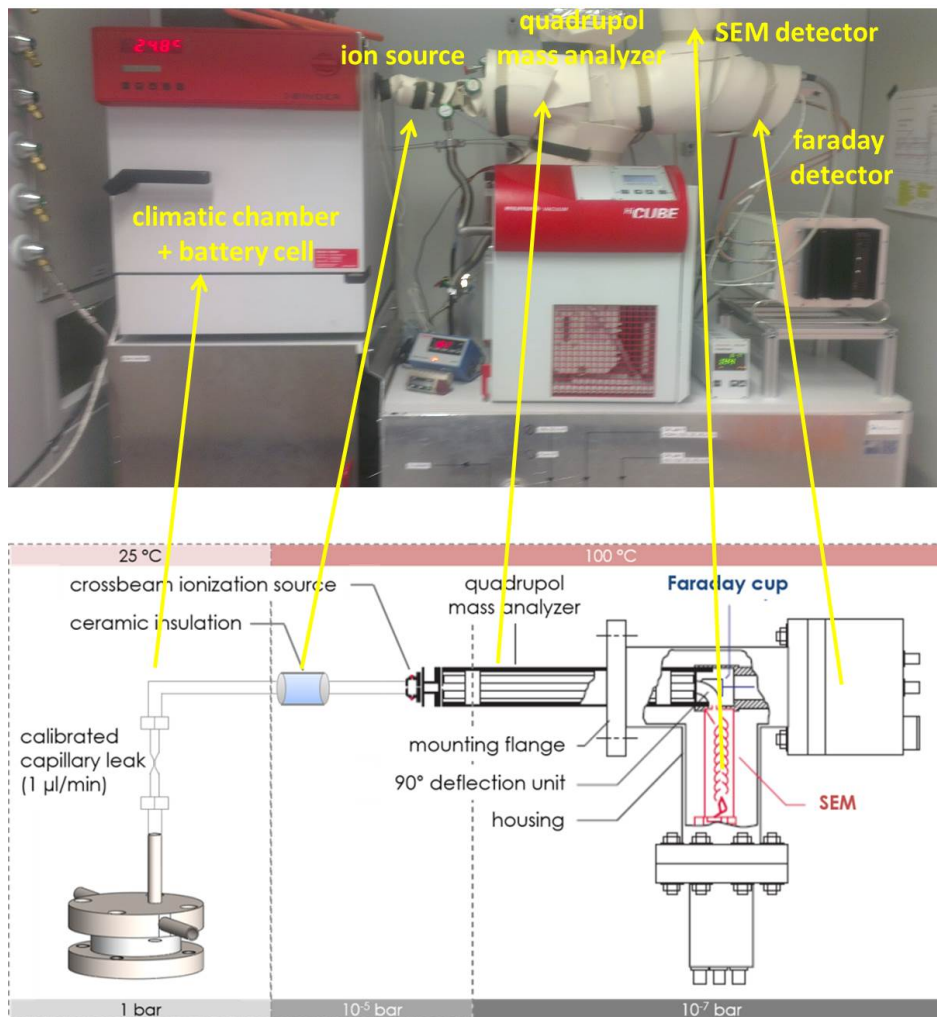
Figure 24: Laboratory OEMS system (top) and schematic illustration (bottom) of the set-up of the OEMS aparatus.

of all, one needs to evaluate the different mass fractions of interest *e.g.* mass = 2 for hydrogen (H_2), mass = 26 for ethylene (C_2H_4) or carbon dioxide (CO_2) mass = 44. Note, that several gases have more than one mass fraction, which can also overlap with others gases and their traces. Therefore, it is necessary to exclude the evolution of side products, which can evolve the same mass traces in parallel.

The mass signals provided from the OEMS have the unity of Ampere [A], which can easily be related to concentration in ppm or mol. The mass trace of interest is normalized to argon, means divided by the mass signal of ^{36}Ar, because it is the isotope of the inert background gas with a constant and non-changeable and high concentration (**Figure 25b)**), to get the so-called integral signal for the measured gas trace. The normalized signal can be calibrated in the next step to get the data of the total gas amount in ppm, which is evolved (see **c)**). If one needs to determine the gas evolution rate in ppm/s, the integral signals are derived in the first order and smoothed. The result is shown in **Figure 25d)**. In the last step of the data treatment, the data from OEMS and from the potentiostat are consolidated and time corrected and subsequently plotted in a single graph, shown in **Figure 25e)**. With this graph, one can follow the gas evolution upon charge and discharge of the sampled cell.

The OEMS technique is very sensitive and allows to detect very small gas amounts, which are evolved in an electrochemical process. For this reason, OEMS was used to study the gassing behavior of different anode materials like LTO and graphite during cycling. One can understand the evolution of different gases in dependency on potential, type of electrolyte and absence of an SEI (see **Chapters 6.5** and **6.6**).
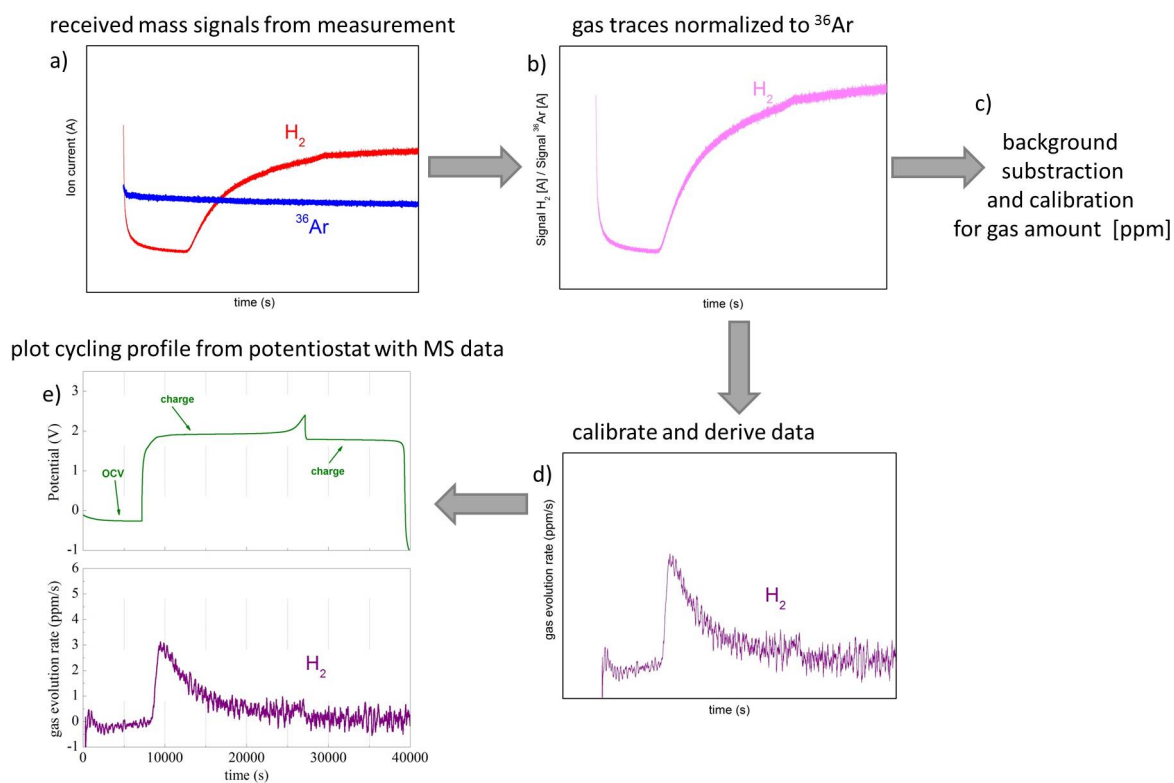
Figure 25: The scheme basically shows the data treatment for the OEMS data. a) Received raw data of gas traces from the MS. b) Gas traces of interest, *e.g.* H_2, are normalized to the ^{36}Ar signal. c) if one wants to look at the total gas amount in ppm, it is now necessary to calibrate from the calibration trace after the measurement. The plot looks similar to plot in b). To calculate the gas evolution rate, the data needs to be calibrated and derived in d). The last step is to combine cycling data of the electrochemical measurement with the MS traces in e).
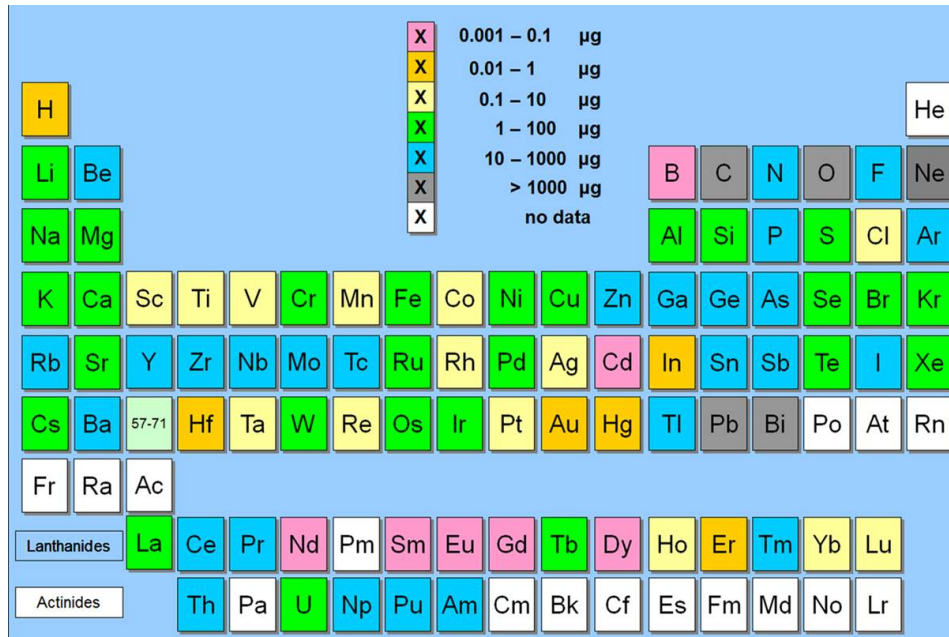
Figure 26: Detection limits of single elements for measurements with the PGAA method [53, 54].

5.8. Prompt Gamma Activation Analysis (PGAA)

5.8.1. Theory

Prompt-gamma activation analysis (PGAA) is a non destructive nuclear analytical method based on the neutron capture in nuclei of the sampled material and the subsequent detection of gamma rays emitted from the illuminated sample. It is used for a quantitative elemental and isotopical analysis of solid samples (down to a ppm-range) in fields like basic research, materials science, geology, archeology, environment, food analysis, research field of semiconductors and supraconduction, analysis of catalysts or crystals and medicine [53]. In addition, liquid and gaseous samples can also be measured in special containers. This method is used for qualifying and quantifying elements of the bulk material of a sample. The advantage of PGAA in contrast to delayed gamma-ray emissions (neutron activation analysis, NAA), particle induced x-ray emission (PIXE) or x-ray fluorescence (XRF) one can also detect very light elements like hydrogen, lithium, nitrogen, carbon and phosphorous. Complementary to NAA, some elements can be measured with PGAA and NAA like *e.g.* copper. The detection limit is dependent on the sample matrix. The denoted detection limits in **Figure 26** are a guide and actually specific for each sample and displays a rule over thumb from already measured samples.

The PGAA method is based on the nuclear phenomenon of neutron capture (cold or thermal neurons) by each element in a sample. The sample nucleus $^A_Z X$ absorbs a neutron ($^1_0 n$) and thus is excited $^{A+1}_Z X^*$. By though emitting specific γ-rays, the nucleus relaxes to the ground state after 10^{-12} to 10^{-9} s forming the state $^{A+1}_Z X$. The detection of the spectrum of emitted prompt γ-rays is done while the sample is exposed to neutron
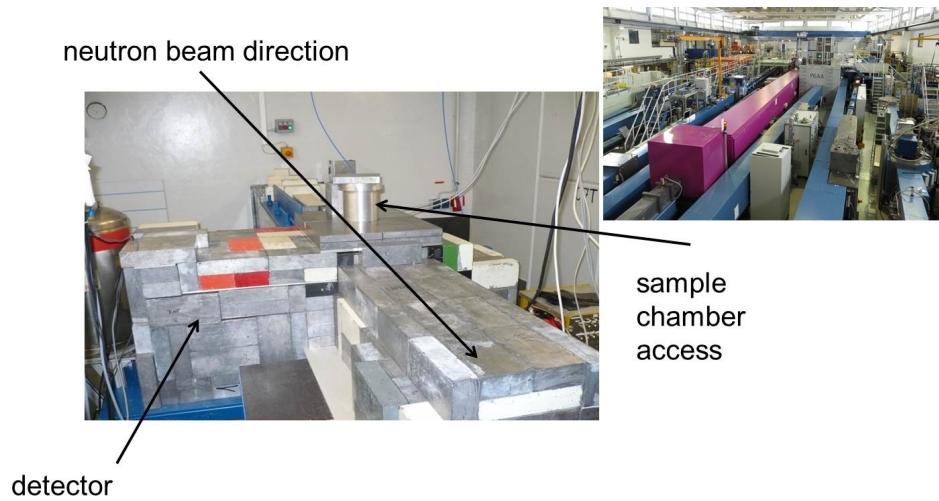
Figure 27: PGAA apparatus in the FRMII in Garching. Picture provided by [56,57].

radiation. The qualification and quantification of each analyzed element or isotope is possible due to the specific energies and area of the emitted prompt γ-rays. If possible, about 25 peaks per element are used to allow a safe, distinctive and unambiguous identification with a high precision [55].

Beside prompt γ-rays the sample can also emit β-rays, or can decompose in a radioactive decay to $_{Z\pm1}^{A+1}X^*$. In this status it can also emit γ-rays. This effect is used in delayed neutron activation analysis (NAA).

5.8.2. Experimental Set-up

The PGAA facility is shown in the picture of **Figure 27** and is supervised by Dr. Petra Kudejova and Dr. Zsolt Revay. The instrument uses neutrons coming from the cold source of the reactor. The average energy at the target position is 1.83 meV (6.7 $\overset{\circ}{A}$). The neutron guide (from source to instrument) has a length of 51 m and a radius of 390 m. The position for measurements can be varied for larger and smaller samples and the neutron flux can be tuned by a set of attenuators from $1 \cdot 10^9$ neutrons/cm^{2}s to $6 \cdot 10^{10}$ neutrons/cm^{2}s [53]. As a shielding material Pb, Cd, B$_4$C and ^{6}LiF-polymer are used. Measuring conditions are usually at a reduced pressure of 0.3 mbar to reduce ambient air in the sample chamber to reduce the signal from nitrogen in the spectrum. The sample weight needs to be between mg and g and should not exceed dimensions of 40 x 40 x 40 mm. For standard PGAA measurements detectors with high purity germanium (HPGe) are used. The working principle of this detector type is similar to gas ionization detectors. The γ-rays produce electron-hole pairs (in case of gas ionization: electron-ion pairs), which are collected by an electric field, generated with high-voltage. The high-voltage is needed to prevent recombination reactions. Even at low ionization energies electron-hole pairs are generated by thermal excitation, for this reason a ger-
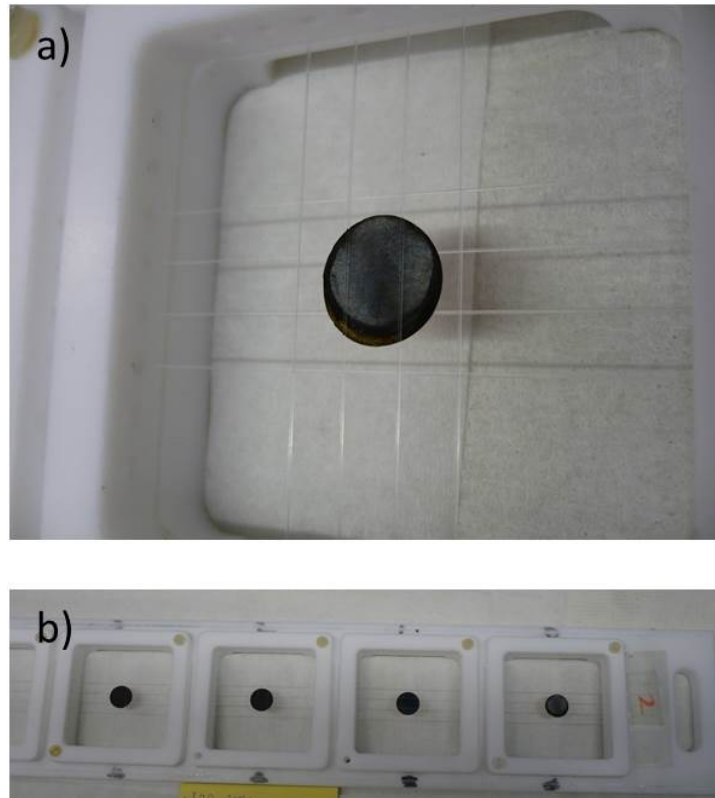
Figure 28: PGAA sample holder with attached electrodes. Pictures provided by Dr. Petra Kudejova.

manium detector is typically cooled down by liquid nitrogen to 77 K (stored in a dewar at the detector).

5.8.3. Sample and Data Treatment

For the PGAA measurement, electrodes were assembled in a special sample holder, which is shown in **Figure 28a)** and **b)**. The frame of the sample holder, as well as the thin meshed fibers, are made of fluorinated ethylene propylene (Fep), which is a sort of teflon and a co-polymer of tetrafluoroethylene and hexafluoropropylene and has a low background signal in the measurement. Like it is shown in **a)**, the electrode is attached between fibers and several samples can be measured in parallel. The neutron beam has always a bigger size than the measured sample.

For the final data treatment, we used the singlet line at 9297 keV for iron detection. Multi-lines are not evaluated because of matrix effects coming from copper (Cu) and titanium (Ti), which are overlapping to many of the typical Fe-lines. This singlet line is specific for iron and is not interfered by other elements or isoptopes. Final iron amounts in the experiments are calculated in relation to copper, which was used as an internal standard, allowing us a precise mass calculation. Copper was used as a current collector

foil for each electrode and was weighted to 0.1 mg precision and is known to be of the same mass.

The analysis was performed in cooperation with researchers from the Forschungsneutronenquelle Heinz Maier-Leibnitz (FRMII; Garching bei München; Dr. Petra Kudejova (experimental treatment and spectra fitting), Dr. Stefan Seidlmayer and Dr. Veronika Zinth (data analysis)) within the assigned beam-time according to the rapid access proposal 9123, which was submitted on the 19th of December 2013.

6. Results and Discussions

6.1. Poly-ethylene glycol di-methyl ether as Solvent for Lithium-Ion Batteries

6.1.1. Abstract

The purpose of this study is to validate a novel, liquid poly-ethylene oxide-based electrolyte for Li-ion batteries, consisting of a mixture of poly-ethylene glycol (500) di-methyl ether (PEG500DME) - lithium bis-(trifluoromethanesulfonyl)-imide (LiTFSI, 1 mol/kg). Data collection, treatment, as well as publication of our results [58] was performed while my visiting doctoral-candidate time in Rome (Italy) at the University La Sapienzá. Due to the high molecular weight of PEG500DME, the solvent shows a high relative viscosity (28 mPas [59]). End capped ether groups of the solvent are reflected for a low vapor pressure, which causes an excellent thermal stability, proofed and demonstrated by thermogravimetric analysis. These characteristics are important for safety issues and show an improvement compared to commonly used organic carbonates. Besides the electrochemical impedance spectroscopy study of the electrolyte demonstrates a Li-transference number of 0.47, an ionic conductivity in the order of 10^{-3} Scm^{-1} and a high inter-phase stability with the lithium metal. The linear sweep voltammetry indicates an electrochemical stability window extending up to 4.8 V$_{Li}$. Furthermore, promising electrochemical performances in terms of reversibility, cycling stability and low charge and discharge polarization were observed using the electrolyte in symmetrical lithium and in Li-ion batteries using lithium cobalt oxide (LCO) as cathode and titanium dioxide (TiO$_2$) as anode. Hence, this electrolyte is a promising candidate for applications in safe, high performance lithium ion batteries.

6.1.2. Introduction

Storage applications for electrical energy bear an important meaning in this century. A suitable candidate for energy storage devices are rechargeable lithium batteries. Nowadays Li-ion batteries are widely used for private portable devices, but, there is also a large demand for storage systems in the automotive field for hybrid electric vehicles (HEVs), plugged-in hybrid electric vehicles (PHEVs), full electric vehicles (EVs) and for storage systems for renewable energies based on wind and solar power. Due to possess of a high energy density and an acceptable long cycle life, lithium ion batteries can be used for these devices. Nevertheless, there are several challenges in terms of safety and costs [60,61]. Safety aspects are mainly associated with volatile and high flammable characteristics of common used carbonated organic electrolytes causing thermal runaway or other burning events [62]. Alternative solvents are those based on poly-ethylene oxide, (PEO) [61]. They are characterized in low cost, high safety and chemical inertness [61] as well as good solvating behavior, acceptable ionic conductivity [63], electrochemical stability

[64], interfacial stability towards lithium metal and good mechanical properties [63,65]. The chosen poly-ethylene oxide based solvent for our study is liquid PEG500DME, which has a high viscosity and was, according to our knowledge, only studied in the late 1990s by Shi et al. (1995) and Appetecchi et al. (1996) [66,67]. However, an additional method to increase life time and safety is the use of anode materials based on titanium oxides like lithium titanate (LTO, $Li_4Ti_5O_{12}$) or titantium dioxide (TiO_2) [68,69], which are operating at elevated voltages. Due to a higher redox potential around 1.0 and 1.5 V_{Li} deposition plating of elementary lithium on the anode side and electrolyte reduction can be avoided [7,40]. To investigate thermal and electrochemical properties of the high viscosity PEG500DME($\approx$ 500 g/mol molecular weight) solvent with LiTFSI as a conductive salt, thermo-gravimetric analysis (TGA) and differential scanning calorimetry (DSC) were used as preferred techniques for the characterization of the thermal properties of the electrolyte and linear sweep voltammetry (LSV) and electrochemical impedance spectroscopy (EIS) for the characterization of the electrochemical behavior. The PEG500DME-LiTFSI electrolyte is then tested in a full cell coupling using a TiO_2 anode and a $LiCoO_2$ cathode to form a new, advanced configuration lithium ion battery.

6.1.3. Experimental Part

The as-received organic solvent poly-ethylene glycol (500) di-methyl ether (PEG500DME, M = 500 g/mol) (Sigma Aldrich) was dried over night under dynamic vacuum at 80°C in a Büchi oven (Switzerland) and afterwards stored over molecular sieves until the water content was below 15 ppm (Karl-Fischer Titration). The electrolyte itself was prepared by mixing lithium bis-(trifluoromethanesulfonyl)-imide (LiTFSI, Sigma Aldrich) in a 1 mol/kg ratio in an argon filled glovebox (< 1 ppm water). The used abbreviation for the studied electrolyte is PEG500DME-LiTFSI. To give a full characterization of the electrolyte, the anodic and cathodic electrochemical stability window of PEG500DME-LiTFSI was studied by linear sweep voltammetry. The experiments were performed by using a Biologic VMP3 multi-potentiostat at a scan rate of 0.2 mV/s in a potential window of 0.01 and 5.0 V_{Li}. Half cell systems in a three-electrode arrangement with lithium metal as counter electrode versus Super P carbon (Timcal) on aluminum foil, respectively copper for the cathodic scan, as working electrode and lithium metal as reference electrode were measured. Lithium-lithium symmetrical Swagelok $^{\textregistered}$ cell systems were used for lithium interface stability measurements, measured by potentiostatic electrochemical impedance spectroscopy (PEIS). The assumed values for the used error bars were calculated by an error distribution analysis, containing errors are the variation in temperature and resistance over time. The ionic conductivity was obtained in an argon filled glove box with a blocking electrode conductivity cell (Metrohm) at various temperatures. In case of ionic conductivity, the error bars are associated with the cell constant and electrolyte resistance. The determination of the lithium transference number was done as well in a symmetrical cell arrangement by a combination of AC

and DC polarization methods. The overall resistance of the initial state was compared with the overall resistance of a steady state after the appliance of 30 mV until achievement of a steady state. The calculation of the lithium transference number was done by using the Bruce & Vincent method, which was reported by Bruce and co-workers in 1987 [70]. Determination of the initial and steady state resistance was done by a nonlinear least squares fit analysis (NLLSQ) reported by Boukamp [71, 72]. In addition, thermal stability of the electrolyte solution was determined with both a thermo gravimetric analysis (TGA) in a constant nitrogen stream within a temperature range of 25°C and 500°C with a heating rate of 10°C/min (Mettler Toledo TGA/SDTA 851) and differential scanning calorimetry (DSC) in sealed aluminum pans under nitrogen atmosphere at a cooling/heating rate of 10°C/min (Mettler Toledo DSC821e), as well. The chosen temperature range was from 25°C down to −95°C and heating up to 90°C with a following cooling back to 25°C. All impedance spectra were performed by using VersaSTATMC (Princeton applied research) in a frequency range of 500 kHz to 10 mHz at OCV. To demonstrate stability under current exposure lithium stripping and deposition was performed in a symmetrical cell and was controlled at 0.1 mA over 500 cycles by MACCOR Series 4000 Battery test system (Maccor Inc.). Besides, the electrolyte was characterized in half cells of the following listed electrodes and full cells with combined both electrodes. Therefore, titanium dioxide (TiO_2) and lithium cobaltoxide (Lco, $LiCoO_2$) electrodes, coated on copper and on aluminum current collectors, respectively, are used in a Swagelok ® T-cell design with two Whatmann ® glass fiber separators soaked in Peg500dme-Litfsi. The cells where tested under galvanostatic cycling at a rate of C/5 (34 mA/g) using a Maccor Series 4000. The synthesis of anatase type TiO_2 followed the description in a publication by Chen et al. [73]. The characterization of this home-made powder is given in the following. Lco is a commercial available powder supplied by Nippon Chem. Industrial Co. Ltd Tokyo, Japan. Both electrode types were composed of active material powder, Super P carbon and Pvdf binder (Solvey) an 80:10:10 weight ratio. Slurries of these solid mixtures and N-methyl-2-pyrrolidone (Nmp) (Aldrich) were casted on the mentioned current collectors. The weight of the electrodes was 3.4 mg/cm^2 and 5.6 mg/cm^2 for TiO_2 respective Lco after drying for at least 5 h under dynamic vacuum at 120°C.

6.1.4. Results and Discussion

For the characterization of Peg500dme-Litfsi, the electrochemical stability within the range of 0.01 to 5.0 V_{Li} and the stability of the lithium interface over time is demonstrated in **Figure 29a)** and **b)**. By a linear sweep technique of a Super P carbon electrode versus metallic lithium the current density versus voltage profile the electrochemical stability is shown in **Figure 29a)**. The anodic stability for this electrolyte is warranted until 4.8 V_{Li}. Beyond this point the current density increases due to electrolyte oxidation. In the other scan direction, the cathodic scan shows stability down
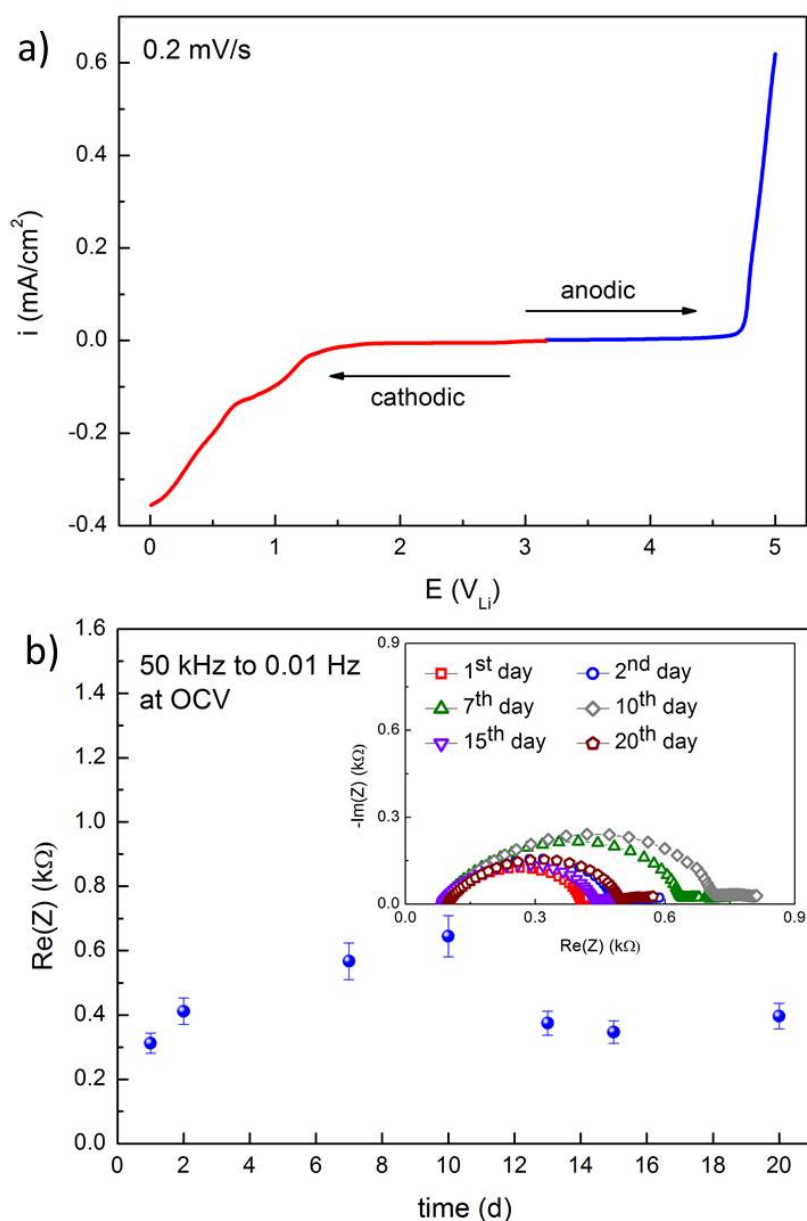
Figure 29: a) Electrochemical stability profile for Peg500dme-LiTFSI within an electrochemical window of 0.01-5.0 V_{Li} vs. at a scan rate of 0.2 mV/s and room temperature. b) Time dependency of the overall resistance is given by PEIS measurement over time of a symmetrical lithium/Peg500dme-LiTFSI/lithium cell. The resistance reached the highest value of 0.64 kΩ after 10 days and decreased afterwards to the initial resistance. The corresponding Nyquist plots measured in a frequency range between 500 kHz and 10 mHz (10 mV signal amplitude) are shown in the inset for this time period.

to 1.5 V_{Li}. At potentials lower than 1.2 V_{Li} one can observe peaks, which are mostly associated to the beginning of the formation of a solid electrolyte interface (SEI) surface film [74]. The shoulder at a potential around 0.5 V_{Li} is assigned to the occurrence of intercalation of lithium ions in the amorphous carbon structure. Beside this, this peak is mainly assigned to the mail SEI formation peak with ethylen gas evolution (see **Chapter 6.6** and publications referred). By potentiostatic electrochemical impedance spectroscopy (PEIS) one can determine the stability of the overall resistance at open circuit conditions of a symmetrical lithium-lithium (Li/Peg500dme-Litfsi/Li) cell over the first 20 days. This is shown in **Figure 29b)**. The inset gives the corresponding Nyquist plots after a selected time. The cell resistance changes over time, whereby the high frequency resistance (HFR) remains constant at around 0.1 kΩ. Within the first ten days the resistance increased to a maximum of 0.64 kΩ and afterwards it is decreasing to 0.31 kΩ, which is equivalent to the value at day 1. Finally, after 20 days one can observe a re-increase of the resistance as expected due to the SEI film formation and re-dissolution process [74]. This is also a typical behavior of Peo based electrolytes, which is still reported [75]. As it is widely known, the ionic conductivity is addicted to the temperature. With a raise in temperature an increase of ionic conductivity is expected due to higher mobility of ions and a decrease of viscosity. **Figure 30** shows the Arrhenius plot in the range from 100°C to RT. It was performed by measuring the resistance of the electrolyte solution at different temperatures by cooling down from 100°C to 25°C and heating back in an insulated container inside an argon filled glovebox. In case of the electrolyte Peg500dme-Litfsi (1 mol/kg) the ionic conductivity is determined to be in a range of 4 mS/cm at ≈ 100°C and 0.45 mS/cm at 25°C. The heating and cooling plots show a good overlapping behavior. Furthermore, this indicates good lithium ion transportation and good thermal stability, as well. Thermo-gravimetric analysis (TGA) gives information about the thermal stability of the electrolyte. The percentage of weight loss is plotted against the raise of temperature in **Figure 31a)**. Under permanent nitrogen flow, with a heating rate of 10°C/min, the first weight loss is reported at around 200°C, which is dedicated to the evaporation of Peg500dme. The massive weight loss > 250°C corresponds to the boiling point of Peg500dme given by the supplier. At around 300°C one expects the beginning of LiTFSI decomposition [76]. This is overlapping with evaporation of Peg500dme. At 350°C we reported a step which corresponds to the adjacent evaporation of LiTFSI. Therefore the electrolyte mixture shows, like expected, a good thermal stability up to 200°C. To determine the stability at lower temperatures and the crystallization point **Figure 31b)** shows the DSC trace of Peg500dme-Litfsi. The chosen temperature range was +40°C to −90°C with a cooling/heating rate of 5°C/min. Peg500dme-Litfsi is liquid until 4°C, which is the crystallization point and it shows a phase change from liquid to solid. At around −80°C glass transition behavior can be observed. An additional fundamental parameter is the lithium transference number t_{Li+}. This dimensionless parameter describes the quotient of charge, which is transported by lithium ions and overall charge. The value can be ranging from 0 and 1. The higher the value, the more lithium ions are involved. The
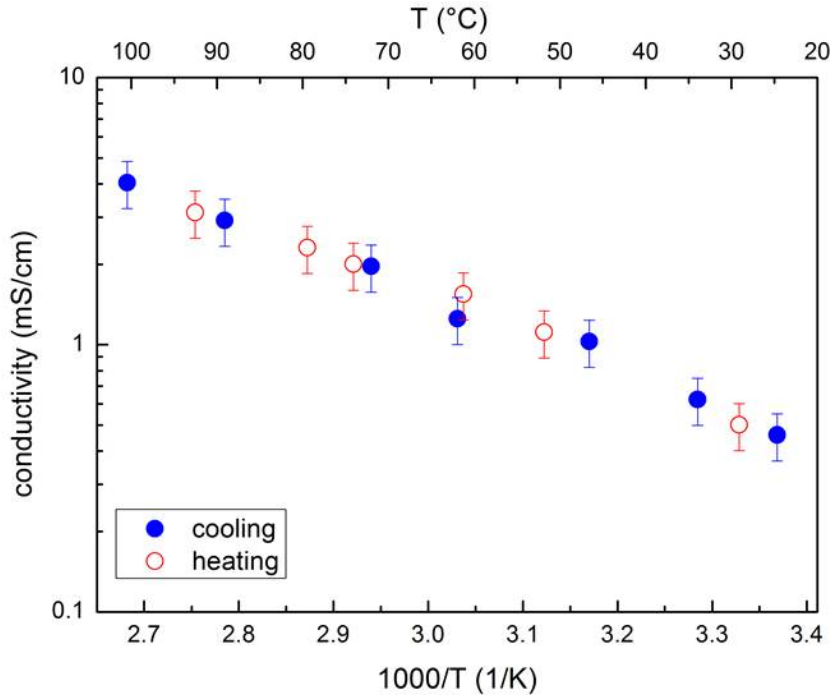
Figure 30: Temperature dependence of ionic conductivity of PEG500DME-LITFSI at various temperatures. Heating and cooling plot shows an accurate overlapping, which stands for a good thermal stability and good lithium ion transport [58].

reduction and oxidation process of lithium cations are reversible on both electrodes. This fact does not apply for the corresponding anions. Due to a coulombic force, like an applied potential, lithium ions are reduced or oxidized on cathode or anode, respectively. Most used cations remain without electrochemical reaction in solution. To keep the electrolyte solution neutral, lithium ions have to be reduced to balance the charge and follow these anions. The better the diffusion of ions through the electrolyte the faster is the lithium transportation and the higher is the transference number. An electrolyte with high viscosity shows an inhibited diffusion process. **Figure 32** shows the AC/DC current versus a time profile and in the inset impedance spectra of the initial and steady state of the lithium-lithium symmetrical cell. The calculated transference number for these data points is $t_{Li+} = 0.47$ calculated by Bruce & Vincent method. The determination of the initial and steady state resistance was done by a nonlinear least squares fit analysis (NLLSF), reported by Boukamp in 1986 [71, 72]. Although the electrolyte shows a high viscosity, the transference number is still good and shows a better value compared to other PEG500DME containing electrolytes [77]. We believe that this high t_{Li+} value is due to the combined effect of the enhanced solvating properties of the PEG500DME liquid and the excellent mobility of the Li^+-ions originated from the LITFSI salt. With lithium deposition and stripping it is possible to demonstrate the stability of the electrolyte while applying a current, which corresponds to the

51
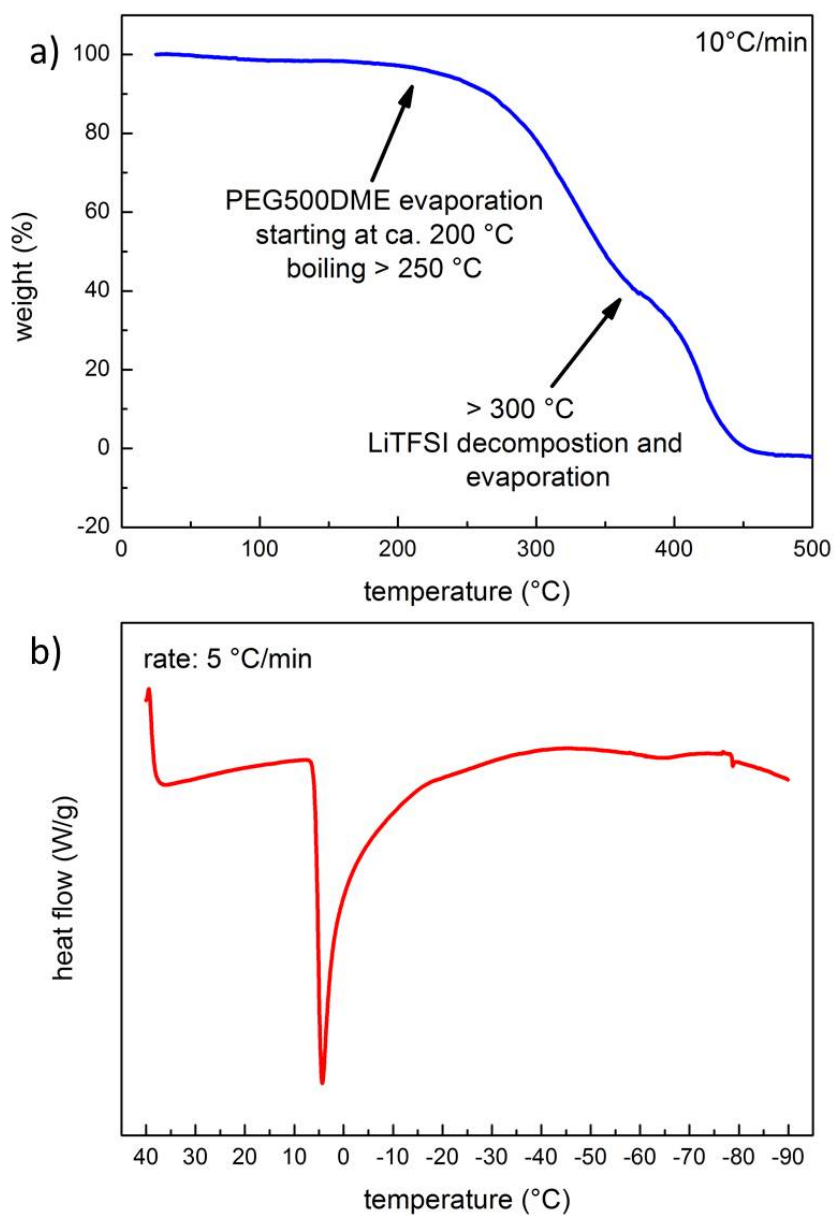
Figure 31: a) TG analysis of Peg500dme-Litfsi from 25°C to 500°C under nitrogen flow. b) DSC traces for a rate of 5°C/min [58].
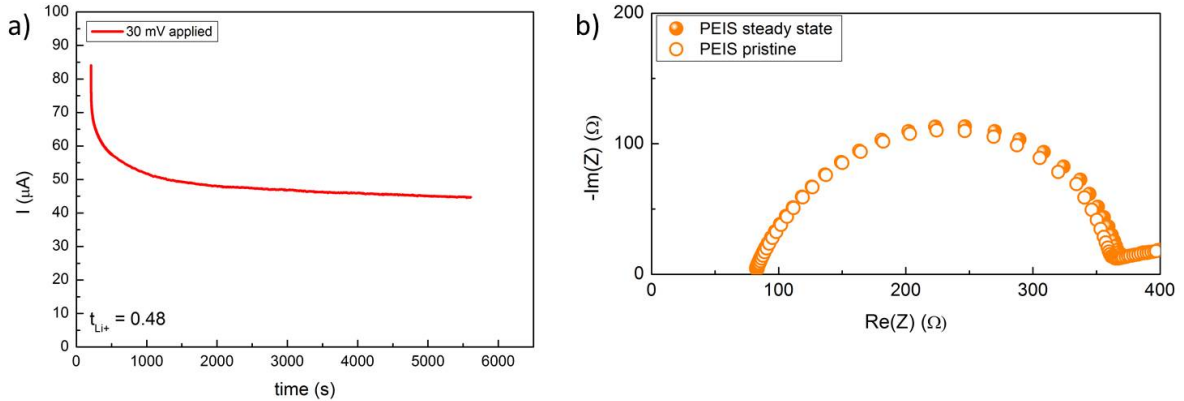
Figure 32: a) Shows the AC/DC characterization for determination of lithium transference number t_{Li+}. 30 mV was applied to a symmetric Li/Peg500dme-LiTfsi/Li cell and the current profile was recorded. Before and after applying the potential, PEIS of the initial and steady state of the cell was measured in b). The Nyquist profiles correspond to the EIS measurement performed at the initial and the steady state condition [58].

charge and discharge current. In **Figure 33** lithium deposition and stripping overvoltage over time is monitored. The profile shows a low overvoltage, low polarization of about 75 mV and a high cycling efficiency. The coulombic efficiency within cycling is $\approx 97\%$ which was calculated by integration. This value stands for a high reversibility and a good compatibility of the electrolyte. The curve progression stays constant over all 500 cycles. The behavior of the Peg500dme-LiTfsi electrolyte in a lithium ion cell was determinate by combining it with a commercial Lco cathode and a TiO_2 anode synthesized in our laboratory. Prior to the use of the home-made TiO_2, the powder was characterized by scanning electron microscopy (SEM) and x-ray diffraction (XRD). The Brunauer-Emmett-Teller (BET) analysis of the TiO_2 powder (data not reported, measured by A. Latini) gave a specific surface area of 73.0 ± 0.2 m^2/g, which confirms the nano-porous morphology of the material. It is be noticed that the specific area obtained by considering only the external surface of the 1 μm spheres, see SEM in **Figure 34a)**, is calculated to be of the order of 1.5 m^2/g, *i.e.* a much less value than the one observed by BET analysis. The particular morphology of this powder is based on spherical particles with a mono-disperse size of around 1 μm. The Rietveld analysis of the XRD reported in **Figure 34b)** reveals specific peaks assigned to a pure anatase phase [58, 78], with cell parameters calculated as a = b = 3.7849 $\mathring{A}$, c = 9.4955 $\mathring{A}$ with a crystallite size of ≈ 20 nm. Finally, in the following part the performance of half and full cells studied in the electrolyte Peg500dme-LiTfsi is demonstrated. In half cell measurements, TiO_2, respective Lco, electrodes were assembled in polymer Swagelok $^{\circledR}$ T-cells versus lithium metal as counter electrode and cycled in a certain potential window at a rate of 34 mA/g. For Lco half cells, the potential window was set between 4.2 and 3.0 V$_{Li}$. For the half cells with the anode material TiO_2 2.4 to 1.0 $_{Li}$ was chosen. **Figure 35a)** shows a direct comparison of the typical charge and discharge profiles of Lco or TiO_2. In case
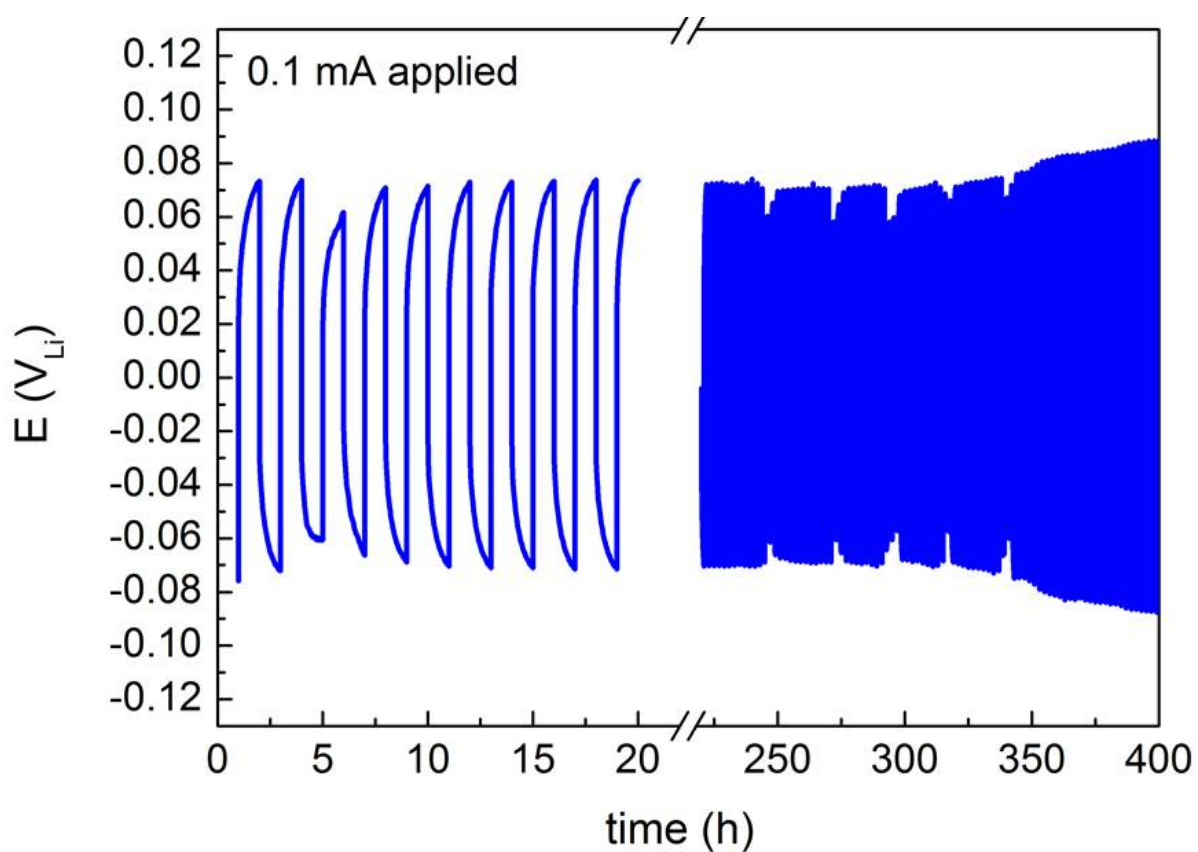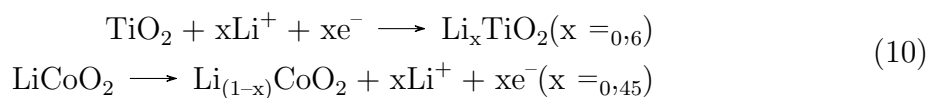
Figure 33: Stable and symmetrical profile of lithium deposition and stripping at 0.1 mA in a Li/Peg500dme-LiTFSI/Li cell over serveral cycles [58].
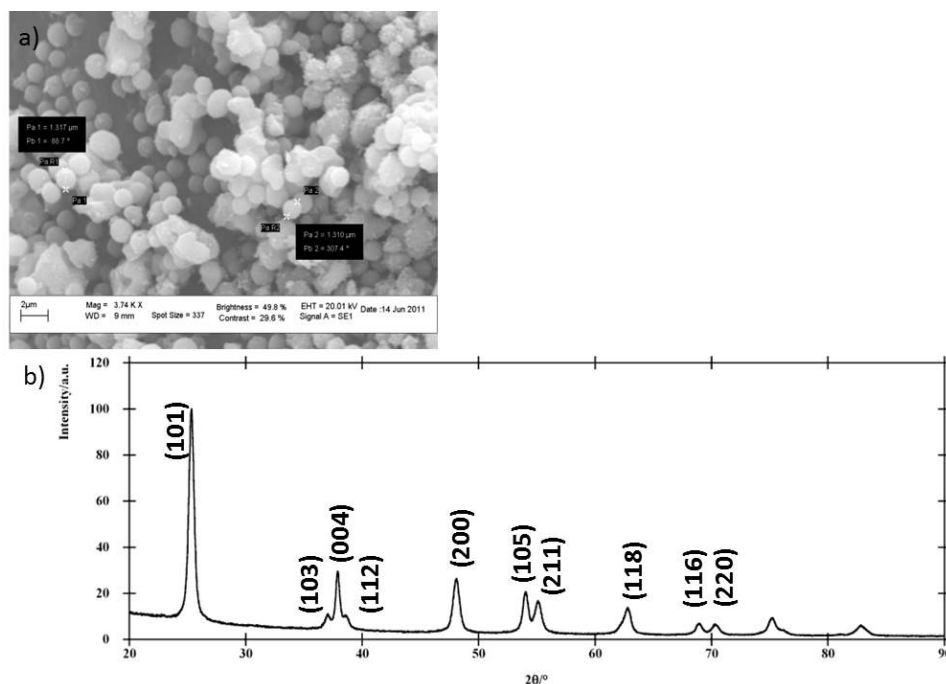
Figure 34: a) SEM picture which shows spherical particles with an average size of 1 μm. b) XRD pattern with typical reflexes attributed to anatase TiO_2 [58].

of Lco we collected a stabilization behavior of the capacity within the first cycles. After 5 cycles the half cells show a stable specific capacity at around 123 mAh/g (theoretical value: 274 mAh/g in a 1 e^- process. Calculated by molecular mass and faraday constant 96485.34 C/mol; pure Lco can reach a maximum of 130 mAh/g [79]). The coulombic efficiency is calculated to be more than 99%. Stable capacity values for several cycles confirm the excellent property of the studied electrolyte. After 5 cycles the profile of TiO_2 ends up at 195 mAh/g (theoretical value: 336 mAh/g in a 1 e^- process). In this case the coulombic efficiency is calculated to be 98%. One can observe only one plateau for both electrodes during charge and discharge which is due to the one electron process occurring during charge, respective discharge. The charge reactions of the half cells are described by **Equations (10)**.

$$
\begin{aligned}
TiO_2 + xLi^+ + xe^- &\longrightarrow Li_xTiO_2(x =_{0,6}) \\
LiCoO_2 &\longrightarrow Li_{(1-x)}CoO_2 + xLi^+ + xe^-(x =_{0,45})
\end{aligned}
\tag{10}
$$

As observed in **Figure 35a)**, and considering the cell reaction mechanisms shown in **Equation (10)**, one sees that the anode capacity exceeds the one of the cathode. This difference is taken under consideration for assuring proper cell balance. That is why, one can calculate the potential and current limits for a full cell combination. The full cell, containing TiO_2 as anode and Lco as cathode, in terms of cathodic limitation, the cell is cycled at 34 mA/g in a potential range of 3.2 and 0.8 V, whereby the redox plateau
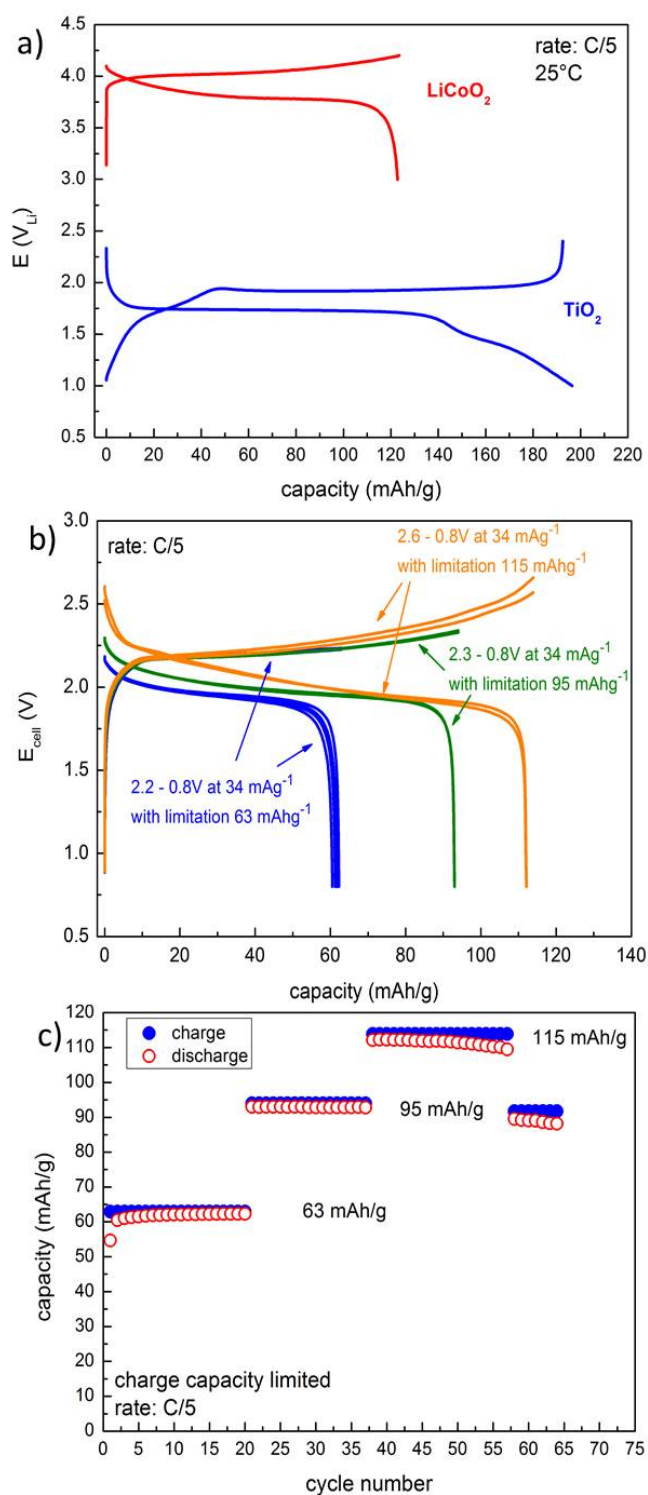
Figure 35: a) A typical voltage profile of Lco and TiO_2, in comparison, for the half cells versus lithium metal prepared using Peg500dme-Litfsi as electrolyte and cycled at a rate of C/5 (34 mA/g) at the fifth charge and discharge cycle. b) Voltage profiles of the constant current charge and discharge tests performed on the TiO_2/Lco full cell at three different capacity limits with a current of 34 mA/g. c) Stable cycling performance over 50 cycles of the TiO_2/Lco full cell showing a good coulombic efficiency and reversible performance [58].

of the cell is located at 2 V, as expected by the combination of voltage range of the two electrodes. To reach a good cycling behavior, the capacity of the full cell was limited to defined capacities at 63 mAh/g, 95 mAh/g and 115 mAh/g. **Figure 35b)** gives the voltage versus capacity behavior of the TiO_2/Lco full cell for the mentioned different capacity limitations. In Peg500dme-Litfsi, the electrode combination possesses a stable capacity over several cycles and at all capacity limits, like shown in **Figure 35c)**. It also shows an excellent charge and discharge coulombic efficiency and reversible behavior.

6.1.5. Conclusions

A full characterization of a novel electrolyte containing poly-ethylene glycol (500) dimethyl ether (Peg500dme; M = 500 g/mol) as solvent and lithium bis-(trifluoro-methanesulfonyl)-imide (Litfsi) as conducting salt was given. This electrolyte was characterized by high safety, due to its low vapor pressure and low flammability. TGA and DSC measurements gave a high thermal stability from 250°C to 4°C and a wide electrochemical window up to 4.8 V_{Li}. half cell tests with lithium cobaltoxide ($LiCoO_2$, LCO) or titantium dioxid (TiO_2) each versus lithium metal as well as full cells combining TiO_2/Lco possessed a good and stable cycling response. This leads to the result, that Peg500dme-Litfsi is proposed to be an excellent electrolyte for advanced Li-ion battery applications.

6.2. Ionic liquid as an Electrolyte Additive in Li-Ion Batteries

6.2.1. Abstract

This is a comparative electrolyte study for PEG500DME as electrolyte solvent with lithium bis-(trifluoromethanesulfonyl)-imide (LiTFSI) with different additions of with 1-Methyl 4-Butyl pyrrolidinium bis-(trifluoromethanesulfonyl)-imide ($Py_{1,4}TFSI$) for Li-ion Batteries. Data collection and treatment was performed while being a visiting doctoral-candidate in Rome (Italy) at the University La Sapienzá.

This part gives a comparative study about the behavior of a liquid, novel and high viscous poly-ethylene oxide-based solvent PEG500DME in different mixtures with $Py_{1,4}TFSI$ as additive for electrolyte applications in lithium batteries. LiTFSI was used as conducting salt with an amount of 1 mol/kg. The high molecular weight and a high relative viscosity of 28 mPa [80] leads, not only to a low vapor pressure, but also to an excellent thermal stability. Additives of $Py_{1,4}TFSI$ induce a further increase of thermal stability. It leads to a higher decomposition temperature and leads to a freezing point depression, which is approved by thermal gravimetric analysis and differential scanning calorimetry, respectively. All mixtures show an assured wide electrochemical window from 1.5 to 4.7 V_{Li} and, to an excellent reversible lithium stripping and deposition behavior, as well. In addition, even at higher temperatures, the electrochemical aluminum corrosion behavior with LiTFSI is shown to be not existent, compared to LiTFSI in common used carbonate containing electrolytes.

6.2.2. Introduction

Due to the demand on the development of battery systems, which are convincing in terms of capacity, energy density, reliability, safety and costs, for applications in hybrid or full electric cars, portable devices and long-term energy storage systems for renewable sources [61], one need to improve advanced lithium ion batteries. Thereby, issues like safety and costs play an important role. The aspect on safety can be guaranteed by replacing common used carbonated organic liquids in electrolyte applications. They are characterized by a volatile and flammable behavior which can promote hazard and burning events like thermal runway [12, 81]. A possible alternative is the use of liquid poly-ethylene oxide based solvents for electrolyte mixtures. They show expedient characteristics like low cost, chemical inertness and no volatile behavior [61]. Besides, they are known to exhibit an adequate ionic conductivity [63] and show stability against metallic lithium [63, 65] and under electrochemical conditions [64]. These solvents are also a possibility in applications like lithium-air batteries, because poly-ethylen oxide based electrolytes inhibit reactions of charge and discharge products, like singlet oxygen [82].

The use of the ideal conducting salt is a big challenge. Because of its characteristics, LiTFSI seems to be a suitable candidate and shows a high thermal stability and has a

good conductive behavior in contrast to lithium-tetrafluoroborate (LiBF$_4$) and lithium-hexafluorophosphate (LiPF$_6$) and is neither hazardous nor toxic, like lithium-perchlorate (LiClO$_4$) or lithium-hexafluoroarsenate (LiAsF$_6$), respectively [12]. The main drawback of LiTFSI is the ability to corrode aluminum metal, which is common used as a current collector material for cathodes, under electrochemical conditions [83, 84]. A separate and more detailed study in terms of aluminum current collector corrosion is given in **Chapter 6.3**. It is known that addition of corrosion inhibitors like polyvinyl alcohol (Pva) and poly-ethylene glycol (Peg), aluminum corrosion can be prevented by forming a protective layer from polymer molecules and Tfsi-anions on top of the metal surface [85, 86]. That is why no aluminum corrosion with LiTFSI is expected with the use of poly-ethylene oxide based solvents.

Ionic liquids are studied since the 1930s and are known to have no flammable behavior, high thermal stability and a low vapor pressure [87]. They are environmentally benign and recyclable [88] and as well stable in contact with air [87]. Characteristics for ionic liquids containing imidazolium ring as cation are known to have a good electrochemical stability and low melting points. It is known that an addition of Py$_{1,4}$Tfsi to electrolyte solution improves thermal stability and ionic conductivity could be increased, due to its large and stabilized anion and the resulting lower lattice energy, which allows a better movement of the ions [89]. It is also known that the addition of ionic liquids to poly-ethylene oxide based enhances the ionic conductivity [90, 91] and shows a wide electrochemical window, a stable inter-facial resistance [92] and a good cycling performance in Li/Lfp cells [90, 93].

With addition of 0%, 10% and 30% Py$_{1,4}$Tfsi to Peg500dme with LiTFSI, we expect beside a higher conductivity, a raise in thermal stability even to low temperatures. The aluminum corrosion behavior should not be influenced by the addition of Py$_{1,4}$Tfsi, because the stabilization of Tfsi-anion is resulted from the coordination with poly-ethylene oxide molecules on top of the aluminum metal surface.

6.2.3. Experimental Part

The preparation of the electrolyte solution was done by mixing Peg500dme (Sigma Aldrich) and Py$_{1,4}$Tfsi in ratios 1:0, 9:1 and 7:3 in an argon filled glove box (<1 ppm O$_2$/H$_2$O). Py$_{1,4}$Tfsi, which is commercial available, was obtained by Solvionic (purtity 99.9%). Both liquids were dried for several hours under dynamic vacuum at 100°C before mixing. The water content, afterwards, was below 15 ppm. LiTFSI (Sigma Aldrich) was added as conducting salt with a molality of 1 mol/kg. All used mixtures are listed in **Table 1** with the abbreviations used in the following text. To give a complete overview about the behavior of these three electrolyte mixtures, we figured out the ionic conductivity was figured out in the range room temperature (RT) to around 100°C, with a Metrohm blocking electrode system and a Biologic VMP3 multipotentiostat. With this data one can calculate the activation energy. To determine the error bars, an error

Table 1: Studied compositions of Peg500dme, Py$_{1,4}$Tfsi and 1 mol/kg LiTFSI and used abbreviations

Composition	Abbreviation
Peg500dme-LiTFSI	Peg0
Peg500dme + 10%Py1,4Tfsi-LiTFSI	Peg10
Peg500dme + 30%Py1,4Tfsi-LiTFSI	Peg30

distribution analysis was done, taking a variation in cell constant and change of resistance into account. Errors for activation energy were estimated by the error of the slope of the Arrhenius plot, containing the error of conductivity. For the calculation of the lithium transference numbers the Bruce & Vincent method was used, reported by Bruce and co-workers in 1987 [70]. Therefore impedance spectra before and after a chrono-amperometric method were performed in a lithium-lithium symmetrical Swagelok ® cell by using VersaSTATMC (Princeton applied research) in a frequency range of 500 kHz to 10 mHz at OCV and at an applied potential of 30 mV for the DC method, respectively. Stability measurements were also done with a symmetrical Li/electrolyte/Li Swagelok ® cell arrangement over time and versus lithium. To determine the stability over time the change of impedance was recorded during the first hours and over several days in a frequency range of 500 kHz to 10 mHz at OCV. The stability of lithium interface was demonstrated by the lithium stripping and deposition method at an applied current of 0.1 mA for 500 cycles with MACCOR Series 4000 Battery test system (Maccor Inc.). Another issue is the comparison of the thermal behavior. Elevated temperatures from 25°C to 500°C were analyzed by thermo gravimetric analysis (TGA) under nitrogen atmosphere with a heating rate of 10°C/min. Whereas, differential scanning calorimetry (DSC) was used for temperatures lower 40°C down to −90°C at a cooling/heating rate of 5°C/min (Mettler Toledo DSC821e). To figure out the electrochemical stability window for the anodic scan up to 5.0 V$_{Li}$ and cathodic scan down to 0.01 V$_{Li}$, a half cell arrangement with Super P carbon (Timcal) on aluminum and copper, respectively, as working electrode was used at a scan speed of 0.2 mV/s. The electrochemical corrosion behavior of those electrolyte solutions was tested by cyclic voltammetry and chrono-amperometric polarization of a metallic aluminum foil versus lithium in a Swagelok ® cell arrangement between 2.5 and 4.5 V$_{Li}$ at 0.2 mV/s for 10 hours, respectively, at room temperature and 50°C. Both, electrochemical stability and electrochemical corrosion measurements were performed with a Biologic VMP3 multipotentiostat. In all half cell arrangements metallic lithium was chosen as counter and reference electrode as well as Whatman ® glass fiber pads as separators. The diameter of all electrodes were 10 mm. For current collector corrosion studies a metallic aluminum disc was used as working electrode.

6.2.4. Results and Discussion

This paragraph shows a detailed characterization and comparison of the used electrolyte mixtures PEG0, PEG10 and PEG30. It is known from previous research that PEG0 is an excellent high viscous solvent for electrolytes with many profitable characteristics *e.g.* high thermal stability and low vapor pressure [58] and to promote a bigger thermal stability window under 0°C and to show the differences in behavior between solid PEO based electrolytes with ionic liquids as an additive and ionic liquid mixtures with some percentages of poly-ethylene glycol, reported elsewhere [89,94]. The mentioned mixtures, PEG500DME with 0%, 10% and 30% $Py_{1,4}TFSI$, respectively, and LiTFSI, were proved in terms of ionic conductivity, lithium transference number, stability over time and of the lithium interface, thermal behavior, electrochemical stability and ability for aluminum corrosion. First of all properties for ionic transportation are reported. **Figure 36** gives the comparative behavior of the ionic conductivity between 25°C and 100°C. As a result, the behavior of these three mixtures is equal. Also the value for the ionic conductivity, including error bars, is in the same range of 0.51 $\pm$ 0.1 mS/cm (see **Table 2**). For PEG30 a small deviation is recorded with a value of 0.76 $\pm$ 0.15 mS/cm. This might be due to a gain in influence of the ionic conductivity behavior of the ionic liquid, which is added with 30% of the solvent. A mixture of 0.5 M LiTFSI in $Py_{1,4}TFSI$ shows an ionic conductivity of 1.7 mS/cm at room temperature [95]. This evidence reaches the conclusion that, in certain cases, we are able to increase the conductivity by increasing the percentage of $Py_{1,4}TFSI$. It is possible to calculate the activation energy (E_A) from the slope of the graph in **Figure 36** with the Arrhenius equation **(11)**. The lower this value the higher is the mobility of charge transporting ions and the better is the ionic conductivity. For all three electrolyte mixtures the slope (m) of Arrhenius plot is almost equal, and therefore the activation energy is similar, see **Table 2**.

$$ln\ k_n = ln\ k_0 \cdot \left(\frac{-E_A}{R \cdot T} \right)$$
$$m = \left(\frac{-E_A}{R} \right)$$
(11)

 An enhancement of activation energy due to adding $Py_{1,4}TFSI$ cannot be seen. For a standard electrolyte LP30 (1 M $LiPF_6$ in EC/DMC 1/1 v/v), which is known to have a good ionic conductivity, the activation energy was calculated to be 0.15 eV. Another aspect for ionic transport properties is the value of lithium transference number (t_{Li+}). This value gives information about the fraction of charge, which is transported by lithium ions during cell reaction. The determination of this value is done by a combination of AC and DC polarization measurements. In the first step an impedance spectrum between 50 kHz and 0.01 Hz is recorded, at OCV, to assign the initial state of charge transfer resistance (R_0). Afterwards a voltage of several millivolt, 30 mV (V), is applied and the current versus time profile is recorded, until a steady state in current is reached (I_{SS}).

Table 2: Overview of ionic conductivity σ, activation energy E_A and lithium transference number t_{Li+} for PEG0, PEG10 and PEG30.

Solvent	$\mathbf{Py_{1,4}Tfsi}$	Salt 1 mol/kg	σ [mS/cm] at RT	$\mathbf{E}_A$ [eV]	$\mathbf{t}_{Li+}$
PEG500DME	0%	LiTFSI	0.5 ± 0.1	0.27 ± 0.02	0.47
PEG500DME	10%	LiTFSI	0.52 ± 0.1	0.29 ± 0.01	0.39
PEG500DME	30%	LiTFSI	0.76 ± 0.15	0.28 ± 0.02	0.19
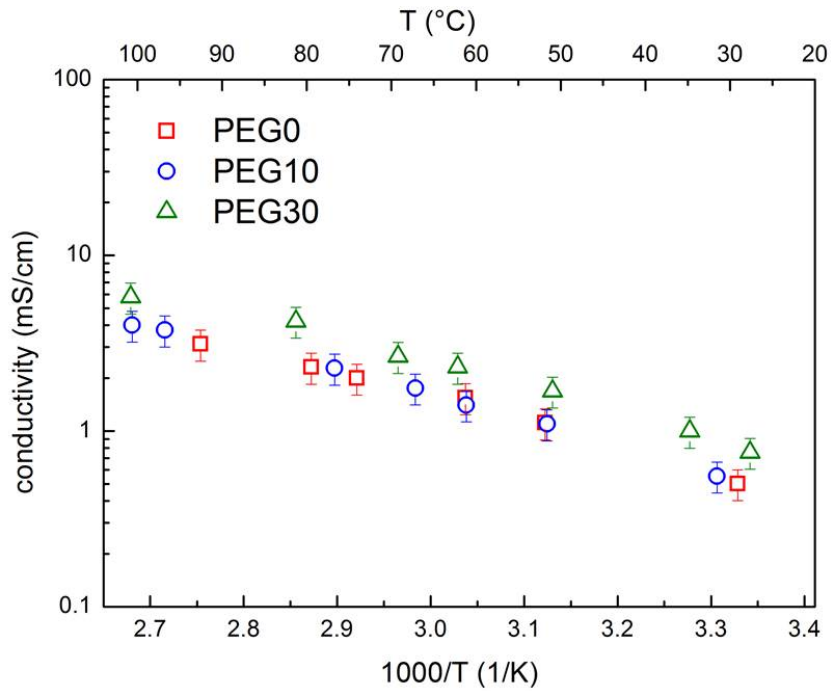
Figure 36: Arrhenius plot for ionic Conductivities of PEG0, PEG10 and PEG30 in a temperature range of 25°C to 100°C [96].
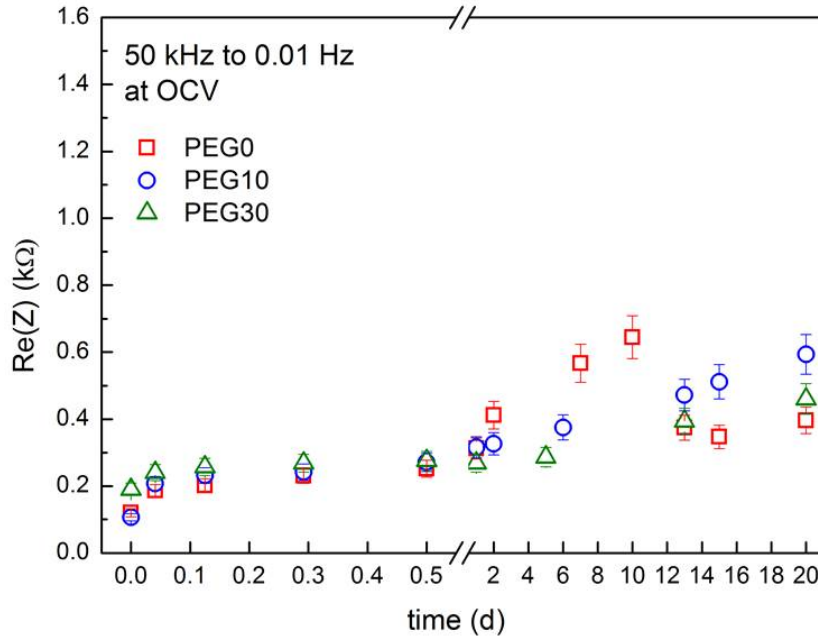
Figure 37: Impedance at OCV for frequencies 50 kHz to 0.01 Hz for symmetrical Li/electrolyte/Li cells over several days [96].

The start value is at t=0 and gives I_0. After reaching a steady state a second impedance spectrum is recorded (R_{SS}). The lithium transference number can be calculated by the Bruce-Vincent equation (see **Equation (12)**), reported in 1987 by Vincent and coworkers [70].

$$t_{Li+} = \frac{I_{SS} \cdot (V - I_0 R_0)}{I_0 \cdot (V - I_{SS} R_{SS})} \tag{12}$$

It can be seen that the more ionic liquid is added, the lower the value for the transference number. In fact, this is expected because the big anion of $Py_{1,4}$Tfsi shows inactions with poly-ethylene oxide molecules. That is why the lithium transportation is inhibited. This will lead to a negative effect concerning the rate capability and an increase of the polarization behavior during the battery cell performance.

Stability properties were tested in terms of stability over the first hours and then over a longer time period (**Figure 37**) and with lithium stripping and deposition for 400 h with an applied current of 0.1 mA (**Figure 38**). Both experiments were performed in a symmetrical Li/electrolyte/Li Swagelok ® cell filled with the appropriate electrolyte mixture. All three mixtures show a very stable inter-facial resistance with almost the same values. The evolution shows within the first hours more or less no difference, if $Py_{1,4}$Tfsi is added or not. Peg0, which has no addition of ionic liquid, shows an oscillating resistance over several days, which can be ascribed to lithium solution and dissolution over time. However, all mixtures show a stabilization of the resistance within the first 12 hours and only a slight increase in resistance over the following days. **Fig-**
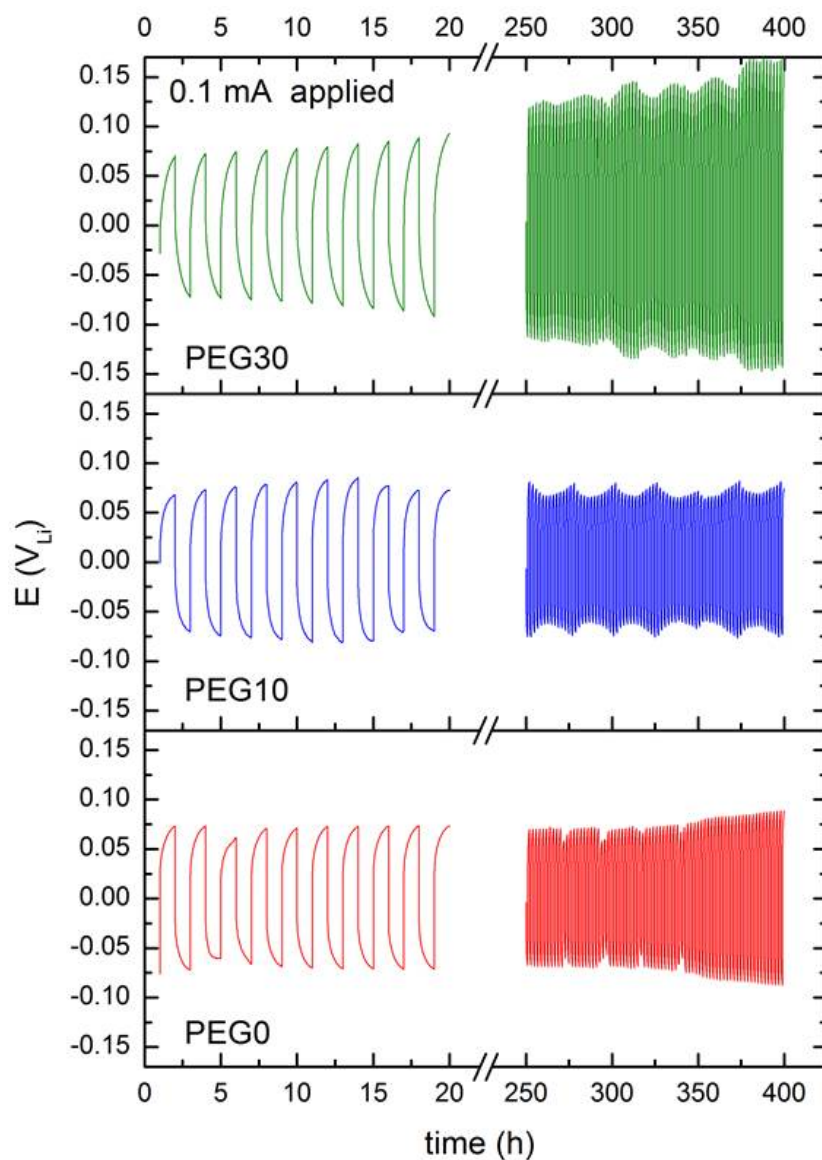
Figure 38: Lithium stripping and deposition measurement with an applied potential of 10 mV for 400 h for a symmetrical Li/electrolyte/Li cell is reported to demonstrate the stability of the lithium interface over time.
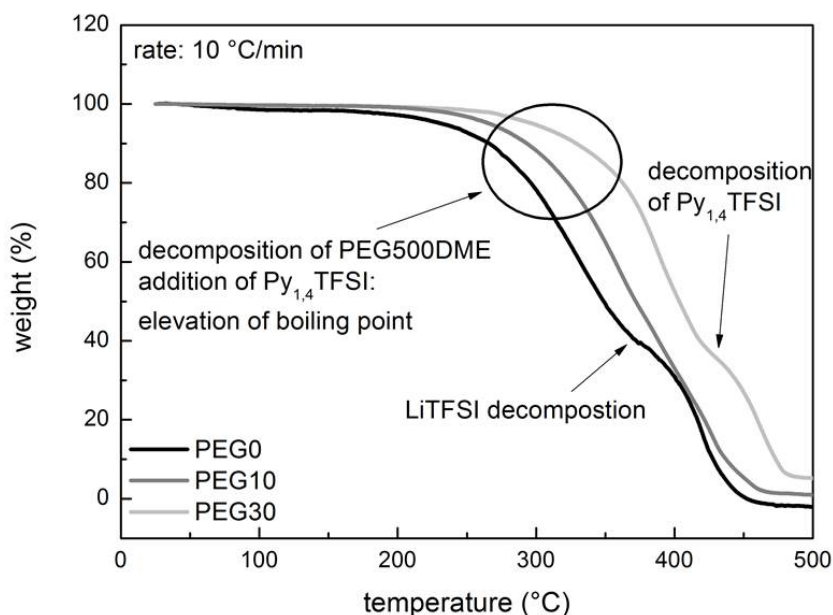
Figure 39: TGA traces of PEG0, PEG10 and PEG30 show the decomposition behavior in temperature dependency in comparison [96].

ure 38 gives an overview about the lithium stripping and deposition behavior during the first 20 hours and the evolution after 250 to 400 hours. At the beginning, the amplitude of PEG0, PEG10 and PEG30 shows the same, very low polarization behavior of around ± 0.07 V. PEG0 did not change within the first 325 hours. Then a slight increase of polarization of around 5 mV is observed. PEG10 shows a slight oscillation of 5 to 10 mV of the polarization while lithium stripping and deposition. Even though, these changes are negligible. The oscillation for PEG10 can be assigned to the day/night change of temperature. But, for PEG30 a continuous increase of polarization can be reported. The voltage is doubled from ± 0.075 V to approximately 0.15 V of polarization. We assume that this effect can be ascribed to the addition of a higher amount of ionic liquid, which leads to increased electrostatic interactions of anion and cation of the ionic liquid.

Thermal properties were analyzed with methods of thermal gravimetric analysis (TGA) and diffraction scanning calorimetry (DSC). For temperatures higher than room temperature, TGA was used until a temperature of 500°C was reached. The measurement was performed at a heating rate of 10°C/min under nitrogen atmosphere. **Figure 39** shows, that for pure PEG500DME as solvent in PEG0 the decomposition of PEG500DME starts at around 200°C with a slight evaporation. At 250°C a sharp decrease of weight starts (black curve). This behavior corresponds to the assumption, because 250°C is the boiling point for PEG500DME given from the supplier. A second loss of weight can be observed in the range of 350°C. This is assigned to the decomposition of the conductive salt LiTFSI [76]. With the addition of $Py_{1,4}$TFSI the thermal stability increases with an elevation of the boiling point. The higher the amount of $Py_{1,4}$TFSI the
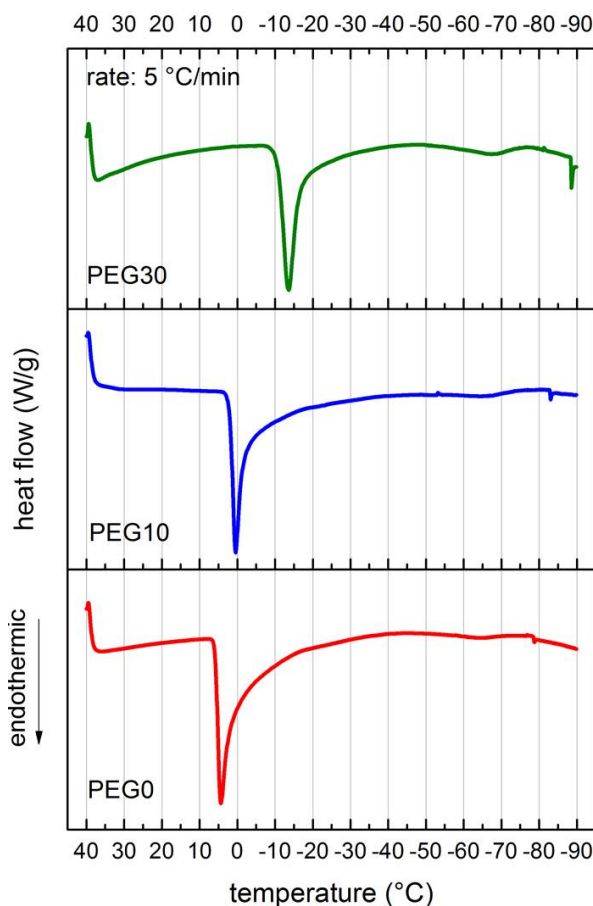
**Figure 40:** Analysis of a lower temperature area with DSC with a rate of 5°C/min [96].

higher the decomposition point. For PEG30 a decomposition temperature of over 300°C is reached. In case of PEG10 the decomposition of PEG500DME and LITFSI has a perfectly overlapping behavior, so it could not be determined when the salt decomposition had started. Like PEG0, PEG30 shows a second decomposition peak at around 420°C. This temperature stands for the decomposition of $Py_{1,4}TFSI$, which is, according to the supplier, at 417°C. LITFSI decomposition is completely superimposed by the elevated boiling temperature of PEG500DME.

A lower temperature area from 40°C to −90°C is shown in **Figure 40** in a comparison of the DSC traces of these three electrolyte mixtures. DSC was also performed under nitrogen atmosphere with a heating/cooling rate of 5°C/min. As well for lower temperatures an increase of the thermal stability is observed due to addition of $Py_{1,4}TFSI$. The peak for the freezing point shifts from 4.3°C for pure PEG500DME to −13.6°C for an addition of 30% $Py_{1,4}TFSI$. For PEG0 the glass transition temperature is situated at −80°C. The addition of $Py_{1,4}TFSI$ leads to a temperature shift to lower temperatures. In case of liquid electrolyte mixtures this temperature does not play an important role because the freezing point of all mixtures is located at much higher temperatures.
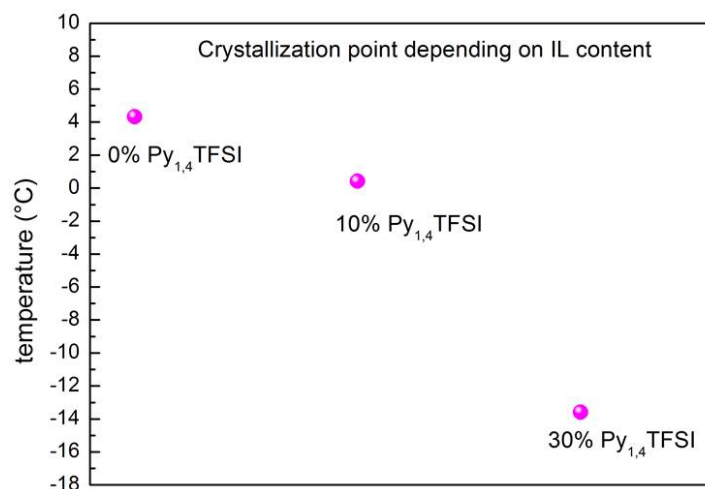
Figure 41: Dependence of the cyrstallization point after the addition of $Py_{1,4}TFSI$. The crystallization point shifts from $4.3°C$ of pure PEG500DME to $-13.6°C$ in addition of 30% $Py_{1,4}TFSI$ [96].

An overview of the change in freezing points is given in **Figure 41**. Electrochemical properties had been carried out by using a Super P carbon working electrode coated on aluminum and copper the anodic and cathodic scan, respectively. The determination was done by linear sweep voltammetry up to 5 V_{Li} and for the cathodic stability down to 0.01 V_{Li} with a scan speed of 0.2 mV/s. **Figure 42a)** to **c)** show the electrochemical stability window for PEG0, PEG10 and PEG30. All three mixtures show a similar behavior in the mentioned potential window. The cathodic scan in **Figure 42b)** shows a peak starting at 1.3 V_{Li} which is assigned to the formation of the solid electrolyte interface (SEI) induced by a starting decomposition of the solvent. In the following process the intercalation of lithium ions into the carbon structure starts at around 0.6 V_{Li}. This process is shifted to 0.8 V_{Li} for mixtures with additions of $Py_{1,4}TFSI$. The anodic scan shows an almost super-imposable behavior. The zoom in **Figure 42c)** shows that decomposition of PEG500DME is only shifted 50 mV from 4.75 V_{Li} (PEG0) to a lower potential for PEG30. So, one can guarantee an electrochemical stability from 1.3 to 4.75 V_{Li} for the studied electrolyte mixtures.
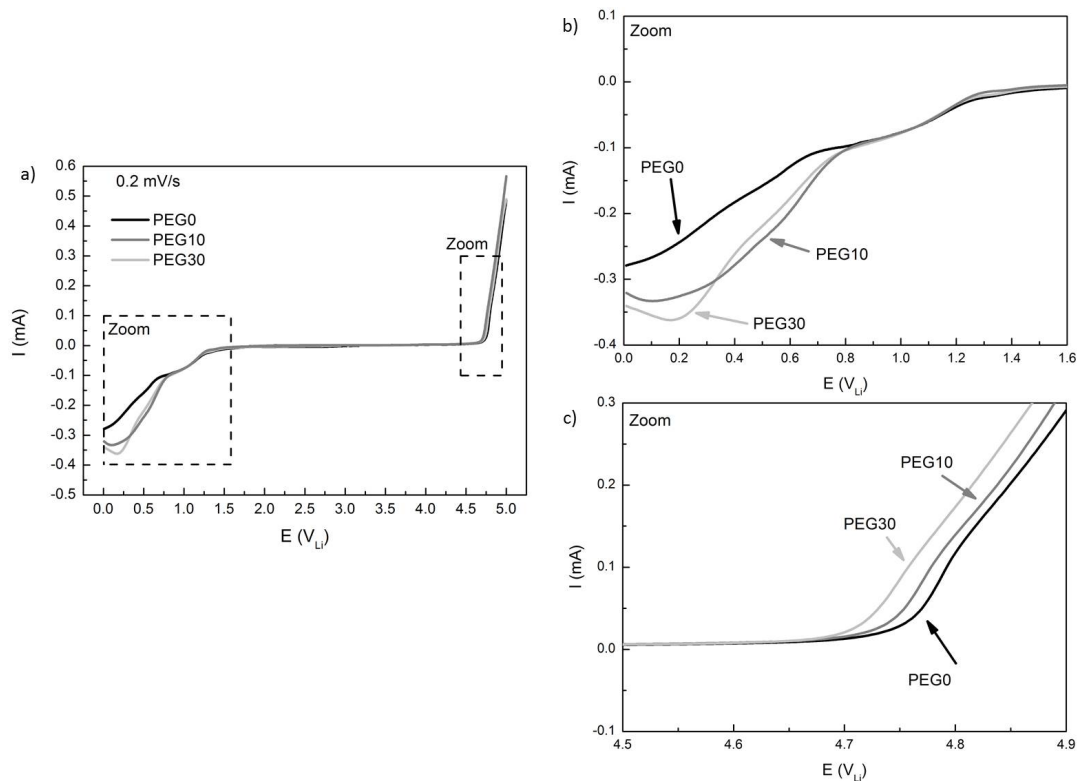
Figure 42: Characteristic current versus potential plot to show the electrochemical stability window for PEG0, PEG10 and PEG30 at room temperature at a scan rate of 0.2 mV/s. Figure b) and c) show the Zoom of the cathodic and anodic scan, respectively.

In addition, the corrosive behavior of LiTFSI in contact with metallic aluminum plays an unimportant role, if poly-ethylene oxide based solvents are used. The electrochemical corrosion was tested with cyclic voltammetry at room temperature and at 50°C in a Swagelok ® cell with pure metallic aluminum as working electrode and with a scan rate of 0.2 mV/s from 2.5 V to 4.5 V_{Li}. It is known from previous research, that in poly-ethylene glycol acts as an inhibitor for aluminum corrosion [85, 86]. In addition, Chen et al. examined in 1999, that LiTFSI in poly-ethylene oxide based solid electrolytes show no significant corrosion during normal battery cycling, but pitting corrosion could be observed during overcharge [97]. In contrast to our measurement at a polarization voltage of 4.5 V_{Li} over 10 h no increase of corrosion current could be detected, see **Figure 43a)**. This adverts to the assumption, that no corrosion happens on the aluminum surface. This might be due to the fact, that the used PEG500DME has end capped ether groups, which allows coordination of solvent molecules and aluminum metal surface. Current density versus voltage in **Figure 43b)** gives a comparison of the corrosion behavior of all three electrolyte mixtures with LiTFSI in a mixture of ethylene carbonate (EC) and dimethyl carbonate (DMC) 1/1 by volume at room temperature. Corrosion of aluminum starts in common used carbonate based solution in the anodic scan at around 3.7 V_{Li}. In reverse scan corrosion current is persistent with a peak current density of
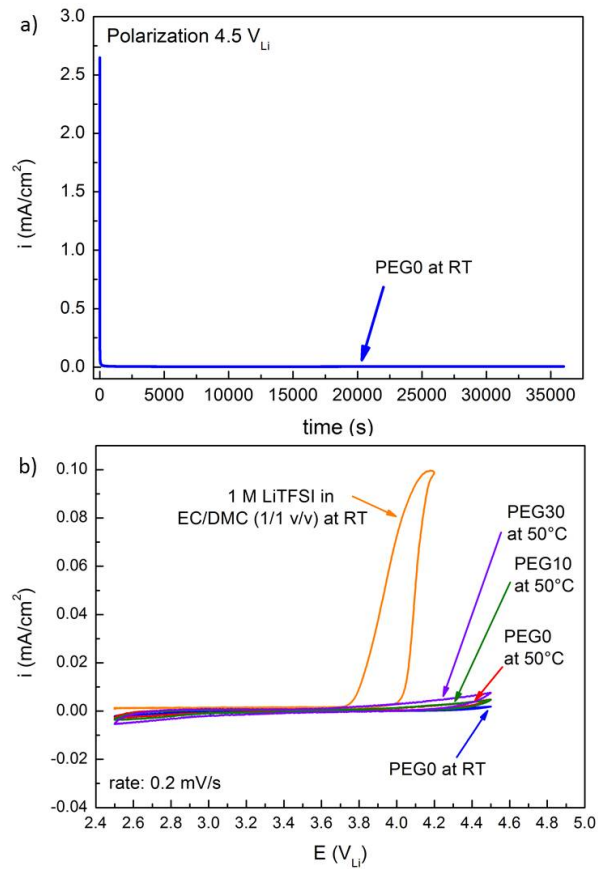
Figure 43: a) Chrono-amperometric polarization in a Li/PEG0/Aluminum cell at RT and 4.5 V_{Li} for 10 h. b) Aluminum corrosion behavior for PEG0, PEG10 and PEG30 at room temperature and 50°C in comparison with LiTFSI in common used organic carbonate based solvent EC/DMC 1/1 (v/v).

0.1 mA/cm^2 and decreases within a potential range of 300 mV. This corrosion behavior makes it impossible to use LiTFSI as conducting salt in combination with aluminum as current collector. On the other hand, PEG500DME shows no corrosion behavior within a potential window from 2.5 V to 4.5 V$_{Li}$. This is also the case for a raised temperature of 50°C and for mixtures with Py$_{1,4}$TFSI in PEG10 and PEG30. According to former research, this fact is due to physical and chemical adsorption interactions of the inhibitor molecule and the metal surface [85, 86]. A more detailed study about aluminum current collector corrosion is given in **Chapter 6.3**.

6.2.5. Conclusions

A detailed comparison between three electrolyte mixtures containing PEG500DME as solvent with additions of Py$_{1,4}$TFSI and LiTFSI as conducting salt was shown. All three mixtures show interesting thermal and electrochemical behaviors and excellent stability with the lithium interface. As expected, the presence of Py$_{1,4}$TFSI improves the thermal stability in areas for higher and lower temperatures, as well. The use within a temperature range of -13.6°C and 300°C will be possible. That is why these mixtures are especially interesting for high temperature applications. Beside these facts, the use of PEG500DME allows simultaneous operations with LiTFSI as conductive salt and aluminum as current collector material, because, even at elevated temperatures, no electrochemical corrosion of the metal is visible within 2.5 and 4.5 V$_{Li}$. Depending on the individual demand, the addition of Py$_{1,4}$TFSI can improve characteristics of the electrolyte and is suitable for applications in advanced lithium batteries.

6.3. Aluminum Current Collector Corrosion with different Lithium Salts

6.3.1. Abstract

As mentioned in **Chapter 6.2** the aging aspect of current collector corrosion in lithium-ion batteries plays an important role. The current collector foils are used as a support for electrode coatings on the anode and cathode side, respectively, whereby copper is used for anodes and aluminum for cathodes [12, 84, 98–101]. The reason for this is, that both materials are electrochemically stable within the required potential window and are relatively cheap and weight light [98]. It is known, that the corrosion behavior is depending on the composition of the electrolyte solution, metallurgy of the current collector and electrochemical potential [12, 84, 101]. In this chapter the focus is on the corrosion behavior of aluminum metal at anodic potentials, whereby the conductive salt plays an important role. It is dependent on the oxidative potential and the stability of metallic aluminum at higher anodic potentials increases in the following order $LiCF_3SO_3$ < $LiN(CF_3SO_3)_2$ (LiTFSI) < $LiClO_4$ < $LiPF_6$ < $LiBF_4$ [12, 84, 101–103].

The corrosion behavior of metals as working electrodes (Al, stainless steel 316L) and different conductive salts ($LiPF_6$, $LiClO_4$, LiTFSI) versus metallic lithium were tested in a three-electrode cell design with cyclic voltammetry in an anodic potential at 25°C and elevated temperatures like 80°C. Imaging scanning electron microscopy was used to show the level of pitting corrosion under the different conditions. Several measurements were performed by Susanne Herden during her Bachelor's Thesis in spring 2012 [104]. Additionally, the corrosion behavior of aluminum, which is mostly used in Li-batteries, was further investigated, whereby a LiTFSI containing electrolyte was used with addtions of small amounts of $LiPF_6$ and poly-ethylene glycol di-methyl ether ($M \approx 250$ g/mol, TEGDME (tetra-ethylene glycol di-methyl ether) and $M \approx 500$ g/mol; PEG500DME), as well as in pure glymes (DME, DEGDME, TEGDME and PEG500DME), which is in dependence on earlier published results from several groups [83, 101, 103].

6.3.2. Introduction

The ideal conductive salt used in electrolytes for Li-ion Batteries should have many advantages and fulfill several criteria. The salt should be completely soluble and dissolved in organic solvents like ethers or organic carbonates, whereby solvated ions should have good kinetics. It is important that the conductive salt is inert towards cell components like separators, electrode active material and other cell materials like current collectors. Besides, electrolyte mixtures should show a good ionic conductivity, electrochemical and thermal stability. The anion itself should be stable against oxidative decomposition on the cathode side and inert against components of the solvent. In terms of safety, the salt should be stable against temperature and reactions between solvents or cell components. Possible lithium salts that were investigated in this study are lithium hexa-fluoro-phosphate ($LiPF_6$), lithium bis-(trifluoromethanesulfonyl)-imide (LiTFSI) and lithium

71

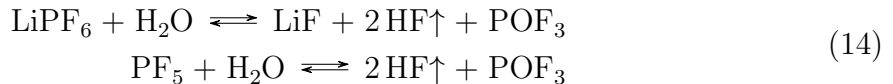**Table 3:** Overview of important characteristics of three different conductive salts. [12]

Salt	Melting point $\mathbf{T}_M$ [°C]	Decomposition temperature $\mathbf{T}_D$ [°C]	σ [mS/cm] 1 M at 25°C in Ec/Dmc 1/1 v/v
LiPF$_6$	200	$ca.$80	10.7
LiClO$_4$	236	> 100	8.4
LiTFSI	234	> 100	9.0

perchlorate (LiClO$_4$). Some important parameters of these salts are shown in **Table 3**. The conductive salt LiPF$_6$ combines positive characteristics and is used since the 1990s in lithium-ion batteries introduced by Sony to the market [6] and is mostly used in battery industry today. LiPF$_6$ fulfill usually the above mentioned criteria and do not promote aluminum current collector corrosion [105]. However, there are several problems within the use of LiPF$_6$. Although it has a relatively high chemical and thermal stability, the equilibrium state changes while a temperature increase higher than 80°C and shifts to the right side of the shown reaction (see **Equation (13)**) [12].

$$\text{LiPF}_6 \rightleftharpoons \text{LiF} + \text{PF}_5\uparrow \qquad (13)$$

LiPF$_6$ thermally decomposes at elevated temperatures in penta-fluoro phosphate (PF$_5$) and HF [83, 105–107]. The P-F-bonding of PF$_5$ is unstable and forms with trace water hydro fluoric acid (HF), which is highly corrosive towards glass and metals. Beside this, LiPF$_6$ itself is sensible towards trace water, which affects its stability. Hydrolysis products are shown in **Equation (14)** [12].

$$\text{LiPF}_6 + \text{H}_2\text{O} \rightleftharpoons \text{LiF} + 2\,\text{HF}\uparrow + \text{POF}_3$$
$$\text{PF}_5 + \text{H}_2\text{O} \rightleftharpoons 2\,\text{HF}\uparrow + \text{POF}_3 \qquad (14)$$

PF$_5$ is a strong Lewis acid, which can also force a ring opening of cyclic carbonates under polymerization or break linear organic carbonates, forming olefines, ethers, carbon dioxide (CO$_2$), fluorinated alkanes or polymerized ethers or alkyl carbonates [12].
As an alternative LiTFSI can be suggested for LiPF$_6$. The [N(SO$_2$CF$_3$)$_2$]$^-$-anion of LiTFSI is good stabilized due to the delocated negative charge. Due to its high decomposition temperature, it is thermal stable and electrochemical stable until 5 V$_{Li}$. It is also non toxic and nonhazardous [12] and shows a comparable ionic conductivity like reported in **Table 3**.
Also, LiClO$_4$ owes a good solubility and ionic conductivity (**Table 3**), as well as a anodic stability up to 5.1 V$_{Li}$ [12, 108]. In contrast to LiPF$_6$, LiClO$_4$ is less hygroscopic and not sensitive to ambient moisture. It is often used for research purposes, because of
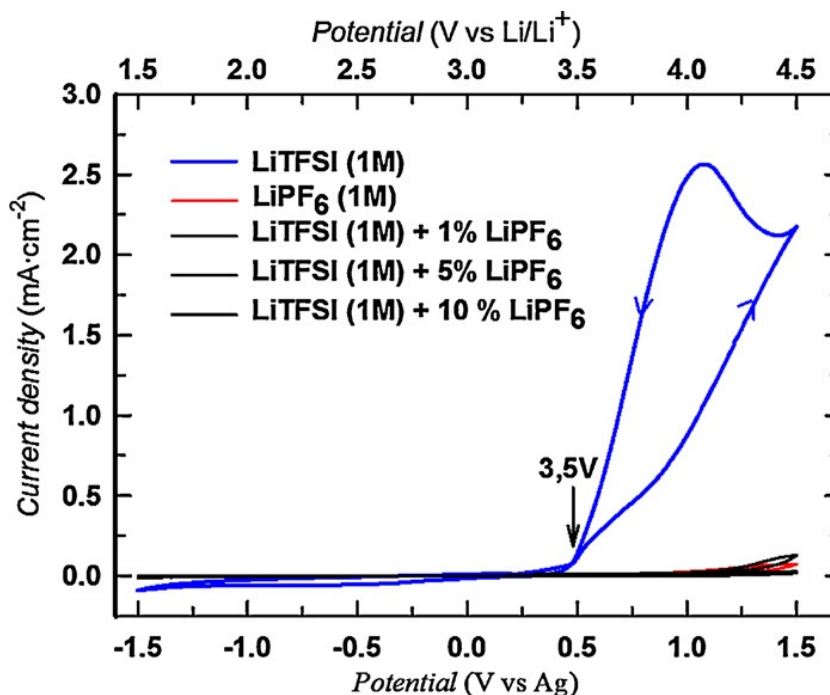
Figure 44: Corrosion behavior in a cyclic voltammogram of aluminum working electrodes with 1 M LiTFSI, 1 M $LiPF_6$ and additives of $LiPF_6$ in different concentrations [83].

its economical usage [12]. However, due to its high oxidation state, $LiClO_4$ is strongly reactive and explosive [83].

The main drawback concerning LiTFSI as conductive salt is that it corrodes the current collector material aluminum during the anodic scan. Aluminum metal is widely used as cathode current collector material [12, 84, 98–103], because it is easy to produce, cheap and lightweight. The current collector material is used in forms of meshes, foams, foils or screens [99]. From the manufacturing process, aluminum has a natural protective Al_2O_3-passivation layer on its surface [84, 101, 102], which is removed at elevated potentials. In the anodic scan the battery is charged to high potentials and the natural passivation film is removed from the metal surface, which leads to pitting corrosion caused by $[N(SO_2CF_3)_2]^-$ anions and corrodes the metal surface step by step [12, 83]. With the non protected metallic aluminum an $Al(TFSI)_3$-complex is formed precipitating on the electrode surface [103]. The active material of the cathode gets passivated, which leads to an increase of the ohmic resistance. Formed products affect the characteristics of the electrolyte and increases the capacity loss and cell aging. Dissolved Al^{3+} cations can be reduced on the anode side, leading to a poisoning of the anode material [101]. From previous research it is known that one can prevent aluminum corrosion with addition of a minor amount of $LiPF_6$. Fluorid anions as decomposition product of $LiPF_6$ can passivate aluminum after the initial Al_2O_3-layer is reduced and forms a thin protective film of hexa-fluoro aluminates $[AlF_6]^-$ on the metal surface [83, 84, 103]. As an example, Dahbi et al. [83] gives in a cyclic voltammogram (**Figure 44**) of aluminum working

73

electrodes its behavior in different electrolytes containing pure 1 M LiTFSI and different additives of LiPF$_6$ in a solvent mixture of Ec/Dmc. The corrosion of aluminum starts in pure 1 M LiTFSI at 3.5 V$_{Li}$ with an increase of the current density. With the use of pure 1 M LiPF$_6$ or just the addition of a small amount of 1%, no increase of the current density is detectable. That means no redox reaction occurs on the aluminum surface. However, other drawbacks of LiPF$_6$-containing electrolytes are the problems of iron dissolution from the olivine structure and the resulting capacity fade and the cell aging of LFP cathodes, caused by LiPF$_6$ [109]. Therefore, one should avoid the use of conductive salts, which are able to form free fluoride ions like LiBF$_4$ and LiPF$_6$ in higher amounts, to prevent the cathode material from aging at higher temperatures. This issue is discussed in detail in **Chapter 6.4**. For this reason, a possible alternative is to add solvent additives to LiTFSI containing electrolytes, which are able to form a protective layer on the aluminum metal surface to prevent it from corrosion, similar like it happens with the use of LiPF$_6$, but do not destroy the structure of the active material.

In dependence of results from previous research [97, 103], poly-ethylene oxide based solvents, namely glymes, are known to protect aluminum from corrosion in LiTFSI containing electrolytes, while forming a protective layer on the aluminum metal surface [85, 86].

For this reason, the corrosion behavior of different current collector materials (aluminum, stainless steel 316L) in combination with different conductive salts (LiPF$_6$, LiClO$_4$ and LiTFSI) and solvent mixtures (glymes and Ec/Dmc) was studied under various conditions and is shown and discussed in the following. Due to previous results [97, 103] the corrosion behavior of aluminum was investigated at different temperatures using several poly-ethylene oxide based solvents, like di-methyl ether (Dme), ethylene glycol (Degdme), tetra-ethylene glycol di-methyl ether (M $\approx$ 250 g/mol, Tegdme) or poly-ethylene glycol di-methyl ether (M $\approx$ 500 g/mol, Peg500dme). Due to its auspicious behavior the last, long chained glyme was also used as additive in mixtures with Ec/Dmc. Beside cyclic voltammetry for corrosion studies, the ionic conductive was also determined of the main electrolyte mixtures. Levels of corrosion of the current collector foils were imaged with SEM and photography in a post-mortem analysis. Also the performance of the most auspicious electrolyte mixture was tested in LFP half cells, demonstrating, that the current collector was prevented from corrosion.

6.3.3. Experimental Part

For different electrochemical experiments, different electrodes were used. Beside simple aluminum (Advent, $\approx$ 99.2 % purity, 20 μm thick) and stainless steel foils (Advent, type 316L, 25 μm thick) with a diameter of 10 mm as working electrode for half cell corrosion tests for different electrolyte mixtures versus metallic lithium and lithium iron phosphate (LFP, LiFePO$_4$, Life Power ® P2, Clariant) as cathode material were used. Powders of the active material were pre mixed in a closed vessel with conductive carbon Super C65 (Tanaka) and polymer binder PVDF (Kynar HSV900) in a 82/10/8 weight ratio for
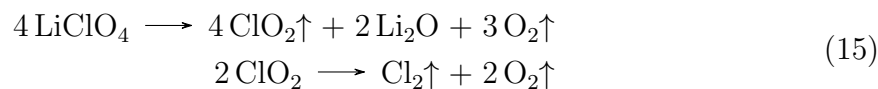
LFP electrodes. N-methyl-pyrrolidone (NMP) was used as solvent (≈ 137 mg$_{solid}$/ml$_{NMP}$ for LFP electrodes). NMP was added stepwise within 10 minutes to the solid mixtures while stirring in a vessel on a magnetic stirrer at 60°C. Electrode inks were stirred with 1200 rpm for 3 h at 60°C. Afterwards, ink was coated with a coating machine (RK Print, Germany) on an aluminum foil (Advent, ≈ 99.2 % purity, 20 μm thick) for LFP electrodes with a gap bars to a wet-film thicknesses of 40 μm and 80 μm. Before coating electrode ink, foils were pre-cleaned with ultra-pure water (Merck Millipore, E-pod ≈ 15 MΩ) and ethanol. For a better adhesive behavior of electrode coatings, aluminum was etched with diluted HCl solution. Base residues were removed with ultra-pure water. After the coating process, the solvent was evaporated overnight at 60°C on a hot plate in ambient air. Afterwards, electrodes with a diameter of 10 mm (LFP) were punched out. Punched electrodes were dried overnight at 120°C under dynamic vacuum in a glass oven (Büchi, Switzerland) and transferred into an Ar filled glove box (MBraun, Germany, $\pm$ 0.1 ppm O_2 and H_2O) without further contact with ambient air. The final average loading of aluminum supported LFP electrodes was 5.4 mg$_{LFP}$/cm^2 with an average electrode thickness ≈ 17 μm (without current collector) and a porosity of ≈ 80 % (LFP), respectively, without any compression. All electrolytes were prepared in an Ar filled glove box (MBraun, Germany, $\pm$ 0.1 ppm O_2 and H_2O) containing either a solvent mixture of ethylene carbonate (EC, anhydrous ≈ 99 %, Sigma-Aldrich) and di-methyl carbonate (DMC, anhydrous ≈ 99 %, Sigma-Aldrich) in weight ratio of 1/1 g/g or with pure di-methyl ether (DME, ≥ 99 %, Sigma-Aldrich), ethylene glycol (DEGDME, ≈ 99.8 %, Sigma-Aldrich), tetra-ethylene glycol di-methyl ether (M ≈ 250 g/mol, TEGDME, Sigma Aldrich) or poly-ethylene glycol di-methyl ether (M ≈ 500 g/mol, PEG500DME, Sigma Aldrich), which was also used in mixtures with EC/DMC. Before use, DMC, DME, DEGDME and TEGDME were dried over molecular sieves (Sylobead MS 564, 3 Å, Grace Division) for several days, whereby EC was used as received. PEG500DME was pre-dried under vacuum at 80°C for 12 h and then further dried with mentioned molecular sieves. Conductive salts like LiPF$_6$ (battery grade ≥ 99.99 %; Sigma-Aldrich) and LiTFSI (≥ 99.95 %; Sigma-Aldrich) were added to the solvents in a different concentrations, variating from 1 mol/L to 1 mol/kg and 0.5 mol/kg. Prior use, LiTFSI was dried at 120°C under dynamic vacuum in a Büchi glass oven for several hours. Cells for electrochemical experiments were assembled in a stainless steel Swagelok ® T-fitting. A detailed description about cell assembling procedure is given in **Chapter 5.4**. In half cell combinations, working electrodes like metal foils or coated electrodes were measured against metallic lithium (Goodfellow, ≈ 99.9 % purity, 450 μm thick) on the counter electrode side. Note that during this period the electrolyte was added in total after assembling electrodes and separators via the hole of the insulating cylinder. The amount of electrolyte was set to 80 μL for measurements at 25°C and to 300 μL for measurements at elevated temperatures between 50°C and 80°C. Temperature details are given in each measurement. Three Celgard ® 2325 polymer separators or VWR ® glass fiber separators with a diameter of 11 mm were used between counter and working electrode. As reference electrode a 6 mm metallic lithium
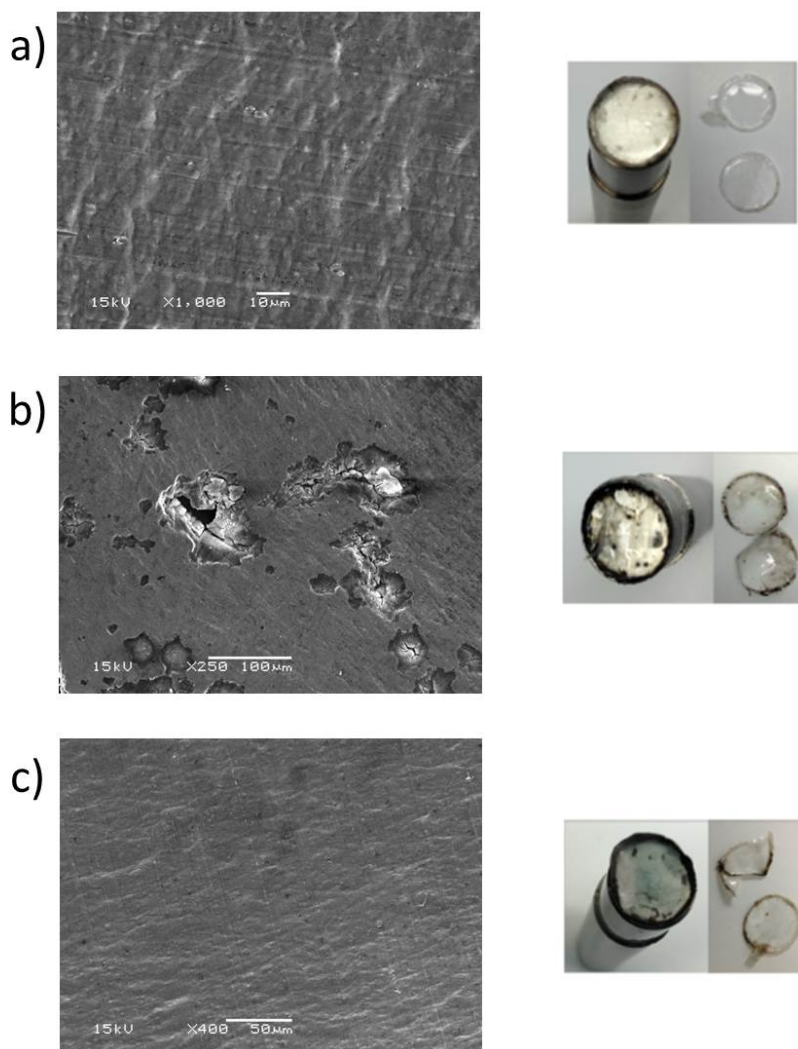
disk was used in all cases. Different electrochemical, imaging and analytical characterizations were performed. Electrochemical corrosion experiments with different current collector materials were performed with cyclic voltammetry a VMP3 multi-potentiostat (Biologic) normally in a potential window of 4.2 and 2.5 V_{Li} at a scan rate of 0.2 mV/s for 4 times (3 times for later measurements using glymes). For electrolyte mixtures in some measurements with pure glymes (DME, DEGDME, TEGDME and PEG500DME), the electrochemical window was enlarged to 4.5 V_{Li}. The exact temperatures are given in the plots or figure descriptions. Cycling tests of half- and full cells were performed on a battery cycler (Maccor Series 4000). Detailed test procedures and conditions are explained and described in the particular sections. The ionic conductivity for some electrolyte mixtures were determined with a LF 1100+ ionic conductivity cell from Schott (Schott $^{®}$, Germany) in a temperature range between 25°C and 80°C in a heating and following cooling step. Postmortem analysis was performed after disassembling cells on electrolyte soaked separators and working electrode metal foils after corrosion experiments. For electrolyte analysis, ATR FT-IR (Attenuated Total Reflection Fourier Transform Infrared spectrometer) analysis was performed using a Perkin-Elmer ATR FT-IR spectrometer (Spectrum Two). Metal foils were analyzed either by scanning electron microscopy (JOEL; JSM5900LV SEM TechSolutions; Fachgebiet Elektronenmikroskopie Dr. Marianne Hanzlik) and by simple photography to demonstrate the level of corrosion and to evaluate the suitability of the particular electrolyte mixture for the use in lithium batteries.

6.3.4. Results and Discussion

To evaluate the corrosion behavior of different conductive salts (LiPF$_6$, LiTFSI and LiClO$_4$) dissolved in common EC/DMC 1/1 g/g mixture in contact with different current collector materials (aluminum (Al) and stainless steel 316L) and to compare this with results shown in literature [83], we performed cyclic voltammetric experiments using current collector materials as WE and metallic lithium as counter and reference electrode, respectively. In **Figure 45** the corrosion behavior of aluminum metal is demonstrated in contact with pure LiPF$_6$ **a)** and LiTFSI **b)** as well as LiTFSI with 5% of LiPF$_6$ **c)** as corrosion inhibitor. Aluminum foils were imaged after cycling at each temperature 25°C, 60°C and 80°C for four times in a potential window between 4.2 and 2.5 V_{Li} at a scan rate of 0.2 mV/s. Beside the SEM of each current collector we show a picture of the lithium counter electrode and the middle separator. The first pictures in **a)** show a SEM of a pristine aluminum foil without any electrochemical treatment and a metallic lithium counter electrode and a Celgard $^{®}$ 2325 separator after cycling in 1 M LiPF$_6$ EC/DMC 1/1 g/g for comparison. After treatment the aluminum WE was shiny and smooth. One could not observe pitting corrosion at any place of the current collector foil. That is why, the pristine and cycled aluminum current collector looks similar. The appearance of the metallic lithium was unchanged in comparison to a pristine foil. The separator was clear, white and without any change in color. As conclusion, the evidence is that no corrosion

occurs on aluminum foils with contact to $LiPF_6$, even at elevated temperatures. This is in accord with data shown from Dahbi et al. [83]. If one compares this to the pictures shown in **b)**, where LiTFSI was used instead of $LiPF_6$, the SEM analysis shows an obvious heavy pitting corrosion of the aluminum surface after the treatment. Black and yellowish decomposition did precipitate on the lithium metal and on the separators. LiTFSI is suitable for the use in lithium-ion cells with an additive or other corrosion protections. As it is known, from results published by Dahbi et al. [83] small concentrations of $LiPF_6$ can prevent the aluminum corrosion, even at elevated temperatures. Our SEM analysis in **c)** shows only a very slight pitting corrosion of the aluminum surface. However, black and yellowish residues are also visible on the metallic lithium and the separator foils, which is a sign of side reactions leading to solid degradation compounds and that corrosion reaction are not fully suppressed. In addition, stainless steel 316L was investigated as possible current collector material. The results are shown in **Figure 46**. Also in this case, we cycled the current collector foil with common electrolyte mixture 1 M $LiPF_6$ in EC/DMC 1/1 g/g for comparison and could see corrosion on the metal surface in **a)**. The surface was shiny and the also here, separators and counter electrode were without residues of decomposition products. The behavior of 316L in $LiPF_6$-containing electrolyte is comparable to that of the aluminum foil. The opposite is shown in **b)**. Like in the previous study, pure LiTFSI was used as conductive salt. The SEM analysis of the 316L current collector shows a very heavy pitting corrosion forming craters and holes on the surface after the treatment. Black decomposition products precipitated on the lithium metal surface and the separators turned dark yellow. If 5% $LiPF_6$ was added to the electrolyte mixture, the corrosion behavior did not change in comparison to pure LiTFSI, which is shown in **c)**. In contrast to aluminum, 316L cannot be prevented by the addition of $LiPF_6$. This can be explained by the fact that F^--ions can form a thin protective film of hexa-fluoro aluminates $[AlF_6]^-$ with the aluminum surface, which was already mentioned in the introduction part [83, 84, 103]. This complex is not formed with iron, maybe also due to several metal additives in the stainless steel 316L alloy, Stainless steel 316L current collector foils were also cycled with 1 M $LiClO_4$ and analyzed with SEM, as well. One can observe slight changing of the surface and also small pitting holes. The color of the separators turned yellowish, as well as the electrolyte solution itself and parts of the metallic lithium foil. A corrosion reaction in contact with steel could not be excluded. For this reason no further corrosion measurements were performed with this conductive salt. The change in color of the electrolyte is a possible thermal decomposition reaction of $LiClO_4$. Beside Li_2O and O_2 an orange gas ClO_2 is formed during the thermal decomposition. The formed gaseous compound is explosive and decomposes at temperatures of 45°C or in contact with oxidative substances under forming Cl_2 and O_2 (see **Equation (15)**). Dissolved ClO_2 or Cl_2 in the electrolyte would lead to a yellow color of the solution [110].

$$4\,LiClO_4 \longrightarrow 4\,ClO_2{\uparrow} + 2\,Li_2O + 3\,O_2{\uparrow}$$
$$2\,ClO_2 \longrightarrow Cl_2{\uparrow} + 2\,O_2{\uparrow}$$

(15)

Figure 45: Imaging of aluminum metal foils (SEM), separators and lithium counter electrodes after cyclic voltammetry at 25°C, 60°C and 80°C. a) SEM of a pristine aluminum foil and a lithium counter electrode and separator after use in 1 M LiPF$_6$ in Ec/Dmc. No corrosion could be observed. The pristine and cycled aluminum current collector looks similar - shiny and smooth. b) SEM of a aluminum foil, lithium counter electrode and separator after use in 1 M LiTFSI in Ec/Dmc. Heavy pitting corrosion - dark and muddy spots c) SEM of a aluminum foil, a lithium counter electrode and separator after use in 1 M LiTFSI in Ec/Dmc with 5 % LiPF$_6$ additive - only slight pitting corrosion. [104]

78
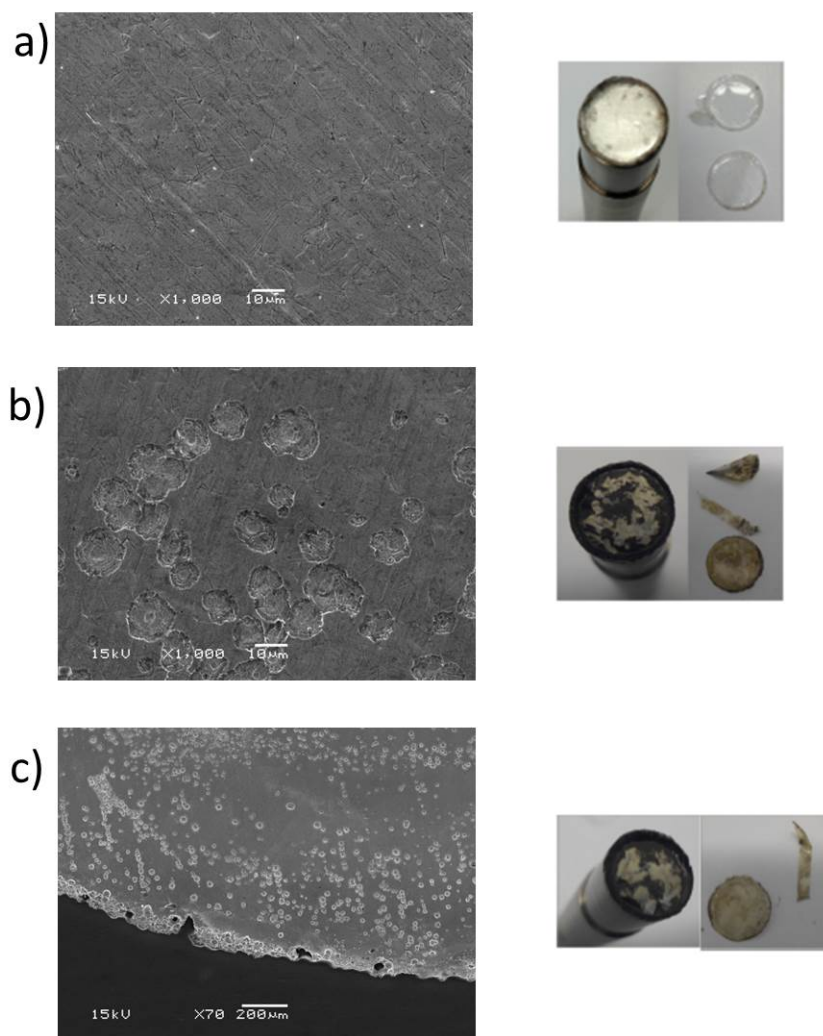
Figure 46: Imaging of stainless steel 316L metal foils (SEM), separator and lithium counter electrodes after cyclic voltammetry at 25°C, 60°C and 80°C. a) SEM of a pristine 316L foil, a lithium counter electrode and separator foil after use in 1 M LiPF$_6$ in EC/DMC for comparison. b) SEM of a 316L foil, a lithium counter electrode and separator after use in 1 M LiTFSI in EC/DMC - heavy pitting corrosion and decomposition products colors separator yellowish. c) SEM of a 316L foil, a lithium counter electrode and separator after use in 1 M LiTFSI in Ec/Dmc with 5 % LiPF$_6$ additive - heavy pitting corrosion of the 316L surface; LiPF$_6$ cannot prevent the corrosion of 316L. [104]
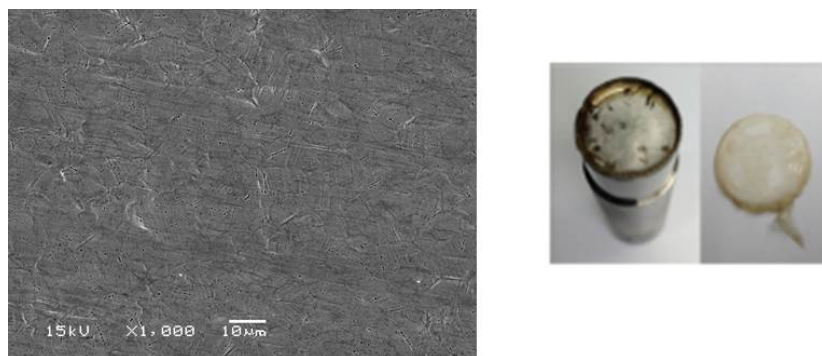
Figure 47: Imaging of stainless steel 316L metal foils used as working electrodes (SEM) in a half cell, separators and lithium counter electrode after cyclic voltammetry with a scan rate of 0.2 mV/s at 25°C, 60°C and 80°C for 4 times at each temperature with 1 M $LiClO_4$ in Ec/Dmc as electrolyte. [104]

The following study concentrates on the common current collector material aluminum. In order to avoid the wetting problem of Celgard ® 2325 separator foils (see **Figure 12** in **Chapter 5.2**), we have used VWR ® glass fiber separator pads for the following experiments and we chose 25°C and 60°C as thermal conditions. As we knew, additives could inhibit corrosion behavior of the aluminum metal. Beside $LiPF_6$, long chained glymes (Tegdme and Peg500dme) were tested as pure solvent component or as additive in Ec/Dmc solvent. We also performed tests in di-methyl ether (Dme) and ethylene glycol (Degdme), but for these solvents the corrosion protection was very poor and therefore the results are not reported here. It is already known that poly-ethylene oxide based solvents (Tegdme (M = 250 g/mol) and Peo (M = $5 \cdot 10^6$ g/mol)) can suppress aluminum corrosion [97, 103]. However, we wanted to investigate the impact on different glymes with different molecular weights and if one can achieve better corrosion protection with higher molecular weights. Also, the idea was to use glymes as additive. Like in the prior measurements, we performed cyclic voltammetry of aluminum working electrodes at a rate of 0.2 mV/s at 25°C. The corrosion behavior of aluminum in the different mixtures is shown in **Figure 48**, whereby **a)** shows the first CV (current density versus working electrode potential) cycle of each measurement. It is shown for 0.5 mol/kg LiTFSI in Ec/Dmc 1/1 g/g (blue), 0.5 mol/kg LiTFSI in Ec/Dmc/Peg500dme 4.5/4.5/1 g/g/g (red), 0.5 mol/kg LiTFSI in Ec/Dmc/Peg500dme 3.5/3.5/3 g/g/g (green), 0.5 mol/kg LiTFSI in Ec/Dmc/Peg500dme 1/1/2 g/g/g (yellow), 0.5 mol/kg LiTFSI in Peg500dme (purple), 0.5 mol/kg LiTFSI in Tegdme (magenta) and 0.5 mol/kg LiTFSI in Ec/Dmc/Tegdme 1/1/2 g/g/g (grey). One can evaluate the corrosive behavior of each mixture from the increase of the current density during the anodic scan at potentials higher 3 V_{Li}. The lower the potential for the beginning increase of the current density and the higher the subsequent peak value, the heavier is the corrosive behavior. As one can see, the aluminum corrosion starts for pure LiTFSI in Ec/Dmc very early at around 3.7 V_{Li} (blue). If Peg500dme was added (10%, 30% and 50%) to the Ec/Dmc solvent, the corrosion could be more and more inhibited. For pure Peg500dme (purple)

no increase of the current density could be detected up to 4.2 V$_{Li}$. A similar behavior could be observed for pure TEGDME. However, a mixture with TEGDME (grey) also leads to a not negligible raise in current density. In **b)** the zoom of the anodic forward scan is shown for each electrolyte. The potential window in the range of 3.9 and 4.1 V$_{Li}$ is shown. As 4.0 V$_{Li}$ is normally used as cut-off potential in half cells using LFP as cathode material, especially current densities until this cut-off potential are interesting and determine the suitability of these electrolytes for further electrochemical measurements. For pure TEGDME, PEG500DME and EC/DMC/PEG500DME 1/1/2 g/g/g the gained corrosion current density is below 0.01 mA/cm^2, which is an acceptable value for electrochemical measurements with LFP electrodes. After investigating the corrosion behavior at 25°C, the temperature was increased to 60°C and the results are shown in **Figure 49**. Note that all electrodes were pre treated with cyclic voltammetry at 25°C for three cycles (previous measurement). That is why all measurement conditions are the same as in the previous plot in **Figure 48**, except the operating temperature. The current density is increased by a factor of 2 for the reference electrolyte 0.5 mol/kg LITFSI in EC/DMC 1/1 g/g (see **a)**). The current density increases also for the other mixtures. However, as shown in **a)**, the corrosion current for pure PEG500DME (purple) and its mixture with EC/DMC/PEG500DME 1/1/2 g/g/g (yellow) is still very low and reach values of ≈ 0.01 mA/cm^2 or slightly higher. Contradictory, the corrosion current of pure TEGDME (magenta) increases and reach comparable corrosion currents of EC/DMC/PEG500DME 3.5/3.5/3 g/g/g (green). Unfortunately, it is not so easy to compare corrosion current densities at 60°C with those of 25°C, due to the fact that aluminum corrosion happens with the first cycle at 25°C and parasitic corrosion products precipitate on separators and electrodes, which also causes a potential shift to higher potentials after a while. However, it is obvious that for solvents causing no corrosion behavior the results are reliable. After the cyclic voltammetry experiments (shown in **Figures 48** and **49**), all cells were disassembled and the aluminum current collectors were harvested. The picture of each aluminum foil treated in a different electrolyte is shown in **50**. For LITFSI in pure EC/DMC 1/1 g/g (blue frame) the pitting corrosion is very heavy in a way that almost the whole current collector foil is consumed. With PEG500DME as additive in a concentration of 10% (red), the corrosion is less heavy, but still very aggressive. Pitting holes are visible and parts of the aluminum foil are consumed. A lower corrosion is visible for EC/DMC/PEG500DME 3.5/3.5/3 g/g/g (green) and EC/DMC/TEGDME 1/1/2 g/g/g (grey). Black solid residues are deposited on the aluminum foil and several pitting holes can be seen on the edge of the aluminum surface. For pure TEGDME (magenta), PEG500DME (purple) and EC/DMC/PEG500DME 1/1/2 g/g/g (yellow) no corrosion is visible on the aluminum surface. All surfaces are shiny and the separators es well as the electrolyte solution did not turn yellow. Therefore, we can conclude that our results on TEGDME are comparable to data shown by Yang et al [103] and support previous results that glymes protect aluminum current collectors from corrosion in contact with LITFSI. We found that the corrosion protection is dependent from the chain length of the glymes: the longer the chain, the better the corrosion protection even at high tem-
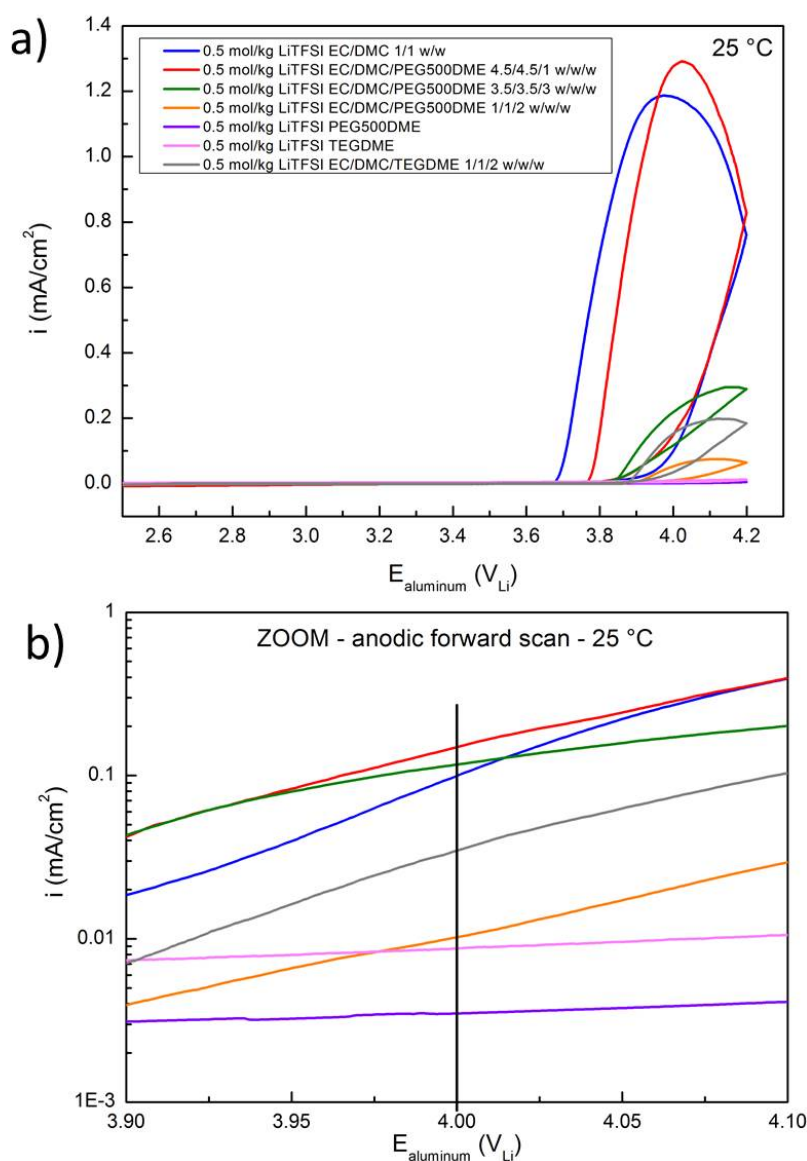
Figure 48: Cyclic voltammetry of aluminum working electrodes at a rate of 0.2 mV/s at 25°C. VWR ® glass fiber was used as separators. Aluminum corrosion behavior is shown for 0.5 mol/kg LiTFSI in Ec/Dmc 1/1 g/g (blue), 0.5 mol/kg LiTFSI in Ec/Dmc/Peg500dme 4.5/4.5/1 g/g/g (red), 0.5 mol/kg LiTFSI in Ec/Dmc/Peg500dme 3.5/3.5/3 g/g/g (green), 0.5 mol/kg LiTFSI in Ec/Dmc/Peg500dme 1/1/2 g/g/g (yellow), 0.5 mol/kg LiTFSI in Peg500dme (purple), 0.5 mol/kg LiTFSI in Tegdme (magenta) and 0.5 mol/kg LiTFSI in Ec/Dmc/Tegdme 1/1/2 g/g/g (grey). a) shows the full first CV cycle of several cells with different electrolyte mixture. b) shows the zoom of the plot in a) for the anodic scan at a potential of 4.0 V_{Li}, which is normally used as cut-off potential in half cells using Lfp as cathode material.
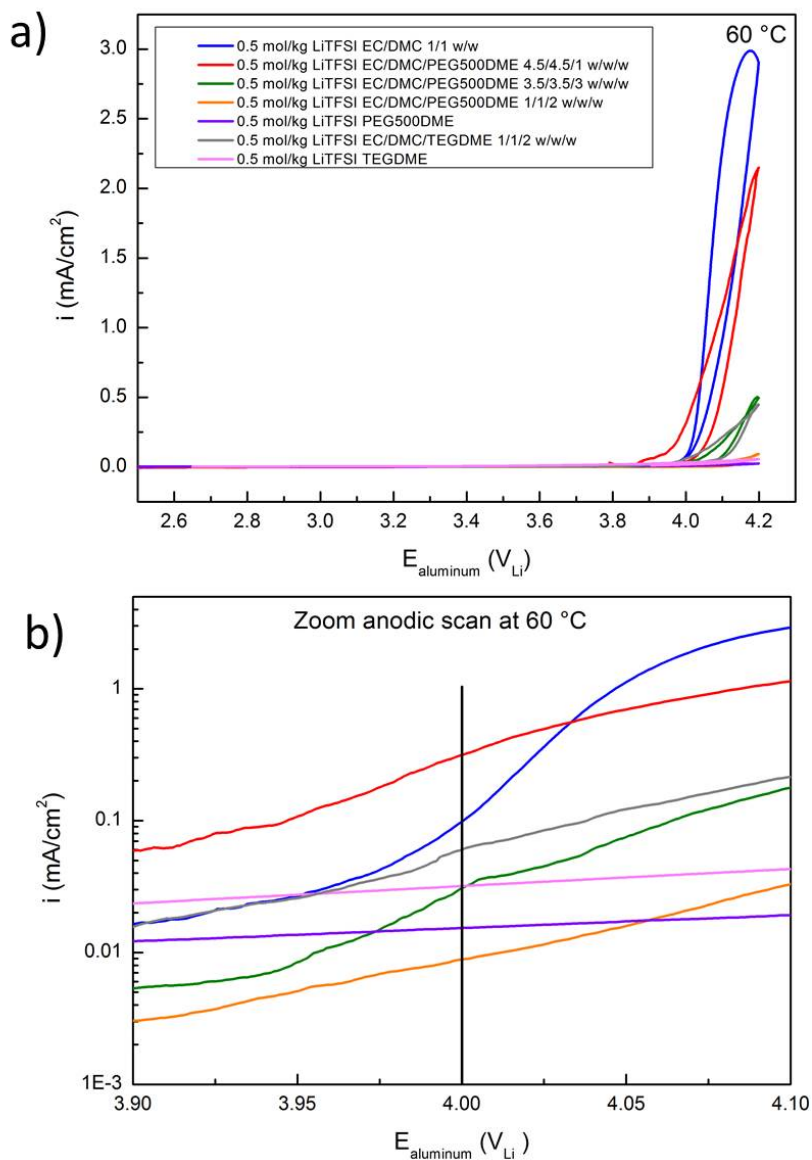
Figure 49: Cyclic voltammetry of aluminum working electrodes at a rate of 0.2 mV/s at 60°C in the first cycle. It is shown for 0.5 mol/kg LiTFSI in Ec/Dmc 1/1 g/g (blue), 0.5 mol/kg LiTFSI in Ec/Dmc/PPeg500dme 4.5/4.5/1 g/g/g (red), 0.5 mol/kg LiTFSI in Ec/Dmc/Peg500dme 3.5/3.5/3 g/g/g (green), 0.5 mol/kg LiTFSI in Ec/Dmc/Peg500dme 1/1/2 g/g/g (yellow), 0.5 mol/kg LiTFSI in Peg500dme (purple), 0.5 mol/kg LiTFSI in Tegdme (magenta) and 0.5 mol/kg LiTFSI in Ec/Dmc/Tegdme 1/1/2 g/g/g (grey). a) shows the full first CV cycle at 60°C. b) shows the zoom of plot a for the anodic scan at a potential of 4.0 V_{Li}.
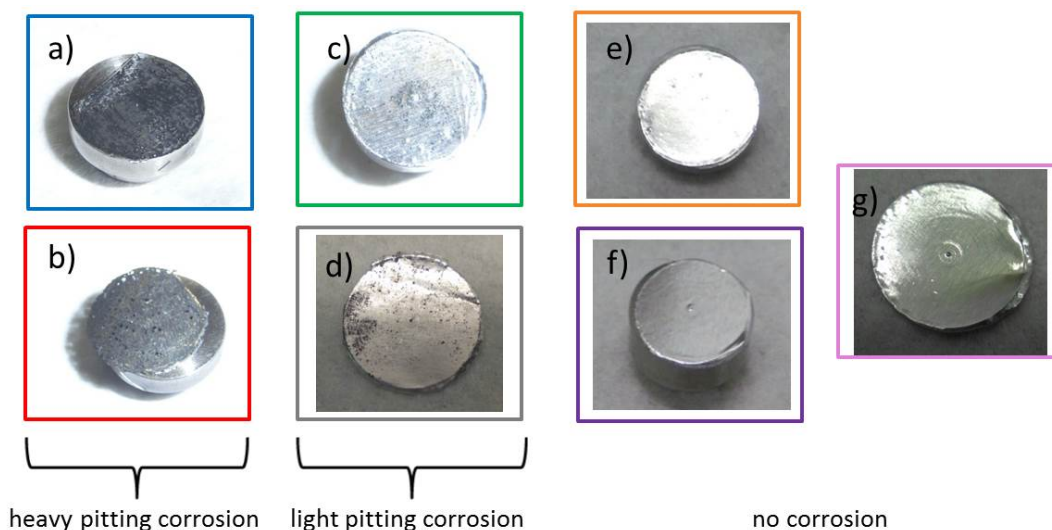
Figure 50: Overview of aluminum working electrodes after cyclic voltammetry at 25°C and 60°C with 3 cycles at each temperature. Electrodes were treated in different electrolyte mixtures: a) blue frame: 0.5 mol/kg LiTFSI in EC/DMC 1/1 g/g b) red frame: 0.5 mol/kg LiTFSI in EC/DMC/PEG500DME 4.5/4.5/1 g/g/g c) green frame: 0.5 mol/kg LiTFSI in EC/DMC/PEG500DME 3.5/3.5/3 g/g/g d) grey frame: 0.5 mol/kg LiTFSI in EC/DMC/TEGDME 1/1/2 g/g/g e) yellow frame: 0.5 mol/kg LiTFSI in EC/DMC/PEG500DME 1/1/2 g/g/g f) purple frame: 0.5 mol/kg LiTFSI in PEG500DME g) magenta frame: 0.5 mol/kg LiTFSI in TEGDME

peratures. PEG500DME can be also used as additive in EC/DMC and suppress corrosion as good as the pure solvent. For this purpose, a proper solvent as additive for corrosion protection seems to be PEG500DME in a mixture of EC/EMC/PEG500DME in a weight ratio of 1/1/2. PEG500DME itself was introduced and characterized as solvent in the previous **Chapters 6.1** and **6.2**.

For the detailed study of corrosion inhibition with PEG500DME, a electrolyte containing 0.5 mol/kg LiTFSI in EC/DMC/PEG500DME 1/1/2 g/g/g was used. First of all, the electrochemical stability was determined with linear sweep voltammetry in a potential window of 0-5 V_{Li} with a scan rate of 0.2 mV/s. For the anodic scan Super C65/PVDF-electrodes on aluminum current collector was used in a half cell arrangement with a lithium metal reference electrode in Swagelok $^{®}$ T-cell and three VWR $^{®}$ glass fiber pads as separators. Respectively, the cathodic part was performed with a Super C65/PVDF-electrodes on copper current collector. The above mentioned mixture was compared to common used 1 M LiPF$_6$ in EC/DMC 1/1 g/g and 0.5 mol/kg LiTFSI without corrosion inhibitor in a mixture of EC/DMC 1/1 g/g. The cathodic reaction below 1.5 V_{Li} is similar for all three electrolytes. The shoulder at around 1.2 V_{Li}, as well as the small peak at around 0.7 V_{Li}, is assignable to the beginning of the SEI-formation. At potentials below 0.2 V_{Li} metallic lithium deposition starts. The anodic scan shows big differences. The current density raises for pure LiTFSI without PEG500DME already at 3.6 V_{Li},
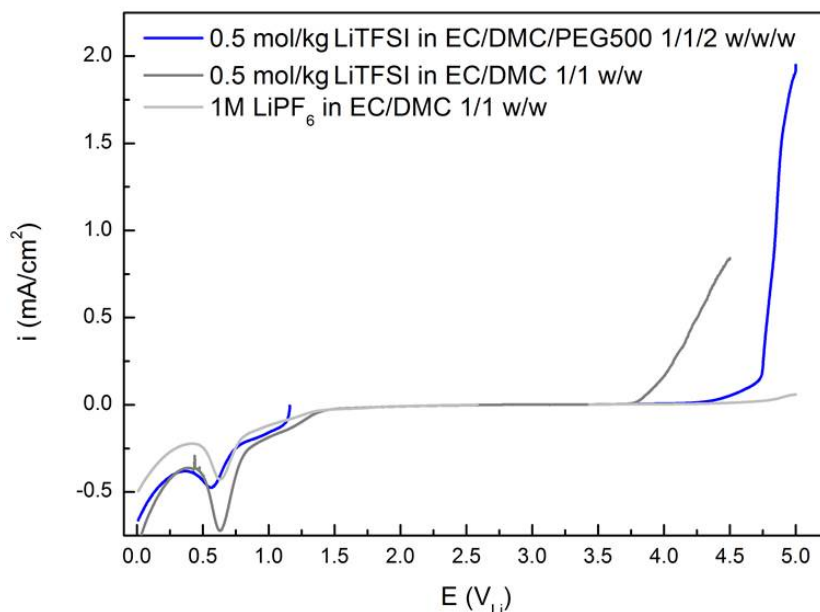
Figure 51: Linear sweep voltammetry of different electrolyte mixtures to determine the electrochemical window of three different electrolytes with a scan rate of 0.2 mV/s. Below 1.5 V_{Li} one can see first the peak for SEI formation and lithium deposition on the working electrode. Oxidative degradation is expectable at potentials higher than 3 V_{Li} and is visible with an increase in current density.

which is in accord with the literature (see **Figure 44**). This phenomenon is caused by the complex formation of the TFSI-anion and metallic aluminum as described above. This is clearly a lower potential as in 1 M LiPF$_6$. The current density increases for electrolyte oxidation at 4.8 V_{Li}. However, if one minimize the LiTFSI salt concentration to 0.5 mol/kg and add 50% of PEG500DME as corrosion inhibitor, the decomposition current increases to 4.3 V_{Li}, which is enough for the use of LFP as cathode material in lithium-ion batteries.

Due to the lower salt concentration it is obvious, that the ionic conductivity will be lower. This is also caused by the higher viscosity of the electrolyte. Nevertheless, **Figure 52** shows a moderate ionic conductivity of 1.83 mS/cm of the electrolyte with 50% PEG500DME as additive at room temperature, namely 25°C. This is an approximate factor of 6 lower than the standard electrolyte 1 M LiPF$_6$ in EC/DMC 1/1 g/g. The behavior of a reduced ionic conductivity, when long chained poly-glycols are added, is known from a latter publication [58]. In addition, one needs to keep in mind, that, to inhibit aluminum corrosion, the salt concentration is only half as high as before. However, the ionic conductivity was measured with a conductivity cell from Schott $^{®}$ in a temperature range between 25°C and 80°C. In the first step, the temperature is increased. At each measurement step, the temperature is hold stable for 30 minutes. After 30 minutes of a stable temperature one measures the impedance of the system (PEIS - potentio electrochemical impedance spectroscopy with a Biologic VMP3 multi-
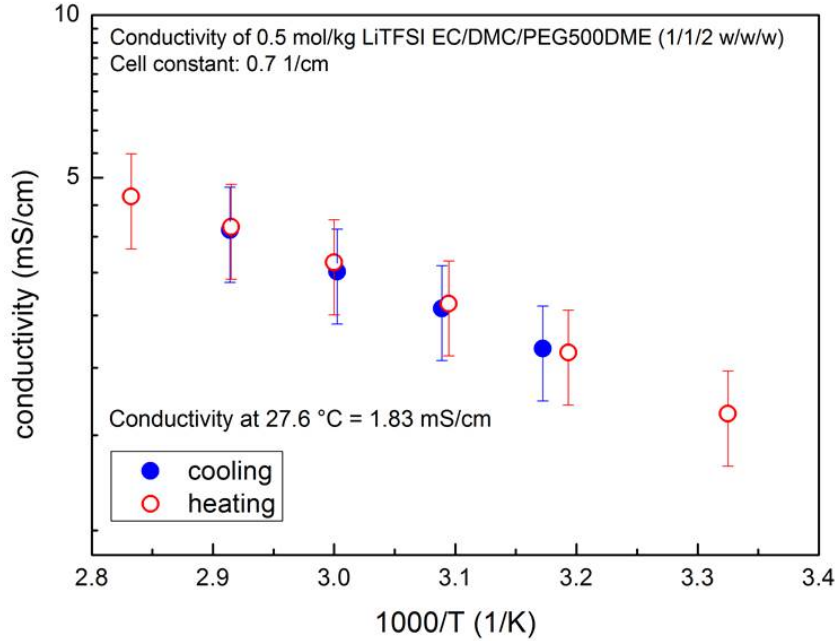
Figure 52: Ionic conductivity measurement of 0,5 mol/kg LiTFSI in Ec/Dmc/ Peg500dme 1/1/2 in a temperature range between 25°C and 80°C.

potentiostat). With the high frequency resistance (HFR) and a previously determined cell constant of the conductivity cell (0.7 cm^{-1}) one can calculate the ionic conductivity at each temperature with the following **Equation (16)**:

$$\sigma = \frac{Z}{R_{HFR}} \tag{16}$$

Whereby σ is the ionic conductivity at a constant temperature in mS/cm, Z is the cell constant, which was measured by a previous experiment with KCl-solutions of different concentrations and R_{HFR} is the measured high frequency resistance in the impedance measurement. In the second step is the cooling step. One measures at the same temperatures like in the previous heating step to show, that the ionic conductivity did not change because of a decomposition of the electrolyte. The heating and the cooling curve should be linear and on top of each other in the Arrhenius fitting, lnσ vs. 1/T. With this plot in **Figure 52** one shows the temperature dependent stability of this electrolyte and a reversible behavior after heating and the cooling step.

Lfp half cells were characterized at 60°C and a rate of C/5 in 0,5 mol/kg LiTFSI in Ec/Dmc 1/1 g/g and 0,5 mol/kg LiTFSI in Ec/Dmc 1/1 g/g with 50% Peg500dme to point out the corrosion of aluminum in test cells. The first and fifth cycle of both Lfp half cells are shown in **Figure 53a)** and **b)**. In **a)** we show the Lfp performance without Peg500dme. As one can clearly see in the first charge (dark green) the capacity reached a value higher than the theoretical specific capacity. The cut-off voltage

is reached at 175 mAh/g$_{L_{FP}}$ and the charging profile differs from the normal curve progression. The detected discharge capacity was 160 mAh/g$_{L_{FP}}$. The charging capacity increases more and more with each cycle and reaches in the fifth cycle (light green) a value of 182 mAh/g$_{L_{FP}}$. The overcharging capacity was assigned to the gain of electrons due to the parasitic current collector corrosion, which occurs in parallel to LFP charging reaction with increasing the cell potential. If one compares this behavior to a LFP half cell, which was cycled instead with 0,5 mol/kg LiTFSI in EC/DMC 1/1 g/g with 50% PEG500DME, shown in **b)**, one can clearly see that the cell reaches a stable capacity for the charge and discharge with an efficiency of $\approx 99\%$. The capacity values remain constant for cycle 1 and 5. This leads us to the conclusion that 0,5 mol/kg LiTFSI in EC/DMC/PEG500DME 1/1/2 g/g/g is a suitable electrolyte for electrochemical test using LFP as cathode material and can be used for experiments, which do not allow the use of the common LiPF$_6$ conductive salt. Examples for these experiments are investigations on performance test with a certain water content (LiPF$_6$ would form HF in contact with trace water) or cell performance at elevated temperatures above the degradation temperature of LiPF$_6$.

6.3.5. Conclusions

We investigated the corrosion behavior of different current collector materials as working electrodes (Al, stainless steel 316L) in combination with different conductive salts (LiPF$_6$, LiClO$_4$ and LiTFSI) in a EC/DMC solvent mixture in our three-electrode test cell design with cyclic voltammetry at several thermal condictions (25°C, 60°C and 80°C). SEM was used to show the level of pitting corrosion under the different conditions and in dependency of the electrolyte solution. In addition, aluminum was further investigated whereby LiTFSI was used as conductive salt and the addition of different concentrations of two different long chained glymes (TEGDME and PEG500DME) was tested for its corrosion protection at 25°C and 60°C. We could proof results from Dahbi et al [83] that aluminum corrosion could be inhibited with the addition of small amount of LiPF$_6$ to a LiTFSI-containing electrolyte. However, the protection is not given at elevated temperatures. According to Yang et al. and Chen et al. [97, 103] poly-ethylene oxide based solvents also form a protective layer on aluminum and protects it from corrosion. Therefore, we have tested the aluminum corrosion behavior of pure TEGDME and PEG500DME and also in mixtures with EC/DMC with cyclic voltammerty. These test resulted in to conclusion that a mixture or 0,5 mol/kg LiTFSI in EC/DMC 1/1 g/g with 50% PEG500DME seems to be good in terms of the corrosion behavior, thermal stability and viscosity for the application in electrochemical cell tests. For this reason we further investigated the electrolyte in terms of ionic conductivity, electrochemical stability and performance in LFP half cells at 60°C. We found a moderate ionic conductivity of 1.83 mS/cm at 25°C and a wide electrochemical window with a stability up to 4.3 V$_{Li}$. The half cell performance of LFP is good in terms of capacity and efficiency. Due to the better thermal stability it is possible to cycle cells at elevated temperatures for a longer
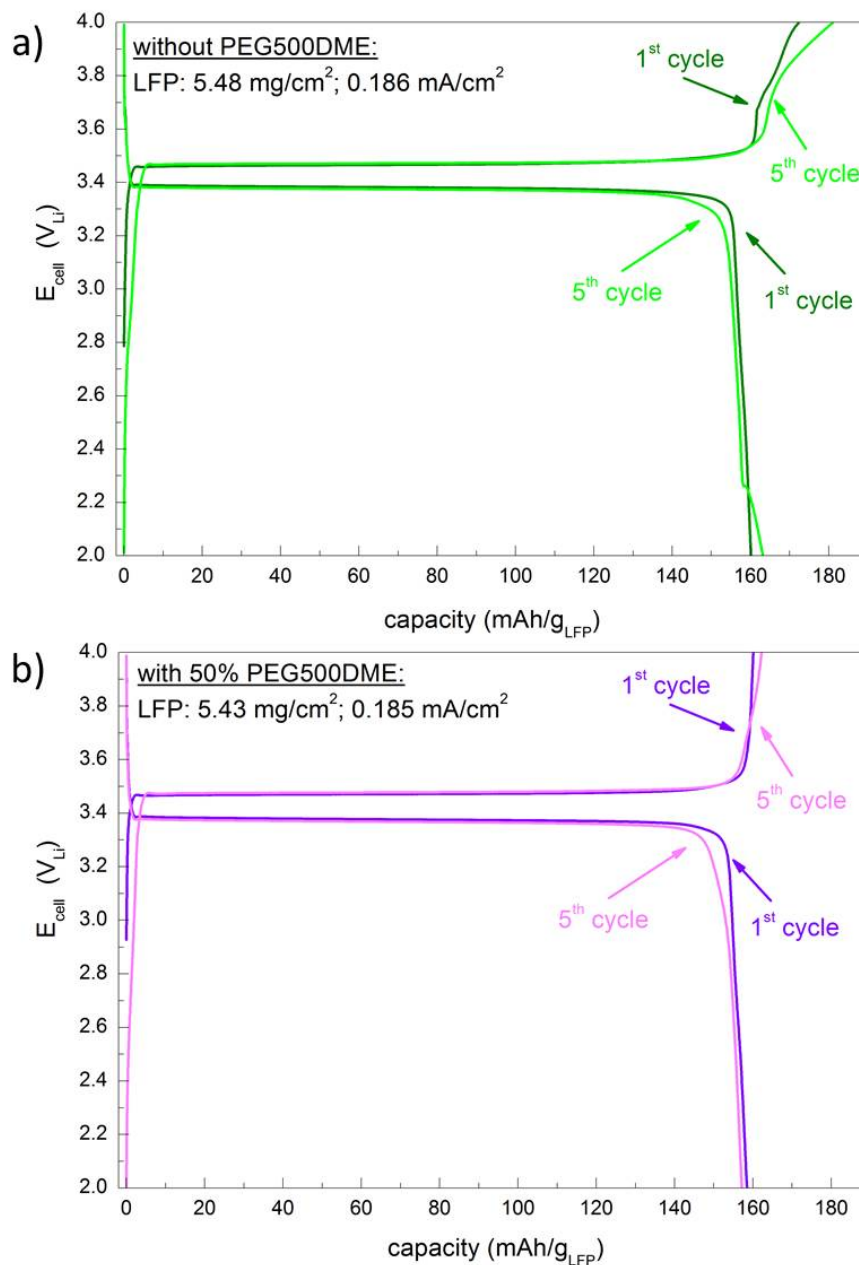
Figure 53: LFP half cells cycled at 60°C at a rate of C/5 with 300 µL of a) 0,5 mol/kg LiTFSI in EC/DMC 1/1 g/g and b) 0,5 mol/kg LiTFSI in EC/DMC 1/1 g/g with 50% PEG500DME. VWR ® glass fiber pads were used as separator.

time period. A thermal decomposition of the salt can be excluded, as well parasitic reactions with trace water. For this reason, the electrolyte is suitable for long-term cycling tests at elevated temperatures or investigations with selected water intrusion without decomposition of the conductive salt.

6.4. Iron Dissolution from Lithium Iron Phosphate in Contact with LiPF$_6$

6.4.1. Abstract

In order to investigate the transition metal dissolution in lithium-ion batteries affected by different applied potentials during cycling and by the contact LiPF$_6$-containing electrolyte solutions, we have analyzed aged anodes prompt gamma activation analysis (PGAA). With this method it was possible to quantify the amount of iron from LFP cathodes, which was dissolved and deposited on LTO anodes while cycling. The amount of dissolved transition metals varies and depends on the temperature and applied potentials, especially during charge. The higher the potential affecting the cathode, the higher the amount of dissolved transition metals.
In the following **Chapter 6.4** we introduce the PGAA technique as an evaluation method in the field of lithium-ion batteries. The method and its background were described in **Chapter 5**.

6.4.2. Introduction

Today Li-ion batteries are widely used in applications such as mobile phones and laptops. Some of the most popular materials for cathodes used in today's Li-ion batteries are LiNi$_{1/3}$Mn$_{1/3}$Co$_{1/3}$O$_2$ (NMC) and LiFePO$_4$ (LFP). Graphite is commonly used anode material. Li$_4$Ti$_5$O$_{12}$ (LTO) is an alternative anode material with some advantages regarding safety. LTO and LFP are also candidates for challenging future applications in electric vehicles and stationary energy storage with high demands for capacity and cycle life.

A main topic is to understand the degradation of the different electrodes separately and in full cell systems. The dissolution of transition metal ions and their deposition on anodes during life time and cycling seems to contribute to aging in NMC as well as in LFP cells, when typical electrolyte solutions containing LiPF$_6$ as a conductive salt are used. The dissolution of Mn, Ni and Co at higher voltages is reported to be one of the major problems contributing to capacity fade and impedance rise for NMC containing cells [111].

The iron-dissolution from LFP is known from previous research by Koltypin et al. in 2007 [109]. Iron dissolution behavior occurs even at elevated temperatures without applied potential in LiPF$_6$-containing electrolytes within 30 days. In samples with LFP stored at 60°C in an LiPF$_6$-containing electrolyte $\approx$ 40% of atomic iron gets dissolved (see **Figure 54**). If the electrolyte contains only 100 ppm of trace water, the iron dissolution increases to 60%. Using a salt, which does not form free F$^-$-ions like LiClO$_4$, this effect disappears. The atomic iron dissolution does not change with temperature and within 30 days. This aging process destroys the olivine structure of LFP and inhibits Li$^+$-ion intercalation while the cathodic step during cycling. This leads to a capacity fade and an increase of electrode resistance and, as well, an aggravation of the cell kinetics. Spec-
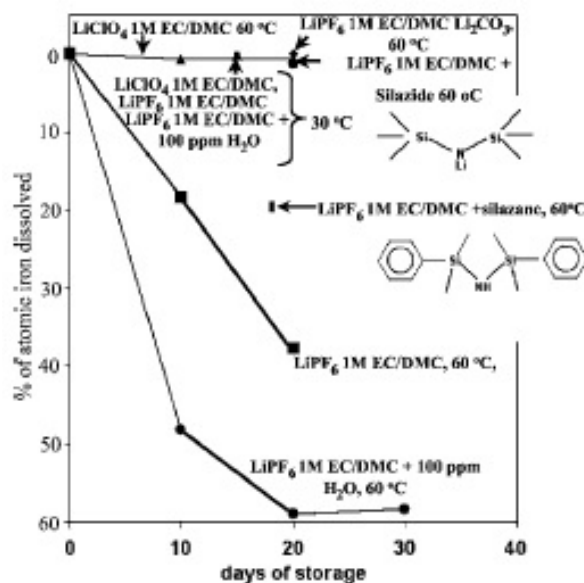
Figure 54: Results from iron dissolution measured by ICP of Lfp samples, which were stored in different electrolytes using LiClO$_4$ or LiPF$_6$ as conductive salt at temperatures of 30°C and 60°C. Effects of three different scavenger additives are also shown [109].

troscopic methods (FTIR and Raman) show formation of a surface film. Besides LiF, components consisting of P-F and O-P-F and organic molecules are detectable on the surface of Lfp samples [109].

With electrolyte additives like silicides, lithium carbonate (Li$_2$CO$_3$), Koltypin et al [109] show a lower iron dissolution, whereby Li$_2$CO$_3$ seems to be very effective, also at elevated temperatures. Beside these additives, it is also known, that glass fiber separators are able to work as HF scavenger [112]. Membranes contain silica oxide functionalized groups, which react chemically in the following **Reaction 17** to silicon tetrafluoride and water.

$$ SiO_2 + 4\,HF \longrightarrow SiF_4 + 2\,H_2O \tag{17} $$
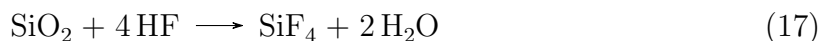
To demonstrate this fact, a Lto/Lfp full cell was cycled 5 times at a rate of C/5 and stored at 60°C for 2 weeks. To separate the electrodes three VWR $^®$ glass fiber separator pads were used with 300 μL 1 LiPF$_6$ in Ec/Dmc 1/1 g/g. After disassembling the cell, the aged electrolyte was analyzed by FTIR and compared with the pristine electrolyte solution. As one can see in the IR spectrum, the reflexes change and characteristic reflexes relating to decomposition products of LiPF$_6$ are absent (see **Figure 55**), when glass fiber separators are used. The reflexes for typical decomposition products of LiPF$_6$ are also listed in **Table 4**. Clearly, reflexes for LiPF$_6$ and LiF at 557 cm^{-1} and 839 cm^{-1}, respectively, are visible, but reduced. Other products, resulting from decomposition, like Li$_2$CO$_3$ (728 cm^{-1}) and LiOCH$_3$ (1197 and 1319 cm^{-1}) are fully absent. This leads to the assumption, that LiPF$_6$ and LiF chemically react with the glass fiber material of the separator, and prevent further decomposition leading to solid lithium salt products
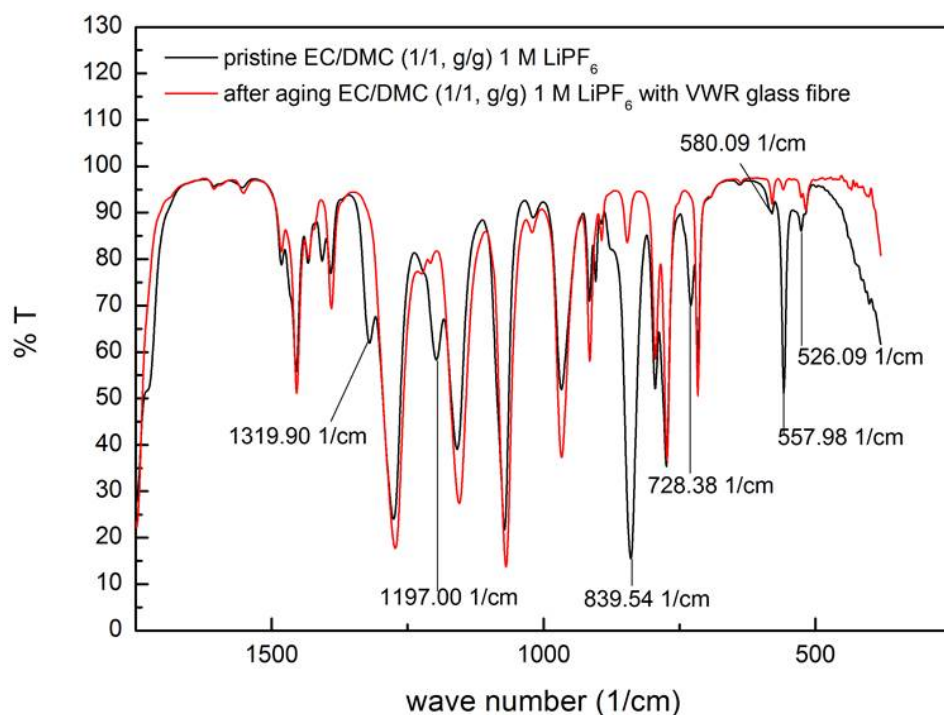
Figure 55: Comparison of pristine (black line) 1 M LiPF$_6$ in Ec/Dmc 1/1 g/g with aged electrolyte (60°C for 2 weeks) (red line) of a LtoLfp full cell using 3 VWR glass fiber separators.

like Li$_2$CO$_3$ and LiOCH$_3$. Unfortunately, glass fiber separators are not suitable for long term cycling and therefore not be used as a fluoride-ion scavenger in Lfp containing cells, because of its high porosity and the fact, that lithium dendrites can grow easily through the fibered structure.

However, to evaluate the iron dissolution from the Lfp olivine structure we performed some pilot tests. First of all, Lfp electrodes were placed into a certain amount of 1 LiPF$_6$ in Ec/Emc 3/7 g/g electrolyte solution for 2 weeks at 60°C. Afterwards, the liquid was analyzed with total reflexion x-ray fluorescence spectroscopy (T-RFA) performed by Dr. Georg Hartmann (Prof. Dr. M. Schuster, TU München, Chair for Analytical Chemistry) to detect dissolved iron in the electrolyte solution and to double-check results gained from Koltypin et al. [109].

For Nmc containing cells Zheng et al. have shown in 2012 that the dissolution of Mn, Ni and Co ions occurs at cut-off voltages above 4.2 V$_{Li}$ and has a significant impact on cell stability [111]. All three transition metals can also be detected on the negative electrode [1, 115, 116] with scanning electron microscopy and energy dispersive x-ray spectroscopy (SEM/EDX) [117]. The authors report the impedance rise on the negative electrode resulting from the deposition of these metal ions as the most important factor for cell aging but gave no quantitative data. A scheme of the influence of transition metal deposition on the negative electrode during the charging process is shown in **Figure 56**. Due to the successive dissolution of the transition metals a degradation and capacity

Table 4: Overview of characteristic reflexes in IR spectroscopy using 1 M LiPF$_6$ as conductive salt and VWR ® glass fiber separator pads in comparison with a pristine electrolyte.

Component	type	wave length [cm^{-1}]	Visible?	Literature
PF$_5$	bending P-F	526 and 580	yes	[113]
LiPF$_6$		557	Yes but reduced	[114]
Li$_2$CO$_3$	C-O bending	728	no	[19]
LiF		839	yes but reduced	[19]
LiOCH$_3$	C-H stretch and bending	1197 and 1319	no	[19]
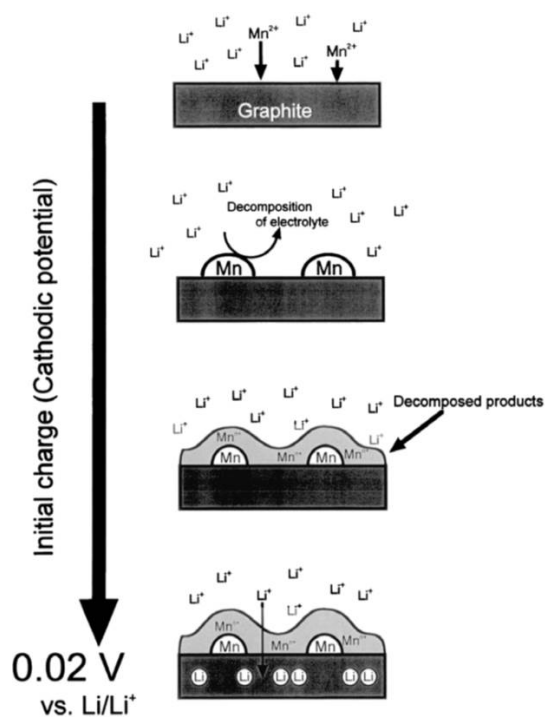
Figure 56: Scheme of the influence of transition metal addition and process of the SEI formation on a graphite negative electrode in presence of manganese (Mn) [117].

93

fade occurs after some cycling. One can also assume that any transition metal deposition needs a substantially low potential.

As we know, that also iron get dissolved from the LFP structure into the electrolyte, one can propose that one can see a deposition of iron ions on the LTO surface, as well. For this reason, we also checked the anode surface (in this case LTO electrodes) with SEM/EDX, after cycling an LTO/LFP cell in 1 LiPF$_6$ in EC/DMC 1/1 g/g at 60°C for 2 weeks at a rate of 1C, as a second pilot test, if iron is detectable on the anode surface. With these traditional methods like SEM/EDX, the deposition of transition metals on the anode electrode can be observed but not quantified. However, the quantification would be required in order to establish a clear correlation between transition metal deposition on the anode and the observed battery performance losses. Therefore, prompt gamma activation analysis (PGAA) was used to quantify the deposition of transition metals on the anode electrode, making use not only of the high quantitative precision of the measurement but also of its non destructive nature. This analysis was performed with aged LTO anodes harvested from cells post-mortem after cycling in 1 LiPF$_6$ in EC/EMC 3/7 g/g at 60°C and 1C for at least 500 cycles. With this method it was possible to quantify iron amounts, which precipitate on the anode surface while cycling, also in dependency of the cycling potential window.

We found with both pilot experiments, T-RFA and SEM/EDX, that iron gets dissolved and obviously precipitates on the anode surface. However, a quantification of the iron amount was only possible with the application of neuron beam on aged LTO anodes with the PGAA method. Prior to the PGAA measurement, T-cells containing LTO and LFP as electrodes were pre cycled and aged in 1 M LiPF$_6$ in EC/EMC 3/7 g/g at 60°C for at least 500 cycles. This work aims at quantifying the amount of deposited Fe ions on the anode with the help of PGAA and correlating it with cell aging data. Cells are cycled to conditions where dissolution is expected (elevated temperatures). After cell disassembly, the LTO anode is then characterized with PGAA. We also wanted to investigate the correlation between charge cut-off potential for the LTO/LFP full cells and the impact of that to the amount of iron on the anode side. Therefore, two different potential windows for charge and discharge were chosen to show that during an overcharge, the amount of deposited iron on the anode increases.

6.4.3. Experimental Part

For the following cycling experiments electrodes for the anode and cathode side were manufactured by mixing solid powders of the active materials Li$_4$Ti$_5$O$_{12}$ (LTO, Clariant) for anodes or LiFePO$_4$ (LFP, Clariant, $\approx$ 2.3% carbon) for cathodes, with Super C65 conductive carbon (Timcal) and a polymer binder PVDF (Kynar, HSV900) at a 80/10/10 weight ratio by hand and then, further, in a closed vessel at 2000 rpm for at least 3 h under ambient pressure with N-methyl-pyrrolidone (3,5 mL NMP per gram of solids) as solvent to get an electrode ink. These inks were coated with an automatic blade-coater (RK Print, Germany) with a wet-film thickness of 500 μm onto a piece of 18 μm thick

copper (MTI) in case of LTO and 15 μm thick aluminum foil (MTI) for LFP electrodes. Electrode coatings were dried on a 60°C warm hot plate under ambient atmosphere over night ($\approx$ 12 h). After the drying process electrodes were punched out at a diameter of 11 mm each and dried for at least 3 hours at 1200°C in a Büchi glass oven (Switzerland) under dynamic vacuum. After the drying step, electrodes were transferred into an Argon filled glovebox (MBraun, Germany < 0.1 ppm O_2 and H_2O) for T-cell assembly. The average electrode loading for LTO anodes was determined to be 7.09 $\pm$ 0.54 mg_{LTO}/cm^2 (ca. 1.24 mAh/cm²) and 5.18 $\pm$ 0.32 mg_{LFP}/cm^2 ($\approx$ 0.88 mAh/cm²). LTO anodes are oversized in terms of areal capacity to be sure that LFP cathodes are the limiting electrodes in the LTO/LFP full cell systems. The N/P ratio was $\approx$ 1.4.

Electrochemical charging and discharging experiments were performed in a mixture consisting of 1 M $LiPF_6$ as conductive salt with ethylene carbonate (EC) and ethyl-methyl carbonate (EMC) in a 3/7 weight ration solution. The electrolyte mixture was prepared in an Argon filled glovebox. Anhydrous EC (Sigma-Aldrich, 99%) was used for the solvent mixture as received. Whereby, EMC (Aldrich, 99%) was dried for several days over molecular sieve (Sylobead MS 564 C, 3 Å, Grace Division) to lower the water content. The water content of the basic solution of the electrolyte was determined by Karl-Fischer-Titration measured with equipment by Analytics to be lower than 20 ppm. $LiPF_6$ was not further purified due to its low thermal stability, and therefore purchased as battery grade (Sigma-Aldrich). As a cell hardware a stainless steel Swagelok ® T-fitting was used as three-electrode test cell body (see also description in **Chapter 5.4**). The LTO/LFP full cell was cycled with a charge and discharge procedure with a CCCV charging step at a MACCOR (Series 4000) in a potential window between 2.4 and 1.1 V_{cell} and 2.8 and 0.9 V_{cell}, respectively, at a rate of 1C and 60°C. The T-cell was assembled with a LTO electrode as an anode (negative electrode, counter electrode (CE)), LFP was used as cathode (positive electrode, working electrode (WE)) and metallic lithium as reference electrode (RE). As separator, three Celgard ® C480 foils were used, wetted with 300 μL of electrolyte. The schematic set-up of the three-electrode T-cell is shown in **Figure 57**. The high amount of electrolyte was necessary to keep the separators, especially the separator flag, wetted to provide a stable ionic contact of the reference electrode with the cell system, even at elevated temperatures. After cycling, the cells were disassembled under inert atmosphere in an argon-filled glovebox. The solvent of the electrolyte was evaporated from harvested LTO anodes and dried in the glovebox atmosphere. Note that at each step, electrodes were only touched with teflon tweezers to avoid iron impurities coming from the cell assembly. Afterwards, electrodes were transferred under argon to the Forschungsneutronenquelle Heinz Maier-Leibnitz. PGAA measurements were performed by Dr. Petra Kudejova. More details about the apparatus and the set-up, as well as the operating mode are given in the experimental part in **Chapter 5.8**. These measurements were part of the rapid access proposal 9123 (submitted 2013-12-19).

For T-RFA pilot tests, LFP-electrodes (10 pieces with $\approx$ 5 mg/cm²) were stored in 1 mL 1 M $LiPF_6$ in EC/EMC 3/7 g/g at 60°C for two weeks under argon atmosphere. The ab-
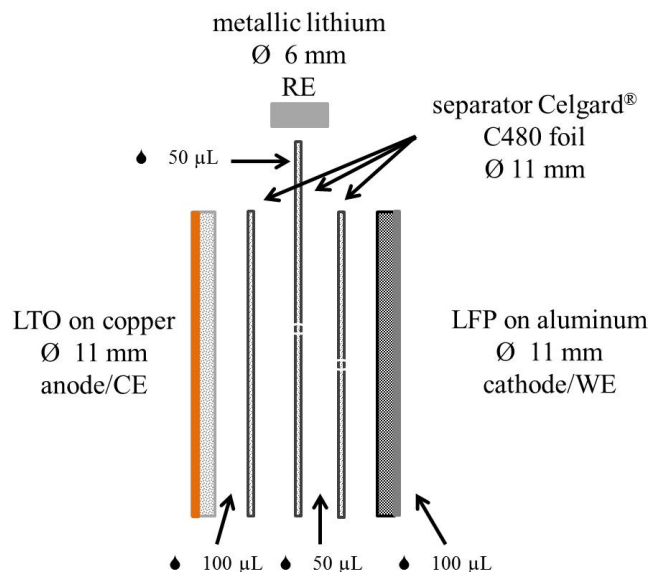
Figure 57: Schematic interior of a Swagelok ® T-fitting used for electrochemcial cycling of LTO/LFP full cells before PGAA post-mortem analysis. The total amount of electrolyte was 300 μL. LTO was used as an anode/counter electrode and LFP as a cathode/working electrode. Metallic lithium was used as reference electrode.

solute mass of LFP was $\approx$ 50 mg in total. We assumed, according on the data shown by Koltypin et al. [109], that $\approx$ 2% of iron can be dissolved in the electrolyte solution. This can be calculated to be an iron amount of $\approx$ 354 ppm or 354 mg/L in the electrolyte. After two weeks of storage, the electrolyte was sampled in air-tight vessels and measured by x-ray fluorescence analysis versus a blank of fresh electrolyte. A quantification was unfortunately not possible, because of the use of internal aqueous vanadium-based calibration standard solutions. One can not compare a sample in organic solvents with the aqueous standard.

For SEM/EDX measurement, aged LTO electrodes were harvested under argon atmosphere from cells, which were cycled for 2 weeks at a rate of 1C at 60°C. The cycling followed the described procedure for PGAA measurements (see **Chapter 5.8**). Afterwards, LTO anodes were washed with 5 mL DMC and dried and later analyzed by SEM/EDX (JOEL JCM-6000).

6.4.4. Results and Discussion

With T-RFA measurements, performed by Dr. Georg Hartmann, we could proof results given by Koltypin et al. [109]. In prepared aged electrolyte samples an elevated amount of iron compared to the fresh blank was detectable.

However, the detection of iron was possible on aged LTO electrodes by SEM/EDX ($\approx$ 1 to 3 μm depth). In this case a quantification was also not possible. The result is given in **Figure 58**. One can see in **a)** the SEM scan of the surface of the aged anode and

below in **b)** the EDX pattern of the same surface part. According to the presence of the FeKα-peak at $\approx$ 6.39 keV, iron was deposited on the anode surface during cycling. If one has a closer look at the potential of the Fe^{2+}/ Fe^0 redox couple (-0.41 V$_{SHE}$), one found a potential of 2.64 V$_{Li}$ (in an aqueous system!) [42]. Therefore, a reduction reaction of the Fe^{2+}-species should be thermodynamically possible on a LTO anode during charge. The Pourbaix diagram in **Figure 59** displays the important standard hydrogen potential (SHE) of redox species versus the pH. Standard potentials of LTO, iron and metallic lithium are given, whereby potentials for LTO and metallic lithium are independent from the pH. Redox potentials are $\approx$ -1.49 V$_{SHE}$ ($\equiv$ +1.55 V$_{Li}$) and $\approx$ -3.04 V$_{SHE}$ ($\equiv$ 0.0 V$_{Li}$) for LTO and lithium, respectively. The standard potential for the Fe^{2+}/ Fe^0 redox couple, which changes as a function of the pH could not be determine in a straightforward manner. The pH of an aprotic solution is not easy to be determined, but it can be estimated by the water content and the equation given in **Equation (18)**.

$$pH \approx 7 - 0.5 \cdot log\left(\frac{c_{H2O}}{1 \ mol/L}\right) \tag{18}$$

In **Equation (18)**, the pH area can be estimated from the water concentration in the electrolyte. With an overall water content in the electrolyte of 20 ppm (10^{-3} mol/L) one can estimate an pH of $\approx$ 7. Both pilot tests show that it is possible to detect traces of iron in the electrolyte and on the anode surface as well, which underlines the assumption that the iron dissolution from the cathode and its subsequent deposition on the anode surface leading to a passivation surface film and a resistance increase causing a strong capacity and performance fade.

For PGAA analysis two LTO/LFP full cells were aged at 60°C during cycling for 535 full cycles at a rate of 1C. **Figure 60** shows the performance in **a)** and the separated full and half cell profile in **b)**. The cell, which was cycled in the normal potential window 2.4 to 1.1 V$_{cell}$ is marked in magenta and the cell for the overcharging window 2.8 to 0.9 V$_{cell}$ is marked in dark blue. Prior to the long term cycling at 1C, both cells were formated three times at a slow rate of C/20 and reached a charging capacity of $\approx$ 165 mAh/g$_{LFP}$, which is almost the value for the theoretical specific capacity of LFP (170 mAh/g$_{LFP}$). In the first discharge the capacity dropped for the magenta cell to 145 mAh/g$_{LFP}$ and for the blue with the overcharging potential to 138 mAh/g$_{LFP}$. Therefore, the cycling efficiency is at 87% and 80%, respectively (data for first formation cycle is not shown here). For the following cycles at 1C, the value for the efficiency is at $\approx$ 99% for both cells. For the cell, which was cycled in the normal potential window between 2.4 and 1.1 V$_{cell}$, the capacity drop was calculated to be $\approx$ 30% from initially 145 mAh/g$_{LFP}$ to 102 mAh/g$_{LFP}$ with 535 cycles (see **Figure 60a)** magenta balls). If one increases the potential window to values between 2.8 and 0.9 V$_{cell}$, the capacity loss was higher, namely 44% (see **Figure 60a)** dark blue balls) from initially 138 mAh/g$_{LFP}$ to 76 mAh/g$_{LFP}$. With the use of a metallic lithium reference electrode, it is possible to separate the potential profile of each electrode (anode and cathode) from the full cell profile (anode - cathode). These
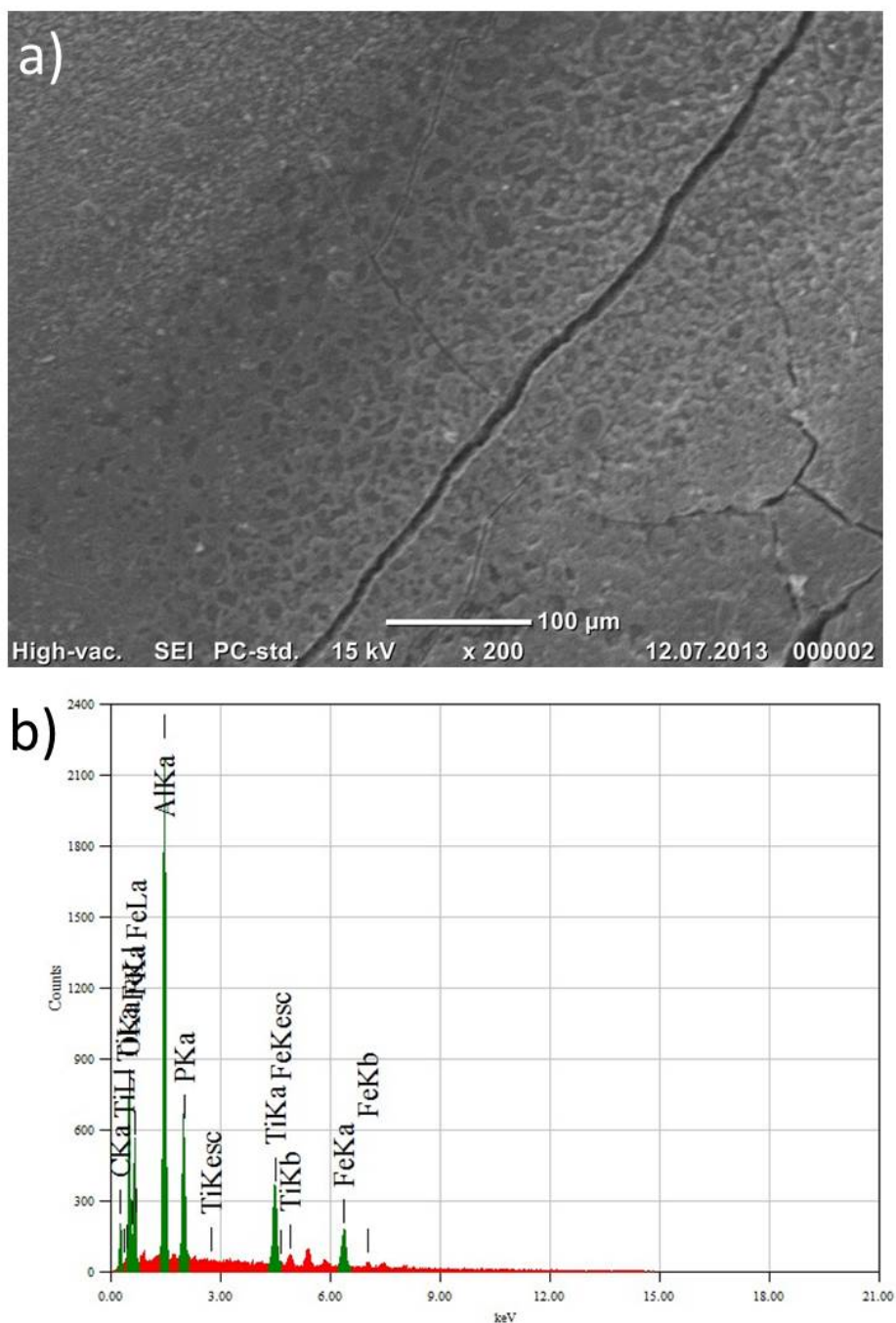
Figure 58: a) SEM and b) EDX of an aged LTO anode after cycling for 2 weeks at 1 C and 60°C in a Swagelok ® T-fitting with 300 μL 1 M LiPF$_6$ in EC/EMC 3/7 g/g. The EDX pattern shows the FeKα peak at $\approx$ 6.39 keV.
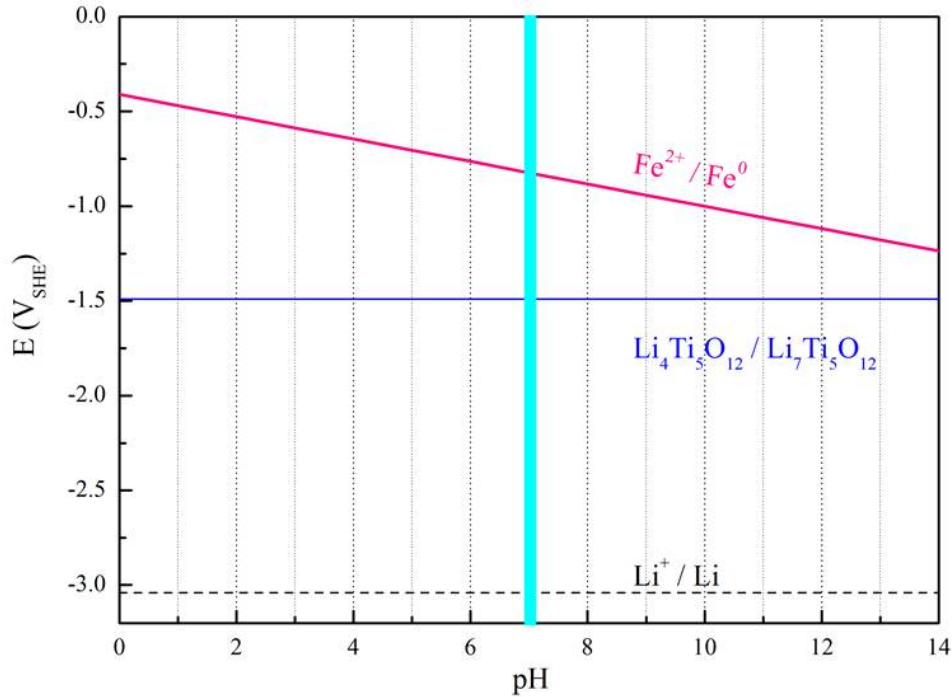
Figure 59: Pourbaix diagram displaying the standard potentials of LTO and metallic lithium, as well as the pH dependent potential of the redox reaction of the Fe^{2+}/ Fe^{0} redox couple.

profiles are shown in part **b)** of **Figure 60** for the charge and discharge, respectively, of the 50th cycle of both cells. The cathode's charge is plotted in red and the discharge in orange (marked as E_{WE}). For the anode, dark blue is labeling the profile of the charge and light blue the discharge (marked as E_{CE}). The profile for the full cell arises from the subtraction of the potential measured on the cathode and the anode, means E_{WE} minus E_{CE}, which is marked as E_{cell} in dark green for the charge and light green for the discharge profile. First of all one should have a look at the dark blue profiles of the LTO anode during charging. Its profile reaches its redox potential plateau at ≈ 1.55 V_{Li} very fast and remains constant for the whole charge. In contrast, the red profile for the LFP cathode is located at its redox potential at ≈ 3.8 V_{Li} as well, but increases near the charging cut-off to 4.0 V_{Li} in case of a charging procedure in the normal potential window and to 4.3 V_{Li} for the enlarged potential window from 2.8 and 0.9 V_{cell}. The behavior of the red and dark blue profiles shows that the cell performance is limited by the capacity of the cathode because it gives the cut-off of the charge, whereby the profile of the anode remains constant. In the dark green profile gives the charging profile of each full cell. During discharge the cell is limited by the performance of the LTO anode (light blue), because the lithium ions de-intercalate from the spinel structure and re-intercalate into the olivine structure of LFP (see reaction equations in **Figure (3)**). After ≈ 45 days and 535 cycles, respectively, the cells were stopped and disassembled under argon atmosphere in an argon filled glovebox. Afterwards the harvested electrodes
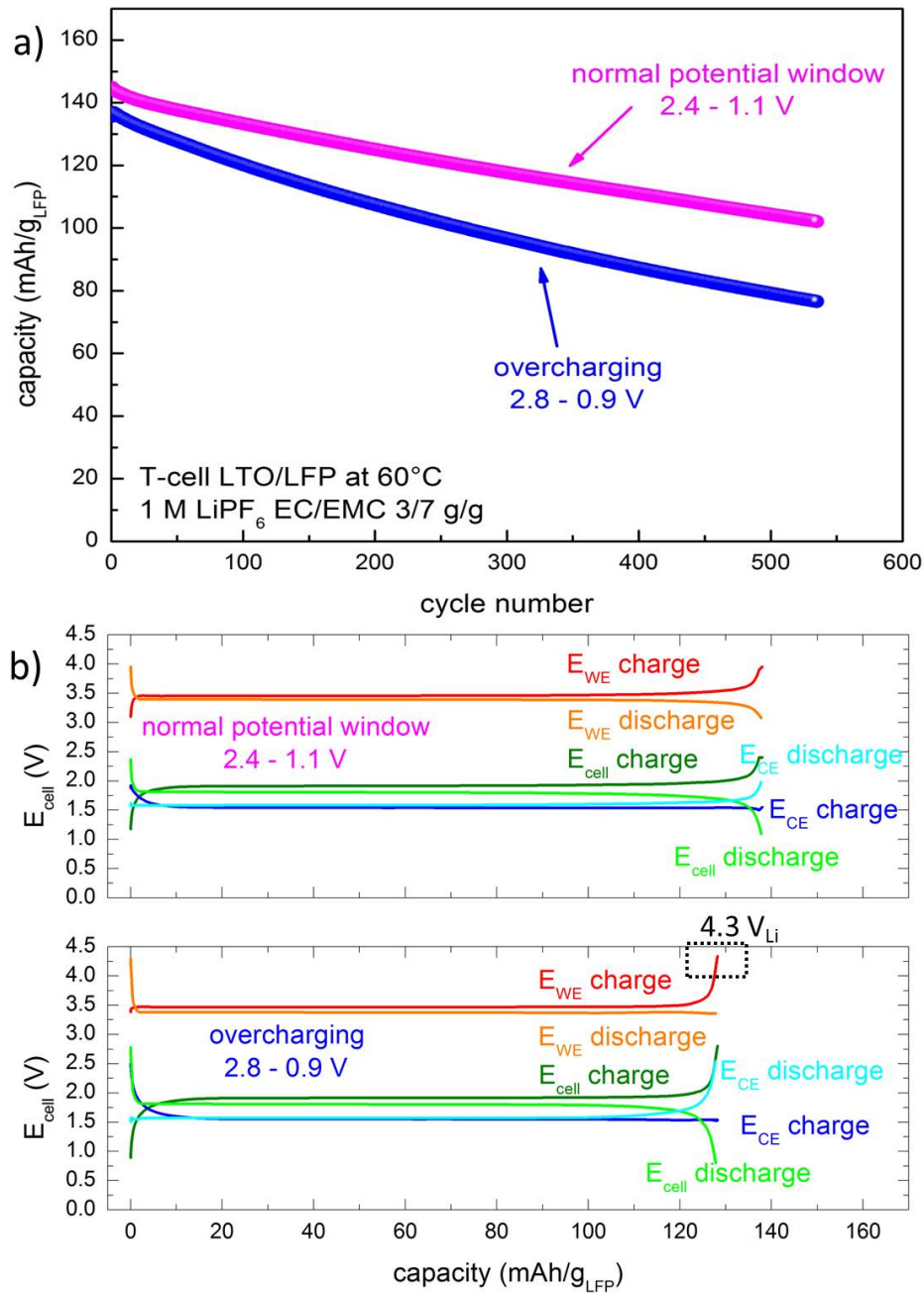
Figure 60: a) Cycling performance of a LTO/LFP full cell in 1 M LiPF$_6$ EC/EMC 3/7 g/g at a rate of 1C and 60°C for 535 cycles. Capacity loss is for the normal window ≈ 30% (magenta), in case of the overcharging potential window ≈ 44% (dark blue). b) Shows the full and half cell profiles of each cell (normal window magenta; overcharging dark blue) of the 50th cycle during charge and discharge.

Table 5: Overview of results of the PGAA measurements. For data treatment of iron detection line at 9297 keV was used (line is specific for iron). The detection limit was calculated to be 10^{-6} g of iron. As shown, 2.1% of the total amount of iron was deposited on the anode, when the cell was charged in the potential window between 2.4 to 1.1 V_{cell}. The iron amount on the anode increased to 3.2% after cycling in the overcharging potential window.

E [V_{cell}]	T [$°C$]	$LFP_{tot.}$ [g]	$Fe_{tot.}$ [g]	Fe_{anode} [g]	$Fe_{anode}/Fe_{tot.}$ [%]	Fe_{anode}/Cu [%]
2.4 - 1.1	60	4.9	$1.73 \cdot 10^{-3}$	$3.61 \cdot 10^{-5}$	2.1	0.259
2.8 - 0.9	60	4.4	$1.55 \cdot 10^{-3}$	$5.03 \cdot 10^{-5}$	3.2	0.391

were transferred under argon gas to the PGAA apparatus to quantify the amount of iron on the LTO anode. The **Table 5** gives the received results from PGAA measurements of both LTO anodes. During data treatment the intensity of line 9297 keV (singlet) was evaluated. Because of the strong signal of copper, which is a matrix element, it was not possible to identify many Fe-signals unambiguously. The detection limit of this line was calculated to be $\approx 10^{-6}$ g_{Fe}. According to the intensity of the line 9297 keV the mass of iron on the anode could be calculated to be $3.61 \cdot 10^{-5}$ g_{Fe} (0.036 mg_{Fe}), based on the total mass of iron available on the cathode of $1.73 \cdot 10^{-3}$ g_{Fe} (1.73 mg_{Fe}) for cycling in the normal potential window. The deposited iron amount on the anode after cycling was 2.1% (related to the total iron amount). We chose copper as internal standard, because the weight of the current collector foil of the anode was the same for both electrodes, so we could also relate the iron mass to the mass of copper. This value was calculated to be 0.259%. If the potential window was increased to 2.8 and 0.9 V_{cell}, also the iron amount on the LTO anode increases to 3.2% related to the total iron amount available from the cathode side. Also the iron to copper ratio increases by a factor of 1.5 to 0.391%.

Besides, a higher charging cut-off potential on the working electrode or cathode, respectively, leads to an increase of the the total iron amount by a factor of 1.5. Due to the limited beam time for each project, it was not possible to analyze washed LTO anodes. Therefore, we cannot prove, if the detected iron was really deposited as solid Fe^0 on the anodes surface or precipitate as Fe^{2+}-salt, due to solvent evaporation. However, the high capacity loss of the LTO/LFP cells cannot be related to the comparable small amounts of iron dissolved from the LFP structure. It is known from several publications that LTO/LFP cells show a very stable capacity with almost no capacity loss within several thousands of cycles at high rates [39,40,118]. Also these cells are performing with $LiPF_6$ as conductive salt and obviously the dissolution of iron does not effect the performance. Besides, our cells were cycled at 60°C instead of 25°C, and, however, the main difference should be the used volume of electrolyte. According to brief assumptions, the ratio of active mass and the volume of electrolyte is very small and estimate between ≈ 0.3 and 0.5 $\mu L_{electrolyte}/mg_{activematerial}$ for commercial cells in the automotive sector [119]. In our laboratory Swagelok ® test cells the ratio of total active mass and electrolyte volume is

$\approx 25\ \mu L_{electrolyte}/mg_{activematerial}$, which is comparably high and by a factor of ≈ 63 higher than in commercial cells. Nevertheless, in this cell design the high electrolyte amount is necessary to assure the ionic contact of the reference electrode to the inner cell compartment at elevated temperatures and for the long time period of the measurement. For measurements at 25°C we use ratios between 4 to 6 $\mu L_{electrolyte}/mg_{activematerial}$. This is in accord with information about laboratory test cells given by Aurbach et al. in 2013 while studying electrolyte additives for LiCoPO$_4$ cathodes [120]. The high electrolyte volume clearly affects the iron dissolution from the cathode, and it is quite obvious that in commercial cells this effect is not as distinctive as in our laboratory test cells. For this point of view one can conclude that the capacity fade in our test cells is not only related to the iron dissolution from the cathode material and the subsequent deposition on the anode. The main reason for the fast capacity loss are side reactions of the electrolyte leading to degradation and formation of solid products, which clog the separator pores and electrode surfaces.

6.4.5. Conclusions

As a summary, we could show in some pilot tests and with prompt gamma activation analysis (PGAA) that the iron dissolution from the olivine structure of LFP in contact with LiPF$_6$-containing electrolytes (used as conductive salt) is detectable as well quantifiable in the electrolyte solution and as a solid on the LTO anode surface. The evaluated data from PGAA of aged LTO anodes (line 9297 keV; specific for iron) and the cycling performance of LTO/LFP full cells could be compared. The cells were both cycled at a rate of 1C at 60°C for 535 cycles (≈ 45 days) in 1 M LiPF$_6$ EC/EMC 3/7 g/g and in a regular potential window of 2.4 and 1.1 V_{cell} and an increased potential window 2.8 and 0.9 V_{cell}, respectively. The detected amount of iron was in case of the normal window 2.1% related to the total available amount inserted by the active material of the cathode. The iron amount raises by a factor of 1.5, if the increased potential window of 2.8 to 0.9 V_{cell} was chosen. This can be explained by the applied elevated potential on the LFP cathode with 4.3 V_{Li} in comparison to 4.0 V_{Li}, if the regular potential window was used. The higher cathode potential during the cell charge forces a higher iron dissolution due to parasitic reactions on the electrode surface. In case of the greater potential window, the capacity decrease is also calculated to be a factor of ≈ 1.5 compared to the capacity of cells cycled in the normal potential window. Dissolved iron as Fe^{2+}-species can be reduced on the anode side to Fe^0 and precipitate as solid on the surface. The loss of iron atoms in the olivine structure leads to a deactivation of the electrochemical active LFP and the subsequent surface film formation with an increase of the inner resistance of the cell. Both leads to a capacity and performance loss after time. However, the capacity loss of the cycled full cells is not in direct relation to the comparably small amount of iron deposited on the anode. Therefore, another reason for the performance loss is, beside the iron dissolution, the problematic of side reactions occurring due to a high amount of electrolyte. The ratio of electrolyte amount and

active mass is calculated to be $\approx 25\ \mu L_{electrolyte}/mg_{activematerial}$, which is by a factor of 63 higher than for commercial cells.

6.5. Gassing Behavior of Lithium Titanate Anodes and its Origins

6.5.1. Abstract

Advanced lithium ion batteries containing lithium titanate $Li_4Ti_5O_{12}$ (LTO) as non-hazardous and "zero-strain" anode material are promising candidates in terms of safety and a long cycling life. Therefore these anodes are interesting materials for applications in the field of a long term energy storage. However, it is known from several tests that LTO containing cells tend to evolve a significant amount of hydrogen gas ("gassing"). LTO based cells were analyzed *in-operando* with on-line electrochemical mass spectrometry (OEMS) and besides the charging profile, real-time concentration of evolved gases were determined. With this method one was able to determine a direct correlation between the amount of evolved hydrogen and the water content of the electrolyte upon charge and discharge. It was proposed that gassing of LTO containing battery cells is caused by water intrusion of water contamination. On the basis of these data a possible reaction mechanism is proposed, whereby a one-electron reduction reaction of water leads to H_2-evolution and formation of hydroxide anion OH^-. Hydroxide anions play a key role in terms of solvent decomposition into CO_2 and carbonate oligomers (detected by ATR-FTIR). These products lead to a formation of passivation layers on the LTO anode side, which is in accord with the performance and capacity loss over a long time period.

6.5.2. Introduction

Nowadays, lithium-ion batteries are assembled with graphite anodes. However, the stability of the anode SEI layer is highly reduced at elevated temperature [121, 122], which leads to an increased electrolyte decomposition. This results in a reduced cycle-life and an increased cell resistance [123, 124]. This increased cell resistance may also promote the hazardous plating of metallic lithium on the negative electrode. One approach towards a longer cycle-life and better safety aspects is to replace the graphite anodes with a lithium titanate $Li_4Ti_5O_{12}$ (LTO) electrode. In contrast to graphite, LTO operates at a relatively high redox potential of 1.55 V_{Li} [40, 121], leading to negligible electrolyte reduction and avoids the deposition of transition metals derived from the degradation of commonly used cathode materials (e.g., manganese ions from high-voltage spinel) and furthermore prevents the plating of metallic lithium during rapid charging. In addition to that, if one compares the use of graphite to LTO anodes the risk of thermal run-away is reduced [125–128]. Besides the described positive characteristics of LTO in comparison to graphite, Zaghib et al. demonstrated a very long cycle life of battery cells consisting of LTO anodes and LFP (LiFePO$_4$) cathodes, achieving a stable capacity with more than 90% perpetuation at 25°C for 20000 to 30000 cycles (about 6000-8000 hours) [40, 118]. However, one of the main challenges for lithium-ion batteries containing LTO as anode material is the observed gas evolution as well during storage and cycling. This

is leading to an observed swelling of pouch bag battery cells and a capacity and power fade. It has been observed in several publications that cells composed of LTO anodes, filled with common used alkyl-carbonate electrolytes, and various high-voltage cathode materials (NMC, LMO) swell during various conditions [129–131]. The gassing behavior is increased at elevated temperatures, caused by the evolution of a high amount of gaseous hydrogen and carbon dioxide [124, 132]. Several studies regarding the problematic gassing issue of LiBs with a LTO anode are shown in literature. As a first example, He et al. [129], studied LTO combined with a NMC cathode in pouch bag cells aged under two temperature conditions, 25°C and 50°C, respectively. In post-mortem gas chromatography analysis of the harvested gas of each cell was analyzed. Cells stored for three months with no previous charging, means in a pristine state, as assembled at 25°C and 50°C, whereby carbon dioxide was the only detectable gaseous product. Unfortunately, they did not give a detailed explanation of the gas evolution under these conditions. In cells, which were stored at only 25°C in the charged state for about 2200h or had been cycled for 400 cycles (corresponding to 1600 h), respectively, hydrogen was the major component (around 50-55 wt%) of the gas phase. Gases like CO_2 ($\approx$ 30 wt%) and CO ($\approx$ 10 wt%) and as well low concentrations of hydrocarbons with a chain-length of C_1 to C_3 (lower than 3 wt% in total). The authors explained their observations with a chemical reaction of the Ti^{4+}-species of the de-lithiated (discharged) LTO with alkyl carbonate molecules from the electrolyte solvent. In their assumption, via this reaction hydrogen-radicals are formed, which would cause the formation of gaseous hydrogen and carbon dioxide [129]. A similar post-mortem study from Wu et al. [124] showed the analysis of evolved gases from pouch bag batteries with LTO anodes and NMC cathodes after cycling or storage (in the charged state) at temperatures ranging from 40°C to 80°C. Also in their study, hydrogen was supposed to be the main gas component with a concentrations of more than 85%. Minor concentrations of CO and CO_2 ($\approx$ 4-8 wt% in total) as well as C_1-C_3 hydrocarbons ($\approx$ 1-7 wt% in total) were detected. The swelling rate was observed to increase substantially with increasing temperature. An accelerated aging of LTO/NMC cells cycled at elevated temperatures was observed. Compared to a capacity retention of 90%, which could be maintained for 5000 cycles (ca. 1000 hours) at 25°C, the was reduced by an order of magnitude to only 400 cycles (ca. 80 hours) at 55°C. A later publication in 2012 by the same group [133], showed that the higher redox potential of LTO would be the cause for the observed gassing rather than the presence of moisture. They rationalized this assumption by postulating a decomposition pathway for linear carbonate molecules with a stepwise formation of gaseous hydrogen via hydrogen radical splitting from end-standing methyl groups *e.g.* in di-methyl-carbonate (DMC). However, further detailed explanation for this postulated reduction reaction, which would not occur at lower operating potentials like the redox-potential of graphite anodes, was not given. Beside these groups, a significant evolution of hydrogen during shelf-life (ca. 3600 h) of charged LTO/LMO ($LiMn_2O_4$) battery cells at 60°C was also detected by a post-mortem gas chromatography study by Belharouak et al. [132]. In contrast to the other hypothesis, they proposed an alternative mechanism for the gassing

behavior and hydrogen evolution in LTO containing cells. In their point of view, hydrogen is produced via the reduction reaction during charge of trace water molecules. However, battery cells with LTO anodes are known to have a high cycle life like reported by K. Amine et al. for LTO/LFP cells [40,118] as well as no gassing was observed during the storage of charged LTO anodes at 100°C for 10 hours reported in a previous research of Belharouak et al. [123]. These contrary results and assumptions about the hydrogen gas evolution led to the following experiments.

All listed and described studies were exclusively based on post-mortem gas phase analyses from stored or cycled cells LTO containing pouch bag cells. A direct correlation between the gassing process and the cell electrochemistry as a function of potential could not be elucidated, yet. Hence, On-Line Electrochemical Mass Spectrometry (OEMS) was used to examine *in-operando* evolved gases as a function of potential during the first charge and discharge cycle of LTO/LFP full cells and LTO/Li half cells, to get an understanding about the correlation of non-aqueous electrochemical and chemical degradation reactions in LiBs leading to a gas evolution. To have a look at the most probable side reaction promoted by moisture added to the electrolyte solution, attempting to simulate the effect of water contamination/intrusion and the hypothesis proposed by Belharouak et al. [132]. Thus, the gas evolution of LTO electrodes in both full cell and half cell configurations using an alkyl carbonate based electrolyte containing different amounts of water, namely 4000 ppm and 4 %. In addition to *in-operando* gas analysis and ex-situ XRD and ATR-FTIR analysis of cycled electrodes was done. With this data it was possible to propose a new reaction mechanism, which points out the role of water contamination with a resulting hydrogen evolution and hydroxide formation through the electrochemical water reduction. CO_2 formation could be explained via a hydroxide-catalyzed ring-opening reaction of cyclic carbonate molecules. A detailed possible reaction mechanism will be shown in the following.

6.5.3. Experimental Part

For the following experiments electrodes for the anode side were manufactured by mixing solid powders of $Li_4Ti_5O_{12}$ (LTO, MTI, > 98 % purity), Super C65 conductive carbon (Timcal) and a polymer binder PVDF (Kynar, HSV900) at a 80/10/10 weight ratio by hand and then, further, in a Thinky planetary mixer (2000 rpm, 5 min, vacuum) with N-methyl-pyrrolidone (3,5 mL NMP per gram of solids) as solvent to get an electrode ink. These inks were coated with an automatic blade-coater (RK Print, Germany) and a wet-film thickness of 250 μm onto a piece of porous three-layer Celgard ® C480 separator. With a porous substrate for the electrode coating, one can provide electrolyte wetability from both sides and no metal blocks the access to the OEMS capillary. The process for the LFP cathode coating is similiar to the previous one. These inks were produced by using a commercial carbon coated $LiFePO_4$ (LFP, $\approx$ 2 wt.% carbon), Super C65, and PVDF at a 80/10/10 weight ratio with NMP (4 mL NMP per gram of solids), as well.

Prepared inks were blade-coated with the mentioned coater with a wet-film thickness of 500 μm onto a 15 μm thick aluminum foil (MTI). Electrode coating were dried on a 60°C warm got plate under ambient atmosphere over night ($\approx$ 12 h). After the drying process electrodes at a diameter of 15 mm (LTO) and 18 mm (LFP) were punched out and dried for 12 hours at 70°C (LTO) and 120°C (LFP) in a Büchi glass oven (Switzerland) under dynamic vaccum. After this final drying step, electrodes were transfered into an Argon filled glovebox (MBraun, Germany < 0.1 ppm O_2 and H_2O) for cell assembly. The LTO electrode loading was determined to be 6.25 $\pm$ 0.15 mg$_{LTO}$/cm^2 (ca. 1.1 mAh/cm^2) and 8.02 $\pm$ 0.21 mg$_{LFP}$/cm^2 ($\approx$ 1.3 mAh/cm^2). LFP cathode needs to be oversized in terms of areal capacity to be sure that LTO anodes are the limiting electrodes in the LTO/LFP full cell systems, which are used in the first part of the gassing study. Electrochemical experiments were performed in electrolyte solutions containing 1 M LiTFSI as conductive salt in a mixture of ethylene carbonate (EC) and ethyl-methyl carbonate (EMC) in a 3/7 weight ration and different water concentration. LiTFSI was chosen to replace the common used LiPF$_6$ to avoid influences of the known parasitic reaction of the PF$_6^-$-anion with trace water molecules forming gaseous HF [12,134,135]. With the salt replacement one can study solvent degradation and resulting gas evolution caused by the fluences of water additive without side reactions coming from the conductive salt. All electrolytes were prepared in an Argon filled glovebox. To purify LiTFSI, it was dried at 120°C for at least 24 h under dynamic vacuum. Anhydrous EC (Sigma-Aldrich, 99%) was used for the solvent mixture as received. EMC (Aldrich, 99%) was dried for several days over molecular sieve (Sylobead MS 564 C, 3 Å, Grace Division) to lower the water content. The water content of the basic solution of the electrolyte without added water was lower than 20 ppm (Karl-Fischer-Titration, Analytics). Water containing solutions were mixed by adding 0.22 mmol/mL and 2.2 mmol/mL of H_2O to the basic electrolyte, this corresponds to $\approx$ 4000 ppm and $\approx$ 4 % H_2O, respectively. All electrolytes were stored in an Ar filled glovebox after preparation. The hardware of the used electrochemical cell (volume ca. 9 cm^3) is discussed in more detail in **Chapter 5.5** and **5.7** and [52]). For measurements performed in connection to the on-line mass spectrometry, the used cells were equipped with a capillary leak to the mass spectrometer. Two main cell configurations are used, namely a *1-compartment* cell design used for LTO/LFP full cells and a *2-compartment* cell design for LTO half cells, whereby an Ohara glass (Ohara, Japan) separates the counter electrode (metallic lithium) from the working electrode (LTO).
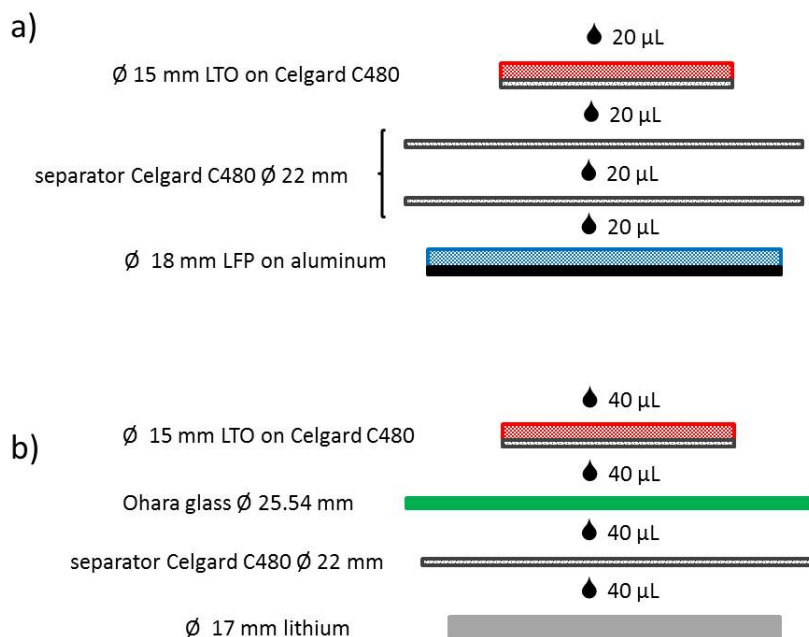
Figure 61: Schematic set-up of a) *one-compartment* cell set up for Lto/Lfp full cells and b) *two-compartment* cell assembled for Lto/Li half cells to investigate the gas evolution behavior of Lto containing cells depending on the water content of the electrolyte.

Figure 61 shows in **b)** the *1-compartment* cell set up used in Lto/Lfp full cells, which are assembled as follows: The aluminum supported Lfp electrode was placed onto the bottom part of the stainless steel cell, which is used as anode current collector. The electrode was wetted with 20 μL of electrolyte and covered with two pieces of 22 mm diameter Celgard $^{®}$ C480 separator disks, whereby again 20 μL of electrolyte was added at each step). The Lto electrode coated on Celgard $^{®}$ is placed onto the separators. Note that Celgard $^{®}$ side needs be placed face down and subsequently the Lto coating facing the top. Then another 20 μL of electrolyte solution was added. The electrical contact between the Lto electrode and the upper current collector (cathode part, insulated from the anode bottom part) was ensured by a stainless steel (316L SS) mesh (22 mm diameter and 0.22 mm wire diameter, 1.0 mm openings) in contact with a stainless steel compression spring (Lee Springs, UK). The cell was sealed with four insulated screws and with a torque of 6 Nm. In contrast, Lto/Li half cells were assembled like it is shown in **Figure 61b)** with a *2-compartment* cell set up. The difference here is the green labeled Ohara glass, which separates the counter electrode (metallic lithium) from the working electrode (Lto). This is necessary to avoid side reactions and gas evolution on the metallic lithium while using water containing electrolyte. The selective Li^{+}-ion conductive glass ceramic allows to use different electrolytes at each compartment side without mixing. Thereby, the compartment of the metallic lithium was kept always water free. The assembling procedure was nearly the same than described above. But, the amount of electrolyte was changed. The compartment of the Lto electrode was

filled with 80 μL electrolyte in total; 40 μL at each step. Note that the LTO electrode was exposed to same overall amount of water containing electrolyte, which was added to full and half cells, respectively, namely 80 μL. In order to avoid contact to ambient air and water, cells were assembled in an Ar filled glovebox. Electrochemical measurements for full and half cells were performed at a Bio-Logic VMP3 multipotentiostat with an initial 2 h OCV rest. Cells are galvanostatically charged at a rate of C/5 - for both combinations with respect to the theoretical capacity of LTO electrodes. For full cells the capacity average is calculated to be 1.1 mAh/cm^2, which corresponds to a current density of 0.22 mA/cm^2 or 0.39 mA total current. The chosen potential window was for the upper cut-off 2.4 V$_{cell}$ and for the lower one -1.0 V$_{cell}$. Full cells were limited by the LTO electrode, which was reached by a overdimension of the capacity of the LFP electrode of a factor of 1.28, and the redox potential of a LFP electrode is located at $\approx$ 3.5 V$_{Li}$ [109, 136]. With this information one can calculate the voltage applicate on the LTO electrode, which is in the window of $\approx$ 1.1 V$_{Li}$ during the charge of the full cell and in the reverse step 4.5 V$_{Li}$. half cells were cycled at the same rate like full cells, namely C/5 with the cut-off voltage of 0.2 V$_{Li}$ for the charge (lithium ion intercalation) and 5.0 V$_{Li}$ for the discharge (lithium ion de-intercalation), respectively. LTO half cells for the analytical part were only charged to 0.2 V$_{Li}$. These charged LTO electrodes were washed and later used for post-mortem ex-situ XRD and ATR-FTIR analysis. To analyze evolved gases, which were formed upon charge and discharge of full and half cells, an On-line electrochemical mass spectrometer (OEMS) was used. The system is explained in detail in **Chapter 5.7**. For a reliable gas quantification in these experiments, analysis of gas traces for H$_2$ (m/z = 2) and CO$_2$ (m/z = 44, 28, 16, 12) was only possible. Ethylene, C$_2$H$_4$, (m/z = 28, 27, 26) is also known to be a decomposition product of electrolyte reduction especially below 0.6 V$_{Li}$ [32], but with these experimental conditions and calibration gas the analysis was not fully reliable, owed due to minimal amounts evolved and a high background of each measurement coming from volatile EMC solvent. Additionally, the quantification of carbon mono-oxide, CO, (m/z = 28, 16, 12) was not fully reliable, too. This is explained by the interference from signals of CO$_2$ and EMC, as well. However, a semi quantitative estimation of these signals from the main m/z channels corresponding to CO (m/z = 28) and C$_2$H$_4$ (m/z = 26) results that evolved masses are negligible compared to H$_2$ (m/z = 2) and CO$_2$ (m/z = 44). These gases are the main ones, which are evolved upon aging of LTO containing cells, as reported in literature [124, 129, 133]. To understand the reactions occurring on the electrode and which solid products were formed, selected LTO half cells were disassembled in the charged state (in water-free and water-containing electrolyte) in an Argon filled glovebox. Harvested and charged LTO electrodes were washed with 10 mL acetonitrile and afterwards dried for 3 h at 50°C. Electrodes were transfered to an Attenuated Total Reflection Fourier Transform Infrared spectrometer (ATR-FTIR) and to X-Ray Diffraction (XRD). ATR-FTIR analysis was performed using a Perkin-Elmer ATR-FTIR spectrometer (Spectrum Two) equipped with a MIRacle germanium ATR (Pike Technologies). All IR-spectra were normalized to a clearly visible peak of the PVDF binder at 876 cm^{-1} [133]. The

PVDF content was identical of each electrode and PVDF was distributed evenly. Another advantage is, that the mentioned PVDF peak has no overlap with other relevant spectral peaks. XRD characterization of the same electrodes was performed using a Stadi MP diffractometer (STOE, Germany) with a 1D silicon strip detector (Mythen 1K, Dectris, Switzerland) and monochromatized $Mo(K\alpha_1)$ radiation ($\lambda = 0.7093$ Å, 50 kV, 40 mA) in a transmission geometry. The electrodes were analyzed in an airtight sample holder, designed in our laboratories, using aluminum foil (15 μm thick) as window. This was also reported in a previous work [50, 137].

6.5.4. Results and Discussion

The OEMS analysis of LTO/LFP full cells without water addition (20 ppm initial water content) and in water-containing electrolyte (4000 ppm and 4% H_2O) cycled in the described *1-compartment* cell configuration is shown in the next **Figure 62**.First of all, one need to have a look at the full cell behavior cycled in the pristine electrolyte without water additive for comparison. **Figure 62a)** gives the characteristic voltage profile of a LTO/LFP full cell. During the initial 2 h OCV period, the cell voltage is located near 0 V_{cell}. Following to this stabilization period, the first charge and discharge cycle with its typical voltage plateau at ≈ 1.9 V_{cell} is shown. The calculated charge capacity is ca. 175 mAh/g_{LTO}, which is known to be the theoretical capacity of LTO, considering a 3 e^- intercalation process. However, the discharge capacity is slightly lower with 150 mAh/g_{LTO}. This is most likely related to the adapted cell assembly for OEMS measurements, which requires an Celgard $^{®}$-supported LTO electrode, which cannot be calendared or compressed. For the dedicated *in-operando* gas traces, one have to look at **Figure 62b)**. As expected, no gas evolution can be detected in the initial rest period. This leads to the first assumption that a gas evolution requires charging of electrodes. And indeed, upon cell charging, the increase of H_2 concentration can be observed in the red line. The overall amount was ca. 1000 ppm at the cut-off potential of the charge. This behavior is consistent with already published post-mortem gas analysis data on cell assembled with LTO anodes, which showed that H_2 is the main evolved gas component. These cells were either cycled or stored in the charged state [124, 129, 132, 133]. During the following discharge, the hydrogen concentration remains more or less stable and only increases slightly to 1400 ppm. Beside the trace of H_2, CO_2 was detected, as well in the blue line. The increase of CO_2 concentration could be detected towards the end of the discharge when LTO potential approaches potentials higher than 4.5 V_{Li} due to anodic electrolyte oxidation and its resulting decomposition. If one concentrate on the suggestion of Belharouak et al. [123], hydrogen may originate from trace water reduction during charge. To examine how feasible this is, is based on the amount of evolved hydrogen in comparison to the overall water content. After the first charge and discharge cycle, the H_2 amount is detected to be 1400 ppm. This corresponds to ≈ 0.51 mol_{H2}, which is calculated by the normal molar volume of gas at 25°C, 24500

mL/mol, and the cell headspace volume of 9 mL (see **Equation (19)**).

$$\frac{gas\ concentration\ [ppm]}{24500\ mL/mol} \cdot cell\ headspace\ [9\ mL] = gas\ concentration\ [mol] \quad (19)$$

If one compares this to the water content of 20 ppm H_2O in 80 μL electrolyte, which corresponds to 0.09 mol_{H2O}, only 0.045 mol of H_2 can be evolved considering a one-electron reduction reaction shown in **Equation (20)**.

$$H_2O \longrightarrow 0.5\,H_2 + OH^- \quad (20)$$

Compared to the experimental values from **Figure 62b)** the theoretical H_2 amount, which can be evolved from the water content, is $\approx$ 11 times lower. However, in this calculation only the water-content of the electrolyte was taken into account. Humidity of electrodes or separators was not considered. A water content of only 0.11 wt% of the LTO electrode would introduce the water amount to reach 1400 ppm of H_2. LTO electrodes were dried at comparable low temperatures (70°C) and, unfortunately, an analytical quantification of this small amount of water was not possible. That is why, the water content of the electrolyte was increased to 4000 ppm, which is significantly higher, to erase influences coming from trace water in the electrodes or electrolyte and to allow a better analysis. In the following **Figure 62c)** and **d)** the changed performance of a LTO/LFP full cell with the use of an electrolyte containing 4000 ppm H_2O is shown. Whereby, **c)** shows the charge and discharge profile and **d)** *in-operando* OEMS siganls versus time for the first cycle. The voltage profile displays, beside the initial OCV period at around 0 V_{cell}, its typical plateau at $\approx$ 1.9 V_{cell}. However, it is clearly visible that the estimated charging time is prolonged. The time for Li-ion intercalation takes about 30 minutes longer, resulting a capacity of 194 mAh/g_{LTO}. And in addition, the discharge capacity is shortened to 124 mAh/g_{LTO}. This can be explained due to the water content, decomposition products are formed during cycling and are deposited on the active surface of the electrode, which inhibits the lithium-intercalation process. Looking at the OEMS traces, they show no gas evolution during the initial OCV period. But, upon initiation of the charging process, CO_2 starts to evolve at potentials around 1.5 V_{cell}. 300 mV later, also, H_2 evolution starts, i.e. once LTO reached its redox potential of 1.55 V_{Li}. Another distinctive increase in CO_2 concentration can be observed near the cut-off potential of the discharge. At this point the potential for LTO must be located around +4.5 V_{Li}, which is known to be high enough for electrolyte oxidation forming mainly CO_2 [32, 52, 139]. An explanation of these observations can be given, if one has a closer look at the 3 e^- charging reaction of LTO, see **Reaction 21**.

$$Li_4Ti_5O_{12} + 3\,Li^+ + 3\,e^- \longrightarrow Li_7Ti_5O_{12} \quad (21)$$
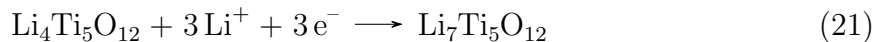
The redox potential for this reaction is located at 1.55 V_{Li}. Assuming that at the moment the LTO electrode reaches this potential value H_2O can be reduced. **Equation (20)**
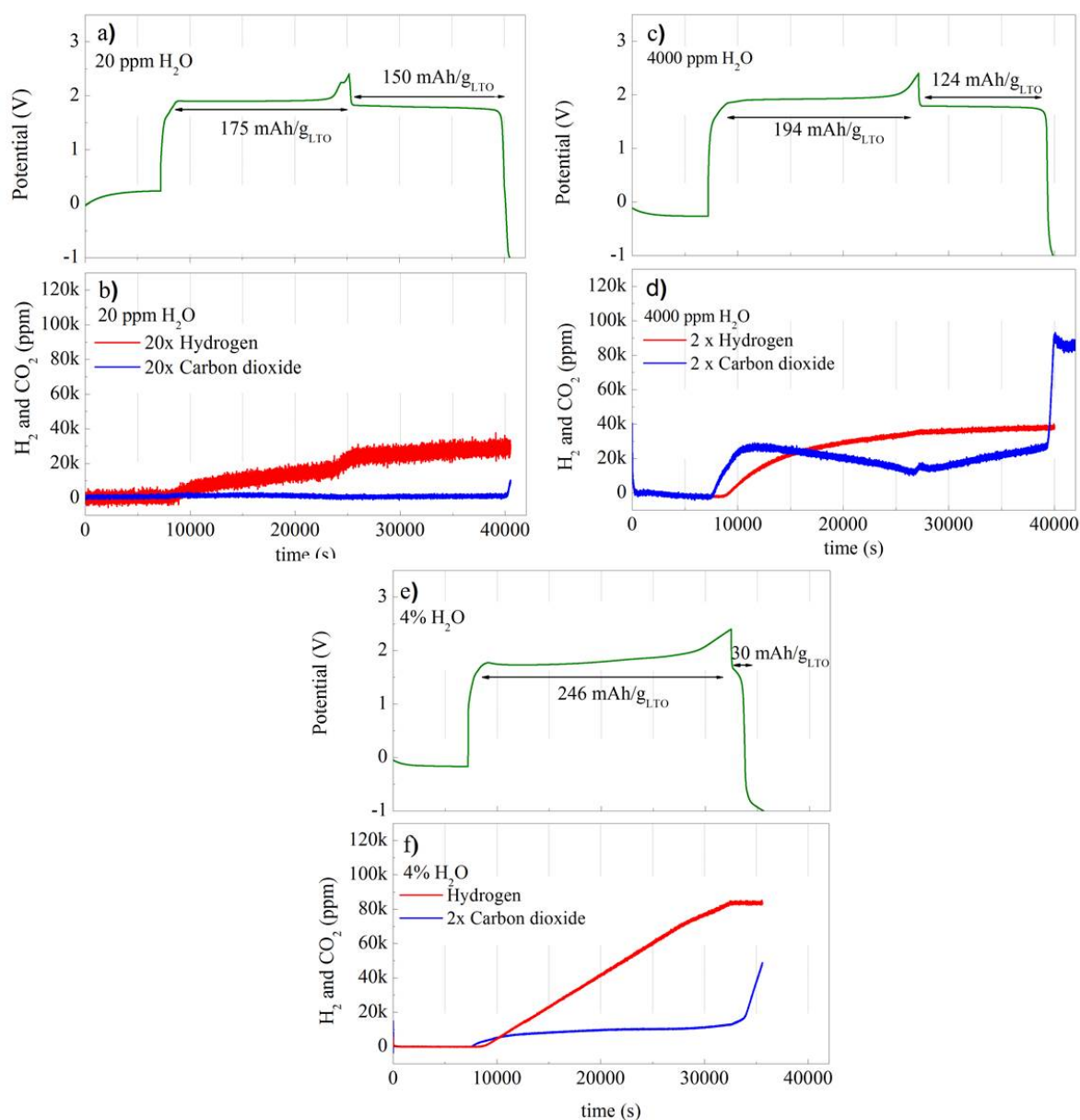
Figure 62: The cell potential versus time during the galvanostatic charge and discharge at a rate of C/5 of a LTO/LFP full cell (6.25 ± 0.15 mg$_{Lto}$/cm^2 and 0.39 ± 0.01 mA) using 80 μL electrolyte: a) without added water. Overall water content 20 ppm, c) with 4000 ppm H_2O and e) with 4% H_2O. The theoretical discharge capacity for the capacity-limiting LTO electrode corresponds to 5 hours or 18000 s (rate: C/5). Figures b), d) and f) show the real-time gas concentrations for H_2 and CO_2 evolved in the cell during cycling. Note that some gas concentration signals were multiplied by a magnification factor for better legibility). All measurements have an initial 2 h rest period of the pristine assembled cells at the open circuit potential (OCV) for background stabilization [138].

and **21** form a sort of redox system, in which H_2O reduces the charged LTO ($Li_7Ti_5O_{12}$) species. This overall reaction shows, that H_2 can be formed in this redox reaction, as it is shown in **Equation (22)**.

$$Li_7Ti_5O_{12} + 3\,H_2O \longrightarrow Li_4Ti_5O_{12} + 1.5\,H_2 + 3\,Li^+ + 3\,OH^- \tag{22}$$
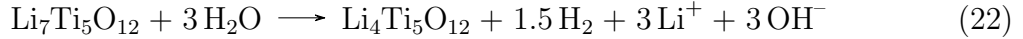
According to this suggestion, it implies that 0.5 mole of H_2 can be produced by reduction of 1 mole H_2O and 1/3 mole LTO ($Li_7Ti_5O_{12}$) can be oxidized by 1 mole H_2O. Due to this parasitic self-discharge reaction, one can explain the extended charging time and the correlated reduced discharging time. To proof this assumption, the measured gas concentration in ppm can be recalculate into the total amount of H_2 in mol using the **Equation (19)**. These calculated values for H_2 amount after charge ($n_{H2(charge)}$) and after the complete first cycle ($n_{H2(ch./disch.)}$) are displayed in **Table 6** for the different water contents in measured full and half cells. In addition, the maximum charge contribution from this parasitic H_2 evolution, ΔQ_{H2}, can be calculated considering that each H_2 requires a 2 e^- reduction process. ΔQ_{H2} can be calculated like follows in **Equation (23)** (whereby F is the Faraday constant 96485 As/mol).

$$\Delta Q_{H2} = 2 \cdot F \cdot n_{H2(charge)} \tag{23}$$

The formula for calculating the increase in charging time, when water gets reduced in the parasitic reaction, Δt_{charge} is shown here, see **Equation (24)**.

$$\Delta t_{charge} = \frac{\Delta Q_{H2}}{current\ [0.39\ mA]} \tag{24}$$

Obtained from this calculation, the resulting Δt_{charge} for a water content of 4000 ppm is $\approx$ 3500 s, which corresponds to a capacity increase of ca. 20 % in the charge capacity. From experiments an capacity increase from 11 % is obtained - 194 mAh/g_{LTO} compared to theoretical 175 mAh/g_{LTO}. If one compares the overall water content of 4000 ppm or 18 μmol with 7.4 μmol of evolved H_2, it suggests, according to **Equation (20)** that 80 % of the water content has been reduced during the first cycle. If one considers all these assumptions and calculations, one need to proof, if the reduction reaction of water (see **Equation (20)**) is thermodynamically possible on a charged LTO electrode. This might be best illustrated by a Pourbaix diagram shown in **Figure 63**. It is a characteristic diagram, which displays the standard hydrogen potential (SHE) of redox species versus the pH. The standard potentials of LFP, LTO and metallic lithium, which are $\approx$ +0.46 V_{SHE} ($\equiv$ +3.5 V_{Li}), $\approx$ -1.49 V_{SHE} ($\equiv$ +1.55 V_{Li}) and $\approx$ -3.04 V_{SHE} ($\equiv$ 0.0 V_{Li}), respectively, are all independent of the pH. Besides the potentials of used electrode materials, the standard potentials for the H_2O/H_2 and CO_2/C redox reaction, which both changes as a function of the pH. However, it is not straightforward to determine the pH in an aprotic organic solvent, but it can be estimated by the water content

Table 6: Overview of calculated values obtained from experimental data: Total amount of H_2 evolved after the charge and discharge cycle, $n_{H2(ch./disch.)}$, and after charge, $n_{H2(charge)}$, for the different cell configurations as function of the electrolyte water content (in % and μmol_{H2O}). A contribution on the charging time, Δt_{charge} was calculated as described. Note that the theoretical capacity at C/5 corresponds to a theoretical charge and discharge time of 18000 s and a charge and discharge current of 0.39 mA. The observed gain in apparent LTOcapacity compared to C_{LTO},th. is shown in the last column [138].

cell type	H_2O content of electrolyte [μmol_{H2O}]	$n_{H2(ch./disch.)}$ [μmol_{H2}]	$n_{H2(charge)}$ [μmol_{H2}]	estim. Δt_{charge}	estim. cap. gain theo.	estim. cap. gain exp.
LTO/LFP; 20 ppm	0.09	0.51	0.37	190 s	ca. 1 %	ca. 0 %
LTO/LFP; 4000 ppm	18	7.4	7.1	3500 s	ca. 19 %	ca. 11 %
LTO/LFP; 4 %	180	31	31	15000 s	ca. 83 %	ca. 41 %
Li/LTO; 20 ppm	0.09	0.47	0.33	160 s	ca. 1 %	ca. -25 %
Li/LTO; 4 %	180	67	63	33000 s	ca. 183 %	ca. 166 %
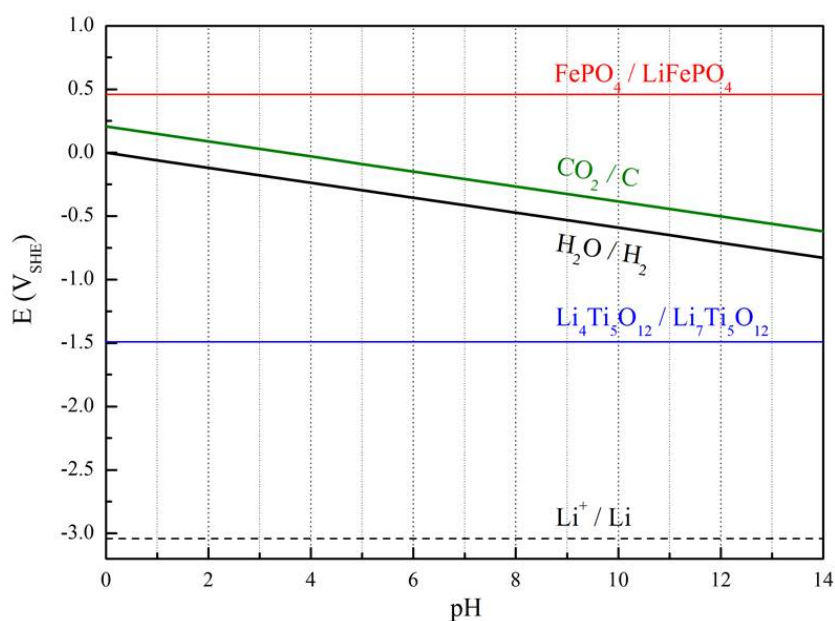
Figure 63: The Pourbaix Diagram is showing the standard hydrogen potential E_{SHE} versus pH for the pH-dependent H_2O/H_2 redox **Equation (20)** (black line) and the redox-potentials of the LFP electrodes ($\approx$ +0.46 V_{SHE} or $\equiv$ +3.5 V_{Li}, red line), the LTO electrodes ($\approx$ -1.49 V_{SHE} or $\equiv$ +1.55 V_{Li}, blue line), and metallic lithium electrodes ($\approx$ -3.04 V_{SHE} and defined as 0.0 V_{Li}, black dashed line), which are pH independent. The reversible potential for electrochemical oxidation of carbon is shown as the green line labeled [138].

Table 7: pH values calculated by **Equation (25)**.

water content [ppm]	water content [mol/L]	pH
20	$\approx 10^{-3}$	7
4000	≈ 0.2	7.3
40 000	≈ 2	8.5

and the following **Equation (25)**.

$$pH \approx 7 - 0.5 \cdot log\left(\frac{c_{H2O}}{1\ mol/L}\right) \tag{25}$$

Thereby, the pH values for the different water concentration can be evaluated and are shown in **Table 7**. According to these values, thermodynamically water can be reduced on a charged LTO electrode like it is given in **Equation (20)** and the back reaction, H_2-oxidation on LFP, is also possible. As mentioned above, the evolution of CO_2 starts in an water containing electrolyte right before H_2 evolution starts (see **Figure 62c)**). This observation will be discussed in the following. In principle, a CO_2 evolution can be caused by water-assisted oxidation of the solvent of the electrolyte or of the carbon, which is present in both, the LFP cathode as particle-coating and the Super C65 conductive carbon powder, which was added to the electrode ink. It is known from literature that CO_2 was the main gas evolved by anodic oxidation reactions of common electrolyte with alkyl-carbonate solvents at potentials higher than 4.5 V_{Li} [32, 52, 139]. Tough, the electrode potential of an LFP electrode, which was used in the described experiments, should be located at 3.5 V_{Li}. Therefore, a CO_2 evolution could only be explainable, if water can trigger an oxidation reaction of alkyl carbonates. Lu et al. demonstrated that the described reaction might be possible [140]. They found that anodic oxidation of a mixture of propylene carbonate/di-methyl-ether (PC/DME) in an aqueous 0.1 M KOH solution occurs on a platinum electrode at ca. 0.5 V_{RHE} (RHE = reversible hydrogen electrode). This potential corresponds to $\approx +3.1$ V_{Li} at pH ≈ 7. With a look at the Pourbaix diagram in **Figure 63**, it is obvious that this potential is negative of the LFP cathode. But, it is not clear, whether this reaction also occur on lower potentials of LFP electrodes. The second possibility for the observed CO_2 evolution is the electrochemical oxidation of carbon, either Super C65 carbon or carbon coating of LFP particles. The oxidation of carbon has been intensively studied in the area of fuel cell research. The following **Equation (26)** is well known and takes place in aqueous electrolytes at a potential of +0.207 V_{RHE} [141, 142].

$$C + 2\,H_2O \longrightarrow CO_2 + 4\,H^+ + 4\,e^- \tag{26}$$
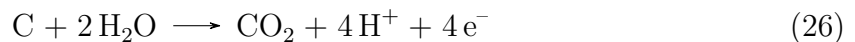
According to calculated pH values for different water contents shown in **Table 7**, the estimated overpotential for CO_2 evolution **Equation (26)** is located between 0.66 and 0.71 V_{SHE}. These values are identical to overpotentials, which are known to be necessary for the given **Equation (26)** in literature [143]. The reversible potential of this **Equation (26)** is positive of the H_2O/H_2 curve and always below the LFP potential, which means that carbon can be thermodynamically be electochemical oxidized by a charged LFP electrode. To conclude, the observed CO_2 evolution in water containing electrolyte is most likely related to the electrochemical oxidation of carbon, either coming from Super C65 of the electrode or from carbon-coated LFP particles, on the cathode side. The higher the water content of the electrolyte, the more pronounced is the H_2 evolution, which is shown in **Figure 62e)** and **f)**. The charge capacity increased to ≈ 246 mAh/g_{LTO}, which corresponds to a capacity gain of ca. 41 %, and the potential plateau of the LTO/LFP reached ≈ 1.7 V_{Li} ($\Delta E = 0.2$ V compared to electrolyte used in **Figure 62a)**). The reduced charging potential can be explained by a mixed potential between charging reaction of LTO, $Li_4Ti_5O_{12}$ to $Li_7Ti_5O_{12}$, and the parasitic water reduction reaction. Using a water content of 4000 ppm the potential variation ΔE is only 0.02 V compared to the electrolyte with 20 ppm H_2O. Subsequently, the discharge capacity in an electrolyte with 4 % water drops further to a capacity corresponding to ≈ 30 mAh/g$_{LTO}$ see **Figure 62e)**. Due to the excessively high H_2 evolution and formation of degradation products coming from the parasitic water reduction reaction, solid non-conductive products can deposit on the electrode surface and passivates it, which causes a drop of the discharge capacity. The amount of evolved H_2 in **Figure 62f)** is around 4-times higher and shows a similar trend compared to the electrolyte with 4000 ppm H_2O (see **Table 6**). As seen before, CO_2 evolution starts immediately upon the beginning of the charging process before H_2 evolution starts, as observed with 4000 ppm water content. But, the CO_2 amount does not increase with the water content, because there is a continuous CO_2 consumption while forming alkyl carbonate oligomers (mechanism will be shown later). Nevertheless, a water content of 4 % in an electrolyte is not realistic, but it was necessary to understand the gassing process of LTO containing battery cells. During the evaluation of LTO/LFP full cells, complications in the data interpretation during discharge appeared due to the limited LFP counter electrode capacity, especially in the presence of water and its parasitic reduction reaction. This complication causes the fact, that the potential of the LTO working electrode is only calculable in the charge and is unknown during the discharge process. In addition, H_2, formed on the LTO anode during charge, can be re-oxidized at the LFP electrode, which causes inconsistency for the calculation of H_2 amount evolved during charge and discharge. For that reason, LTO half cells were investigated. The metallic lithium has a roughly 90-fold higher capacity (C_{Li}) than LFP electrodes (≈ 1 mAh/g_{LFP} compared to ≈ 90 mAh/g_{Li}). This can be calculated by product of specific capacity ($C_{spec.Li}$) and densitiy of metallic lithium (ρ_{Li} amd the thickness of the foil ($t_{Li-foil}$) shown in the

following **Equation (27)**:

$$C_{Li} = C_{spec.Li} \ [3600 \ mAh/g_{Li}] \cdot \rho_{Li} \ [0.534 \ g/cm^3] \cdot t_{Li-foil} \ [0.045 \ cm] \qquad (27)$$

To avoid a reaction of water molecules with metallic lithium, the electrodes were separated by a lithium-ion selective conductive glass ceramic, which is not permeable for water molecules. The behavior of half cells without and with added water to the electrolyte is shown in **Figure 64** with charge and discharge profiles and the *in-operando* OEMS signals for H_2 and CO_2. As expected, the OCV of the pristine LTO electrode is located at ≈ 3 V$_{Li}$ and no gas was evolved. The voltage profile of a Li/LTO half cell without added water is in **Figure 64a)**, whereby the potential plateau is centered at ≈ 1.5 V$_{Li}$. This relatively high overpotential is related to the higher ohmic resistance coming from the use of the Ohara glass separator. This fact is also most likely the reason for the lower charge capacity of 130 mAh/g$_{LTO}$, compared to 175 mAh/g$_{LTO}$ specific capacity, of the LTO half cell, which was evaluated for a potential, of 1.0 V$_{Li}$. As reported in **Table 6**, the amount of H_2, in **Figure 64b)**, evolved is essentially the same compared to full cells, while no CO_2 is evolved during the charging and discharge process until the LTO electrode reaches a potential of ≈ 4.5 V$_{Li}$. A closer look at OEMS hydrogen trace using a water free electrolyte is possible in the next figure, which shows a sort of enlargement of the previous described measurement. The clearly detectable amount of H_2 (red data) over time (x-axis) accounting to a total amount of ca. 850 ppm (right red axis) after the first charge and discharge is indeed evolved. The corresponding LTO half cell profile is given in the green line (left green axis). That concentration in the gas phase of the OEMS data is summarized in **Table 6**.
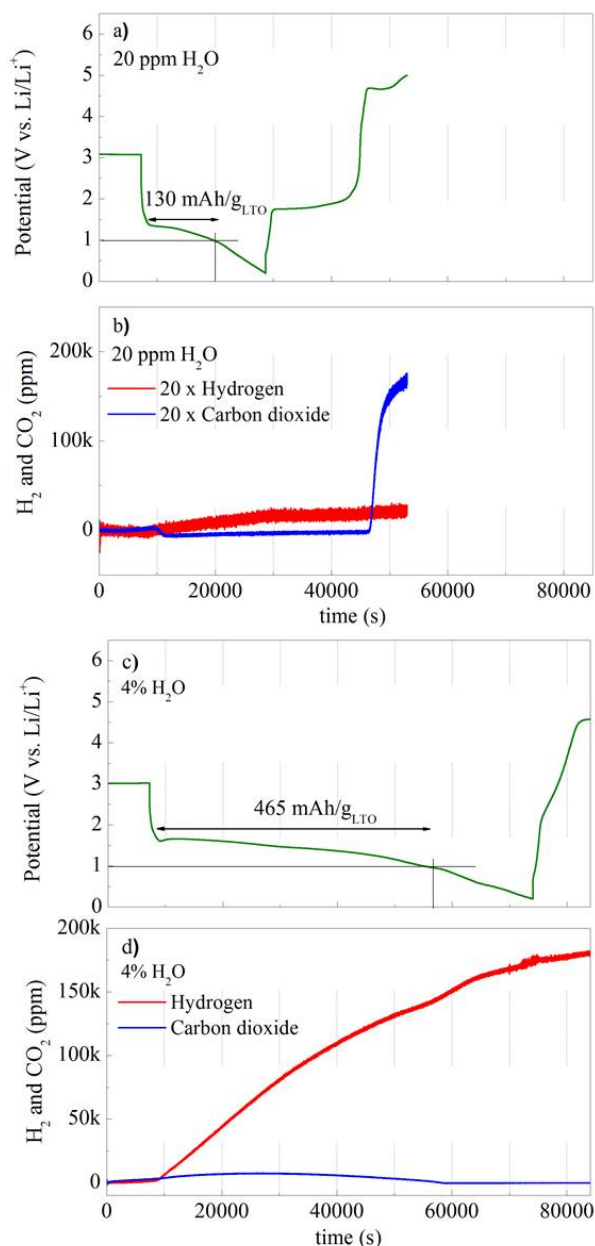
Figure 64: Characterization of Li/Lᴛᴏ half cells at C/5 (0.39 mA) using 80 μL 1 M Liᴛꜰꜱɪ in Eᴄ/Eᴍᴄ (3/7 g/g) per side in a *2-compartment* cell configuration, whereby the side of the counter electrode is always water free. The cell potential versus time during the first galvanostatic charge and discharge cycle is shown a) without water added to the electrolyte on the Lᴛᴏ side and c) with 4 % H_2O added. The maximum theoretical discharge capacity of the Lᴛᴏ electrode is 18000 s corresponding to a rate of C/5. Graphs b) and d) show the corresponding real-time H_2 and CO_2 concentration in the cell determined by the OEMS. Like in the previous full cell measurements, Lᴛᴏ half cells are started with a 2 h OCV period for stabilization [138].
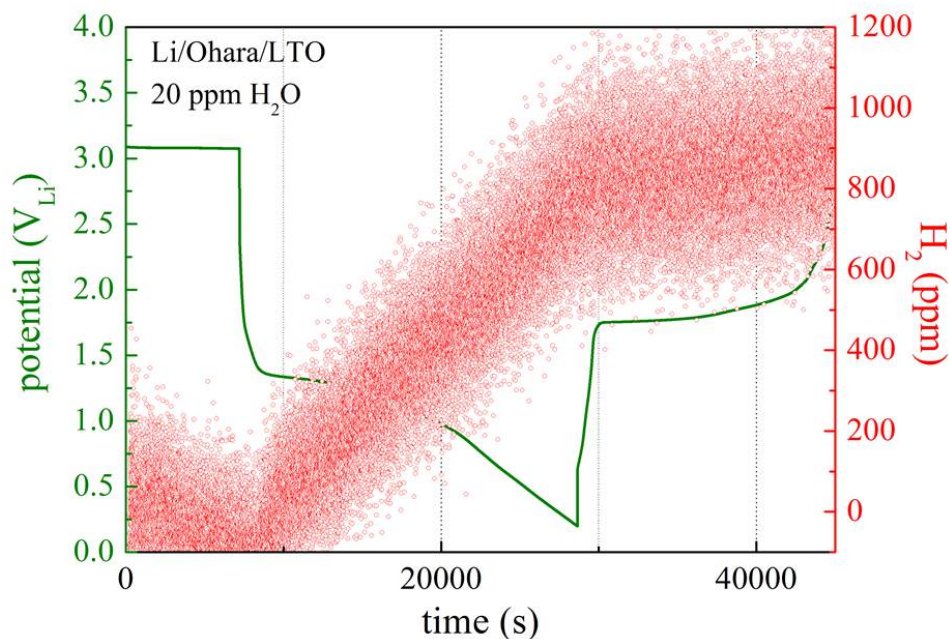
Figure 65: Fusion and Zoom of **Figure 64a)** and **b)**: Galvanostatic charge of a Li/LTO half cell (6.25 ± 0.15 mg$_{LTO}$/cm^2) at 0.22 mA/cm^2 using 1 M LiTFSI in EC/EMC 3/7 g/g with no water addition and real-time hydrogen gas concentration.

The following **Figure 64c)** and **d)** shows the characterization of a half cell containing 4 % of water. It is conspicuous that the charge capacity in **c)** is large and is amounting to ≈ 465 mAh/g$_{LTO}$ at 1.0 V$_{Li}$. Looking at the gas signals in **d)**, H$_2$ evolution initiates with reaching the redox-potential of LTO. In contrast to full cells, the H$_2$ concentration evolved in half cells is much higher and amounts to 67 μmol. One can explain the higher H$_2$ yield in half cells with the fact, that H$_2$ can be re-oxidized in full cells on the LFP cathode in full cells, whereby a smaller overall amount is evolved (see Pourbaix diagram in **Figure 63**). Looking at the the CO$_2$ trace, its concentration increases during the charging period and is subsequent consumed, shown with a decrease of the concentration. Due to high influence of the parasitic side-reaction, the discharge capacity is extremely low, as it was shown for full cells with 4 % added water. These investigations can be concluded as follows. The gas evolution of Li/LTO half cells is negligible small in water-free electrolytes. Gassing of cells with LTO electrodes occurs only during charge and discharge (Li$_7$Ti$_5$O$_{12}$ species is present), never during the preliminary OCV period when the LTO is pristine. This is consistent with results from literature [129,133]. If an electrolyte has a certain water content, the charging capacity increases combined with a lowered redox potential plateau, due to the mixed LTO- and H$_2$O-reduction-potential. The main gas component, which is evolved within the first cycle was H$_2$. In parallel, CO$_2$ is evolved, which is probably caused by hydroxide anions (OH$^-$) formed during the water reduction precess (see **Equation (20)**). As a result of this parasitic electrochemical reduction of water, charge of LTO lasts longer than expected on the basis

of its theoretical capacity. The amount of CO_2 decreases during the charging process. To explain the reactions leading to the evolved gases, one should have a look at the reaction mechanism of OH^--catalyzed decomposition of alkyl carbonates, which was described by Aurbach [32]. According to this, OH^--anions force a ring-opening reaction of cyclic carbonates like PC or EC, which leads to the formation of di-alcoholates and carbon dioxide evolution. These alcoholates can further react with evolved CO_2 while forming alkyl-carbonates with different chain-lengths [supporting information of [144]]. To proof this, LTO electrodes (pristine and charged in the different electrolytes) were analyzed by ATR-FTIR. IR absorption bands of the study of Freunberger et al. [144] match with those observed on LTO electrodes, which were charged in cell containing 4000 ppm and 4 % water (lines c) and d) in **Figure 66**). Typical IR-bands for insoluble lithium-alkylcarbonate oligomers with a typical formula of $LiO_2C(OC_2H_4)_nOCO_2Li$, whereby n = 1, 3 and 5) are 1650 cm^{-1}, 1450 cm^{-1}, 1330 cm^{-1}, and 1280 cm^{-1}. A complete analysis for all IR-bands were done and an overview of additional and important adsorption peaks, which were detected on the LTO electrodes, are listed in **Table 8**.
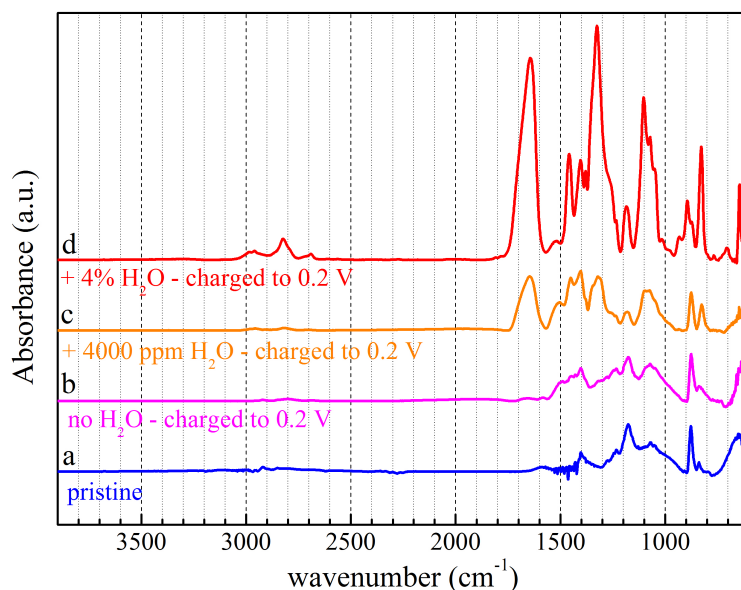
Figure 66: FTIR-ATR spectra from bottom to top of pristine and charged LTOelectrodes: a) pristine LTOelectrode (bottom blue line); b) in 1 M LiTFSI in EC/EMC 3/7 g/g (middle green line); c) in 1 M LiTFSI in EC/EMC 3/7 g/g + 4000 ppm H_2O (4th orange line) and d) in 1 M LiTFSI in EC/EMC 3/7 g/g + 4 % H_2O (top red line). All electrodes are supported on Celgard ® C480 and charged until 0.2 V_{Li} followed by washing each electrode with 10 mL acetonitrile and dried for 3 hours at 50°C under vacuum [138].

With an increase of the water content, the amount of deposited oligomers should in-

Table 8: ATR-FTIR bands of 66 [138].

wavelength [cm^{-1}]	Component	Comment	Ref.
2960 - 2850	-CH_3 & -CH_2-	stretching mode	[145]
1650	C=O	asymmetric stretching	[146]
1450	C=O	carbonyl vibrations	[144]
1400	PVDF	n.a.	[133]
1330	C=O	carbonyl vibrations	[144]
1280	O-C-O	carbonyl-oxygen stretching	[147]
1280	O-C-O	carbonyl-oxygen stretching	[147]
1185	PVDF	n.a.	[133]
1050	LTO	n.a.	[133]
876	PVDF	for normalization	[133]
830	PVDF	n.a.	[133]
658	LTO	Ti-O vibrations	[148]

crease. With the normalization of all bands to the PVDF band located at 876 cm^{-1} [133], it is possible to compare the intensity of all bands. Distinctive adsorption bands at 1650 cm^{-1} and 1330 cm^{-1} increase from line c) (4000 ppm H_2O) to line d) (4 % H_2O) dedicated to oligomer compounds. These bands are not detectable on pristine LTO electrodes a) and for LTO electrode charged without water additive b) (blue and magenta line, respectively). Based on this ATR-FTIR analysis, one can now explain the development of the CO_2 concentration within the first cycle using a water-containing electrolyte. CO_2 first increases to a certain or critical amount until only di-alcoholates have been produced. After reaching a peak concentration of di-alcoholates, oligomerization starts and subsequently CO_2 decreases, because CO_2 evolution coming from carbon corrosion reactions or EC/EMC oxidation with water becomes slower. All these processes and reactions are illustrated an reaction scheme in **Figure 67**. H_2 evolves due to a parasitic side reduction of H_2O, leading to a subsequent self-discharge of $Li_7Ti_5O_{12}$-species. A reduction of H_2O results in a formation of OH^--anions, which force a ring-opening reaction of EC under forming lithium di-alcoholates and gaseous CO_2 [32]. Under CO_2 consumption solid lithium oligomers are formed in the last step. These solid products form a passivation layer, contributing observed capacity and performance losses. In addition to that, the replacement of electrolyte in porous electrodes, due to gas bubble formation in water containing electrolytes, support this negative behavior. Surprisingly, adsorption bands of obvious products like LiOH or LiOH · H_2O, expected at ≈ 3700 cm^{-1} [137], are absent in the ATR-IR spectrum in **Figure 66**. These products might be expected from the reaction with Li^+, contained in the electrolyte, and OH^{-1}, formed in the one electron reduction reaction of water additive. IR absorption bands of Li_2CO_3 and those of the formed carbonate oligomers are mainly overlapping and are not distinguishable from each other (see supporting information [144]). Therefore, in addition, XRD analysis was
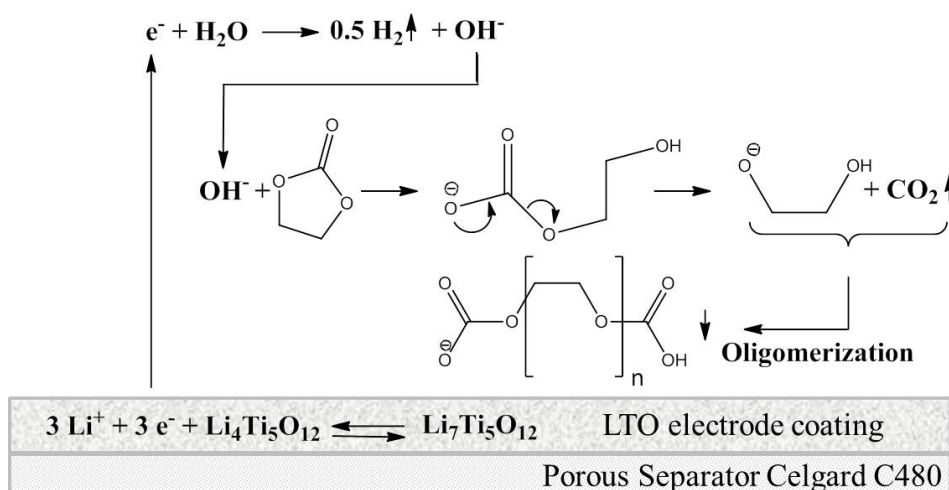
Figure 67: Schematic mechanism of reaction sequences concluding from experiments, post-mortem analysis of different LTO electrodes and data from literature [138].

performed in air-tight cell to double-check this observation and to confirm the proposed mechanism in **Figure 67**. If one have a look at the XRD pattern, neither peaks for LiOH (magenta) and LiOH · H_2O (light green) nor Li_2CO_3 (dark green) are observed in **Figure 68**. Subsequently, a reaction of OH^--anions with Li^+-cations forming LiOH will not take place, rather the ring-opening reaction of OH^--anions with cyclic carbonates seems to be the thermodynamically favored reaction and prevents beside a formation of LiOH or LiOH · H_2O also a further reaction of these products with CO_2 to Li_2CO_3. These products are solid and not soluble in the electrolyte and would precipitate on LTO anodes.

The given analysis leads to conclusion that cells with LTO anodes and the presence of water tend to substantial gassing, where H_2 is the main gas component. However, the last remaining question is, how one can rationalize the amount of evolved hydrogen of cells with LTO anodes as reported in literature [123, 124, 129–131, 133]. In these published experiments, the amount of produced H_2 can be either explained by a certain water content of used electrolytes and electrodes or by continuous permeation of water molecules through the cell sealing. The latter case can be examined by evaluating the gas permeation rate through the polymer sealing (mostly poly-propylene, PP) of pouch-bag cells. The continuous permeation through the lamination sealing of pouch bag cell could represent a key aspect leading to the water intrusion and the resulting swelling of pouch cells. Considering the typical material used for sealing pouch cells and its dimension, one could calculate the continuous flux of water vapor in a certain time period. In this example we compare the calculated flux of water and the corresponding H_2 evolution by reaction at the LTO electrode with the experimental results given by Wu et al. [133]. They described experiments using a 383450 pouch cell , with an approximate polypropylene sealing perimeter of 17 cm and a seal thickness of 45 μm (corresponding
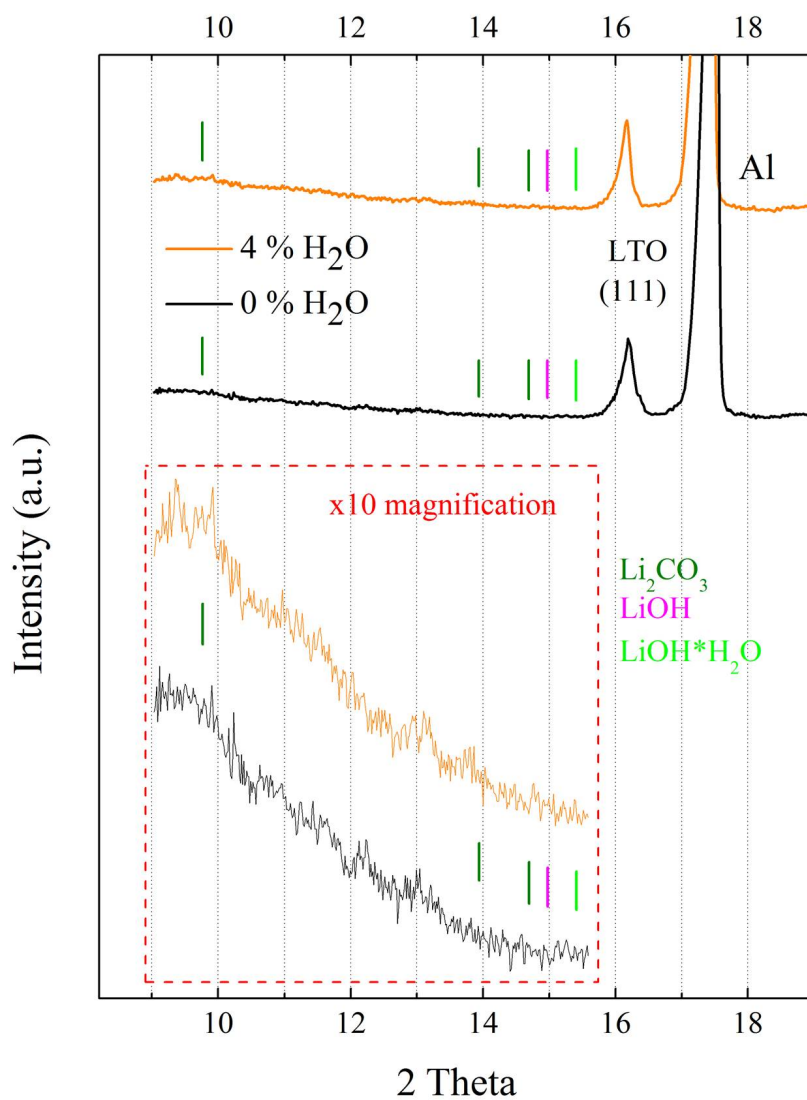
Figure 68: X-ray diffraction pattern of LTO electrodes from disassembled Li/LTO half cells, which were charged in electrolyte without added water (black) and in electrolyte with 4 % water (orange) to a cut-off potential of 0.2 V_{Li}. Cells were disassembled in an argon filled glovebox and reassembled in an air-tight X-ray sample holder with aluminum foil windows. The positions of the diffraction lines for Li_2CO_3, LiOH, and LiOH · H_2O are indicated by the short vertical lines, dark green magenta and light green, respectively. For a refinement, the intensity of reflexes in the mentioned area of 2 Theta angle values was enlarged [138].

Table 9: Estimated water permeability values through poly propylene sealing in terms of standard cm^3 (cm^3_{STP} evaluated at 1 atmosphere and 25°C) as a function of temperature obtained from [149] and **Equation (28)**.

Temperature [°C]	Permeability [cm^3_{STP} cm s^{-1} cm^{-2} Pa^{-1}]
25	25 x 10^{-13}
55	105 x 10^{-13}
80	300 x 10^{-13}

to a seal cross section of ≈ 0.077 cm^2), and with a sealing frame with a width of 6 mm. Using comparable values for water vapor diffusion through polypropylene (PP) at different temperatures [35] and **Equation (28)**, one can estimate a water diffusion rate at different temperatures. Whereby ρ corresponds to the water vapor flux in cm^3_{STP}/s through the PP sealing, $K_{PP\ foil}$ is the value for water vapor permeability at different temperatures, $A_{PP\ foil}$ is the area of the sealing weld, Δp the difference of water partial pressure from outside and inside and finally $w_{PP\ foil}$ is the width of the sealing frame.

$$\rho = K_{PP\ foil} \cdot \frac{A_{PP\ foil} \cdot \Delta p}{w_{PP\ foil}} \tag{28}$$

The molar flux of water across the seals based on a permeability of 300x10^{-13} cm^3_{STP} cm s^{-1} cm^{-2} Pa^{-1} at 80°C (see **Table 9**) amounts to ≈ 6.2x10^{-9} cm^3_{STP}/s ($\equiv 2.5$x10^{-13} mol/s) considering an estimated water vapor pressure of ≈ 16 mbar or ≈ 1600 Pa (corresponding to 50% relative humidity in ambient air at 25°C). According to these values and the given equation, the estimated amount of water vapor permeation through the sealing weld of pouch-cells within 120 h cycling at 80°C [133] is ≈ 0.003 cm^3_{STP}. Unfortunately, this value is more than three orders of magnitude lower than experimental values of ≈ 10 cm^3_{STP} observed by Wu et al. [133]. Furthermore, the coefficient for H_2 permeability through PP is ≈ 2 times lager than that for H_2O [150], concluding that H_2 would permeate out of the cell at a faster rate than water and could not lead to a pouch-cell inflation. Therefore, it is not possible that water permeation through the sealing cause the huge amount of H_2 gas evolved, that is why, a certain amount of water would have to be already inside the cell *e.g.* water content of poorly dried electrodes or cell components, or is produced inside the cell while cycling. The investigated cells of Wu et al. [133] contained 3.3 g of electrolyte and 4 g of electrode material, whereby a total amount of only ≈ 0.8 mmol H_2O (≈ 2100 ppm) is necessary and would have to be in the cell for the observed H_2 evolution of ≈ 10 cm^3_{STP}. Considering that, most likely, the total water amount was contained only in the electrodes, this would be equal to a water content of 0.4 wt.%. This amount could be possible in the case that electrodes were not dried properly, or stored and assembled under ambient atmosphere. And, in fact, a closer look into literature, which was introduced in the upper part of this chapter, cycle-/

and shelf-life data of LTO containing pouch bag cells show a strikingly different gassing behavior. For example, Wu et al. [124] reported a gas evolution in LTO/NMC cells, where H_2 was the main gas component, and a capacity loss of 20 % within 120 hours of a cycling rate of 10C. On the other hand, Belharouak et al. [132] do not detect gases and observe a capacity loss of only 5 % of LTO/LMO cells, when cells are cycled at 6 C in a comparable time period. A reason for these contradictory results might be preparative differences for electrode drying or cell assembly. And indeed, comparing gassing behavior and capacity fading, cells, which where specified assembled in a glove-box or dry room [39, 118, 132], showed a much better performance without gas evolution than those, which were not specified [123, 124, 129, 133] and no detailed assembling procedure was given. In all those articles, H_2 was the main gas component. This fact is just a hint for the reason of the gassing behavior of LTO cells and not a proof that cell components are not proper dried or water was introduced during the assembling procedure. Another fact, which one cannot neglect, is that water is one of the most abundant degradation products, which are formed in non-aqueous electrolytes, especially as product coming from anodic oxidation reaction at higher potentials. In this case one should announce that alkyl-carbonates and glymes form water in the presence of oxygen at high anodic potentials. A previous report shows significant amount of water formed in lithium-air cells cycled to > 4.5 V_{Li} in DME [151] and in EC/EMC [152]; but, note that these experiments were performed in an oxygen atmosphere.

However, the formation of water in an anodic oxidation process in alkyl carbonates is very likely, especially at elevated potentials. If one combines LTO anodes with high voltage cathodes *e.g.* spinels like LMO or oxides like NMC, water could be produced during electrolyte decomposition, which would get reduced on the LTO anode, following the mechanism, which was shown from results of the previous experiments.

6.5.5. Conclusions

In this chapter, the investigation on the gassing behavior of LTO anodes in full and half cells was shown. Evolved gases of LTO based cells using electrolytes with different water content (20 ppm, 4000 ppm and 4 %) were analyzed *in-operando* by on-line electrochemical mass spectrometry (OEMS) during the first charge and discharge cycle at a rate of C/5. OEMS results show that H_2 and CO_2 are the main evolved gases, which is in accord with the relevant literature. However, cells, which were assembled using a nominally water-free electrolyte show a negligible gas evolution upon the charge and discharge cycle. This is in contrast to the substantial H_2 and CO_2 evolution in cells built using water containing electrolyte. A gas evolution could only be detected when LTO based cells are held in the charged state (or are being charged), but never prior to charging in an initial OCV step. This led to the conclusion that electrochemical reduction of water occur at LTO surfaces forming hydrogen gas and hydroxide anions. This one-electron reduction reaction is responsible for observed hydrogen gassing, which is confirming the

hypothesis reported by Belharouk et al. [123] that trace water reduction is the reason for H_2 evolution. Therefore, the occasionally reported gassing of battery cells with LTO anodes can be caused by the residual water content in poorly dried electrodes and separators, by water intrusion during cell assembly in ambient air, or by water formed by the anodic oxidation of electrolyte solvents when high voltage cathode materials, like LMO or NMC, are used. Consequently, careful drying of cell components and cell assembly under dry conditions as well as tuning the electrolyte anodic stability at high potentials, are key aspects to ensure long cycle life of LTO based batteries. The shown mechanism demonstrated that water triggers/catalyzes several parasitic reactions. Moreover, online mass spectrometry in combination with ex-situ analysis methods like ATR-FTIR and XRD one could show that OH^- anions, which were produced in the electrochemical reduction step of H_2O, cause a ring opening reaction of cyclic carbonates like EC. This parasitic reaction leads to a CO_2 evolution and to the formation of lithium alkyl carbonate oligomers. The latter deposit as a clogging passivation layer on the LTO anode and leading to a hindered lithium-ion transport and, subsequently, to a strong capacity loss.

At this point, one may ask the question, whether these observation of H_2 and CO_2 evolution and the resulting product formation could also be made on graphite electrodes. Since excessive gassing over a longer time period while cycling or storage is typically not observed with graphite anodes, it is possible that the protective SEI layer, which is formed on graphite anod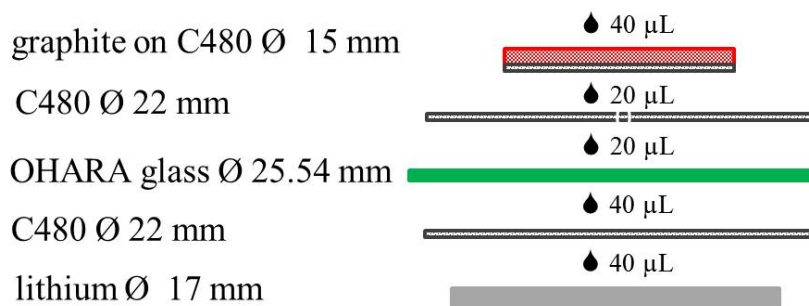es, sufficiently suppresses the kinetics of water reduction. A detailed study about this continuative issue is shown in the **Chapter 6.6**.

6.6. Gas Evolution of Graphite Anodes in H$_2$O-contaminated Electrolyte

6.6.1. Abstract

From gassing studies with lithium titanate (LTO) as anode material it is shown by previous research, that trace water can play an important role in terms of gas evolution during cycling [138], like proposed by I. Belharouk et al. in 2011 [123]. Theoretically, graphite anodes should show a different behavior. A hypothesis by Wu et al. was, that gas evolution is strongly potential dependent and a loss of solid electrolyte interface (SEI) protection at elevated redox potentials, like it is the case for LTO anodes, is accountable for gas evolution of H$_2$ and CO$_2$ [133]. This is leading to the assumption that if a protective SEI layer is formed during the formation of a battery at slow rates, the electrode is protected against further reduction reactions on its surface. For studying the gassing behavior of graphite anodes during and after SEI formation, a special *two-compartment* cell set-up was used to investigate these phenomena. The same cell arrangement was already used in the study introduced in **Chapter 6.5** and [138].
In the following study, graphite half cells are investigated by On-Line Electrochemical Mass Spectrometry (OEMS) using different electrolytes and 4000 ppm H$_2$O as additive. We could show that pre cycling of a graphite electrode in a water-free environment, before the addition of water, can reduce the total H$_2$ gas formation by a factor of 5 after re-assembling with water containing electrolyte. This phenomenon is explained by the formation of a stable SEI layer during the formation process. The quality of the SEI is depending on the type of electrolyte and its SEI-supporting additives.

6.6.2. Introduction

Today's lithium-ion batteries, which are available on the market, often consist of different electrode combinations with graphite anodes. Graphite electrodes are known to have an irreversible capacity loss within the first charge while lithium-ion intercalation into the graphite layered structure. The capacity loss is explained by the reduction reaction of electrolyte components on the anode surface, which irreversibly consumes lithium-ions and form a protective and passivation layer, called solid-electrolyte interphase (SEI) on the negative electrode. On the one hand, the SEI inhibits further reduction reactions on the anode surface by its electronically insulating nature, on the other hand it is on the one hand still permeable for lithium-ions and is thus no obstacle to the intercalation chemistry [20, 153–159]. The SEI formation process is not fully understood, yet [157]. The gaseous components, which are formed during electrolyte reduction on graphite anodes, are ethylene (C$_2$H$_4$) or other hydro carbons like propylene (depending on the cyclic carbonate, which is used in the electrolyte mixture) and hydrogen [123, 155, 160, 161]]. Furthermore, organic radicals, oligomers and polymers can be formed [162]. Recent work by the group of Brett Lucht showed that lithium ethylene carbonate (LECD) and LiF are the main constituents of the SEI layer, when an ethylene carbonate (EC) based

128

electrolytes are used, whereby the sort of the conductive salt plays no role [153, 163]. However, no carbon dioxide (CO_2) formation can be observed during SEI formation [159]. In contrast, additives like, *e.g.*, CO_2 are used as reactive additives, which are easily reducible, to support the formation of SEI layer on graphite anodes. Other additives, which allow a good modification of electrolytes in terms of SEI formation, are known to be unsaturated carbonates like vinylene carbonate (VC) and SO_2 [161, 164]. In contrast, the conductive lithium salt of the electrolyte has no influence on the SEI forming procedure [153, 163]. If one replaces the graphite anode with a lithium titanate $Li_4Ti_5O_{12}$ (LTO) electrode, the operating redox potential of the anode is increased to 1.55 V_{Li} [40, 121]. The elevated redox potential leads for example to negligible rates of electrolyte reduction, and, therefore, almost no SEI formation on the negative electrode. One of the main differences between the use of graphite and LTO anodes, is the fact, that LTO containing lithium-ion pouch bag cells tend to swell after several cycles or during storage in the charged state ("gassing"), whereby the main gas component is H_2 ($\approx$ 50 wt%) [124, 129, 132, 133]. However, pouch cells containing graphite electrodes do not show a gassing behavior. There are several in-situ gassing studies of graphite anodes examined with differential electrochemical mass spectrometry (DEMS). The first study was performed by R. Imhof and P. Novak in 1998 [160]. They found that during SEI formation in an EC/DMC containing electrolyte ethylene gas was evolved in a potential window between 0.8 and 0.3 V_{Li}. Hydrogen was formed as by-product of water traces, which starts to evolve at potentials around 1.3 V_{Li}. In addition, they postulate, that an SEI-layer, which was formed under "wet" conditions (water additive into the electrolyte), has a poor quality. One year later F. Joho et al. [157] performed DEMS measurements on graphite half cells in the presence of water with different concentrations (250 ppm, 1000 ppm and 4000 ppm H_2O). They observed that the amount of ethylene (m/z = 27) drops with elevated water concentrations and is also shifted to lower potentials. According to their assumption, water influences the SEI formation procedure and the protective layer is built differently. In addition, the amount of hydrogen increases with increasing water content. P. Novak investigated in 1999 that CO_2 is not a product of electrolyte reduction in the SEI formation process [159]. The latest DEMS study on graphite electrodes was performed in 2001 by M. Lanz and P. Novak [155]. They confirmed again the type of evolved gases, namely ethylene and hydrogen, during SEI formation. In addition, they postulated, that on thick electrodes ($\approx$75-100 μm) the SEI formation process is not completed after the first charge and discharge cycle.

At this point, one may ask the question, whether the observed H_2 evolution and the resulting product formation in LTO containing cells [138], could also be observed on graphite electrodes. Since excessive gassing over a longer time period while cycling or storage is typically not observed with graphite anodes [123]. It is possible that the protective SEI layer, which is formed on graphite anodes at lower potentials [124], sufficiently suppresses the kinetics of water reduction.

With this study we want to continue the study on LTO gassing (reported in **Chapter 6.5** and [138]) and investigate the effect of a protective SEI layer in combination

with water-containing electrolytes. We use On-Line Electrochemical Mass Spectrometry (OEMS) to examine the evolved gases in different graphite half cells upon applying a cyclic voltammetry (CV) procedure. We focus on the comparison between gas evolution of pristine and pre cycled graphite electrodes, respectively, in a water-containing electrolyte (4000 ppm H_2O). The pre cycling was performed in different water-free electrolytes, a model electrolyte and a commercial one with 2% Vc. Based on the results shown below, we propose that an intact SEI layer is able to inhibit water reduction reaction on the graphite surface during charge and provide a good protection against cell swelling over a longer time period.

6.6.3. Experimental Part

The graphite electrodes were prepared by mixing Graphite SLP30 powder (Timcal®) and Pvdf (Kynar, HSV900) at a 90/10 weight ratio in a Thinky mixer (2000 rpm, 5 min, 50 mbar) with N methyl-pyrrolidone (2.2 mL Nmp per gram of solids). The resulting inks were blade-coated at a wet film thickness of 150 μm using an automatic coater (RK Print, Germany) (at the speed mode 1) onto a porous Celgard® C480 separator. This allows electrolyte access and gas diffusion from both sides of the graphite electrode, a prerequisite for measurements with the OEMS system to get a stable signal. Afterwards, the coating was dried in ambient atmosphere on a hot plate held at 60°C overnight. After drying, electrodes with a diameter of 15 mm were punched and again dried for 12 hours at 90°C under dynamic vacuum in a Büchi (Switzerland) glass oven. Subsequently, the electrodes were transferred into an Ar filled glovebox (MBraun, Germany, < 0.1 ppm O_2 and H_2O) without further contact with ambient air. The average graphite loadings were 5.82 ± 0.31 $mg_{SLP30}cm^{-2}$ (1C = 2.09 mAhcm^{-2}).

For all OEMS experiments a 1 M LiTFSI in Ec/Emc (3/7 g/g ratio) electrolyte was used with and without addition of 4000 ppm H_2O. LiTFSI was chosen instead of the more common LiPF$_6$ to avoid parasitic reactions caused by side reactions of the PF$_6^-$ anion with trace water. A main product of this reaction is gaseous HF beside solid LiF [12, 134, 135]. With the replacement of the conductive salt, uncontrollable degradation reactions caused by water contamination could be studied without any interference from side reaction coming from the salt. For the electrolyte LiTFSI was dried under dynamic vacuum in a Büchi (Switzerland) glass oven at 120°C for not less than 24 h before use. Anhydrous ethylene carbonate (Sigma-Aldrich, 99%) was used for the mixture as received. The liquid ethyl methyl carbonate (Emc) (Aldrich, 99%) was dried over molecular sieves (Sylobead MS 564 C, 3 Å, Grace Division) for at least three days prior to electrolyte preparation. The overall water content of the initial electrolyte without added water was less than 20 ppm (Karl-Fischer-Titration, Analytics). In addition, for some selected pre formation experiments of graphite half cells an electrolyte consisting of 1 M LiPF$_6$ in Ec/Emc (3/7 g/g ratio) with and without 2% vinylene carbonate (Vc) (LP57 and LP 572; provided by BASF SE) was employed. After preparation, electrolyte mixtures were stored in the glovebox. To determine the effect of water reduction on

graphite on C480 Ø 15 mm
C480 Ø 22 mm
OHARA glass Ø 25.54 mm
C480 Ø 22 mm
lithium Ø 17 mm

40 µL
20 µL
20 µL
40 µL
40 µL

Figure 69: Schematic set-up of a *two-compartment* test cell to investigate graphite gassing behavior [165].

graphite electrodes, a LiTFSI containing electrolyte with nominally 4000 ppm of H_2O was prepared by adding 0.22 mmol/mL of H_2O to the standard electrolyte mixture.

To perform electrochemical tests a special cell hardware ($\approx$ 9.5 cm^3 internal volume), which is discussed in our previous work [52] was used. In **Figure 69** one can see the schematic cell set-up.

This *two-compartment* test cell consists of a 316Ti SS anode current collector bottom part. At the cathode side a stainless steel mesh current collector is used, which is connected with a 316L SS compression spring to the upper cell body. Both, the top and the bottom part are separated by a Kel-F spacer. With two Teflon O-rings the sealing of the system is ensured. For OEMS measurements, the cell is equipped with a capillary leak to the mass spectrometer (see [52, 138] for further details). For a *two-compartment* set-up, a Li$^+$-ion conductive glass ceramic (Ohara, Japan) was placed between the separator sheets, in order to avoid side reactions of added water with the metallic lithium on the anode side (0.45 mm thick foil; Rockwood Lithium). To protect the Ohara glass from reactions with metallic lithium, it is sandwiched between two Celgard $^®$ separator foils placed onto the lithium metal and the graphite working electrode. During cell assembly, a lithium metal disk with 17 mm diameter is placed onto the bottom part, which is used as counter and reference electrode. 40 µL of electrolyte was placed on the lithium and was then covered with a 22 mm diameter Celgard $^®$ C480 separator. Again 40 µL of electrolyte was added. On the separator the Ohara glass was placed and the added amount of electrolyte changes from 40 µL to 20 µL. To protect the Ohara glass from dendrites formed on the graphite electrode a second Celgard $^®$ was placed on the Ohara glass, following by the graphite working electrode. The cell assembly is performed in an Ar filled glove box. Further assembling details are given in **Chapter 5.5.2**.

Also in this study, the evolved gases from graphite-cells were analyzed using on-line electrochemical mass spectrometry (OEMS) [52, 138]. For quantification of gas evolution rates from graphite electrodes by OEMS, a second calibration gas containing H_2, C_2H_4, O_2 and CO_2 in argon was used (2000 ppm each; Westfalen AG, Germany). As in **Chapter 6.5** and [138] described, the signals of the ion current detected by the mass spectrometer can be translated into concentrations in parts per million (ppm) and

derived to obtain evolution rates in parts per million per second (ppm/s). With the calibration gas we can quantify the gas evolution of H_2 (m/z = 2), C_2H_4 (m/z = 28, 27, 26) and CO_2 (m/z = 44, 28, 16, 12). Based on earlier publications, ethylene (m/z = 28, 27, 26) is known to be one of the main decomposition products of electrolyte reduction during the SEI-formation between 0.8 and 0.6 V_{Li} [32, 159, 160]. For the quantitative calculations in our experiments one must consider the elevated background at the m/z values for C_2H_4 resulting from the EMC used as solvent. To analyze the evolved C_2H_4 amount, in every measurement m/z = 26 was used, because quantification of m/z = 27 and 28 are not fully reliable due to interference from mainly CO_2 and also CO.

Graphite cells were electrochemically analyzed by cyclic voltammetry (CV) using a Gamry multi-potentiostat at a scan rate of 0.5 mV/s in a potential window of 0 to 1.5 V_{Li}. Several electrodes were cycled for pre formation with a MACCOR Series 4000 at a rate of C/10 for three and ten times, respectively, using a constant current/constant voltage (CCCV) charge and CC discharge procedure. The chosen potential window for the pre formation step was from 0.01 to 1.5 V_{Li}.The rate was calculated with respect to the theoretical capacity of the SLP30 electrode (360 mAh/g), which corresponds to an average current density of 0.21 mA/cm² or an absolute current of 0.37 mA at C/10. Electrochemical measurements at the MACCOR and OEMS were performed after a 2 h rest at OCV (open circuit voltage) for background stabilization, whereby the OCV step is not shown in the CV and OEMS spectra. Time 0 h means the start of the CV cycling. The OCV was used for system stabilization and no gas evolution was detected during this prior step.

For potentiostatic electrochemical impedance spectroscopy (PEIS) on graphite SLP30 half cells, a stainless steel Swagelok ® T-fitting was used as three-electrode test cell body. he graphite (working electrode, WE) half cell was cycled at a Biologic VMP3 multipotentiostat in a potential window between 0.01 and 1.5 V_{Li} at a rate of C/10, as well. After each cycle a PEIS of the WE was recorded in a frequency range of 800 kHz to 100 mHz and an amplitude of 10 mV at the discharged state at 1.5 V_{Li} . The T-cell was assembled with metallic lithium as a counter (CE) and reference electrode (RE), respectively. As separator, three VWR ® glass fiber pads were used as separator and 120 μL of 1 M $LiPF_6$ in EC/EMC (3/7 g/g) with and without 2% VC (LP57 and LP572, both provided by BASF SE) as electrolyte, respectively. The schematic set-up of the three-electrode T-cell is shown in **Figure 70**. With this method it was possible to record the change of the charge frequency resistance (CTR) (value of low frequency resistance (LFR) minus high frequency resistance (HFR)) of the graphite electrode after several charge and discharge cycles. A raise of the LFR value could be assigned to the formation of a thick and stable SEI. In comparison, graphite electrodes with lower LFR values possess a thin and less stable SEI.
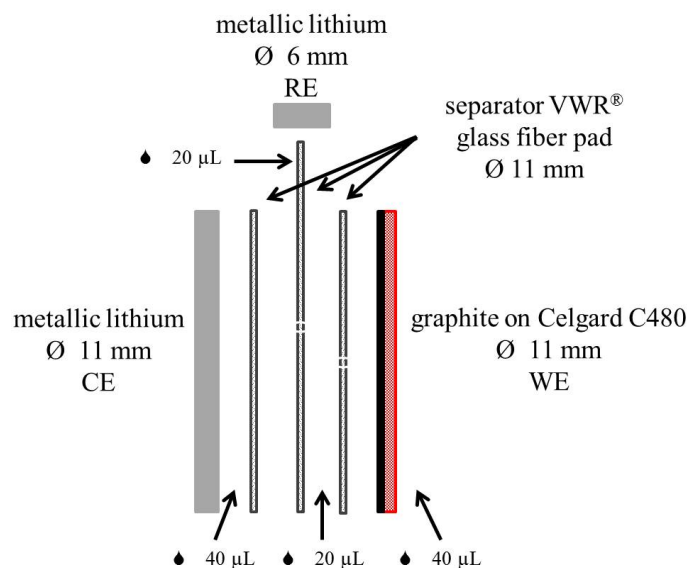
Figure 70: Schematic interior of a Swagelok ® T-fitting used for PEIS measurements of the SEI formation on graphite SLP30. The total amount of electrolyte was 120 μL placed on the marked components. Graphite was used as a working electrode, whereby metallic lithium was used as counter and reference electrode, respectively [165].

6.6.4. Results and Discussion

To demonstrate that the cell design with the Ohara glass protection works in a proper way for cycling graphite half cells, **Figure 71** shows the specific profile of a graphite half cell [3, 166]. In the first charge (blue), thereby the total capacity is slightly higher (≈ 375 mAh/g$_{SLP30}$) than the theoretical value (≈ 360 mAh/g$_{SLP30}$), which is assigned to parasitic electrolyte reduction reactions. The charging profiles for the second and third cycle (red and orange, respectively) are equal and the charge capacity is located at ≈ 355 mAh/g$_{SLP30}$. The profiles for all three discharge cycles are also overlapping, reaching a reversible discharge capacity of ≈ 350 mAh/g$_{SLP30}$. To conclude, the cell design is suitable for the measurement with graphite electrodes. However, cyclic voltammetry was chosen as electrochemical method for OEMS experiments instead of the galvanostatic cycling. This can be justified with the low intensity of the ion current signals during the OEMS measurements at slow C-rates (C/10), which are, unfortunately, necessary to cycle graphite half cells with Ohara glass in a proper way and to reach the specific capacity. If one uses a small cycling current on the OEMS, the signals of the mass traces are not well defined and noisy, which would make a complete data treatment and calibration impossible. For that reason, we decided to use the CV method at a scan rate of 0.5 mV/s, with this method it was possible to follow the relevant gas traces and to evaluate the amount and rate of evolved gases in a reliable way. In the beginning, the formation process of a pristine graphite electrode was under investigation to validate the method in comparison to results published in literature [123, 155, 157, 159, 160, 162, 167].
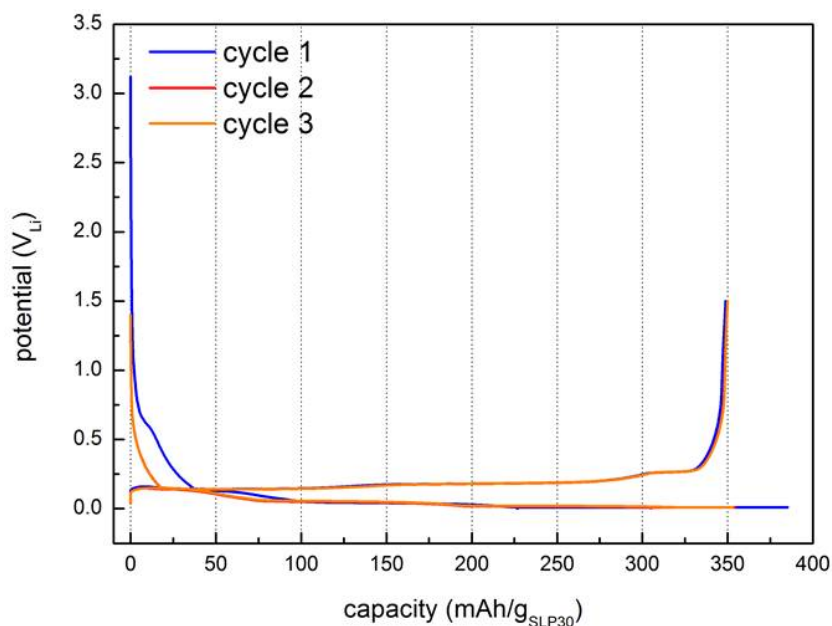
Figure 71: Proof of method: Characteristic charge and discharge profile of SLP30 graphite (loading: 5.36 mg_{SLP30}/cm^2) in a half cell set-up in a *two-compartment* cell design at a rate of C/10 (0.193 mA/cm^2) in initial water-free electrolyte for three cycles in a potential window of 0.01 V_{Li} to 1.5 V_{Li} with a CCCV (constant current, constant voltage) charging and CC discharge procedure [165].

Traces for all gases remain at zero ppm during the OCV period (not displayed in **Figure 72**). With the start of the first cycle (magenta) of the cyclic voltammogram, C_2H_4 (green) starts to evolve at potentials lower than 0.8 V_{Li}. With the shoulder of the CV at around 0.5 V_{Li} the C_2H_4 evolution rate reaches the highest value of 1.8 ppm/s and a total amount of $\approx$ 2000 ppm is released. As C_2H_4 is being evolved, CO_2 (blue) gets consumed ($\approx$ 200 ppm). This can be explained by the fact that CO_2 is known to be incorporated into the SEI formation [153]. The small amount of CO_2 consumption is possible, due to a certain concentration of CO_2 in the glovebox atmosphere that is also present in the head space volume of the cell. Besides this, also a very small amount of 250 ppm H_2 (red) is evolved, corresponding to 0.09 μmol_{H2}. This is around double than expected from the theoretic water content of only 0.09 μmol_{H2O} (calculated by dividing ppm-values with molar gas volume at 25°C (24.5 L/mol) and multiplying by the cell volume of 9.5 mL), shown in **Table 10**. This is around double than expected from the theoretic water content of only 0.1 μmol_{H2O}, which can evolve 0.045 μmol_{H2}, considering a one-electron reduction reaction of water. The conversation of one mole of H_2O to form 0.5 moles of H_2 is shown in **Equation (20)** [138, 159–161]. The increased hydrogen amount can result from not properly dried cell components like electrodes or separator foils. In the following two cycles of the CV, no further gas evolution is detectable. Over the whole formation process no CO_2 evolution is detectable, which is in agreement with data from literature [159].

134
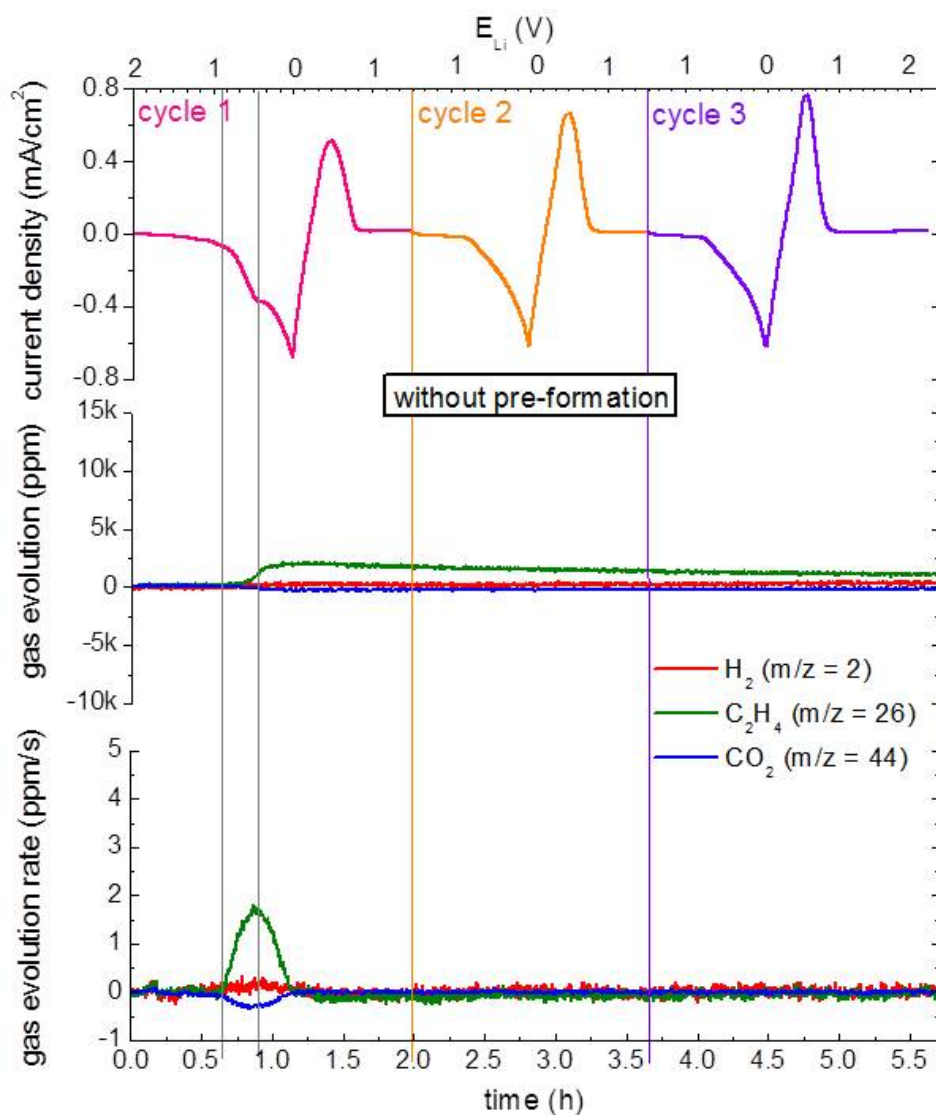
Figure 72: Formation behavior of a pristine SLP30 graphite electrode assembled in a two-compartment half cell with a water-free electrolyte 1 M LiTFSI in EC/EMC 3/7 g/g (20 ppm H_2O). The upper panel displays 3 cycles of a cyclic voltammogram starting after 2 h of OCV (OCV step not displayed) between 0 V_{Li} and 1.5 V_{Li} at a scan rate 0.5 mV/s. In the middle panel, *in-operando* gas evolution [ppm] and in the bottom part in-operando gas evolution rate [pmm/s] is plotted for the gases H_2 (m/z = 2), C_2H_4 (m/z = 26) and CO_2 (m/z = 44).[165].

If one compares this to a pristine graphite cell, which was cycled with a water containing electrolyte (1 M LiTFSI in Ec/Emc 3/7 g/g with 4000 ppm H_2O), one can see that the behavior of the graphite electrode is comparable to that previously shown for LTO anodes (see **Figure 73**). Again, no gas is evolved during the 2 h OCV step. Lowering the potential to 1.5 V_{Li} or less, H_2 starts to evolve - the total amount after the first cycle is $\approx$ 8000 ppm. The C_2H_4 evolution is shifted to about 100 mV lower potential and starts at 0.7 V_{Li}. After formation the total ethylene (green) amount is quantified to be 1700 ppm. Both observations, namely that the higher water content leads to reduced ethylene evolution during the first cycle and that water shifts the ethylene evolution to lower potentials, have been reported in the literature [160]. Prior to the H_2 evolution, the trace for CO_2 increases and subsequently gets consumed. The earlier CO_2 evolution can be explained by a decomposition reaction of organic carbonates with trace water. Linear carbonates, as well as cyclic carbonates, can react with trace water. These products of this hydrolysis reaction are CO_2 and alkyl alcoholates, which is shown in the **Equation (74)** [168, 169].

However, it needs also to be considered that water follows an auto-protolysis in the self-ionization reaction forming protons and hydroxide anions [152, 170]. As it is already known from literature, hydroxide anions can cause a ring opening reaction of cyclic carbonates (shown in **Equation (75)a)** and **b)**) under formation of alkyl di-alcoholates and CO_2 [32, 58]. Further CO_2 evolution finally comes from the main OH^- formation during water reduction reaction, which further drive the ring-opening shown in **Equation (75)b)** of ethylene carbonate and its subsequent consumption due to oligomerization of formed di-alcoholates with CO_2 to carbonated lithium oligomers, as shown and characterized in the previous LTO-study (see **Equation (76)b)**) [138]. We also assume that another reason for the foregoing CO_2 evolution is the reaction of surface functional groups of graphite (e.g. -CO and -OH) forming CO_2 in the beginning of the charging step. In the following cycles, no ethylene is evolved. However, the H_2 and CO_2 traces further increase stepwise during each charging step. The amount of H_2 released is highest for the first cycle and decreases in the subsequent cycles. The total amount of evolved H_2 reaches 12500 ppm corresponding to 4.9 μmol_{H2}. The theoretically possible amount is 9 μmol_{H2} (see **Table 10**), based on the fact that 4000 ppm H_2O are present in the electrolyte.

A further step in this study is to pre-cycle graphite electrodes to form a protective SEI-layer on the surface. For this reason a graphite electrode was cycled in the initial water-free electrolyte at a rate of C/10 (CCCV) for 3 cycles in a potential window of 0.01 to 1.5 V_{Li}. The pre-cycled cell was disassembled inside the glove box and the extracted electrode was washed in 5 mL Emc to remove old electrolyte. Afterwards the Emc was evaporated for 30 min inside the glovebox. The washed electrode was then re-assembled in the OEMS cell with water-containing electrolyte. The behavior of an electrode after pre formation is shown in **Figure 77**. Clearly visible in the bottom CV plot is that the shoulder at 0.5 V_{Li} and the evolution of ethylene gas is not absent. This is obvious evidence, that the formation is not fully completed. However, no CO_2 is evolved within
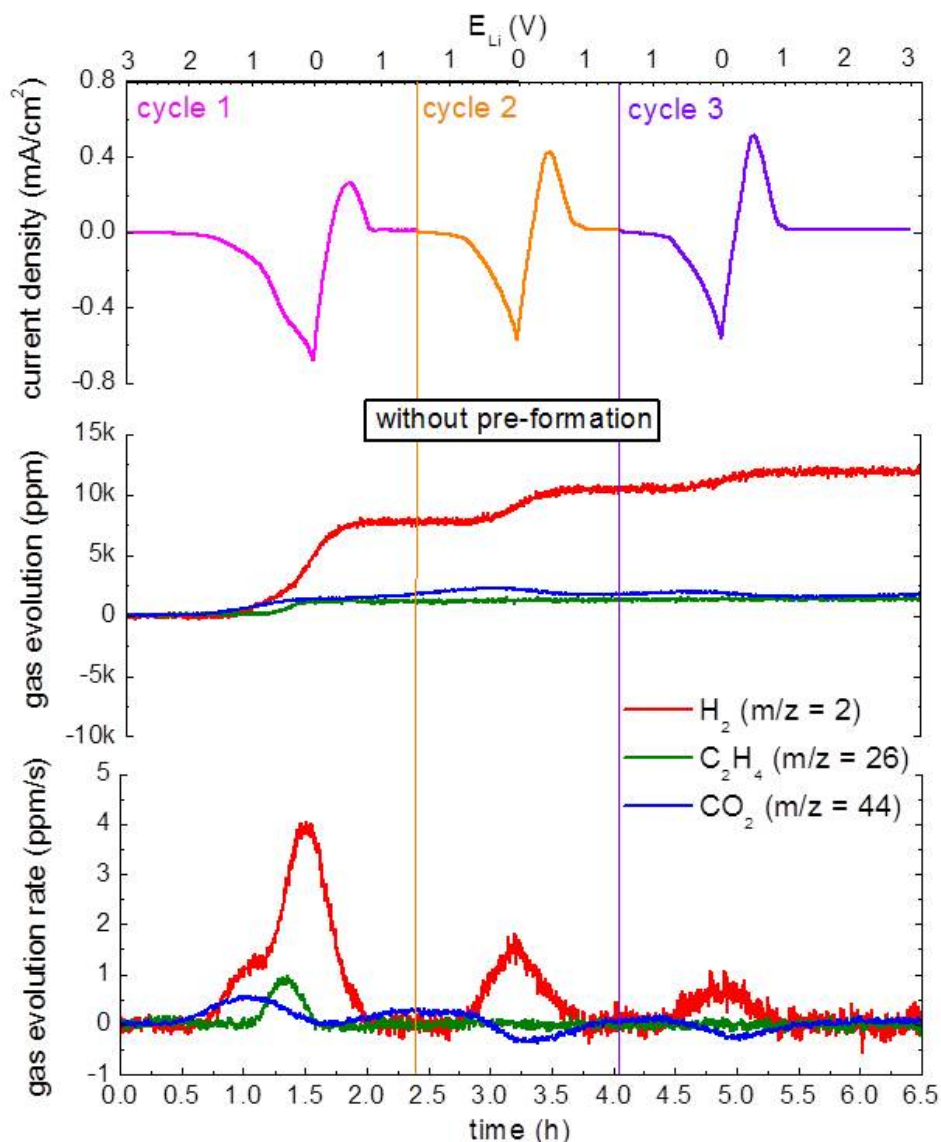
Figure 73: Formation behavior of a pristine SLP30 graphite electrode assembled in a *two-compartment* half cell with 1 M LiTFSI in Ec/Emc 3/7 g/g with 4000 ppm H_2O as additive. The upper part is displaying 3 cycles of a cyclic voltammetry starting after 2 h of rest at OCV (OCV step not displayed) to 0 V_{Li} at a scan rate of 0.5 mV/s. In the middle part, *in-operando* gas evolution [ppm] and in the bottom part *in-operando* gas evolution rate [pmm/s] is plotted for H_2 (m/z = 2), C_2H_4 (m/z = 26) and CO_2 (m/z = 44) [165].
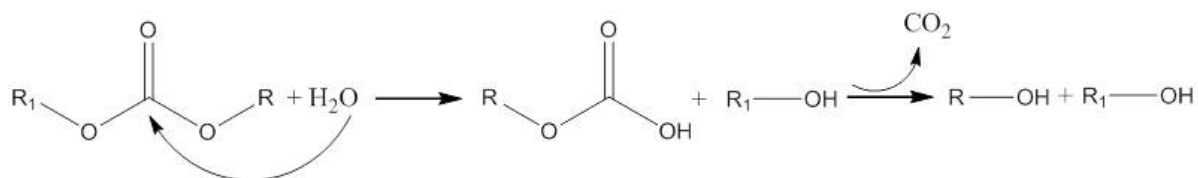
Figure 74: Reaction scheme with linear organic carbonates and water forming CO_2.
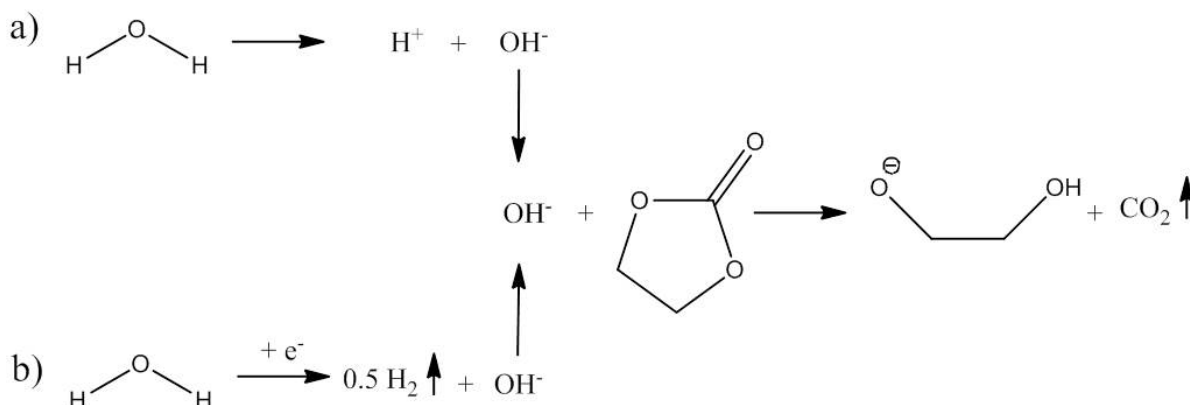
Figure 75: Reaction scheme with cyclic organic carbonates and water forming CO_2.
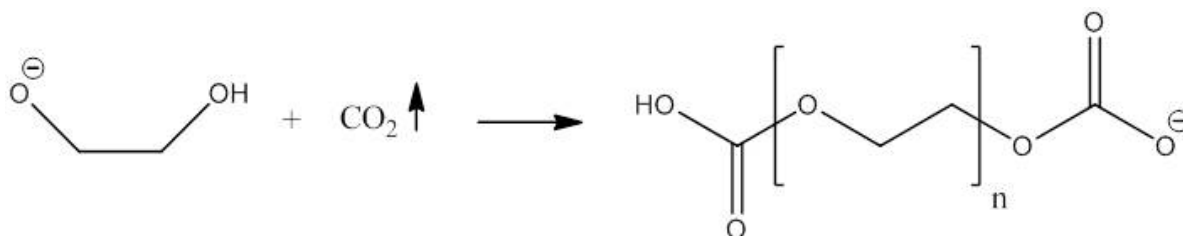
Figure 76: Reaction scheme for oligomerization after ring opening reaction in **Equation (74)**.

the three CV cycles. One can see a stepwise consumption, which is comparable to that in **Figure 72**. Nevertheless an explicit explanation for the CO_2 decrease is not found yet. There is an assumption: Water reduction will occur on electrodes, which is leading to a following decomposition of cyclic carbonates. The potential of pre-cycled electrodes relax to a voltage above 1.5 V_{Li}. CO_2 evolves and is further consumed for further SEI formation. This assumption can be explained by an increased background of CO_2 and H_2. The more stable the SEI, the less parasitic reactions on the graphite surface and the lower the subsequent CO_2-consumption. If one have a look at the H_2 traces, the gas evolution behavior is comparable to that in **Figure 73**. As well as the amount of H_2 within cycling is more or less equal. The overall evolution reaches after the pre formation for three times 13000 ppm. This can be calculated to be 5.04 μmol_{H2}, which is a comparable value to that without previous formation in **Figures 73**. This result leads us to the conclusion, that a pre formation of only three cycles at C/10 is not enough to form a stable SEI.

 Therefore, the following measurement was performed. The OEMS data after ten times pre formation of a graphite electrode is shown in **Figure 78**. It is obvious that H_2 evolution decreases compared to the previous two measurements. The stepped hydrogen evolution is less pronounced. After the first CV cycle 5000 ppm of H_2 are released. This is about 1.6 times less than the amount, which was obtained without pre formation **Figures 73** and after three cycles, shown in **77**. After the third cycle overall H_2 amount is 8000 ppm (= 3.1 μmol_{H2}).
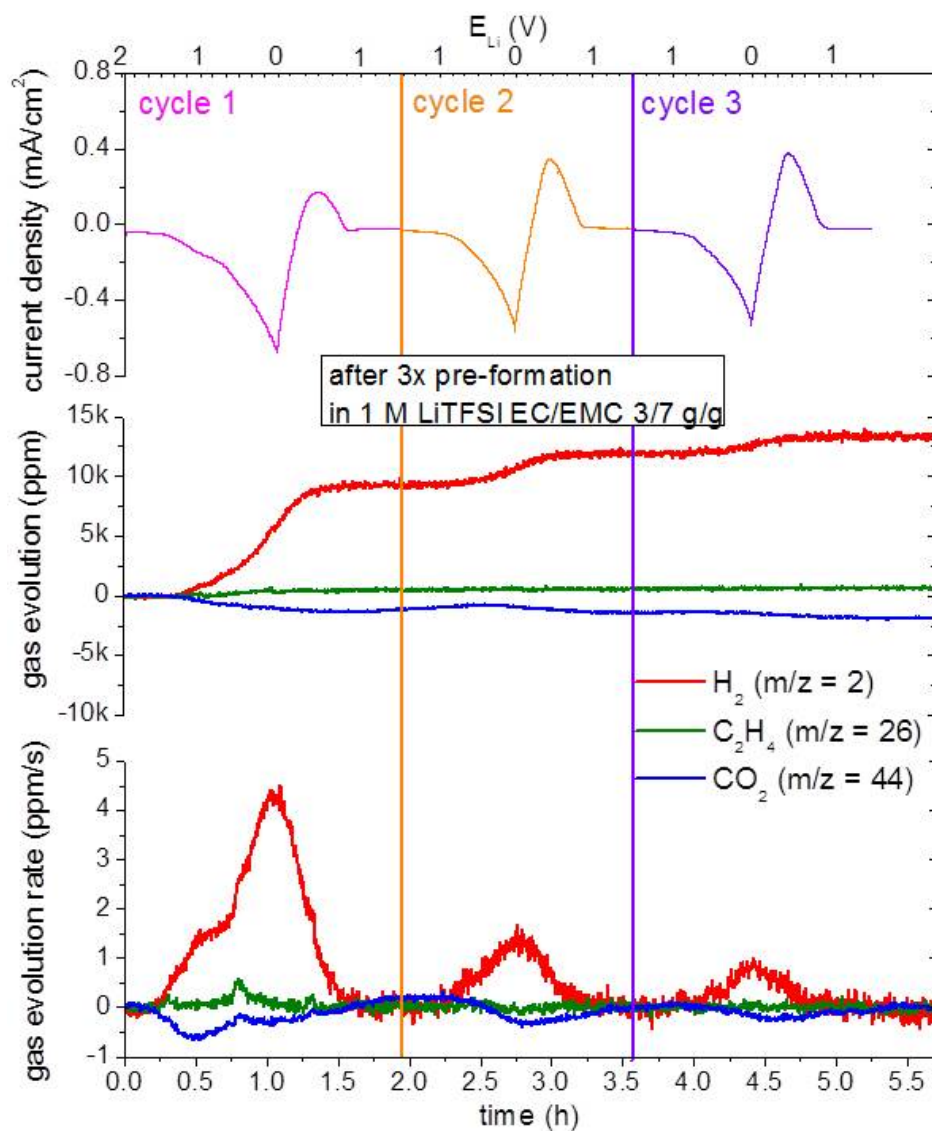
Figure 77: CV of a graphite half cell in a *two-compartment* cell design in water-containing 1 M LiTFSI Ec/Emc (3/7 g/g) (4000 ppm) with a scan rate of 0.5 mV/s in a potential window window from OCV (OCV step not displayed) to 0 V_{Li} after three times pre formation at C/10 (0.01 V_{Li} to 1.5 V_{Li}) in the water-free electrolyte 1 M LiTFSI Ec/Emc (3/7 g/g). The upper part is displaying 3 cycles of a cyclic voltammetry starting after 2 h of rest at OCV to 0 V_{Li} at a scan rate of 0.5 mV/s. In the middle part, *in-operando* gas evolution [ppm] and in the bottom part *in-operando* gas evolution rate [pmm/s] is plotted for gases H_2 (m/z = 2), C_2H_4 (m/z = 26) and CO_2 (m/z = 44) [165].

139
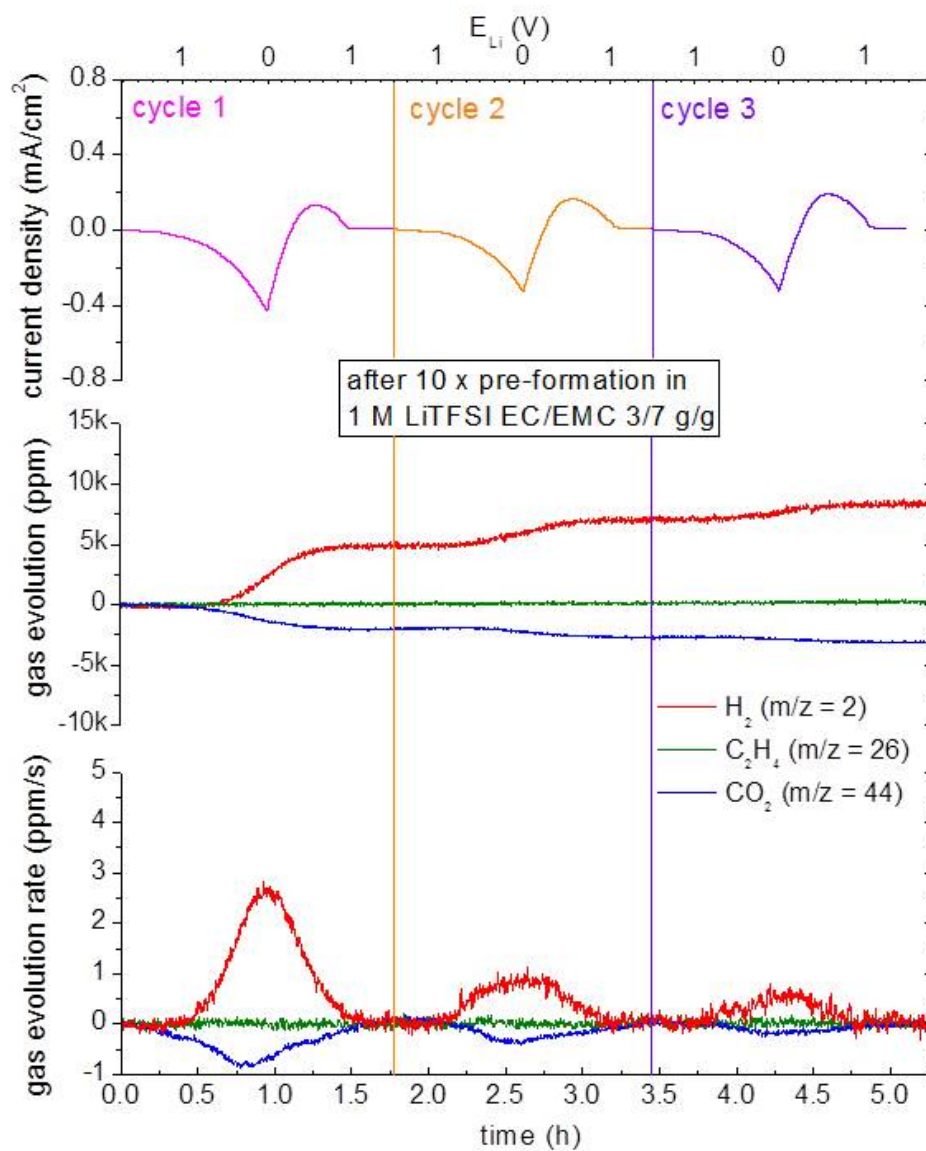
Figure 78: CV of a graphite half cell in a *two-compartment* cell design in water-containing 1 M LiTFSI
Ec/Emc (3/7 g/g) (4000 ppm) with a scan rate of 0.5 mV/s in a potential window from
OCV to 0 V_{Li} after ten times pre formation at C/10 (0.01 V_{Li} to 1.5 V_{Li}) in the water-
free electrolyte 1 M LiTFSI Ec/Emc (3/7 g/g). The upper part is displaying 3 cycles of a
cyclic voltammetry starting after 2 h of rest at OCV to 0 V_{Li} at a scan rate of 0.5 mV/s.
In the middle part, *in-operando* gas evolution [ppm] and in the bottom part *in-operando*
gas evolution rate [pmm/s] is plotted for gases H_2 (m/z = 2), C_2H_4 (m/z = 26) and CO_2
(m/z = 44) [165].

To conclude these results, a protective SEI-layer can prevent water reduction on the graphite surface and leads to a decreased H_2 evolution. With 10 cycles of pre formation, one can reduce the hydrogen amount by a factor of 1.7 from initial 4.59 μmol_{H2} to 3.1 μmol_{H2}.

With 10 cycles of pre formation, one can reduce the hydrogen amount by a factor of 1.7 from initial 4.9 μmol_{H2} to 3.1 μmol_{H2} (see **Table 10**). According to a publication of Nie et al in 2012 and Ein-Eli in 1999 [163, 164] the conductive lithium salt may not influence the quality and efficiency of the SEI layer. To proof this assumption we replaced LiTFSI with the more commonly used conductive salt 1 M $LiPF_6$ to perform the pre formation cycling. The solvent mixture was EC/EMC 3/7 g/g as in the previous measurement, resulting in the electrolyte formulation LP57.

As in the previous measurements, the electrode treatment after 10 times pre formation at a rate of C/10 is equal and as described before. In **Figure 79** we show the *in-operando* behavior of the electrode, which was pre-cycled in $LiPF_6$ containing electrolyte. Also in this case, the OEMS measurement was performed in the model electrolyte containing LiTFSI and 4000 ppm H_2O to avoid parasitic reactions with water and the conductive salt. CV cycles are displayed in the upper plot and are comparable to those shown in **Figure 78**. However, prior to the main H_2 evolution, a small amount is evolved with a simultaneous CO_2 consumption. The first increase of the H_2 is assorted to a small bump in the CV at around 1.5 V_{Li}. During all three cycles no C_2H_4 is detected, which is evidence for the assumption that the main ethylene evolution takes place within the first cycle. The evolution of H_2 and CO_2 is more or less equal to the previous measurement using LiTFSI as conductive salt. The H_2 amount after the first cycle (magenta) reaches an amount of 5800 ppm and after the third cycle (purple) 9800 ppm (≈ 3.8 μmol_{H2}). These values are comparable, but slightly higher, to those shown in **Figure 79** after pre-cycling the cell with LiTFSI (see also **Table 10**). The overall CO_2 consumption is equal to the previous measurement. According to this, we can confirm the assumption that the conductive salt does not influence the quality of the SEI layer. The composition of the SEI layer is mainly consisting from lithium ethylene dicarbonate (LECD) coming from the reduction of EC and LiF assorted to the decomposition of the conductive salt [163]. In the last OEMS measurement the electrode was pre-cycled in a more commonly used electrolyte mixture containing 1 M $LiPF_6$ as conductive salt and 2% of vinylene carbonate (VC) (LP572), which is used as supporting agent for the SEI-formation and is known to influence the efficiency of the protective layer [170]. The treatment for this electrode was the same like described before. After washing and drying, the electrode was re-assembled in the OEMS cell with 1 M LiTFSI EC/EMC (3/7 g/g) and 4000 ppm H_2O. It is obvious from **Figure 80** that the hydrogen evolution further decreases compared to previous measurements. After the first cycle a value of only 600 ppm H_2 is reached with an evolution rate of 0.5 ppm/s. After three cycles the amount increases to 2500 ppm H_2 (≈ 1.0 μmol_{H2}). This is about a factor of 5 smaller compared to the electrode without previous formation and 3.2 times smaller than for an electrode, which was pre-cycled for ten times in the model electrolyte with LiTFSI and $LiPF_6$ with no VC,
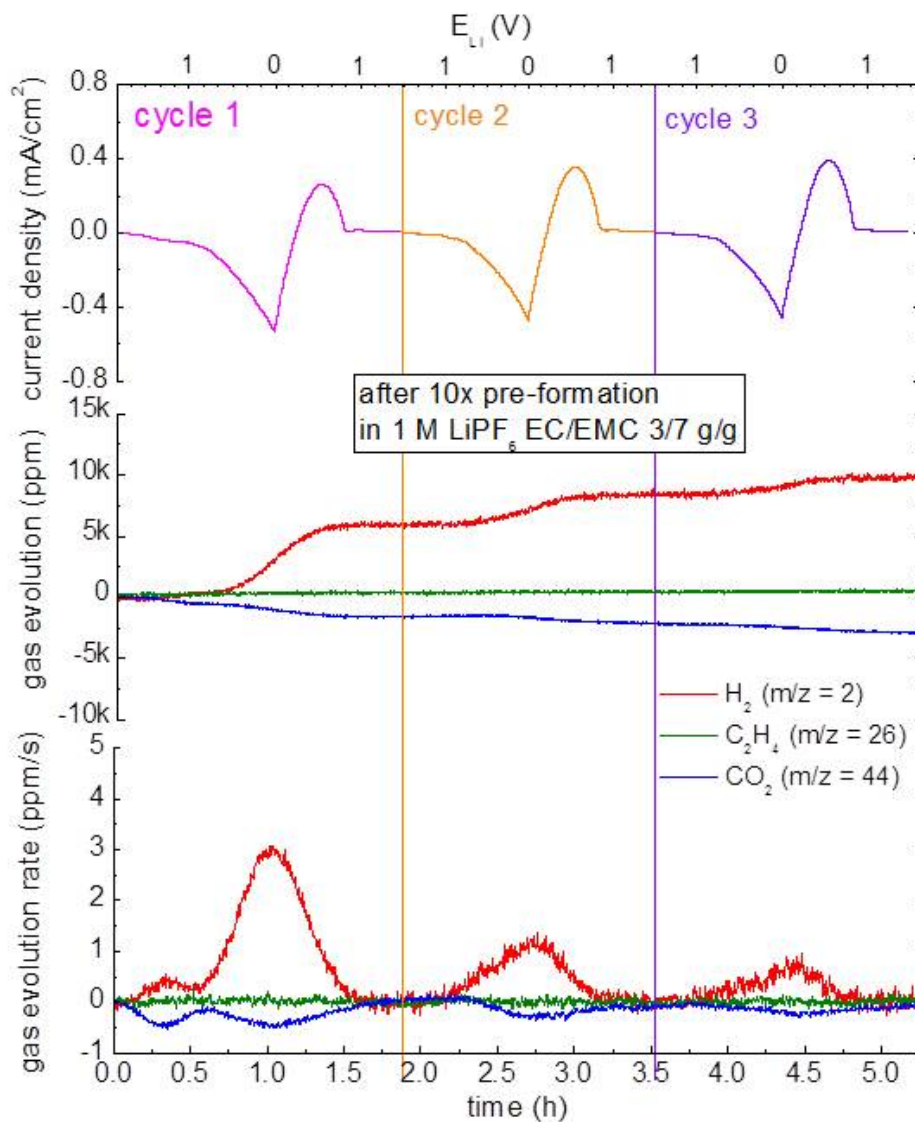
Figure 79: CV of a graphite half cell in a *two-compartment* cell design in water-containing 1 M LiTFSI EC/EMC (3/7 g/g) (4000 ppm) with a scan rate of 0.5 mV/s in a potential window from OCV (OCV step not displayed) to 0 V_{Li} after ten times pre formation at C/10 (0.01 V_{Li} to 1.5 V_{Li}) in the water-free LP57 electrolyte 1 M LiPF$_6$ EC/EMC (3/7 g/g). The upper part is displaying 3 cycles of a cyclic voltammetry starting after 2 h of rest at OCV to 0 V_{Li} at a scan rate of 0.5 mV/s. In the middle part, *in-operando* gas evolution [ppm] and in the bottom part *in-operando* gas evolution rate [pmm/s] is plotted for gases H$_2$ (m/z = 2), C$_2$H$_4$ (m/z = 26) and CO$_2$ (m/z = 44) [165].
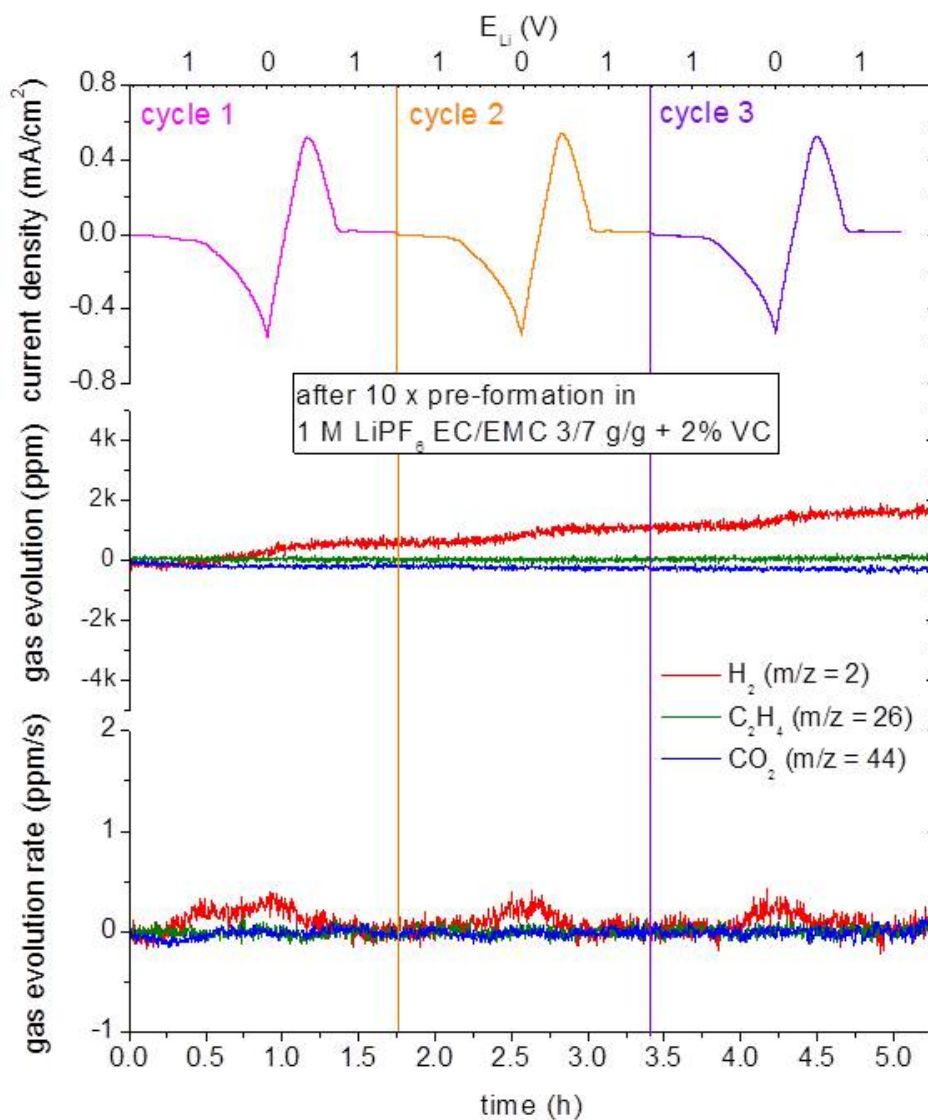
Figure 80: CV of a graphite half cell in a *two-compartment* cell design in water-containing 1 M LiTFSI Ec/Emc 3/7 g/g (4000 ppm) with a scan rate of 0.5 mV/s in a potential window from OCV (OCV step is not displayed) to 0 V_{Li} after ten times pre formation at C/10 (0.01 V_{Li} to 1.5 V_{Li}) in the water-free commercial LP572 electrolyte 1 M LiPF$_6$ Ec/Emc (3/7 g/g) + 2% Vc. The upper part is displaying 3 cycles of a cyclic voltammetry starting after 2 h of rest at OCV to 0 V_{Li} at a scan rate of 0.5 mV/s. In the middle part, *in-operando* gas evolution [ppm] and in the bottom part *in-operando* gas evolution rate [pmm/s] is plotted for gases H$_2$ (m/z = 2), C$_2$H$_4$ (m/z = 26) and CO$_2$ (m/z = 44) [165].

Table 10: Overview of evolved hydrogen (H_2) and ethylene (C_2H_4) amounts, as well as the comparison between the expected (theo.) and the evolved detected hydrogen amount in μmol$_{H2}$ (calculated by the gained ppm-value after the third cycle divided by the molar gas volume at 25°C (24.5 L/mol) and multiplied by the head-space volume of the cell (9.5 mL)), detected by the OEMS, shown in the previous figures. The OEMS measurements were performed in 1 M LiTFSI in Ec/Emc 3/7 g/g containing different water contents; in **Figure 72** 20 ppm H_2O (0.09 μmol$_{H2O}$) was used, which theoretically could gain 0.045 μmol$_{H2}$, if one assumes a one-electron reduction reaction of water. For all other measurements (**Figure 73** and **Figure 77** to **Figure 80**) the water content of the electrolyte was 4000 ppm (18 μmol$_{H2O}$), gaining theoretically 9 μmol$_{H2}$.

cell	formation (10 cycles, 0.1C) in Ec/Emc with	evol. H_2 1st cycle [ppm]	evol. H_2 3rd cycle [ppm]	evol. H_2 3rd cycle [μmol$_{H2}$]	C_2H_4 1st cycle [ppm]
Fig. 72	no formation	250	250	0.1	2000
Fig. 73	no formation	8000	12500	4.9	1700
Fig. 77	1 M LiTFSI	9000	13000	5.1	0
Fig. 78	1 M LiTFSI	5000	8000	3.1	0
Fig. 79	1 M LiPF$_6$	5800	9800	3.8	0
Fig. 80	1 M LiPF$_6$ + 2% Vc	600	2500	1.0	0

respectively. Due to the small amount of evolved H_2, also almost no CO_2 was consumed during the three CV cycles. This leads to the conclusion that hydrogen evolution and a subsequent CO_2 consumption is connected to each other, resulting in the formation of solid carbonate oligomers on the electrode surface, as shown in our previous publication [138]. The SEI-formation in Vc containing electrolytes is better, because its reduction occurs at potentials above 1.0 V_{Li}, reduces the gas evolution within the first cycles and shows a better thermal stability. SEI layers made from Vc decomposition consists of polymer species like oligomers, ring-opened polymers and polyacetylene [170]. All OEMS data is summarized in the following **Table 10**. The formation of an SEI is a dynamic process, which is performed in every cycle at potentials lower than 0.8 V_{Li}. Solvent molecules get reduced and form a more and more growing solid passivation layer on the graphite surface, which should reach an equilibrium state after a certain time. The growth of this surface can be mapped with the low frequency (charge-transfer resistance plus high frequency resistance) of the graphite WE using electrochemical impedance spectroscopy after each cycle for a longer time period, which is shown in **Figure 81**. The cell was cycled with a rate of C/10 (CCCV) in a potential window of 0.01 to 1.5 V_{Li}. An estimated time for each cycle is around 20 h. The PEIS was recorded after every discharge (once a day) at 1.5 V_{Li}. The development of the low frequency resistance (LFR) is shown versus cycle number (each cycle corresponds to a time of $\approx$ 1 day). The LFR (interception of the real resistance on the x-axis) values were plotted, which corresponds to the minimum of the semi-circle of a Nyquist plot and is assigned to the
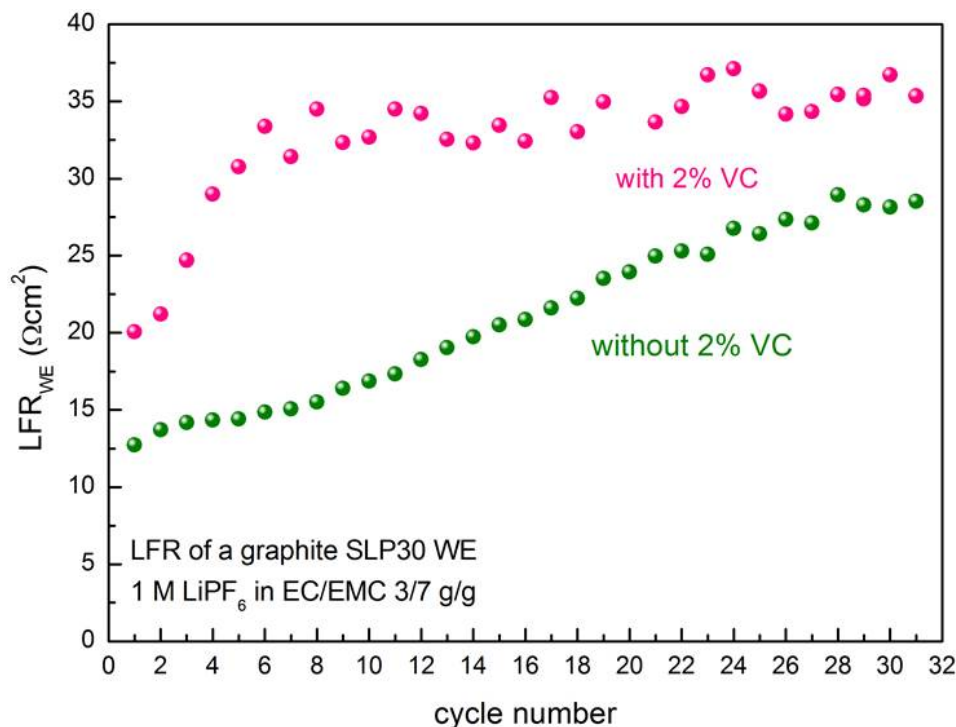
Figure 81: Development of the low frequency resistance (LFR) within the first month (31 days) of cycling.

sum of the high frequency and charge-transfer resistance of the graphite electrode. With these experiments, we wanted to point out that the use of suitable additives can support the formation of a good SEI within a few cycles and to underline that a good SEI prevents side reactions occurring on the electrode surface. Therefore, cells were assembled with two different electrolytes using no VC additive and 2% VC, respectively. In both cases LiPF$_6$ was the conductive salt. In case of the VC free cell (see **Figure 81**; green balls), the LFR is increasing from initial 12.7 Ωcm^2 after the first cycle to 16.4 Ωcm^2 after 10 cycles/days (31 days: $\approx$ 29 Ωcm^2). The charge-transfer resistance is increasing due to the slight growing SEI-layer in the electrode surface and reaches an equilibrium state after 28 cycles. If one compares this to the LFR values for the cell cycled with 2% VC (see**Figure 81**; magenta balls), one can see that these values are higher. After the first cycle, the LFR is 20.2 Ωcm^2, which increases fast to $\approx$ 35 Ωcm^2 after 6 cycles and remains more or less constant until the end of the measurement. With the help of the shown LFR data, one can explain the reduced H$_2$ evolution during cycling, if the electrode was pre-cycled in a 2% VC containing electrolyte. The LFR of electrodes cycled ten times is about 2 times higher compared to those cycled without the addition of 2% VC. The SEI formation process is fully completed and in equilibrium, the electrode surface is protected from parasitic reactions and a H$_2$ formation combined with cell swelling is inhibited.

6.6.5. Conclusions

In this work, the gassing behavior of graphite half cells was investigated by OEMS measurements to detect and evaluate formed gases during three CV cycles. Beside a water-free 1 M LiTFSI Ec/Emc (3/7 g/g) electrolyte, also 4000 ppm of water additive was used in the OEMS measurements, to analyze the gas traces of graphite cells compared to Lto anodes, shown in our previous work [138]. The OEMS results show, that in case of water-free electrolyte, ethylene (C_2H_4) is the main evolved gas, beside a negligible amount of H_2. The detected C_2H_4 evolution occurring on pristine graphite electrodes in the first cycle and the CV data is in accord with literature [123,155,157,159,160,162,167]. If the OEMS experiment was carried out with water-containing electrolyte (1 M LiTFSI Ec/Emc (3/7 g/g) + 4000 ppm H_2O), H_2 is the main gas component, which was evolved during three CV cycles. These OEMS results on graphite electrodes are comparable with data shown on Lto anodes in our previous publication (see **Chapter 6.5** and [138]). With a pre formation procedure of graphite electrodes in a water-free electrolyte, the amount of evolved H_2 can be reduced by a factor of 1.6 (see **Table 10**), if the LiTFSI containing electrolyte was used for formation. In addition, we used the commercial electrolytes LP57 (1 M $LiPF_6$ Ec/Emc3/7 g/g) and LP572 (1 M $LiPF_6$ Ec/Emc 3/7 g/g + 2% Vc) instead of the model electrolyte mixture with LiTFSI. The simple salt replacement of LiTFSIwith $LiPF_6$ (LP57) itself, did not result in a reduction of the evolved gas amount. Using LP572 instead of LP57 the hydrogen amount could be reduced by a factor of 5 (see **Table 10**). We could show that the quality of an SEI plays an important role in terms of the gassing behavior of anode materials. If an intact and effective SEI is formed on the graphite anodes, parasitic side reactions, like the reduction of water can be inhibited. The protective SEI can only be formed at potentials lower than 0.8 V_{Li}, due to electrolyte reduction reactions. The potential is increased to $\approx$ 1.0 V_{Li}, if Vc is used as an electrolyte additive. However, for that reason, a SEI layer is absent on anodes with higher redox potentials, like Lto, and the water reduction reaction can occur unhindered. Nevertheless, also the electrolyte is important to support the formation of the SEI layer. Additives like vinylene carbonate (Vc) lead to a faster growth of the protective layer and once the layer is formed, it remains at a constant thickness and an intact SEI should suppress the transport of solvent molecules and electrodes and the subsequent SEI growth [171,172]. This phenomenon could be shown with electrochemical impedance spectroscopy and the evaluation of the low frequency resistance (LFR) of graphite electrodes using a Vc containing electrolyte and a mixture without Vc for comparison. After ten charge and discharge cycles, the LFR for electrodes cycled in a Vc containing electrolyte is about two times higher than for electrodes, which were cycled without Vc. in summary, gas evolution in battery cells would lead to a swelling of pouch bag cells, which can be observed in cells containing anodes, which are not able to form an SEI layer like Lto anodes. In cells with graphite electrodes, a swelling can be prevented, because of the formation of an SEI layer.

7. Conclusions

Nowadays, there is a high demand of energy storage systems for renewable energies like wind, water and solar power, due to nuclear incidents and increasing green-house gas emission of coal-fired power plants and gasoline-driven cars. For this reason, politicians, researchers and engineers are faced with big challenges to find storage solutions, which do not further boost the global warming, are affordable and are able to fulfill future demands and requirements in terms of safety, life-time and efficiency. For this purpose, lithium-ion batteries seem to be a promising candidate for the application in the field of energy storage. As it is widely known, in the field of lithium-ion battery research there are several unknown aspects about aging, capacity fading and life-time for almost all known lithium-ion battery systems. Aspects like for example overcharging, high temperature, impurities of electrodes and electrolytes, leaky systems, loss of electric or ionic contact or increase of the overall resistance of the battery system are already known to play an important role in terms of the battery's performance. The purpose of this work was to investigate novel electrolyte solvents, which could also be used as additives, for advanced lithium-ion batteries and to study different degradation ("aging") phenomena. The measurements of lithium-ion battery systems were performed in half cell and full cell test set-up using LTO, LFP, LCO, TiO_2 and also graphite as active material.

This doctoral thesis is the result of my time as doctoral candidate at the Chair of Technical Electrochemistry (TEC) at the Technical University of Munich (Chemistry Department, D-85748 Garching) under the supervision of Prof. Dr. Hubert A. Gasteiger at TEC and Prof. Dr. Bruno Scrosati during my stay at University La Sapienzá in Rome, Italy (May to August 2012). In the frame of the laboratory works, we developed a test cell system for a three-electrode set-up allowing the connection to a reference electrode. This development was included in a diploma thesis conducted by Frank Kindermann [49] (Chair of Electrical Energy Storage Systems (EES)). The master thesis was a cooperation project between TEC and Ralph Karl and Prof. Dr. Andreas Jossen from EES. Fruitful input for the cell design was given by Dr. Milos Vracar (Karlsruhe Institute of Technology (KIT)). In addition to that, we focused on the development of an optimized coating and drying process of test-electrodes, which are used for our electrochemical tests. After several improvements, the T-cells and home made electrodes deliver reproducible electrochemical data, also for long-term studies. However, several open aspects like the optimization process of the position of the reference electrode, a low electrolyte volume and electrode coating calendaring for porosity adaptation are still under investigation.

During the visiting doctoral-candidate period in Rome, the research focus was on an alternative electrolyte solvent for lithium-ion batteries to assure high safety through the use of low vapor pressure solvents with a low flammability. The results are shown in **Chapters 6.1** [58] and **6.2**. We show a full characterization of a long chained glyme poly-ethylene glycol (500) di-methyl ether (PEG500DME; M = 500 g/mol) in a mixture with lithium bis-(trifluormethanesulfonyl)-imide (LITFSI) as conducting salt. In addi-

tion to the characterization of the electrochemical stability window of the electrolyte, the ionic conductivity was measured in wide temperature range, and the thermal characteristics were determined by TGA and DSC. These characterizations result in a wide electrochemical window up to 4.8 V_{Li} and high thermal stability up to 250°C and down to 4°C. Besides, the electrolyte was characterized in Lco and TiO_2 half cells as well as in full cell combinations. All cells possessed a good and stable cycling response. For this reason, we proposed Peg500dme as suitable and safe solvent for advanced lithium ion battery applications. However, due to its comparably low ionic conductivity it is not useful for applications in high rate systems. Detailed results were published in 2012 [58]. As a second topic, mixtures containing Peg500dme as solvent with additives of different concentrations of $Py_{1,4}$Tfsi were characterized in a similar way than the pure solvent. As expected from the literature, the presence of $Py_{1,4}$Tfsi improves the thermal stability and increases the temperature window [89] from −13.6°C to 300°C. For this reason, these mixtures are especially interesting for batteries in high temperature applications. Depending on the individual purpose, by the addition of $Py_{1,4}$Tfsi one can influence the characteristics of the electrolyte.

We also did some investigations on the corrosion behavior of different current collector materials like aluminum and stainless steel 316L in contact with the conductive salts $LiPF_6$, $LiClO_4$ and Litfsi in a Ec/Dmc solvent mixture in our three-electrode test cell design with cyclic voltammetry at several thermal conditions (25°C, 60°C and 80°C), shown in **Chapter 6.3**. Several measurements were performed by Susanne Herden while her Bachelor's thesis [104]. It was possible to prove results given in the literature [83, 97, 103] and to find a solvent mixture containing Litfsi, which does not corrode aluminum even at high temperatures. The level of pitting corrosion after treatment under the different conditions could be estimated by the raise in current density during the different CV cycles and was analyzed after cell disassembly by SEM. In addition, the corrosion behavior of aluminum with Litfsi in two different long chained glymes (Tegdme and Peg500dme) were analyzed and their suitability as a corrosion protection agent were evaluated at 25°C and 60°C. We could prove that small amounts of $LiPF_6$ can inhibit aluminum current collector corrosion, due to the formation of a protection layer on the surface; however the inhibition collapses at elevated temperatures. In addition to $LiPF_6$, also glymes can form a protective layer on aluminum and protect it from corrosion. Based on several CV cycling tests we came to the conclusion that a mixture of 0,5 mol/kg Litfsi in Ec/Dmc 1/1 g/g with 50% Peg500dme is a good alternative in terms of the corrosion behavior, as well as in thermal stability and viscosity for the application in electrochemical cell tests. Its ionic conductivity was measured to be 1.83 mS/cm at 25°C and the anodic stability reached 4.3 V_{Li}. As a result, this electrolyte is suitable as a model electrolyte for laboratory tests to study long-term cycling tests at elevated temperatures but low rates. Due to the use of Litfsi as conductive salt it is possible to investigate the influence of water intrusion into laboratory test cells without decomposition of the salt.

As another aging effect, we investigated the iron dissolution of the Lfp olivine structure

in contact with $LiPF_6$ with prompt-gamma-ray activation analysis (PGAA) in cooperation with researchers from FRM II (Forschungs-Neutronenquelle Heinz Maier-Leibnitz, Garching bei München), which is shown in **Chapter 6.4**. According to the results, we could show with two prior pilot tests and with PGAA that the iron dissolution from the olivine structure of LFP occurs in contact with $LiPF_6$-containing electrolytes and precipitate on the anode surface while cycling at elevated temperatures. Iron (Fe) is detectable in the electrolyte solution and as a solid layer on the LTO anode surface and was, as well, quantifiable by the neutron activation method PGAA by analyzing cycled LTO anodes. The electrodes were analyzed post-mortem after cycling LTO/LFP full cells at a rate of 1 C and 60°C for 535 cycles ($\approx$ 45 days) in 1 M $LiPF_6$ EC/EMC 3/7 g/g. Afterwards, we could compare the PGAA data of aged LTO anodes (line 9297 keV; specific for iron) and the cycling performance. Two cells were cycled in a regular potential window of 2.4 and 1.1 V_{cell} and an increased potential window between 2.8 and 0.9 V_{cell}, respectively. In case of the regular cycling window, PGAA detected 2.1% Fe on the aged LTO anode (amount is related to the total Fe amount contained in the cathode active material). If the cell was cycled in the wider potential window, the Fe amount increased by a factor of 1.5. This fact was explained by the higher Fe dissolution caused by an elevated cathode potential ($\approx$ 4.3 V_{Li}) compared to only 4.0 V_{Li}, if the regular potential window was used. Higher cathode potentials force parasitic oxidation reactions, which cause a higher iron dissolution from the cathode surface. The dissolved iron Fe^{2+}-species can be reduced on the anode surface to Fe^0 and deposit on its surface. This surface layer on the anode increases the inner resistance of the cell and causes a subsequent capacity loss. In addition, the loss of iron atoms from the olivine structure leads to a deactivation of the electrochemically active LFP, results in a capacity and performance loss after time. However, the capacity loss which is shown by analyzed cells is not in relation to the small amount of iron on the anode surface detected by PGAA on the anode surface. Another reason for the performance loss can also be referred to the comparable high amount of electrolyte (factor of 63 higher than in commercial cells.), which is necessary in our cell design at elevated temperatures and could causes additional side reactions leading to a capacity loss.

In the last two **Chapters 6.5** and **6.6** the gassing behavior of different cell combinations with different anode materials (LTO and graphite) and electrolytes were under investigation. At first, we have shown the gassing behavior of LTO anodes in full and half cells. Evolved gases of LTO based cells were analyzed by *in-operando* on-line electrochemical mass spectrometry (OEMS) using electrolytes with variating water contents (20 ppm, 4000 ppm and 4%), observing gas evolution during the first charge and discharge cycle at a rate of C/5. H_2 and CO_2 were the main evolved gases, which is in accord with the relevant literature [124, 129–133]. On the other hand, cells cycled with a nominally water-free electrolyte show only a negligible gas evolution upon the first charge and discharge cycle. In recent publications, a gas evolution of LTO based cells was only detectable, if cells were are held in the charged state (or are being cycled), never prior to charging in a pristine state or at an initial OCV step. This led us to the conclusion

that a electrochemical reaction, namely reduction of water, occurs at LTO surfaces while forming H_2 gas and OH^- anions. According to our results, the one-electron reduction reaction of water is responsible for the observed H_2 formation. This is in accord with the hypothesis reported by Belharouk et al. [123] that trace water reduction is the reason for H_2 evolution. Therefore, the occasionally reported gassing of battery cells with LTO anodes can be caused by the residual water content in poorly dried electrodes and separators, by water intrusion during cell assembly in ambient air, or by water formed by the anodic oxidation of electrolyte solvents when high voltage cathode materials, like LMO or NMC, are used. Consequently, careful drying of cell components, cell assembly under dry conditions as well as electrolyte stability at high potentials, are key aspects to ensure long cycle life of LTO-based batteries. In addition, we have shown a detailed mechanism demonstrating that water triggers/catalyzes several parasitic reactions. Moreover, ex-situ analysis methods like ATR FTIR and XRD were combined with OEMS and could show that OH^- anions cause a ring opening reaction of cyclic carbonates like EC, leading to CO_2 evolution and to the formation of lithium alkyl carbonate oligomers. The latter deposit as a clogging passivation layer on the LTO anode. This insulating layer hinders the lithium-ion transport and causes a strong capacity loss.

Based on these findings, the question arises why significant long-term gassing has not been observed in cells assembled with graphite anodes. For these cells, it is known that gassing occurs only during the first charge and never after re-evacuation during cycling. Therefore, we proposed that H_2 and CO_2 evolution may not occur in cells containing graphite anodes, because of the ability of graphite to form a protective solid electrolyte interface (SEI), which sufficiently suppresses the kinetics of water reduction as well as other reduction reactions. A detailed study on this issue is shown in **Chapter 6.6**. Gas evolution of graphite half cells was also investigated by OEMS measurements to quantify gases formed during initial CV cycles with and without previous formation in water free electrolytes to allow the growth of an SEI layer. Besides a water-free model electrolyte containing 1 M LITFSI in EC/EMC 3/7 g/g, also the addition of 4000 ppm H_2O was used to analyze the gas traces of pristine graphite cells during the first three CV cycles. If one compares these data, the behavior of both, graphite and LTO anodes are similar in terms of H_2 and CO_2 evolution. In case of graphite ethylene (C_2H_4) was the main evolved gas component in the initial water-free electrolyte, beside a negligible amount of H_2. The detected C_2H_4 evolution occurring on pristine graphite electrodes in the first cycle and the CV data is in accord with literature [123, 155, 157, 159, 160, 162, 167] and is typical for anodes performing at low potentials. Therefore, C_2H_4 evolution was not detected using LTO anodes, because its performance was above 1.0 V_{Li}. If one carries out the OEMS experiment in a water-containing electrolyte (1 M LITFSI EC/EMC 3/7 g/g + 4000 ppm H_2O), H_2 is the main gas component, which was evolved during the initial three CV cycles. These OEMS results are comparable those shown on LTO anodes in our previous publication (see **Chapter 6.5** and [138]). This behavior looks different, if a pre formation procedure was applied on graphite electrodes (10 cycles at a rate of C/10 in a potential window between 1.5 V_{Li} and 0.01 V_{Li}). Pre formation experiments were al-

ways carried out in a water-free electrolyte solution. The amount of evolved H_2 could be reduced by a factor of 1.64, if the pre formation was done in the model electrolyte using 1 M LiTFSI in EC/EMC 3/7 g/g. In addition, with the use of the commercial electrolyte LP572 (1 M LiPF$_6$ EC/EMC 3/7 g/g plus 2% VC) instead of the model mixture with LiTFSI or 1 M LiPF$_6$ in EC/EMC 3/7 g/g (LP57), reduces the hydrogen amount after first three CV cycles further by a factor of 5. With these experiments, we could show that the quality of an SEI plays a very important role in terms of the gassing behavior of anode materials. If an intact SEI layer is formed on the graphite anodes, parasitic side reactions, like water reduction reaction, are inhibited to a minimum. A protective SEI layer can only be formed at electrodes with potentials lower than 0.8 V_{Li}. The SEI layer consists of degradation products like LiF and lithium ethylene carbonate (LECD) [163] due to electrolyte reduction reactions. The composition of these products is dependent on the use of different conductive salts as well as the ratio between salt and solvent. However, on anodes operating at higher redox potentials, *e.g.* LTO the SEI layer is not formed on the electrode surface and for this reason, the water reduction reaction can occur unhindered. Nevertheless, electrolyte additives like vinylene carbonate (VC) are important to support the formation of the SEI layer. Additives promote a faster growth of the protective layer. As a conclusion, cells containing anodes, which are not able to form an SEI layer like LTO anodes lead to a swelling behavior, due to the absence of a protective SEI layer.

In 2010, the chair of Technical Electrochemistry started research with these projects in the field of lithium-ion technology. Nowadays, several group members are dealing with different topics and investigations on different active materials like high-voltage phospho olivines (LCP, LiCoPO$_4$) (part of the PhosPhoLiCat project, cooperating with group of Prof. Nilges (Fachgebiet Synthese und Charakterisierung innovativer Materialien), BMW AG and Toyota), nickel manganese cobalt oxide (NMC) or different graphite types as anode material, as well as the set-up for lithium-ion pouch and coin cells (part of the ExZellTUM project, cooperating with FRMII, iwb (Institut für Werkzeugmaschinen und Betriebswissenschaften), RMV (Fraunhofer Institut), EES and industry partners like BMW AG and TÜV SÜD; founded by the German Ministry of Education and Research (BMBF). The newest project is an interdisciplinary project called EEBatt, which cooperates with 14 different chairs of TUM, ZAE (Bayerisches Zentrum für Angewandte Energieforschung) and VARTA Storage GmbH. The Bavarian Ministry of Economic Affairs and Media, Energy and Technology approved $\approx$ 30 million Euro for the EEBatt project. The aim of this research project is to investigate decentralized stationary energy storage systems for the efficient use of renewable energies and the support of the network stability.

References

[1]   DuPasquier, A. ; et al.: In: *Journal of Power Sources* 81-82 (1999), 54 S.

[2]   Zhou, J. ; Notten, P.H.L.: In: *Journal of Power Sources* 177 (2008), 553 S.

[3]   Yazami, R. ; Reynier, Y. F.: In: *Electrochimica Acta* 47 (2002), 1217 S.

[4]   http://www.spiegel.de/politik/deutschland/schwarz-gelbe-atomwende\
       \-die-neue-anti-akw-bewegung-a-751078.html-2014

[5]   Wagner, U.: *Nutzung regenerativer Energien.* Bd. IfE-Schriftenreihe Heft 1. 11.
       Lehrstuhl für Energiewirtschaft und Anwendungstechnik, TUM, 2010. – ISBN
       978–3–9805179–3–5

[6]   Ozawa, K.: In: *Solid State Ionics* 69 (1994), 212 S.

[7]   Ozawa, K.: *Li-Ion Rechargable Batteries.* Wiley VCH Weinheim, Germany

[8]   Scrosati, B. ; et. al: Lithium-Sulfur and Lithium-Air: The super batteries of
       the future. In: *221st ECS Meeting*, 2012

[9]   Van Noorden, R.: In: *Nature* 507 (2014), 26 S.

[10]   Patoux, S. ; et al.: In: *Journal of Power Sources* 189 (2009), 344 S.

[11]   Nakayama, M. ; et al.: In: *Chemistry of Materials* 16 (2004), 3399 S.

[12]   Xu, K.: In: *Chemical Review* 104 (2004), 4303 S.

[13]   Broussely, M. ; et al.: In: *Electrochimica Acta* 45 (1999), 3 S.

[14]   Harris, S.J. ; et al.: In: *Chemical Physics Letters* 485 (2010), 265 S.

[15]   U.S. Patent 3 042 896

[16]   Abraham, K.M. ; et al.: In: *Journal of the Electrochemical Society* 143 (1996),
       1 S.

[17]   Colbow, K.M. ; et al.: In: *Journal of Power Sources* 26 (1989), 397 S.

[18]   Rossen, E. ; et al.: In: *Solid State Ionics* 62 (1993), 53 S.

[19]   Nazri, G.-A. ; Pistoia, G.: *Lithium Batteries - Science and Technology.* Springer
       Science+Business Media LLC, New York (USA), 2003

[20]   Buga, H. ; et al.: In: *Ionics* 6 (2000), 172 S.

[21] Xu, K.: In: *Journal of the Electrochemical Society* 156 (2009), A751 S.

[22] Ketterer, B. ; et al.: *Lithium-Ionen Batterien: Stand der Technik und Anwendungspotenzial in Hybrid-, Plug-In Hybrid- und Elektrofahrzeugen.* FZKA 7503; ISSN: 0947-8620. Wissenschaftliche Berichte der Helmholtz-Gemeinschaft, 2009

[23] Marom, R. ; et al.: In: *Journal of Materials Chemistry* 21 (2011), 9938 S.

[24] Nakahara, K. ; et al.: In: *Journal of Power Sources* 117 (2003), 131 S.

[25] Jhan, Y.R. ; Duh, J.G.: In: *Journal of Power Sources* 198 (2012), 294 S.

[26] Christensen, J. ; et al.: In: *Journal of the Electrochemical Society* 153 (2006), A560 S.

[27] Panero, S. ; et al.: In: *Ionics* 6 (2000), 461 S.

[28] Huang, S. ; et al.: In: *Jorunal of Power Sources* 165 (2007), 408 S.

[29] Chen, J. ; et al.: In: *Solid State Ionics* 178 (2008), 1676 S.

[30] Guerfi, A. ; et al.: In: *Journal of Power Sources* 175 (2008), 866 S.

[31] Srinivasan, V. ; Newman, J.: In: *Journal of the Electrochemical Society* 151 (2004), A1517 S.

[32] Aurbach, D.: *Nonaqueous Electrochemistry.* Marcel Dekker Inc., New York/Basel

[33] Imhof, R. ; et al.: In: *Journal of the Electrochemical Society* 146 (1999), 1702 S.

[34] Takami, N. ; et al.: In: *Journal of the Electrochemical Society* 149 (2002), A9 S.

[35] Son, B. ; et al.: In: *Journal of Power Sources* 243 (2013), 641 S.

[36] Xue, R. ; et al.: In: *Journal of Power Sources* 55 (1995), 111 S.

[37] Gunawardhana, N. ; et al.: In: *Journal of Power Sources* 203 (2012), 257 S.

[38] Karulkar, M. ; et al.: Half- and Full-Cell Performance of Silicon-Carbon Anodes Using the Capacity Control Methode. In: *225th ECS Meeting, Orlando, Florida (USA)*, 2014

[39] Guerfi, A. ; et al.: In: *Journal of Power Sources* 195 (2010), 845 S.

[40] Zaghib, K. ; et al.: In: *Journal of Power Sources* 196 (2011), 3949 S.

[41] Bard, A.J. ; Faulkner, L.R.: *Electrochemical Methods - Fundamentals and Applications.* John Wiley and sons, Inc., 2001. – ISBN 13 978–0–471–04372–0

[42] HAMANN, C.H. ; HAMNETT, A. ; VIELSTICH, W.: *Electrochemistry*. Wiley-VCH Verlag GmbH, Weinheim, 2007. – ISBN 978–3–527–31069–2

[43] SCROSATI, B. ; ABRAHAM, K.M. ; SCHALWIJK, W. van ; HASSOUN, J.: *Lithium Batteries - Advanced Technologies and Applications*. John Wiley and sons, Inc., 2013. – ISBN 978–1–118–18365–6

[44] MARKS, T. ; ET al.: In: *Journal of the Electrochemical Society* 158 (2011), A51 S.

[45] https://de.vwr.com/app/catalog/Product?article$\-$number=513-0011-2014

[46] http://www.celgard.com/trilayer-pp.aspx-2014

[47] http://www.celgard.com/pdf/library/Celgard$\-$Product$\-$Comparison$\-$10002.pdf-2014

[48] http://www.goodfellow.com/E/Polytetrafluoroethylene.html-2014

[49] KINDERMANN, F.: *Elektrodenoptimierung und Alterungsverhalten bei Lithiumtitanat-Lithiumeisenphosphat Batterien*, Technische Universität München, Diplomarbeit, 2012

[50] MEINI, S.: *The Influence of Irreversible Electrochemical Reactions on the Fundamental Mechanisms Governing Capacity and Cycle Life of Li-O$_2$ Batteries*, Technische Universität München, Diss., 2013

[51] XU, W. ; ET al.: In: *Journal of Power Sources* 196 (2011), 3894 S.

[52] TSIOUVARAS, N. ; ET al.: In: *Journal of the Electrochemical Society* 160 (2013), A471 S.

[53] http://www.mlz-garching.de/pgaa-2014

[54] SEIDLMAYER, S: Neutrons for Batteries - quantifying cation deposition by PGAA and some in-situ SANS results on NMC pouchbag cells; EE-Batt Projektmeeting AP2.8 / Forschungsneutronenquelle FRMII, 85748 Garching. 2013. – Forschungsbericht

[55] PERRY, D.L. ; ET al.: In: *Journal of Analytical Atom Spectrometry* 17 (2002), 32 S.

[56] FRMII: PGAA - Prompte Gamma Aktivierungs-Analyse - Akript zum Physikalischen Fortgeschrittenenpraktikum / Forschungsneutronenquelle FRMII, 85748 Garching. 2010. – Forschungsbericht

[57] https://www.ph.tum.de/studium/praktika/fopra/versuche/61/PGAAAnleitung. pdf

[58] BERNHARD, R. ; ET al.: In: *Journal of Power Sources* 226 (2013), 329 S.

[59] HORIE, H. ; ET al.: In: *World Electric Vehicle J.* 2 (2008), 25 S.

[60] TARASCON, J.-M. ; ARMAND, M.: In: *Nature* 414 (2001), 359 S.

[61] BRUCE, P.G. ; ET al.: In: *Angewandte Chemie* 120 (2008), 2972 S.

[62] WAKIHARA, M. ; YAMAMATO, O.: *Lithium Ion Batteries*

[63] APPETECHI, G.B. ; ET al.: In: *Journal of Power Sources* 124 (2003), 246 S.

[64] XIONG, H.-W. ; ET al.: In: *Solid State Ionics* 159 (2003), 89 S.

[65] WIECZOREK, W. ; ET al.: In: *Journal of Physical Chemistry* 102 (1998), 8725 S.

[66] SHI, J. ; ET al.: In: *Electrochimica Acta* 40 (1995), 2425 S.

[67] APPETECCHI, G.B. ; ET al.: In: *Journal of the Electrochemical Society* 143 (1996), 6 S.

[68] CAO, F.-F. ; ET al.: In: *Journal of Physical Chemistry C* 114 (2010), 10308 S.

[69] BRUTTI, S. ; ET al.: In: *Journal of Power Sources* 196 (2011), 9792 S.

[70] EVANS, J. ; ET al.: In: *Polymer* 28 (1987), 2324 S.

[71] BOUKAMP, B.A.: In: *Solid State Ionics* 20 (1986), 31 S.

[72] BOUKAMP, B.A.: In: *Solid State Ionics* 18-19 (1986), 136 S.

[73] CHEN, D. ; ET al.: In: *Journal of American Chemical Society* 132 (2010), 4438 S.

[74] AURBACH, D.: In: *Journal of Power Sources* 89 (2000), 206 S.

[75] CROCE, F. ; ET al.: In: *Journal of Power Sources* 119-121 (2003), 399 S.

[76] OHNO, H. ; ET al.: In: *Electrochimica Acta* 48 (2003), 2079 S.

[77] SONG, J.Y. ; ET al.: In: *Journal of Power Sources* 77 (1999), 183 S.

[78] THAMAPHAT, K. ; ET al.: In: *Natural Science* 42 (2008), 357 S.

[79] YABUUCHI, N. ; OHZUKU, T.: In: *Journal of Power Sources* 119 (2003), 171 S.

[80] SCHOENHAMMER, K. ; ET al.: In: *Pharmaceutical Research* 26 (2009), 2568 S.

[81] LEVI, S.C. ; BRO, P.: *Battery Hazards and Accident Prevention of Cell Components with the Thermal Behavior of a Complete Cell Plenum Press*

[82] HASSOUN, J. ; ET al.: In: *Angewandte Chemie Int. Ed.* 30 (2011), 2999 S.

[83] DAHBI, M. ; ET al.: In: *Journal of Power Sources* 196 (2011), 9743 S.

[84] MORITA, M. ; ET al.: In: *Journal of Power Sources* 119-121 (2003), 784 S.

[85] UMOREN, S.A. ; ET al.: In: *Journal of Applied Polymer Science* 105 (2007), 3363 S.

[86] UMOREN, S.A. ; ET al.: In: *Journal of Applied Polymer Science* 113 (2009), 3533 S.

[87] ARMAND, M. ; ET al.: In: *Nature Materials* 8 (2009), 621 S.

[88] OLIVIER-BOURBIGOU, H. ; MAGNA, L.: In: *Journal of Molecular Catalysis A: Chemical* 182-183 (2002), 419 S.

[89] WETJEN, M. ; ET al.: In: *ChemSusChem* 6 (2013), 1037 S.

[90] APPETECCHI, G.B. ; ET al.: In: *Journal of Power Sources* 196 (2011), 6703 S.

[91] SHIN, J.-H. ; ET al.: In: *Electrochemical Communication* 5 (2003), 1016 S.

[92] KIM, G.-T. ; ET al.: In: *Journal of Power Sources* 171 (2007), 861 S.

[93] SHIN, J.-H. ; ET al.: In: *Journal of Power Sources* 156 (2006), 560 S.

[94] SHIN, J.-H. ; CAIRNS, C.A.: In: *Journal of Power Sources* 117 (2008), 537 S.

[95] PATEL, M. ; ET al.: In: *Journal of Material Chemistry* 21 (2011), 17419 S.

[96] ELIA, G.A. ; ET al.: In: *manuscript in preparation* 00 (2014), 00 S.

[97] CHEN, Y. ; ET al.: In: *Journal of the Electrochemical Society* 146 (1999), 1310 S.

[98] WHITEHEAD, A.H. ; SCHREIBER, M.: In: *Journal of the Electrochemical Society* 152 (2005), A2105 S.

[99] MYUNG, S.-T. ; ET. al: In: *Electrochimica Acta* 55 (2009), 288 S.

[100] BRAITHWAITE, J.W. ; ET. al: In: *Journal of the Electrochemical Society* 146 (1999), 448 S.

[101] ZHANG, S.S. ; JOW, T.R.: In: *Journal of Power Sources* 109 (2002), 458 S.

[102] KRÄMER, E. ; ET. al: In: *ECS Electrochemical Letters* 1 (2012), C9 S.

[103] YANG, H. ; ET. al: In: *Journal of the Electrochemical Society* 147 (2000), 4399 S.

[104] HERDEN, S.: *Elektrolytuntersuchungen für Lithiumtitanat und Lithiumeisenphosphat Batteriezellen*, Technische Universität München, Bachelor's Thesis, 2012

[105] KRAUSE, L.J. ; ET. al: In: *Journal of Power Sources* 68 (1997), 320 S.

[106] WANG, H. ; ET. al: In: *Journal of Power Sources* 169 (2007), 375 S.

[107] AURBACH, D. ; ET. al: In: *Electrochimica Acta* 50 (2004), 247 S.

[108] TARASCON, J.M. ; GUYOMARD, D.: In: *Solid State Ionics* 69 (1994), 293 S.

[109] KOLTYPIN, M. ; ET al.: In: *Electrochemical and Solid-State Letters* 10 (2007), 40 S.

[110] HOLLEMANN, A.Fr. ; WIBERG, E.: *Lehrbuch der Anorganischen Chemie Aufl. 102.* deGruyter, 2007

[111] ZHENG, H. ; ET al.: In: *Journal of Power Sources* 207 (2012), 134 S.

[112] SHARABI, R. ; ET al.: In: *Electrochemistry Communication* 13 (2011), 800 S.

[113] YANG, H. ; ET. al: In: *Journal of Power Sources* 161 (2006), 573 S.

[114] TANNAI, H. ; ET. al: In: *Angewandte Chemie* 19 (2007), 7242 S.

[115] AMATUCCI, G. ; ET al.: In: *Journal of Power Sources* 69 (1997), 11 S.

[116] DUPASQUIER, A. ; ET al.: In: *Journal of the Electrochemical Society* 146 (1997), 428 S.

[117] KOMABA, S. ; ET al.: In: *Electrochimica Acta* 47 (2002), 1229 S.

[118] ZAGHIB, K. ; ET al.: In: *Journal of Power Sources* 216 (2012), 192 S.

[119] GAINES, L. ; CUENCA, R.: Costs of Lithium-Ion Batteries for Vehicles. / Center for Transportation Research; Argonne National Laboratory. 2000. – Forschungsbericht

[120] AURBACH, D. ; ET. al: Cycling performance of $LiCoPO_4$ cathodes: reasons for capacity fading and effect of the electrolyte composition. In: *224st ECS Meeting*, 2013

[121] CHEN, Z. ; ET al.: In: *Advanced Functional Materials* 23 (2013), 959 S.

[122] HOLZAPFEL, M. ; ET al.: In: *Electrochimica Acta* 49 (2004), 581 S.

[123] BELHAROUAK, I. ; ET al.: In: *Journal of Power Sources* 196 (2011), 10344 S.

[124] Wu, K. ; et al.: In: *Journal of Applied Electrochemistry* 42 (2012), 989 S.

[125] Scrosati, B. ; Garche, J.: In: *Journal of Power Sources* 195 (2010), 2419 S.

[126] D'Andrea, S. ; et al.: In: *Ionics* 6 (2000), 127 S.

[127] Ohzuku, T. ; Garche, J.: In: *Journal of the Electrochemical Society* 142 (1995), 1431 S.

[128] Jiang, C. ; et al.: In: *Electrochimica Acta* 52 (2007), 6470 S.

[129] He, Y.-B. ; et al.: In: *Scientific Reports* 2 (2012), 913 S.

[130] DuPasquier, A. ; et al.: In: *Journal of Power Sources* 115 (2003), 171 S.

[131] Lu, X. ; et al.: In: *Advanced Materials* 24 (2012), 3233 S.

[132] Belharouak, I. ; et al.: In: *Journal of the Electrochemical Society* 159 (2012), A1165 S.

[133] Wu, K. ; et al.: In: *Journal of Power Sources* 237 (2013), 285 S.

[134] Etacheri, V. ; et. al.: In: *Energy Environmental Science* 4 (2011), 3243 S.

[135] Aurbach, D. ; et al.: In: *Solid State Ionics* 148 (2002), 405 S.

[136] Ruffo, R. ; et al.: In: *Ionics* 11 (2005), 213 S.

[137] Meini, S. ; et al.: In: *Physical Chemistry Chemical Physics* 15 (2013), 11478 S.

[138] Bernhard, R. ; et al.: In: *Journal of the Electrochemical Society* 161 (2014), A497 S.

[139] McCloskey, B.D. ; et al.: In: *Journal of Physical Chemistry Letters* 2 (2011), 1161 S.

[140] Lu, Y.-C. ; et al.: In: *Journal of the Electrochemical Society* 157 (2010), A1016 S.

[141] Gallagher, K.G. ; Darling, R.M. ; T.F., Fuller: *Handbook of Fuel Cells.* Wiley West Sussex, UK

[142] Kinoshita, K.: *Carbon - Electrochemical and Physicochemical Properties.* John Wiley & sons, Berkley California USA

[143] Roen, L.M. ; et al.: In: *Electrochemical and Solid State Letters* 7 (2004), A19 S.

[144] Freunberger, S. ; et al.: In: *Journal of the American Chemical Society* 133 (2011), 8040 S.

[145] Choi, H. ; et al.: In: *Bulletin Korean Chemical Society* 31 (2010), 2519 S.

[146] Zhang, X. ; et al.: In: *Journal of the Electrochemical Society* 148 (2001), A1341 S.

[147] Soga, K. ; et al.: In: *Polymer Letters Edition* 14 (1976), 161 S.

[148] Goa, Y. ; et al.: In: *Journal of Power Sources* 245 (2014), 684 S.

[149] Hamilton, R.L.: In: *The Bell System Technical Journal* 46 (1967), 391 S.

[150] http://www.goodfellow.com/G/Polypropylen.html-2013

[151] McCloskey, B.D. ; et al.: In: *Journal of Physical Chemistry Letters* 3 (2012), 3043 S.

[152] Meini, S. ; et al.: In: *Journal of the Electrochemical Society* 161 (2014), A1306 S.

[153] Ein-Eli, Y. ; et al.: In: *Electrochimica Acta* 39 (1994), 2559 S.

[154] Peled, E.: *Lithium Batteries; J.-P. Gabano (Ed.)*. Academic press, London, UK, 1983

[155] Lanz, M. ; Novak, P.: In: *Journal of Power Sources* 102 (2001), 277 S.

[156] Winter, M. ; et al.: In: *Advanced Materials* 10 (1998), 725 S.

[157] Joho, F. ; et al.: In: *Journal of Power Sources* 81-82 (1999), 243 S.

[158] Winter, M. ; et al.: In: *Journal of the Electrochemical Society* 145 (1998), 428 S.

[159] Novak, P. ; et al.: In: *Journal of Power Sources* 81-82 (1999), 212 S.

[160] Imhof, R. ; Novak, P.: In: *Journal of the Electrochemical Society* 145 (1998), 1081 S.

[161] Huang, L.H. ; et al.: In: *Review Advanced Material Science* 36 (2014), 13 S.

[162] Novak, P. ; et al.: In: *Journal of Power Sources* 97-98 (2001), 39 S.

[163] Nie, M. ; Lucht, B.L.: In: *Journal of the Electrochemical Society* 161 (2014), A1001 S.

[164] Ein-Eli, Y.: In: *Electrochemical and Solid State Letters* 2 (1999), 212 S.

[165] Bernhard, R. ; et al.: In: *manuskript in preparation* 00 (2014), 00 S.

[166] SHU, Z. X. ; ET al.: In: *Journal of the Electrochemical Society* 143 (1996), 2230 S.

[167] HOLZAPFEL, M. ; ET al.: In: *Journal of Power Sources* 174 (2007), 1156 S.

[168] MINDEMARK, J.: *Functional Cyclic Carbonate Monomers and Polycarbonates*, Uppsala University, Diss., 2012

[169] YANG, Y.-L. ; ET. al: In: *Journal of Biological Chemistry* 273 (1998), 7814 S.

[170] OTA, H. ; ET. al: In: *Journal of the Electrochemical Society* 151 (2004), A1306 S.

[171] PLOEHN, H.J. ; ET. al: In: *Journal of the Electrochemical Society* 151 (2004), A456 S.

[172] PINSON, M.B. ; BAZANT, M.Z.: In: *Journal of the Electrochemical Society* 160 (2013), A243 S.

A. Abbreviations

A	active surface of electrode area [cm^2, m^2]
a$_{Red}$/a$_{Ox}$	activity of the oxidized or reduced species
AC	alternating current
AM	(electrochemical) active material
α	symmetric factor of Butler-Volmer equation
ATR FT-IR	attenuated total reflection fourier transform infrared spectrometry
BET	explains the physical adsorption of gas molecules on a solid surface and gives the possibility to calculate the specific surface; Brunauer-Emmett-Teller theory [m^2/g]
BEV	battery electric vehicle
C	specific capacity [mAh/g or mAh/cm^2]
CC	constant current; procedure used for charging and discharging cells
CCCV	constant current constant voltage; procedure used mainly for charging cells
CE	counter electrode also known as anode or negative electrode
CTR	charge transfer resistance [Ω; Ωcm^2]
CV	constant voltage; procedure used mainly for charging cells **OR** electrochemical method; cyclic voltametry
D	spring constant [N/mm]
DC	direct current
DEMS	differential electrochemical mass spectrometry
DSC	a thermo-analytical technique; differential scanning calorimetry
ΔE$_{ohmic}$	ohmic overpotential [V]
ΔL	compression length of spring [4 mm]
Δp	difference (water) vapor pressure [Pa]
Δt$_{charge}$	contribution on charging time [s]
E	cell potential [V]
E$_A$	activation energy [J/mol]
E$_{CE}$	potential counter electrode [V]
E$_{cell}$	cell potential (E$_{WE}$ - E$_{CE}$) [V]
E$_{equ}$	reversible equilibrium potential [V] from Nernst equation
E$_{WE}$	potential working electrode [V]
E$_0$	standard potential [V]
e$^-$	electron
EDX	elemental analysis or chemical characterization; coupled with SEM; Energy-dispersive X-ray spectroscopy
EES	Chair of Electrical Energy Storage Systems (TU München)
EIS	electrochemical impedance spectrometry

EMS	electrochemical mass spectrometry
F	natural constant; Faraday constant 96485.3365 A·s/mol
I	current [mA, A]
i	current density [mA/cm^2]
i$_0$	exchange current density [mA/cm^2]
	from Butler-Volmer equation
IHP	inner helmholz plane
HEV	hybrid electric vehicle
HFR	high frequency resistance [Ω; Ωcm^2]
K$_{PPfoil}$	water vapor permeability for PP foils
Kel-F	thermoplastic chlorofluoropolymer;
	poly-chlorotrifluoro-ethylene (-(C$_2$ClF$_3$)$_n$-)
KIT	Karlsruhe Institute of Technology
LFR	low frequency resistance [Ω; Ωcm^2]
LSV	linear sweep voltammetry
M	molecular mass [g/mol]
m	slope
MS	mass spectrometry
NAA	neutron activation analysis of delayed γ-rays
n$_{H2}$	amount of evolved hydrogen [μmol]
NLLSF	non linear least squares fit analysis
η	kinetic overpotential of Butler-Volmer equation
OCV	open circuit voltage (also called open circuit potential (OCP))
OEMS	on-line electrochemical mass spectrometry
Ohara	lithium-ion conductive glass ceramics
OHP	outer helmholz plane
PEIS	potentiostatic electrochemical impedance spectrometry
PGAA	radiative neutron activation method;
	prompt gamma activation analysis
pH	a measure of the acidity or basicity of an aqueous solution
PHEV	plug-in hybrid electric vehicle
ppm	unit; parts per million (10^{-6})
R	natural constant; gas constant 8.314 J/mol·K
R$_{electrode}$	resistance of electrode [Ω; Ωcm^2]
R$_{ext}$	external electric resistance [Ω; Ωcm^2]
R$_{internal}$	R$_{ionic}$ + R$_{electrode}$ [Ω; Ωcm^2]
R$_{ionic}$	ionic resistance of the electrolyte [Ω; Ωcm^2]
ρ	density [kg/m^3; g/cm^3]
RE	reference electrode
RHE	reversible hydrogen potential [V$_{RHE}$]
RT	room temperature [298 K; 25°C]
SEI	solid electrolyte interface

SEM	scanning electron microscopy
SHE	standard hydrogen potential [V_{SHE}]
σ	ionic conductivity [S/m; mS/cm]
T	temperature [K; °C]
t	time [s, min, h] **OR** thickness [μm]
t_{Li+}	lithium transference number
T_D	decomposition point [K; °C]
T_M	melting point [K; °C]
TEC	Chair of Technical Electrochemistry (TU München)
TGA	method of thermal analysis; thermogravimetric analysis
T-RFA	method for qualitative and quantitative elemental analysis; X-ray fluorescence spectroscopy
Θ	angle for phase shift of AC current
U	voltage [V]
UV	ultra violett
V_{cell}	unit; cell potential [V] of a full-cell
V_{Li}	unit; cell potential [V] versus lithium (-3.05 V_{SHE})
V_{SHE}	unit; cell potential [V] versus standard hydrogen potential (0 V_{SHE})
w_{PP}	width of Pp sealing frame
WE	working electrode also known as cathode or positive electrode
ω	angular frequency
XRD	analysis method of crystal structures; X-ray diffraction
Z	used for calculation of the ionic conductivity; cell constant [1/m; 1/cm]

B. Chemical compounds

Al	chemical element; aluminum
AlF_6^-	product of aluminum corrosion; complex aluminum hexa fluoro phosphate
$Al_2O3]$	natural protective layer on aluminum; aluminum oxide
B_4C	boron carbide (radiation protection)
C	conductive carbon (Super C65)
Cd	chemical element; cadmium
Cl_2	gaseous compound; chlorine
ClO_2	gaseous compound; chlorine dioxide
C_2H_4	gaseous compound; ethylene
CO	gaseous compound; carbon mono-oxide
Co	chemical element; cobalt
CO_2	gaseous compound; carbon dioxide
Cu	chemical element; copper
DEGDME	organic solvent; di-ethylene glycol dimethyl ether (also called diglyme) ($C_6H_14O_3$)
DMC	organic solvent; di-methyl carbonate ($C_3H_6O_3$)
DME	organic solvent; dimethoxyethane (also called monoglyme) ($C_4H_{10}O_2$)
DMSO	organic solvent; di-methyl sulfoxide (C_2H_6OS)
EC	organic solvent; ethylene carbonate ($C_3H_4O_3$)
EMC	organic solvent; ethyl methyl carbonate ($C_4H_8O_3$)
Fe	chemical element; iron
FEP	co-polymer similar to teflon; fluorinated ethylene propylene
FP	charged LFP; iron phosphate ($FePO_4$)
HCl	aqueous acid; hydrochloric acid
HDPE	thermoplastic polymer; high density poly-ethylene
HNO_3	aqueous acid; nitric acid
HF	gaseous compound; hydrofluoric acid
H_2	gaseous compound; hydrogen
H_2O	liquid or gaseous compound; water
KOH	aqueous base; potassium hydroxide
LCO	active material of the cathode side; lithium cobalt oxide ($LiCoO_2$)
LCP	active material of the cathode side; lithium cobalt phosphate ($LiCoPO_4$)
LECD	product of SEI layer; lithium ethylene carbonate
LFP	active material of the cathode side;

	lithium iron phosphate ($LiFePO_4$)
$LiAsF_6$	conductive salt for electrolytes; lithium hexa-fluoro arsenate
$LiBF_4$	conductive salt for electrolytes; lithium tetra fluoro borate
$LiClO_4$	conductive salt for electrolytes; lithium perchlorate
LiF	product of electrolyte decomposition; lithium fluoride
Li_2O	solid compound; lithium oxide
$LiOCH_3$	product of electrolyte decomposition; lithium methyl ester
$LiPF_6$	conductive salt for electrolytes; lithium hexa-fluoro phosphate
LiTFSI	conductive salt for electrolytes;
	lithium bis-(trifluoromethanesulfonyl)-imide
Li_2CO_3	product of electrolyte decomposition; lithium carbonate
LMO	active material of the cathode side;
	lithium manganese oxide ($LiMn_2O_4$)
LP30	pre-mixed standard electrolyte; 1 M $LiPF_6$ in EC/DMC 1/1 g/g
LP57	pre-mixed standard electrolyte; 1 M $LiPF_6$ in EC/EMC 3/7 g/g
LP572	pre-mixed standard electrolyte;
	1 M $LiPF_6$ in EC/EMC 3/7 g/g + 2% VC
LTO	active material of the anode side; lithium titanate ($Li_4Ti_5O_{12}$)
Mn	chemical element; manganese
MnO_2	active material of the cathode side in primary batteries;
	manganese oxide
Ni	chemical element; nickel
NMC	active material of the cathode side;
	lithium nickel manganese cobalt oxide ($LiNi_{1/3}Mn_{1/3}Co_{1/3}O_2$)
NMP	solvent for electrode inks; N-methyl pyrrolidone (C_5H_9NO)
O_2	gaseous compound; oxygen
OH^-	hydroxide anion
Pb	chemical element; lead
PE	thermoplastic polymer; poly-ethylene ($-(C_2H_4)_n-$)
PEG	see PEO
PEG500DME	organic solvent; poly-ethylene glycol dimethyl ether
	($M \approx 500$ g/mol) ($CH_3O(CH_2CH_2O)_nCH_3$)
PEO	organic solvent; poly-ethylene oxide
	also called poly-ethylene glycol (PEG)
	($H(CH_2H_4O)_nOH$)
PF_5	product of electrolyte decomposition; gaseous
	penta fluoro phosphate
PP	thermoplastic polymer; poly-propylene ($-(C_3H_6)_n-$)
PTFE	synthetic fluoropolymer; poly-tetrafluoro-ethylene
	(also called Teflon) ($-(C_2F_4)_n-$)
PVA	poly-vinyl alcohol ($-(C_2H_4O)_n-$)
PVDF	polymer binder for electrodes, soluble in NMP;

	polyvinylidene difluoride (-$(C_2H_2F_2)_n$-)
$Py_{1,4}TFSI$	ionic liquid; ($C_{11}H_{20}F_6N_2O_4S_2$)
	1-Methyl-4-Butyl-Bis-(trifluoromethanesulfonyl)-Imide
SLP30	graphite powder
SO_2	gaseous compound; sulfur dioxide
TEGDME	organic solvent; tetraethylene glycol dimethyl ether
	(also called tetraglyme) ($C_10H_22O_5$)
Ti	chemical element; titanium
TiO_2	active material of the anode side; titanate oxide
VC	organic solvent; vinylene carbonate ($C_3H_2O_3$)
Zn	chemical element and active material of the anode side
	for primary batteries; Zinc
^4He	isotope of helium
^6LiF	lithium fluoride (radiation protection)
^{36}Ar	isotope of argon

166

C. Curriculum Vitae

Rebecca Juliane Bernhard

Personal Information

Name: Rebecca Juliane Bernhard

Name at birth: Zeh

Adress: Albert-Rosshaupterstrasse 76b; 81369 München (Germany)

Born: 29.03.1986; Stuttgart (Germany)

Nationality: German

Family status: Married

Languages: German (mother tongue), English (fluent)

Education

Doctoral Thesis (October 2010 - September 2014):
Technische Universität München (TUM);
Chair of Technical Electrochemistry;
Lichtenbergstrasse 4; 85748 Garching bei München (Germany)

Supervisor: Prof. Dr. Hubert A. Gasteiger

Topic:
"Novel Electrolyte Solvents and Additives for Lithium-Ion Batteries and Different Materials Degradation Phenomena"

Scholarship: Stiftung Nagelschneider; München (Germany)
(October 2010 - October 2013)

International Collaborations (May 2012 - August 2012):
Universitá La Sapienza;
Dipartimento di Chimica;
Piazzale Aldo Moro 5; 00185 Rome (Italy)

Supervisor: Prof. Dr. Bruno Scrosati; Dr. Jusef Hassoun

Project: *"Characterization of poly-ethylene glycol di-methyl ether and ionic liquid ($Py_{1,4}TFSI$) as electrolyte and additive for advanced lithium-ion batteries."*

Summer School (July 26, 2011 - August 05, 2011)
BASF - SE, Ludwigshafen a. Rhein (Germany)
"121st BASF International Summer Course

Diploma Thesis (April 2010 - September 2010)
Technische Universität München (TUM);
Physics Department E-19;
James-Franck-Strasse 1; 85748 Garching bei München (Germany)

Supervisor: Prof. Dr. Ulrich Stimming, Dr. Holger Wolfschmidt

Thesis: *"Ruthenium and HOPG - Electrochemical Oxidation, Intercalation and SPM"*

Final Mark: 1.1

Research Training (March 2009)
University of Berne;
Department of Chemistry and Biochemistry;
Freiestrasse 3;
3012 Berne (Switzerland)

Supervisor: Prof. Dr. Jean-Louis Reymond, Dr. Nicolas Uhlig

Project: *"Synthesis of different resin based peptide dendrimers"*

Education University (October 2005 - September 2010)
University of Ulm; Chemistry Department
89069 Ulm (Germany)

Subject: Chemistry (main subject: energy engineering)

Final Mark: Diplom 1.7

Education School (September 1996 - September 2005)
Immanuel-Kant Gymnasium;
70771 Leinfelden-Echterdingen (Germany)

Subjects: Mathematics, German, English, Biology, Geography

Final Mark: Abitur 2.2

Accomplishments

2 peer reviewed publication; 2 manuscripts in preparation; 1 oral presentation in an international conference; and 4 posters

October 13, 2014

D. List of publications

Published Manuscripts

1. **R. Bernhard**, S. Meini and H. A. Gasteiger,
   "On-Line Electrochemical Mass Spectroscopy Investigations on the Gassing behavior of $Li_4Ti_5O_{12}$ Electrodes and Its Origins",
   Journal of The Electrochemical Society **161** (4) A497 - A505 (2014)

2. **R. Bernhard**, A. Latini, S. Panero, B. Scrosati and J. Hassoun,
   "Poly(ethyleneglycol)dimethylether - lithium bis(trifluoromethanesulfonyl)imide, PEG500DME-LiTFSI, as a high viscosity electrolyte for lithium ion batteries",
   Journal of Power Sources **226** 329 - 333 (2013)

Manuscripts in Preparations

1. G. A. Elia, **R. Bernhard** and J. Hassoun,
   "A lithium-ion oxygen battery using a polyethylene glyme electrolyte added by ionic liquid",
   in preparation

2. **R. Bernhard**, M. Metzger and H. A. Gasteiger,
   "On-Line Electrochemical Mass Spectrometry - a Study on the Gas Evolution Behavior of Graphite Anodes Depending on the Water Content and the Quality of the SEI Layer.",
   in preparation

3. M. Philipp, **R. Bernhard**, B. Rieger and H. A. Gasteiger,
   "A green route - from Carbon Dioxide to Silyl Substituted Carbonate Electrolytes for next Generation Lithium-Ion Batteries",
   in preparation

Conference Oral Presentation

1. 225th ECS Meeting May 11 - 15, 2014 Orland Florida (USA);
   "Gassing behavior of $Li_4Ti_5O_{12}$ Electrodes and Its Origins"

Poster Presentation

1. Fundamental and Engineering Needs for Sustainable Development;
   Munich (Germany), September 17 - 19, 2012 *and*

2. Ionic Liquids for Electrochemical Devices - ILED3;
   Rome (Italy), May 30 to June 01, 2012
   Title: *"Current Collector Corrosion Studies with Different Conducting Salts for a Lithium Iron Phosphate and Lithium Titanate Battery System"*

3. 2nd Colloquium of the Munich School of Engineering (2CMSE) - Energy Challenges - Germany 2050;
   Munich (Germany); June 28, 2012 *and*

4. 6th International Renewable Energy Storage Conference and Exhibition - IRES 2011;
   Berlin (Germany); November 28 - 30, 2011
   Title: *"Long-Lasting Energy Storage System for Renewable Energies"*

On-Line Electrochemical Mass Spectrometry Investigations on the Gassing Behavior of Li₄Ti₅O₁₂ Electrodes and Its Origins

Rebecca Bernhard, Stefano Meini,[a,*,z] and Hubert A. Gasteiger[**]

Chair of Technical Electrochemistry, Technische Universität München, Garching D-85748, Germany

Lithium ion batteries containing lithium titanate (LTO), Li₄Ti₅O₁₂, as anode material are promising energy storage systems for their safety and long cycle-life. However, while there are few studies that demonstrate very long cycle-life of LTO-anode based batteries, a significant number report extensive evolution of hydrogen during cycling or storage of LTO cells ("gassing"), accompanied by strong capacity fading and poor cycling performance. Here, we analyzed LTO cells *in-operando* with on-line electrochemical mass spectrometry (OEMS) and determined the real-time concentration of evolved gases. With this method, we were able to determine a direct correlation between the amount of evolved hydrogen and the water content of the electrolyte upon charge and discharge. Our analysis suggests that the one-electron reduction reaction of water leads to hydrogen evolution and to the formation of hydroxide anions. The latter trigger a ring-opening reaction of cyclic carbonates and lead to solvent decomposition into CO₂ and carbonate oligomers (detected by ex-situ ATR-FTIR). The deposition of the latter on the electrodes is likely responsible for the performance and capacity loss over a longer time period. We propose that the gassing of LTO batteries reported in some studies is caused by water intrusion during cell assembly or by water contained in improperly dried electrodes.
© 2014 The Electrochemical Society. [DOI: 10.1149/2.013404jes] All rights reserved.

The demand for advanced energy storage systems for portable, automotive and stationary applications has dramatically increased in the last decades, triggering intensive research in the field of lithium-ion batteries (LIBs) for applications in battery electric vehicles (BEVs), plug-in hybrid electric vehicles (PHEVs), hybrid electric vehicles (HEVs) as well as for large-scale storage of renewable energy. Despite many advantages, battery safety and cycle-life, particularly at high temperatures, are critical issues that still need to be resolved. Unfortunately, for current lithium-ion batteries with graphite anodes, the stability of the anode SEI layer is dramatically reduced at elevated temperature,[1,2] leading to electrolyte decomposition, substantially reduced cycle-life, and increased cell resistance,[3,4] which may also promote the hazardous plating of metallic lithium on the negative electrode. One approach toward lithium-ion batteries with longer cycle-life and improved safety is to replace the graphite anode with a lithium titanate Li₄Ti₅O₁₂ (LTO) electrode. LTO operates at a relatively high redox potential of 1.55 V vs. Li⁺/Li,[1,5] which leads to negligible rates of electrolyte reduction, avoids the deposition of transition metals derived from the degradation of commonly used cathode materials (e.g., manganese ions from high-voltage spinel), and prevents the plating of metallic lithium during rapid charging; in addition, if compared to a graphite anode, an LTO anode reduces the risk of thermal run-away.[6–9]

The high stability of LTO was demonstrated by Zaghib et al., reporting very long cycle life of battery cells with LTO anodes and LFP (LiFePO₄) cathodes, achieving >90% capacity retention at 25°C for 20000 to 30000 cycles (≈6000–8000 hours).[5,10] However, as was pointed out recently,[1] one of the main challenges for LIBs based on LTO anodes is the frequently observed gas evolution ("gassing") during storage or cycling, leading to an observed swelling of pouch bag battery cells and a concomitant loss of capacity and power. It has been observed that pouch bag cells composed of LTO anodes, alkyl-carbonate electrolytes, and various cathode materials (NMC, LMO) swell during storage and cycling,[11–13] caused by the evolution of mostly hydrogen and carbon dioxide.[4,14]

There are several studies on the gassing issue of LTO-containing batteries. For example, He et al.,[11] studied LTO/NMC pouch cells aged under various conditions at 25°C and 50°C. The evolved gas of each cell was analyzed post-mortem with gas chromatography. It was shown that for cells stored for three months with no previous charging at 25°C and 50°C, carbon dioxide was the exclusive gaseous product which could be detected by post-mortem gas analysis (the extent of

swelling under these conditions was unfortunately not discussed). On the other hand, hydrogen was the major component (≈50–55 wt%) of the gas phase extracted from cells, which were stored in the charged state (≈2200 h) or had been cycled extensively (400 cycles lasting for ≈1600 h) at only 25°C; other gas phase constituents were CO₂ (≈30 wt%) and CO (≈10 wt%) as well as low concentrations of C₁–C₃ hydrocarbons (at <3 wt% in total). The substantial amount of evolved gas from charged and cycled cells was demonstrated qualitatively by photographs showing strongly swollen pouch bag cells after these tests. The authors rationalized their observations with a purely chemical reaction of Ti⁴⁺-species of the delithiated (i.e., discharged) Li₄Ti₅O₁₂ with alkyl carbonate solvents, which would cause the evolution of hydrogen and carbon dioxide.[11]

In similar post-mortem studies, Wu et al.[4] analyzed the evolved gases from pouch bag batteries with LTO anodes and NMC cathodes after cycling or storage (in the charged state) at temperatures ranging from 40 to 80°C. They also found hydrogen to be the main gas component at concentrations of more than 85%, together with minor concentrations of CO and CO₂ (≈4–8 wt% in total) as well as of C₁-C₃ hydrocarbons (≈1–7 wt% in total). Qualitatively, the rate of swelling was observed to increase substantially with increasing temperature. Another observation they made was a significantly accelerated aging of LTO/NMC cells cycled at elevated temperatures: while capacity retention of 90% could be maintained for 5000 cycles (≈1000 hours) at 25°C, this was reduced by an order of magnitude to only 400 cycles (≈80 hours) at 55°C.

In a later publication by the same group,[15] they hypothesized that the higher redox potential of LTO compared to graphite would be the cause for the observed gassing rather than the presence of moisture, which they rationalized by postulating a decomposition pathway for linear carbonates by which hydrogen is formed via hydrogen radical splitting from end-standing methyl groups in DMC. However, the reason for this postulated reduction process, which would not occur at the even lower operating potential of graphite anodes, was not explained.

Significant evolution of predominantly hydrogen during storage (≈3600 h) of charged battery cells with LTO anodes and LMO (LiMn₂O₄) cathodes at 60°C was also detected by means of post-mortem gas analysis by Belharouak et al.[14] In contrast to the above gassing hypotheses, these authors proposed an alternative mechanism for the evolution of hydrogen in battery cells with LTO anodes in pouch cells, namely that the hydrogen might be produced via the electrochemical reduction of water traces present inside the cell.

All of these reports on the observed strong gassing of battery cells with LTO anodes make it difficult to rationalize the exceptionally high cycle life reported for LTO/LFP cells[5,10] as well as the fact that no gassing was observed during the storage of charged LTO

Short communication

Poly(ethylenglycol)dimethylether–lithium bis(trifluoromethanesulfonyl)imide, PEG500DME–LiTFSI, as high viscosity electrolyte for lithium ion batteries

Rebecca Bernhard [b], Alessandro Latini [a], Stefania Panero [a], Bruno Scrosati [a], Jusef Hassoun [a],*

[a] Department of Chemistry, Sapienza University, Piazzale Aldo Moro 5, 00185 Rome, Italy
[b] Department of Chemistry, TU München, Lehrstuhl für Technische Elektrochemie

HIGHLIGHTS

► A PEG500DME–LiTFSI high viscosity, safe electrolyte is here reported.
► The electrolyte shows enhanced electrochemical properties.
► A battery using TiO_2 anode, $LiCoO_2$ cathode and the electrolyte is studied.
► The 2 V-battery is characterized by high stability and low polarization.
► The electrolyte is a promising candidate for application in Li-ion battery.

ARTICLE INFO

ABSTRACT

In this paper we report a poly(ethylenglycol)dimethylether–lithium bis(trifluoromethanesulfonyl) imide (PEG500DME–LiTFSI) as high viscosity, safe electrolyte for lithium ion batteries. The high molecular weight of the end-capped ether solvent is reflected as low vapor pressure and excellent thermal stability of the electrolyte, as demonstrated by thermogravimetry, this resulting in remarkable safety content. The electrochemical impedance spectroscopy study of the electrolyte demonstrates a Li-transference number of 0.48, a conductivity of the order of 10^{-3} S cm^{-1}, and a high interphase stability with the lithium metal, the linear sweep voltammetry indicates an electrochemical stability window extending up to 4.8 V vs. Li/Li$^+$. Furthermore, promising electrochemical performances in terms of reversibility, cycling stability and low charge–discharge polarization are observed using the electrolyte in lithium and in lithium ion batteries using lithium cobalt oxide (LCO) as cathode and titanium dioxide (TiO_2) as anode. Hence, this electrolyte is a promising candidate for applications in safe, high performance lithium ion batteries.

© 2012 Elsevier B.V. All rights reserved.

1. Introduction

Storage applications for electrical energy bear an important role in this century. In this respect lithium ion batteries, now largely used in the portable devices, are considered the most promising candidates as power supplies for hybrid electric vehicles (HEVs), plugged-in hybrid vehicles (PHEVs), full electric vehicles (EVs), as well side systems for renewable energies production plants, such as those based on wind and solar power. However, improvements in terms of safety and cost [1–3] are still needed in order to match the severe targets required by these emerging markets. Safety concerns are mainly associated with the high flammability of the volatile carbonated organic electrolytes commonly used in lithium ion

batteries with consequent risks of thermal runaway leading to fire or even explosive hazards [4]. Valid alternative electrolytes, characterized by low cost and high safety content, are those based on poly(ethyleneoxide), (PEO) [3]. PEO-based electrolytes in their solid amorphous state demonstrated favorable properties, such as good ionic conductivity [5], satisfactory electrochemical and interfacial stability [6] and excellent mechanical properties [5,7]. Liquid, highly viscous glymes were studied in the late 1990s by Shi et al. (1995) and Appetecchi et al. (1996) [8,9]. The results demonstrate that these electrolytes can be safely used in lithium cells. However, to fully assume cell safety, the use of anodes operating at voltages values that avoid the electrolyte decomposition is recommended. Relevant examples are lithium titanium oxide ($LiTi_5O_{12}$, LTO) and titanium dioxide (TiO_2) [10,11], that are characterized by a working voltage ranging between 1.0 and 1.5 V vs. Li/Li$^+$ [12,13].

In this scenario it has appeared to us of interest to investigate the thermal and the electrochemical properties of an electrolyte

List of Figures

177

List of Tables